Jet physics at LHC: cross-section measurement and search for new phenomena at $\sqrt{s}$ = 7 TeV with the ATLAS experiment

Dissertation
zur Erlangung des Grades
DOKTOR DER NATURWISSENSCHAFTEN
am Fachbereich Physik
der Johannes Gutenberg-Universität
in Mainz

von
Eugen Ertel
geboren in Krasnoturjinsk

Mainz, den 27.Mai 2015

Datum der mündlichen Prüfung: 14.01.2016

Abstract

The Standard Model of particle physics is so far successful in describing the fundamental particles and their interactions through the electromagnetic, weak, and strong force. However, some hints suggest physics beyond the Standard Model. At the Large Hadron Collider protons are brought to collision at high energies. The resulting final-states can be used in order to probe the Standard Model. One possibility is to use highly energetic quarks and gluons, which are observed as jets. Jet measurements can be examined for existence of particles and phenomena predicted by a number of models. Additionally, jets can be used to obtain information about phenomenological components such as the parton density distribution within the proton.

This thesis reports on the measurement of inclusive jet and dijet cross-sections using the ATLAS detector at center-of-mass energies of 7 TeV. The data used was recorded in 2011 and corresponds to an integrated luminosity of 4.5 fb^{-1}. Jets are defined using the anti-k_T algorithm with distance parameters $R = 0.4$ and $R = 0.6$. The measurement of the inclusive jet cross-section covers the kinematic region 100 GeV $\leq p_T <$ 2 TeV for rapidities of $|y| < 3.0$. The measurement of the dijet cross-section covers the dijet mass region 260 GeV $\leq m_{12} <$ 5 TeV and dijet rapidity separation of $y^* < 2.5$. The measured spectra are corrected for detector effects and are compared with theoretical predictions. The theoretical predictions are consistent with the experimental measurements within the theoretical and experimental uncertainties.

The dijet mass spectrum is used for the search of new resonant-like phenomena. The data set used for this purpose was recorded in 2011 and corresponds to an integrated luminosity of 4.8 fb^{-1}. Jets are reconstructed using the anti-k_T algorithm with the distance parameter $R = 0.6$. The dijet mass region covered is 850 GeV $\leq m_{\text{jj}} <$ 4 TeV. To suppress t-channel processes the dijet rapidity separation is constrained to $y^* < 0.6$. The background is estimated using data-based techniques. The search for local excesses and the calculation of exclusion limits for a number of heavy resonances is performed using statistical tools. No evidence for significant local discrepancies between the measurement and background was found. Therefore exclusion limits were determined. To name an example: Excited quarks with masses below 2.94 TeV were excluded at 95% Credibility Level.

Kurzfassung

Das Standardmodell der Teilchenphysik ist bisher erfolgreich in der Beschreibung der fundamentalen Teilchen und ihrer Wechselwirkungen mittels der elektromagnetischen, schwachen und starken Kraft. Es gibt jedoch Hinweise für Physik jenseits des Standardmodells. Am Large Hadron Collider werden Protonen unter hohen Energien zur Kollision gebracht. Die dabei entstehenden Endzustände können verwendet werden, um das Standardmodell der Teilchenphysik zu testen. Eine Möglichkeit der Überprüfung eröffnet sich in der Produktion hochenergetischer Quarks und Gluonen, die als Jets beobachtet werden. Jet-Messungen können verwendet werden um Teilchen und Phänomene, die durch einige Modelle vorhergesagt werden, auf ihre Existenz zu untersuchen. Jets können zusätzlich Informationen über phänomenologische Komponenten, wie die Partondichteverteilung im Proton, liefern.

Diese Dissertation berichtet über die Messungen des inklusiven Jet- und Dijet-Wirkungsquerschnitts unter Verwendung des ATLAS-Detektors bei Schwerpunktsenergien von 7 TeV. Die verwendeten Daten wurden im Jahre 2011 aufgezeichnet und entsprechen einer integrierten Luminosität von 4.5 fb^{-1}. Jets werden dabei durch den anti-k_T Algorithmus mit den Abstandsparametern $R = 0.4$ und $R = 0.6$ definiert. Die Messung des inklusiven Jet-Wirkungsquerschnitts erfolgt dabei in den kinematischen Bereichen 100 GeV $\leq p_T <$ 2 TeV für Jet-Rapiditäten $|y| < 3.0$. Die Messung des Dijet-Wirkungsquerschnitts deckt den Dijet-Massenbereich 260 GeV $\leq m_{12} <$ 5 TeV für Dijet-Rapiditäten $y^* < 2.5$ ab. Die gemessenen Spektren werden auf Detektoreffekte korrigiert und mit theoretischen Vorhersagen verglichen. Innerhalb der theoretischen und experimentellen Unsicherheiten stimmen die Messungen mit den theoretischen Vorhersagen überein.

Das Dijet-Massenspektrum wird verwendet, um nach neuen resonanten Phänomenen zu suchen. Der hierfür verwendete Datensatz wurde im Jahre 2011 aufgenommen und entspricht einer integrierten Luminosität von 4.8 fb^{-1}. Jets werden mit dem Abstandsparameter $R = 0.6$ unter Verwendung des anti-k_T Algorithmus rekonstruiert. Der abgedeckte Dijet-Massenbereich ist 850 GeV $\leq m_{\text{jj}} <$ 4 TeV. Zur Unterdrückung von Prozessen im t-Kanal werden die Dijet-Rapiditäten auf den Bereich $y^* < 0.6$ eingeschränkt. Für die Bestimmung des Untergrunds wird eine datenbasierte Methode verwendet. Die Suche nach lokalen Überhöhungen und die Bestimmung von Ausschlussgrenzen für eine Reihe von schweren Resonanzen wird unter Verwendung statistischer Werkzeuge durchgeführt. Es wurden keine lokalen signifikanten Abweichungen zwischen der Messung und dem Untergrund gefunden. Deshalb wurden Ausschlussgrenzen berechnet. Beispielsweise wurden angeregte Zustände der Quarks mit Massen unterhalb von 2.94 TeV mit 95% Credibility Level ausgeschlossen.

Contents

1 Introduction

Modern particle physics was born in the 1930s and 1940s [1]. At the beginning of this period it was considered that protons and electrons, interacting through the exchange of photons, form all matter [2]. In the 1950s and 1960s, the development of new detector and particle accelerator technologies has led to the discovery of a large number of previously unknown strongly interacting particles called hadrons. Based on these measurements a classification scheme for hadrons was developed and was used to predict the existence of the so-called omega-minus Ω^- particle [2], which was discovered in 1964 [3]. In the same year, Gell-Mann [4] and Zweig [5] proposed that hadrons could be made of particles called quarks. Results of deep-inelastic scattering experiments started in late 1960s finally suggested the existence of quarks. The subsequent developments have led to the consensus that hadrons are composed of quarks and bound by gluons and quantum chromodynamics (QCD) is the correct theory of the strong interactions [2]. Also in 1964 the so-called Higgs mechanism was proposed by different groups independently (see e.g. [6]), which provides the gauge bosons of the weak interaction with mass and introduces a new massive particle called Higgs boson. The unification of the electromagnetic and weak forces called electroweak theory exploiting the Higgs mechanism was proposed in the mid-1960s by Salam and Weinberg [7] and was experimentally confirmed in 1978 [8]. The QCD and the electroweak theory are now ingredients of the basic theory of matter called the Standard Model of particle physics.

In the following years further experimental improvements connected with the increase of accelerator energies led to the discovery of more particles. To name a few examples: the discovery of the force carriers of the weak interaction, $W^{\pm}$ and Z^0, in 1983 by the UA1 and UA2 experiments [9, 10] and the experimental evidence for the existence of the heaviest quark called top-quark by the D0 and CDF experiments at Tevatron in 1995 [11, 12]. The construction and successful commissioning of the Large Hadron Collider (LHC) and the associated experiments led to the discovery of a new particle in 2012. Essential properties of this particle as the spin [13] and the signal strength measured in various channels [14] indicate that it is the Higgs boson predicted in the context of the Standard Model.

All particles and interactions experimentally observed to-date are successfully described and predicted by the Standard Model. Nevertheless, observations made in astronomy lead to the conclusion that only around 5% of the observable universe consists of baryonic matter and approximately 27% of the so-called dark matter [15, 16], where the latter is not covered by the Standard Model. This example indicates that the Standard Model provides an incomplete picture and that physics beyond the Standard Model has to exist. Also theoretical considerations give rise to the conclusion that the Standard Model provides an imperfect description of nature. An example is the so-called hierarchy problem. It is related to the question why the two fundamental scales, the electroweak scale and the scale of gravity called Planck scale, are very different. This problem has been one of the

driving motivations for models beyond the Standard Model.The LHC enables the possibility to test the Standard Model in unprecedented kinematic regions and search for new physics beyond the Standard Model. The dominant processes at LHC are governed by the strong interaction where quarks and gluons are involved. Final states of quarks and gluons can be observed as so-called jets. The measurement of the production cross-section of jets can be used to test QCD predictions. Jets can also be exploited in order to search for resonant-like phenomena in invariant mass distributions. A range of theoretical models predicting particles beyond the Standard Model are available, which can be used to determine exclusion limits using jet measurements.

This thesis covers the measurement of the inclusive jet and dijet cross-section and the search for new resonant-like phenomena exploiting dijet final states. The measurements were performed using the ATLAS experiment at LHC. In Chapter 2 the theoretical framework focusing on the strong interaction is summarized and a brief overview of new physics models used is given. In Chapter 3 the theoretical predictions made for the cross-section measurements in order to test the QCD predictions are presented. An introduction to the LHC and the ATLAS experiment is provided in Chapter 4. The techniques used in order to calibrate the jets are presented in Chapter 5 and 6. Furthermore the performance of the jets within the given experimental environment is discussed. In Chapter 7 the systematic uncertainties are briefly reviewed, which are essential in order to assess the results of comparisons between measurements and predictions. The correction for detector effects plays an essential role in order to directly compare the measurements and predictions. This subject, the results of the measurements and their comparison to the predictions are discussed in Chapter 8. In Chapter 9 the search for resonant-like phenomena is presented. The techniques used to search for new physics are reviewed and the results are discussed.

2 The theoretical framework

2.1 The Standard Model

The Standard Model (SM) of particle physics describes the interactions between elementary particles according to the strong, weak, and electromagnetic force, which are three of the four known forces. In this context two types of elementary particles are postulated. The first type of particles are fermions, which carry a half-integer spin as for example the electron. The second type of elementary particles with integer spin are the so-called bosons. These include gauge bosons, which act as force carriers between the fermions, and the Higgs boson.

In the 1950s and 1960s a large number of new particles were discovered. The new particles were classified in baryons and mesons according to their mass, which form subclasses of the so-called hadrons. The attempt to classify the newly discovered hadrons finally led to the development of the quark-model [4]. In the quark-model, hadrons are bound-states of a new type of elementary particles, the so-called quarks. In the context of this model, a quark (q) and anti-quark ($\bar{q}$) can be of three flavors (up (u), down (d) and strange (s)) and carries an electrical charge of $\pm\frac{1}{3}e$ and $\pm\frac{2}{3}e$, where e is the charge of the electron. The mesons are composed of $q\bar{q}$ pairs and the baryons of three quarks. For instance, a neutron is composed of two down-quarks and one up-quark denoted as ddu. The model was successful in classifying the observed hadrons and e.g. predicted the Ω^- baryon, which was discovered in 1964 [3].

However, this model was not able to explain some observations at that time. In order to explain the existence of particles as e.g the Δ^{++} baryon an extension of the quark model became necessary. In the quark model, the Δ^{++} baryon is composed of three up-quarks. Baryons as well as quarks are fermions and have to be described by an antisymmetric wave function. The Δ^{++} is a baryon, but has a symmetric wave function, which contradicts to the Pauli exclusion principle. This problem was solved by the introduction of a new quantum number carried by the quarks and referred to as color. The quarks carry the colors red (R), green (G), and blue (B), while anti-quarks carry anti-red ($\bar{R}$), anti-green ($\bar{G}$), and anti-blue ($\bar{B}$). As a force carrier between the color-charged quarks, the gluon was introduced, which carries color and anti-color. In order to account for the fact that quarks and gluons were not observed as free particles, the assumption was made, that bound-states only occur as color-singlet (i.e. color-neutral) states. This property and the fact that quarks within the proton behave nearly as free particles resulted in the so-called confinement.

In the course of time three additional quarks were discovered referred to as charm (c), bottom (b), and top (t). Along with the leptons and the force carriers, quarks belong to the class of elementary particles of the SM. An overview of the elementary particles and a selection of its properties is given in Fig. 2.1. The elementary particles as well as

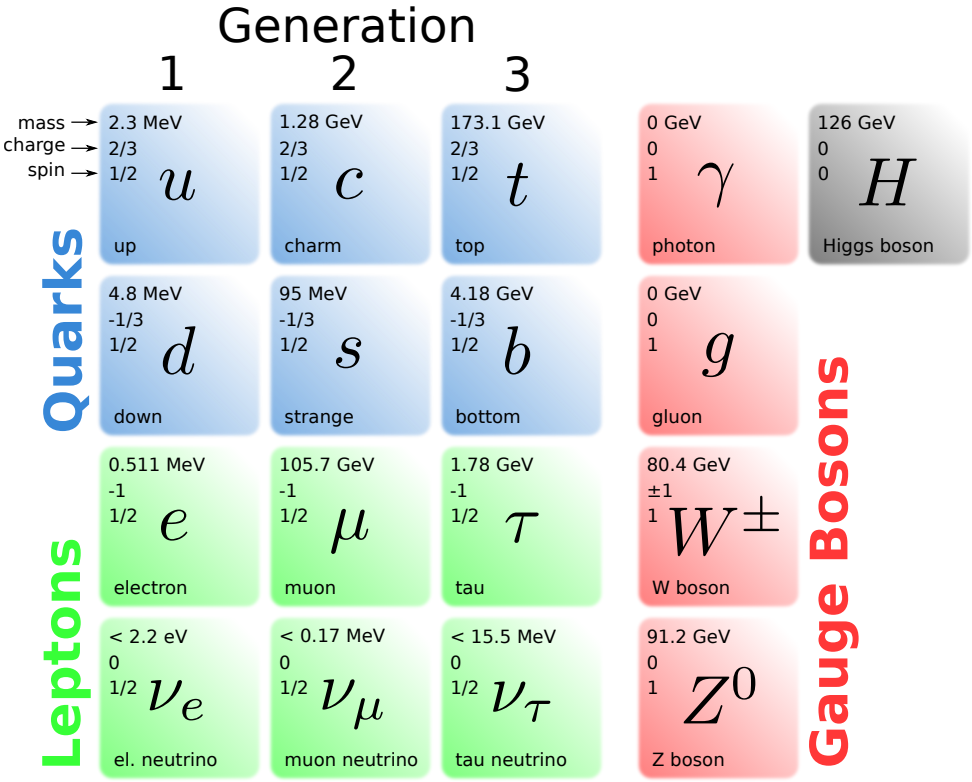

Figure 2.1: The elementary particles of the Standard Model and a selection of corresponding properties. For each fermion an anti-particle with opposite charge exists. The properties are taken from Ref. [17]. In this case natural units with $\hbar = c = 1$ were used.

two force mediators carry mass, which can be introduced through the Higgs mechanism [6] in the SM. Furthermore, they are assumed to be point-like supported by the existing experimental results. Leptons and quarks can be categorized in three generations. For example, the first generation of quarks include the up- and down-quark and in case of leptons, the electron and the corresponding neutrino. Except for the mass, the properties of the particles of different generations are the same. With increasing generation number, the mass increases leading to the fact, that higher generation particles decay into stable first-generation particles. Thus, the stable matter is composed of particles of the first generation.

2.1.1 The Electroweak Theory

The unification of the Quantum Electrodynamics and the weak theory is called the electroweak (EW) theory and was introduced by Glashow, Weinberg, and Salam [7]. The electroweak theory is based on the assumption, that the electromagnetic and weak interactions are two manifestations of the same force. It can be described in group theory as SU(2)×U(1) and the requirement of local gauge invariance under local gauge transformation results in four gauge fields. The photon γ, the Z^0 and the $W^{\pm}$ are the so-called gauge bosons and are the consequence of mixed states of the gauge fields. In the context of the electroweak theory all gauge bosons are predicted to be massless. However, in nature the force carriers Z^0 and the $W^{\pm}$ are massive.

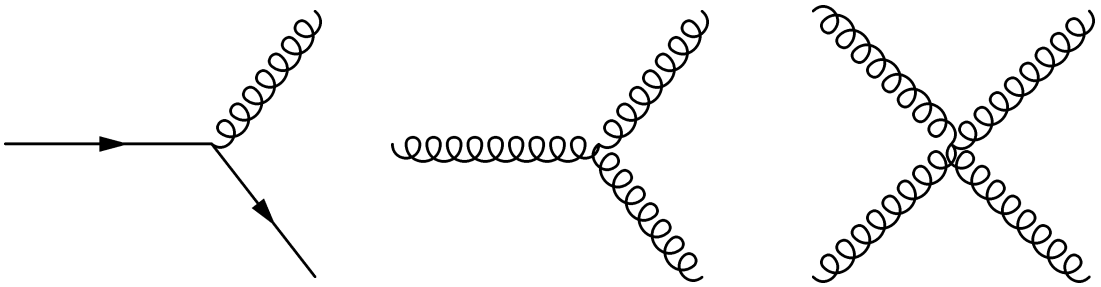

(a) (b) (c)

Figure 2.2: The fundamental interaction of the QCD. The solid lines represent fermions (quarks) and the curly lines represent gluons. The diagrams can be conceived as follows: a quark emits a gluon (a), a gluon splits into two gluons (b), and the four-gluon interaction (c). By rotating of e.g. the representation (a) the diagram can represent a quark-antiquark annihilation or gluon splitting into a quark-antiquark.

As a consequence the underlying symmetries have to be broken. The masses of the gauge bosons as well as of the fermions are introduced by a concept called spontaneous symmetry breaking. In the SM the spontaneous symmetry breaking is realized by adding a complex scalar doublet Higgs field, which interacts with particles. This mechanism provides the Z^0 and the $W^{\pm}$ bosons with mass. The introduction of the Higgs field implies a massive neutral scalar boson called Higgs boson, which was one of the main motivations for the realization of the LHC and the associated experimental apparatuses. The masses of the fermions can be introduced through their coupling to the Higgs field denoted as Yukawa-couplings. With increasing strength of this coupling to the Higgs field the mass of the particle increases.
In 2011 and 2012 a significant excess in several decay modes was observed. Fundamental properties of this particle as the spin [13] and the signal strength measured in various channels [14] indicate that it is the Higgs boson predicted in the context of the Standard Model.

2.1.2 Quantum Chromodynamics

The theory of gluon and quark interactions is called Quantum Chromodynamics (QCD). Quarks and gluons carry the charge of the strong interaction, the so-called color. Three types of QCD-colors exist: red (R), green (G), and blue (B). By analogy with the EW theory, the requirement of the invariance under the symmetry group SU(3) introduces eight gauge fields, which represent the gluons. In contrast to QED with its electrically neutral force carrier, the gluons carry color-charge. A consequence of this property is the gluon self-interaction, which is an implication of the non-Abelian structure of SU(3).

The dynamics of the strong interaction is described by the following Lagrangian density [17]:

$$\mathcal{L}_{\mathrm{QCD}} = \sum_q \bar{\psi}_{q,a}(i\gamma^\mu \partial_\mu \delta_{ab} - g_s \gamma^\mu t^C_{ab} \mathcal{A}^C_\mu - m_q \delta_{ab})\psi_{q,b} - \frac{1}{4} F^A_{\mu\nu} F^{A\,\mu\nu}, \tag{2.1}$$

where γ^μ are the Dirac γ-matrices, $\mathcal{A}_\mu^C$ are the gluon fields with the color-index C running from 1 to 8, $\psi_{q,a}$ are the quark-field spinors for a quark of flavor q and mass m_q [1] with the color-index a running from 1 to 3, t_{ab}^C are the generators of the SU(3) group, and g_s is the QCD coupling constant. The gluon field tensor $F_{\mu\nu}^A$ in the purely gluonic part of Eq. 2.1 is given by:

$$F_{\mu\nu}^A = \partial_\mu \mathcal{A}_\nu^A - \partial_\nu \mathcal{A}_\nu^A - g_s f_{ABC} \mathcal{A}_\mu^B \mathcal{A}_\nu^C \text{ with } [t^A, t^B] = i f_{ABC} t^C, \tag{2.2}$$

where f_{ABC} are the so-called structure constants of the SU(3) group defined through the commutators $[t^A, t^B]$. The three fundamental vertices, which can be used to construct any QCD process, are described by the Lagrange density $\mathcal{L}_{\text{QCD}}$ and are shown in Fig. 2.2. The three terms (cf. Eq. 2.1) within the brackets are the Dirac-Lagrangian of the free fermion including the term $g_s \gamma^\mu t_{ab}^C \mathcal{A}_\mu^C$, which describes the interaction between gluons and quarks (a). The term $\frac{1}{4} F_{\mu\nu}^A F^{A\,\mu\nu}$ describes the gluon self-interaction. The triple-gluon vertex (b) comes from the product of $\partial_\mu \mathcal{A}_\nu$ and $g_s f_{ABC} \mathcal{A}_\mu^B \mathcal{A}_\nu^C$, while the four-gluon vertex (c) originates from the product of the two double gluon field terms. Thus, the interactions (a) and (b) are of order g_s and the four-gluon vertex (c) is of order g_s^2. The gluon self-interaction is a major difference to the QED and leads to the so-called asymptotic freedom and confinement. At short distances (high energy scales) the gluons and quarks behave as free particles and are confined at large distances (low energy scale). The properties of the QCD are discussed in more detail in the sub-sections below.

Perturbative QCD

The observables connecting the theoretical predictions and experimental measurements are e.g. cross-sections. Feynman diagrams can be used to calculate the cross-section of an arbitrary process by deploying the so-called Feynman rules, which provide a mathematical description of each fundamental interaction (cf. Fig. 2.2). This tool allows to calculate the cross-section of complex processes, which are represented by Feynman diagrams consisting of several fundamental interactions.

QCD can be treated in a perturbative way at energy scales much larger compared to the fundamental scale of this theory and is denoted as pQCD. The cross-section can then be written as expansion in powers of the strong coupling constant $\alpha_s = \frac{g_s^2}{4\pi} \ll 1$ as follows[2]:

$$\hat{\sigma} = \sigma_1 \alpha_s + \sigma_2 \alpha_s^2 + O(\alpha_s^3) \tag{2.3}$$

where σ_k are cross-section contributions at a given order of α_s. The result of Eq. 2.3 is the so-call partonic cross-section $\hat{\sigma}$ for processes with quarks and gluons in the initial- and final-states. Examples of Feynman diagrams contributing to the cross-section at leading-order (LO) and next-to-leading (NLO) order are shown in Fig. 2.3. For the $2 \to 2$ parton scattering the LO contributions to the cross-section are of $O(\alpha_s^2)$ and examples are shown in Fig. 2.3 (a). The NLO corrections are of $O(\alpha_s^3)$ and comprise real contributions ($2 \to 3$ scatterings as shown in Fig. 2.3 (b)) and virtual contributions ($2 \to 2$ scattering with one loop as shown in Fig. 2.3 (c)).

[1] The mass of the quarks can be explained through Yukawa interactions with the Higgs field (cf. Sec. 2.1.1).

[2] The coupling α_s depends on the energy scale as discussed in Sec. 2.1.2. This approach is reasonable for energy scales, which are large enough to allow perturbative calculations.

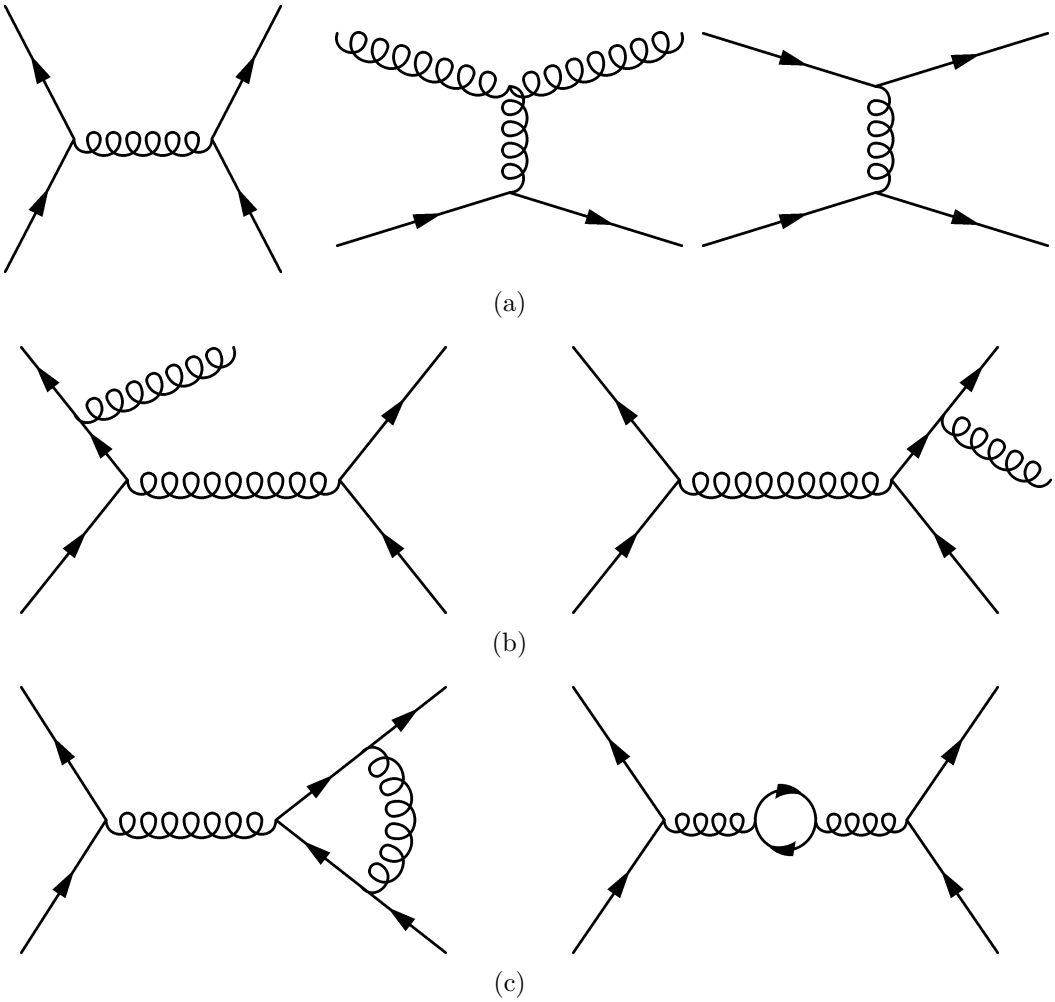

Figure 2.3: An exemplary selection of QCD Feynman diagrams at LO and NLO. (a) Tree-level (LO) diagrams. (b) Real NLO contributions: initial-state radiation (ISR, left) and final-state radiation (FSR, right). (c) Virtual one-loop NLO contributions. Quarks are represented by lines and gluons are shown by curly lines. The point at which lines come together is called vertex.

In general, real emissions of the type shown in Fig. 2.3 (b) and loop corrections as shown in Fig. 2.3 (c) lead to divergencies, which can be categorized in collinear, infrared (IR), and ultraviolet (UV) divergencies. The collinear and IR divergencies are due to the fact, that the probability for a quark to radiate a gluon becomes infinite for $\theta_{qg} \to 0$ (collinear) and $E_g \to 0$ (soft or infrared), where θ_{qg} is the angle between the partons and E_g is the energy of the emitted gluon. However, the cross-section must be finite. The real as well as the virtual contributions are divergent on their own and must cancel. This is realized by the regularization in the real emission phase-space integral and for the integration over loop momenta of the virtual contributions. The cancellation is valid for the class of the so-called collinear- and IR-safe observables, which have a minimal sensitivity to physics at low-energy scale (see Sec. 2.2).

Final-states in e.g. NLO pQCD calculation of the $2 \to 2$ process do not comprise subsequent soft radiations, which might change the observables and their inner structure.

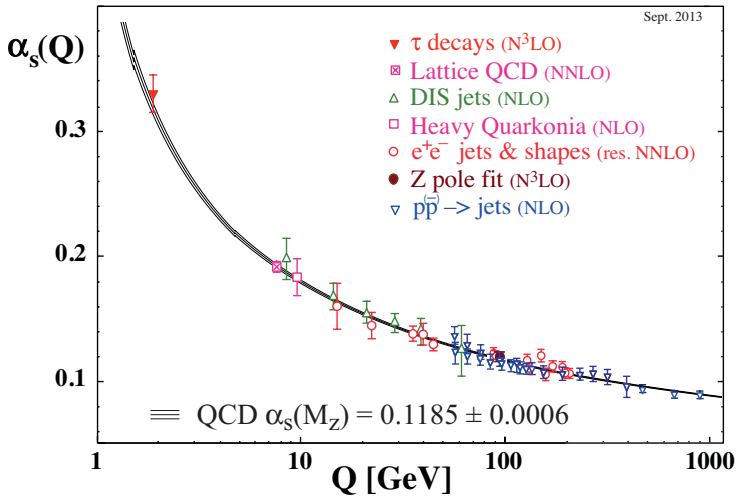

Figure 2.4: The running of the strong coupling α_s as function of the energy scale Q [17].

The incoming and outgoing partons of the $2 \to 2$ process undergo a splitting into further partons called parton shower. The generation of splitting is modeled using the so-called Sudakov form factor, which is the probability of not radiating a gluon between the scales Q_0 and Q. The splittings are generated ordered in Q between the scales Q_i and Q_{i-1}, where $[Q_0, Q]$ is divided in sub-intervals $[Q_{i-1}, Q_i]$. The procedure is repeated until the next generated gluon is below a non-perturbative cutoff scale Q_0. The choice of the ordering quantity Q can be e.g. p_T, which is realized in the PYTHIA 6 [18] Monte Carlo generator. For the HERWIG++ generator [19] angular ordering is used. [20]

Running of the Strong Coupling

Ultraviolet (UV) divergencies due to infinite vacuum polarization loop momenta appearing in QCD calculations have to be renormalized to provide meaningful finite results. In the context of the charge renormalization, the bare charge q_0 is substituted by the measured charge $q(\mu)$ at a given energy scale μ, which contains contributions from the vacuum polarization. The dependence of the strong coupling constant on the energy scale is described by the so-called renormalization group equation, which evolves the physical parameter α_s from one scale to another [17]:

$$\mu^2 \frac{\partial \alpha_s(\mu^2)}{\partial \mu^2} = \beta(\alpha_s(\mu^2)), \text{ with } \beta(\alpha_s) = -\alpha_s^2(b_0 + b_1\alpha_s + O(\alpha_s^2)), \tag{2.4}$$

where $b_0 = (11C_A - 2N_f)/12\pi$, and $b_1 = (17C_A^2 - 5C_A N_f - 3C_F N_f)/24\pi^2$. The parameters defining the coefficients b_0 and b_1 are the number of quark flavors N_f, and the QCD color factors $C_A = 3$ and $C_F = 4/3$. An exact solution of equation Eq. 2.4 at lowest order of the β-function is then given as:

$$\alpha_s(\mu^2) = \frac{\alpha_s(\mu_R^2)}{1 + b_0\alpha_s(\mu_R^2)\ln\frac{\mu^2}{\mu_R^2}} = \frac{1}{b_0 \ln\frac{\mu^2}{\Lambda_{QCD}^2}}, \tag{2.5}$$

where μ_R is a reference scale also denoted as renormalization scale and $\Lambda_{QCD} \approx 200$ MeV the fundamental scale of the QCD. Due to gluon self-coupling, the β-function has a neg-

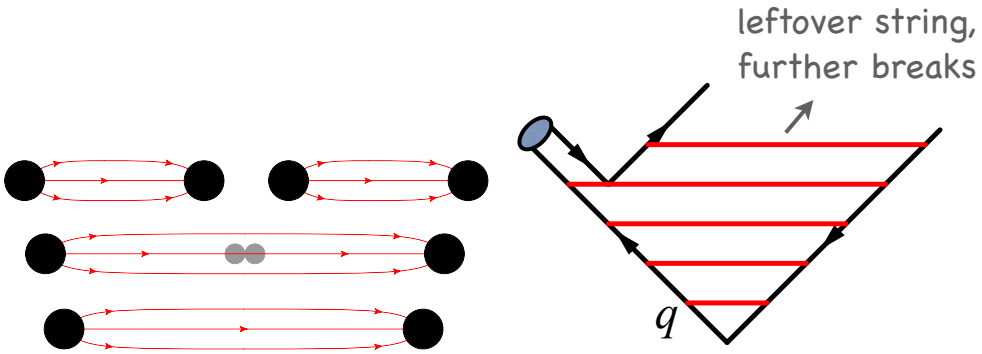

Figure 2.5: Left: pictorial representation of a string break with increasing distance between the quarks and the creation of a new quark-antiquark pair. Right: sketch of the hadronization process as realized e.g. in the Lund String model [21].

ative sign which results in the asymptotic freedom[3]. The running of the strong coupling constant α_s as function of the energy scale $\mu \sim Q$ is shown in Fig. 2.4. The $\alpha_s(Q)$ values were determined experimentally and are shown together with the theoretical prediction. The world average of the strong coupling was determined to be $\alpha_s(M_Z) = 0.1185 \pm 0.0006$ at the mass M_Z of the Z^0 boson [17].

The running of the coupling constants can be interpreted as a screening of the particle charge. In case of the QED, the screening is due to e.g. virtual e^+e^--pairs produced in the vacuum, which are polarized due to the electric field of a single charged particle. The effective charge of the particle is reduced by the fermion-anti-fermion pairs with increasing distance. The running of the electromagnetic coupling constant α reflects this effect: the coupling decreases with increasing distance. By analogy with the QED, virtual $q\bar{q}$-pairs can be produced out of gluons and cause a screening of the color charge. Because of the gluon self-interaction virtual gg-pairs are produced, which increase the color charge with increasing distance. This effect compensates the screening caused by $q\bar{q}$-pairs and is denoted as anti-screening.

As a consequence of the running of coupling constant α_s, strong interaction can be subdivided into two regimes. At low-energy scales, where α_s increases (confinement), the QCD regime is called non-perturbative. Perturbative treatment of QCD is not possible in this regime and theoretical predictions are produced using phenomenological models. At high-energy scales α_s decreases (asymptotic freedom), and thus the QCD can be treated perturbatively. Furthermore, the running of α_s as function of the energy scale Q has experimental implications as discussed in the next sub-section.

Non-perturbative QCD

As a consequence of confinement, quarks can not be observed as free particles and occur in color-less bound states the so-called hadrons. Collimated spray of hadrons, which form so-called jets (cf. Sec. 2.2), can then be detected by an experimental apparatus. The

[3]This holds in case of QCD, where the corresponding number of quark flavors $N_f = 5$ and color factors $C_A = 3$ and $C_F = 4/3$. A larger number of flavors result in a theory which is not asymptotic free.

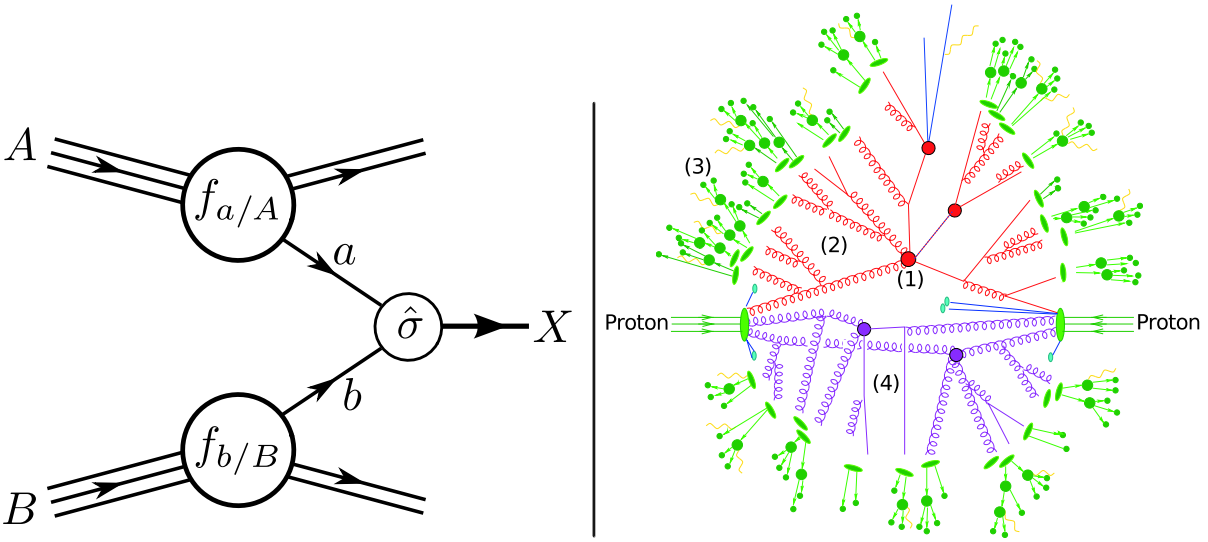

Figure 2.6: Left: illustration of the hard scattering process. Right: an example of a pp collision and the resulting interactions covering different aspects of the QCD - hard scattering (1), ISR, FSR, and parton shower (2), hadronization (3), underlying event (4) [22].

process of forming hadrons is denoted as fragmentation or hadronization. The transition from partons to hadrons is of non-perturbative nature and cannot be solved from first principles. Several models exist, which aim to describe the hadronization process. These models contain a number of parameters which have to be tuned against experimental results. Two examples are the Lund String Model and the Cluster Model. The former is implemented in the PYTHIA 6 [18] Monte Carlo generator and the latter e.g. in the HERWIG++ generator [19].

With increasing distance r between the quark and the anti-quark, the potential energy $V(r) \propto r$ increases[4] forming a string-like potential. New quark-antiquark pairs can be produced inside the string field, breaking the string into two separate ones as illustrated in Fig. 2.5 (left). The new strings can break resulting in further strings. If the relative momentum of a quark-antiquark pair is low enough, on-mass shell hadrons are produced and the cascade stops. In the Lund String model the string breaking start with the leading hadrons, which contain the initial quarks. The breaking of the string is iterated towards the center of the string, generating a single on-shell hadron at each step, where the side at which the fragmentation occur is alternated randomly. This procedure is illustrated in Fig. 2.5 (right). In the Cluster hadronization model, the perturbative evolution of gluons and quarks results in color-singlet pairs located close in phase-space. These pairs are referred to as clusters. The clusters decay isotropically according to their phase-space into hadrons. [21]

2.1.3 Proton-proton collisions

Due to the confinement, partons do not exist as free particles for a time longer than $1/\Lambda_{\mathrm{QCD}}$. Nevertheless, interactions between partons can be realized e.g. in proton-proton

[4]The short-distance Coulomb term $\propto \frac{1}{r}$ is neglected in the context of the Lund String model [18].

(pp) collisions. The proton is a composite object. It consists of three so-called valence quarks (uud), which exchange gluons and are responsible for the proton quantum numbers. These gluons can split in quark anti-quark pairs, which are denoted as sea quarks. Within the proton, partons are permanently emitted and absorbed. In case the proton is boosted such that the transverse momenta of the partons become negligible, the momentum p_{part} of the parton can be expressed as the fraction x of the proton momentum P: $p_{\text{part}} = xP$. The quantity x is referred to as Bjorken-x.

In order to calculate the partonic cross-section the knowledge of the incoming parton momenta is needed. In the experimental environment, the types as well as the momenta of the interacting partons can only be controlled to a certain extent[5] and are distributed within the proton. This distribution is described by so-called Parton Density Functions (PDF). The PDFs are considered to be independent of a particular process and cover the long-distance QCD regime. The independence of long-distance and short-distance processes is reflected by the factorization theorem [21]. As illustrated in Fig. 2.6 (left), it is then possible to calculate the cross-section $\sigma^{AB\to X}$ to produce a final-state X as a convolution of non-perturbative PDFs $f(x, \mu_F^2)$ and perturbatively calculated partonic cross-secion $\hat{\sigma}^{ab\to X}$ [21]:

$$\sigma^{AB\to X} = \sum_{a,b} \int_0^1 dx_a \int_0^1 dx_b f_{a/A}(x_a, \mu_F^2) f_{b/B}(x_b, \mu_F^2) \hat{\sigma}^{ab\to X}(Q^2, \mu_R^2, \mu_F^2), \tag{2.6}$$

where A/B are the incoming protons, and a/b are the parton types. The PDF $f_{a/A}(x, \mu_F^2)$ is a parametrization of the parton distribution inside the proton A. It is the effective density of partons of type and flavor a for a given momentum fraction x_a, when the proton A is probed at the scale μ_F and contains all unresolved emission below μ_F. The partonic cross-section $\hat{\sigma}^{ab\to X}$ is calculated in pQCD as expansion in α_s and comprises hard emissions above the scale μ_F only. Thus the factorization scale μ_F can be thought of as a scale that separates the non-perturbative and perturbative components given in Eq. 2.6. For the cross-section predictions in context of the upcoming analysis, the factorization scale μ_F was set to be equal to the renormalization scale μ_R (cf. Chap. 3).

A more complete picture of a pp collision and the resulting interactions is shown in Fig. 2.6 (right). Because of the composite structure of the proton, more than one pair of partons can interact in the same pp collision. After the partons participating in the hard process have been scattered off, the remaining partons (beam remnants), which carry a fraction of the incoming proton momenta can participate in additional interactions. This fact is denoted as multiple parton interactions (MPI) resulting in the so-called underlying event (UE), which increases the amount of energy per unit area. Usually it is modeled by additional $2 \to 2$ scatterings, which take place at scales of the order of few GeV. In order to be able to compare theoretical predictions and experimental results, the UE has to be modeled, which introduces parameters. These parameters have to be extracted from measurements as done e.g. in Ref. [23]. The process of iteratively improving the model parameters is called tuning.

[5] This can e.g. be realized through the center-of-mass energy $\sqrt{s}$ of the colliding protons.

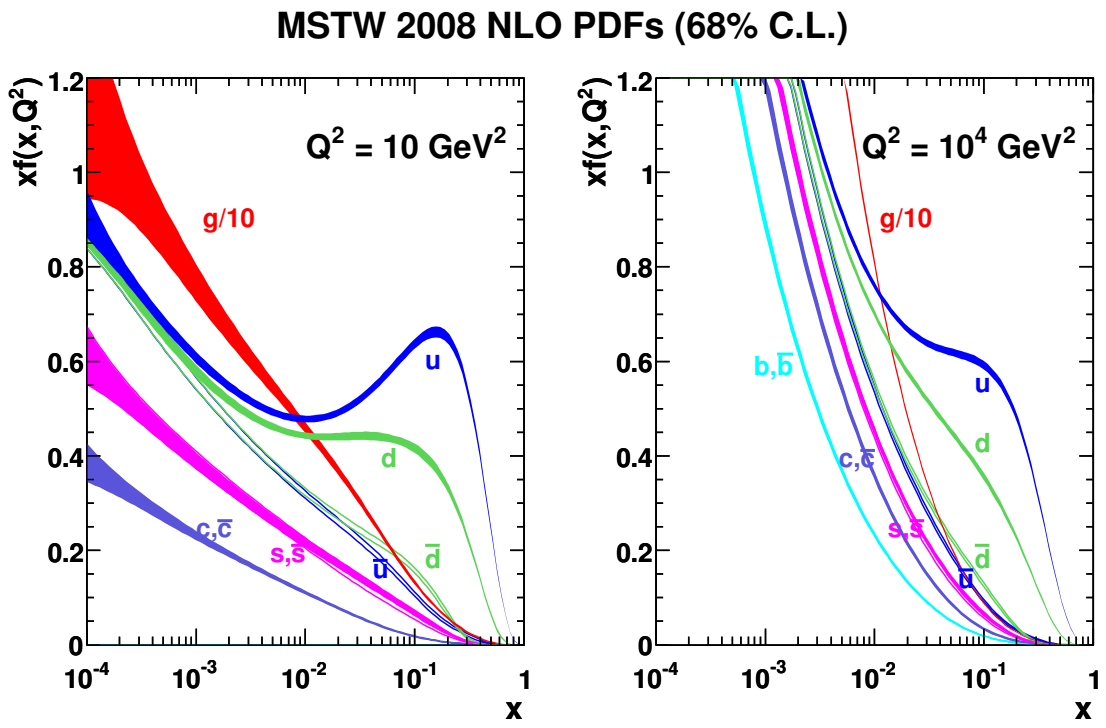

Figure 2.7: MSTW 2008 PDF NLO for the momentum transfers $Q^2 = 10$ GeV^2 and $Q^2 = 10^4$ GeV^2 [24]. The colored bands correspond to PDF uncertainties.

2.1.4 Parton Distribution Function

The PDFs cover the non-perturbative part of the cross-section calculation and their normalization at a given scale μ_F is not provided by calculations. In contrast to α_s, where UV divergencies are regularized (cf. Sec. 2.1.2), the PDFs absorb the collinear and infrared divergencies. The PDFs are determined in fits using various numbers of experimental results as input. The time-dependent dynamics inside the proton is dominated by partons which are constantly being emitted and absorbed. The probabilities for theses processes are given by the so-called Altrarelli-Parisi splitting functions $P_{ab}(z)$ [25]. For instance, the probability for a quark to radiate a gluon with the remaining momentum fraction z of the original quark momentum is given by the splitting function:

$$P_{qq}(z) = C_F \left(\frac{1+z^2}{1-z} \right), \tag{2.7}$$

where $C_F = \frac{4}{3}$ is the gluon color factor. For the infrared divergence $(1-z) \to 0$ (gluon becomes soft) the probability becomes infinite. The splitting functions are components of the so-called DGLAP equations, which are used to propagate PDFs between different energy scales.

As an example, the PDFs at two different scales Q^2 are shown in Fig. 2.7. In the context of a 'naive' quark model the three valence quarks are expected to carry the total proton momentum. However, in nature approximately 50% of the proton momentum is carried by gluons and 50% by the valence- and sea-quarks. The largest change of the PDFs as function of the scale Q^2 can be observed for the distribution of sea-quarks and

gluons in the low-x regime. This effect is due to the increasing probability to resolve soft $q \to qg$, $g \to q\bar{q}$, and $g \to gg$ splittings with increasing scale Q^2. Thus, the intrinsic proton structure depends on the scale at which the proton is probed and the evolution described by the DGLAP equations can be conceived of as the effect of increasing the resolution scale.

The shape and normalization of PDFs are not provided by pQCD calculations and have to be determined experimentally. For this purpose so-called PDF fits are performed, which make use of the DGLAP equations to treat the experimental results determined at different energy scales. The parton distributions are parametrized at an arbitrarily chosen starting scale Q_0, typically of the order of a few GeV. Several considerations enter the choice of the function which is used to parametrize the PDFs at a given momentum scale. For example, the valence quark distribution has a maximum around $\frac{1}{3}x$, while the gluon distribution is expected to increase with decreasing x due to enhanced splittings into gluons. At each iteration of the fitting procedure, the initial parametrization is evolved to the scale of the measurement at which the experimental outcome is compared to the theoretical predictions at e.g. NLO. As observable for this comparison e.g. the inclusive jet cross-section can be used, whose measurement is detailed in chapter 8. The PDF parameters are determined by minimizing the χ^2 determined from this comparisons[6]. Several collaborations provide PDFs by fitting experimental results. The PDFs used in the context of this thesis are: CT10 [26], MSTW 2008 [24], and NNPDF 2.3 [27].

Various sources of uncertainties contribute to the total uncertainty on the PDFs. The total uncertainties are shown as bands in Fig. 2.7. Contributions to the total uncertainty arise from experimental uncertainties consisting of statistical and systematic uncertainties, uncertainties due to the choice of parametrization at the scale Q_0, and theoretical uncertainties. The latter comprise for example uncertainties due to the DGLAP evolution, and factorization and renormalization scale choice. The treatment of uncertainties differs between the PDF collaborations. Also the strong coupling $\alpha_s(M_Z)$ is treated differently by the PDF groups. It is used as a free parameter in the fitting procedure, as well as a fixed parameter. The uncertainty is estimated by varying α_s according to the α_s value provided by the PDF groups. For each value of α_s a separate PDF is provided.

2.2 The Jet Finding Algorithm

In order to be able to compare experimental data with pQCD predictions, jet algorithms are used. The jet algorithm is a set of rules describing how to transform a list of particles to a list of jets. The behavior of a given jet algorithm is controlled by the parameter R, which quantifies the angular reach. As input for the jet algorithm, 4-vectors of e.g. particles are used. The method describing how to combine the 4-vectors inside a jet is

[6] Thus, the PDF is extracted from e.g. measured cross-sections. It is not physically observable and can only be defined within a particular factorization scheme for a fixed order in perturbation theory. A simple probabilistic interpretation of the PDFs holds only at leading-order, where it is the parton density number. For example at NLO, a more complicated connection between the measured cross-section and the PDFs exists, which originates from the interplay between the NLO corrections to the LO cross-section and the PDFs. For a more detailed discussion see Ref. [21].

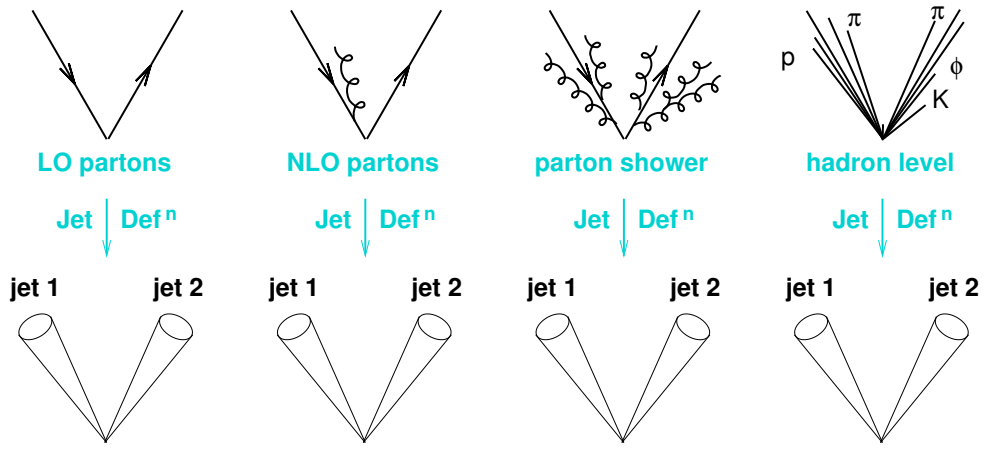

Figure 2.8: Sketch of possible levels of simulation at which a jet can be reconstructed [20]. The reconstruction of jets at detector-level, which is not indicated in this figure, is introduced in Sec. 5.3.

denoted as recombination scheme[7]. A jet is defined through the algorithm, the corresponding parameter R, and the recombination scheme and result in a massive jet[8].

The jet definition is required to be insensitive to modifications through soft and collinear emissions, which occur e.g. in parton showers. This fact is reflected in Fig. 2.8 showing different types of inputs which can be used to reconstruct jets and produce theoretical predictions. The parton-level jets are reconstructed using final-state partons predicted in the context of e.g. NLO perturbative QCD calculations (second from left). Jets can also be reconstructed at particle-level (hadron-level) using particles resulting from hadronization (right). The aim of a jet algorithm is to provide a quantity which should be independent of a particular level at which the jet was reconstructed. Thus, in an ideal scenario the reconstructed jets are required to be identical at each input-level.

Two types of jet definitions are briefly discussed in the following: the cone algorithms and the sequential-recombination algorithms. A more detailed discussion is given in Ref. [29, 20]. In general, the cone algorithms group together particles within a cone with a radius R in pseudorapidity and azimuth (cf. Sec. 4.2.1). As an example, the intermediate steps of a simple iterative cone algorithm are summarized in the following:

1. For a given event, the final-state particles are sorted according to the transverse momentum p_T. The particle with the highest p_T is used as starting point, which is denoted as seed.

2. All particles within a cone of the radius R around the seed particle are identified.

3. The particles are recombined and the direction of the sum of the momenta is determined. In case the direction of the sum does not correspond to the direction of the seed, the direction of the sum is used as the new seed direction. This procedure

[7] The scheme of simply adding 4-momenta is called *E-scheme* and is used in the upcoming analyses. The description of other recombination schemes can be found in Ref. [28]
[8] As a consequence jets are not the direct representation of the massless partons.

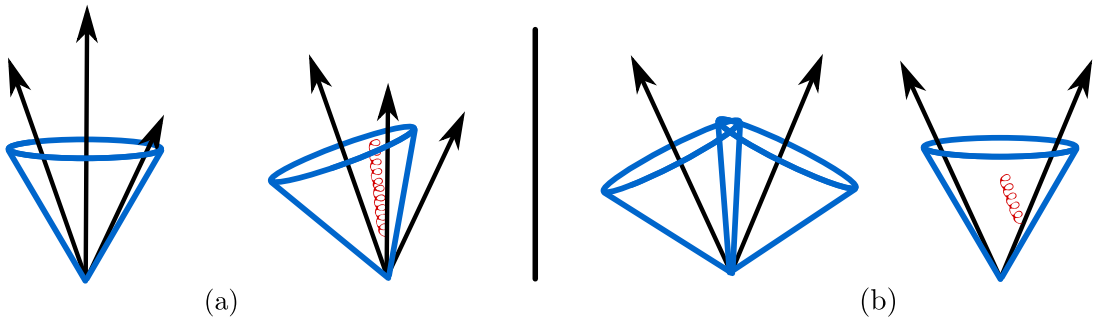

Figure 2.9: (a) Example of an algorithm, which is not collinear-safe. The presence of an additional collinear gluon (red) in the event leads to a new leading parton and therefore affects the jet reconstruction. (b) Example of a jet finding algorithm, which is not infrared-safe. A soft gluon emission affects the number of reconstructed jet in the event.

is repeated until a stable cone is found. This is the case, if the direction of the sum corresponds to the direction of the seed.

4. All particles contributing to the new jet are removed from the list of final-state particles. The steps 1-3 are repeated until the list of particles is empty.

The cone algorithm described above does not meet the requirement on collinear-safety. This is due to the fact that the transverse momentum p_T is used to find the first seed. The problem is illustrated in Fig. 2.9 (a). The kinematic variable p_T is not collinear-safe and another particle can become the particle with the highest p_T, if p_T changes in case of collinear splitting. As a consequence a different set of jets can be reconstructed in the same event.The collinear-unsafety can be avoided e.g. by using all particles as seed. This procedure results in a list of stable cones for each seed particle. A split and merge method is then applied to assign particles to a single jet, which are covered by multiple stable cones. But such a jet algorithm introduces an IR-unsafety as illustrated in Fig. 2.9 (b). An additional soft particle changes the list of seeds and can result in an additional stable cone, which can modify the final jets list of the event. Many implementations of the cone algorithms exist, which are either collinear-unsafe or IR-unsafe. However, an example for a cone algorithm, which is collinear- and IR-safe is the so-called Seedless Infrared Safe Cone (SISCone) [30].

The second class of jet algorithms is based on the sequential recombination of particle pairs, trying to invert the splittings of the parton shower. For each pair of particles ij an inter-particle distance is defined as follows:

$$d_{ij} = \min(p_{T,i}^{t}, p_{T,j}^{t}) \frac{\Delta R_{ij}^2}{R^2}, \tag{2.8}$$

where $p_{T,i}^{t}$ is the transverse momentum of particle i for the algorithm type defined by parameter t, $\Delta R_{ij}^2 = (y_i - y_j)^2 + (\phi_i - \phi_j)^2$ is the inter-particle distance in the y-ϕ-plane[9], and R is the parameter of the algorithm. These algorithms are based on the so-called k_t algorithm using $t = 2$. The basic steps of the procedure are given in the following:

[9] ϕ is the azimuth angle and y the rapidity, which is defined as follows: $y = \frac{1}{2}\ln\frac{E+p_z}{E-p_z}$.

- Calculate the distance d_{ij} (Eq. 2.8) for each pair of particles in the event.
- Calculate the beam distance $d_{iB} = p_{T,i}^{t}$ for each particle.
- Find the smallest value of all inter-particle distances d_{ij} and beam distances d_{iB}.
- If a d_{ij} provides the smallest value, the correspondent particles i and j are recombined. If it is d_{iB}, then the particle is removed from the list and is called a jet.
- Repeat the procedure starting at the first step until the particle list is empty.

Because of their seed-less nature, all algorithms based on the k_t algorithm are collinear- and IR-safe. The jets reconstructed with the k_t algorithm are non-circular shaped and complicate the treatment on the experimental side[10]. It can be shown, that the choice of $t = -2$ generates circular shaped jets [31], which combines the advantages of both jet algorithm classes. A performant implementation of the anti-k_T jet finding algorithm is provided by the FastJet [28] package and is used in the context of this thesis. The size of the distance parameter depends on the context of the analysis (see e.g. Ref. [32]) and the experimental environment[11]. The distance parameters $R = 0.4$ and $R = 0.6$ are used in this thesis.

2.3 New Physics Beyond the Standard Model

The Standard Model provides precise predictions which were confirmed by a large number of experiments. However, there are several unsolved problems which indicate the existence of physics beyond the SM. For example, it turns out that the strength of the weak force is orders of magnitudes larger compared to the gravitational force. This theoretical problem is referred to as hierarchy problem. Various new physics models with multi-layered motivations exist attempting to solve the open issues. In this chapter four models are introduced which are used in the context of the search for new resonant-like structures (see Chap. 9) in dijet final-state. These models were used as benchmark for the discovery mass reach of the LHC.

2.3.1 Excited Quark

The idea that quarks consist of more fundamental particles originates partly from lessons learned from history. For instance, in the beginning of modern particle physics it was considered that protons are elementary particles [2]. Due to the increase of accelerator energies it turned out that protons are made of more fundamental particles called quarks. Thus it seems obvious that due to the increase of center-of-mass energy quark substructure may be revealed. Quarks as composite objects are also candidates to answer some outstanding questions in particle physics for example related to the observed charges of the quarks or the number of quark generations. The scale of constituent binding energies is called compositeness scale Λ. In the Standard Model it is assumed that $\Lambda \to \infty$ and as

[10] It is e.g. more complicated to calculate corrections due to a low acceptance of a detector in poorly instrumented regions. In case of circular-shaped jet a simple subtraction of the energy included within the jets originating from e.g. underlying event (cf. Sec. 2.1.3) can be performed.

[11] For instance, the presence of so-called pile-up e.g. originating from multiple proton-proton interactions can influence the choice of parameter R.

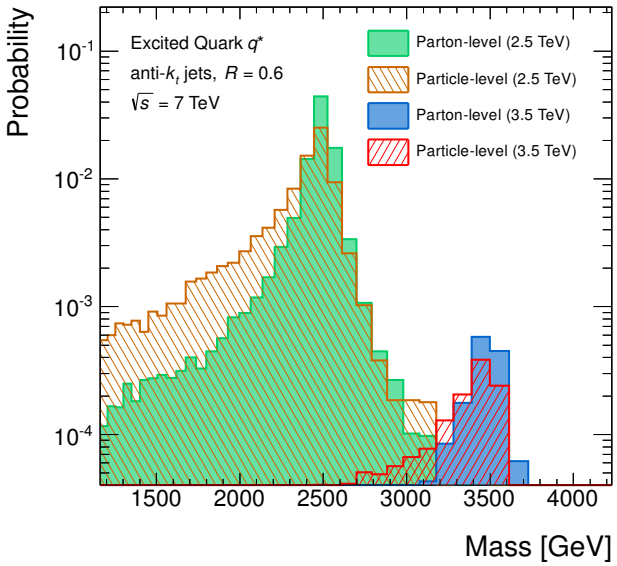

Figure 2.10: The invariant mass distributions at parton-level and the particle-level for two different excited quark masses: $M_{q^*} = 2.5$ TeV and $M_{q^*} = 3.5$ TeV. At particle-level the jets were reconstructed using the anti-k_T jet algorithm with the distance parameter $R = 0.6$.

a consequence quarks are point-like, which is supported by experimental data. In case of a finite compositeness scale $\Lambda \approx \sqrt{s}$, new interactions could be observed between quarks, which are suppressed at energies much less than Λ. One approach is to search for the four-fermion contact interactions which are expected to appear below Λ [17]. For this purpose dijet angular distributions are utilized [33]. The substructure of quarks could also result in new exited states such as excited quarks q^*, which are expected to appear at energies above Λ. These resonances could be observed in dijet invariant mass distributions and would be one of the most convincing evidences for compositeness of quarks.

The production of excited quarks could take place through different mechanisms. Proton-proton collisions at high energies provide an excellent environment to search for the first generation excited quarks u^* and d^*. Only the first generation was considered. One possibility is to produce a q^* together with an ordinary quark via contact interaction in a qq collision or a $q\bar{q}$ annihilation. The decay can be mediated via contact interaction or gauge bosons and can result e.g. in three-jet or four-jet final states. Another possibility is the production via quark-gluon fusion $qg \to q^*$. The decay modes are of the following type $q^* \to qg$, $q^* \to q\gamma$, $q^* \to qZ^0$, and $q^* \to qW^{\pm}$, assuming that contact interactions have no significant impact on the q^* decays [34]. The decay channel $q^* \to qg$ is the dominant one with a branching ratio of around 0.8 for excited quark masses M_{q^*} between 1 TeV and 3 TeV, slightly decreasing with increasing mass M_{q^*} [35].

The excited quark model is an important benchmark, which was used by various experiments to quantify the discovery reach (see exemplary [36, 37, 38]). This allows the comparison of the discovery mass reach between different experiments and decay channels. For the simulation of excited quarks, hadronization, and showering the Pythia 6 [18] event generator was used. The compositeness scale Λ was chosen to be equal to the

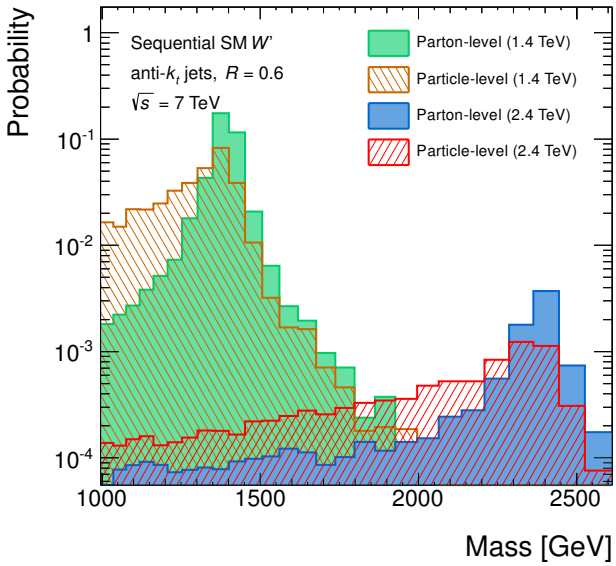

Figure 2.11: The invariant mass distributions at parton-level and the particle-level for two different W' masses: $M_{W'} = 1.4$ TeV and $M_{W'} = 2.4$ TeV. At particle-level the jets were reconstructed using the anti-k_T jet algorithm with the distance parameter $R = 0.6$.

mass of the individual excited quarks. The coupling constants f, f' and f_s, which are parameters determined by the composite dynamics[12] [34], were set to 1. The generated q^*s are the result of the quark-gluon fusion process only. The invariant mass distributions for two different q^* masses at parton-level and particle-level are shown in Fig. 2.10. The total decay width is approximately 85 GeV for $m_{q^*} = 2.5$ TeV and 115 GeV for masses at $m_{q^*} = 3.5$ TeV [13]. PDF effects and the parton shower lead to a broader distribution with an enhanced low-mass tail. The cross-sections for masses shown in Fig. 2.10 are: 0.2 pb at 2.5 TeV and 0.004 pb at 3.5 TeV. For the q^* with the mass of 3 TeV the provided cross-section is 0.026 pb.

2.3.2 Sequential Standard Model W'

The charged $W^{\pm}$ and neutral Z^0 gauge bosons were discovered at CERN [9, 10] and their measured properties are in good agreement with the Standard Model predictions. A new heavy boson called W' with spin 1 and electric charge $\pm 1e$ appears in many extensions of the SM [17]. In the context of the search for new physics in Chap. 9 the so-called sequential standard model (SSM) W' was used. It is the extended gauge model discussed in Ref. [39], where the coupling of W' to WZ is set to zero [40]. As a consequence the decay channels $W' \to q\bar{q}$, which are of particular interest in the context of this thesis, are dominant over the entire range of possible W' masses $M_{W'}$. The SSM W' has the same SM couplings and quantum numbers as the heavy SM gauge boson $W^{\pm}$. The difference compared to the SM $W^{\pm}$ is the mass, which exceeds the production threshold for

[12] The choice of f, f' and f_s have an impact on the production cross-section of excited quarks. If for example, $f = f' = f_s = 0.1$ the discovery limits for the q^* production via gauge interactions would be around a factor of 2 smaller [34].

[13] The total decay width was estimated using equations of the partial decay widths for the electroweak and QCD channels given in Ref. [35].

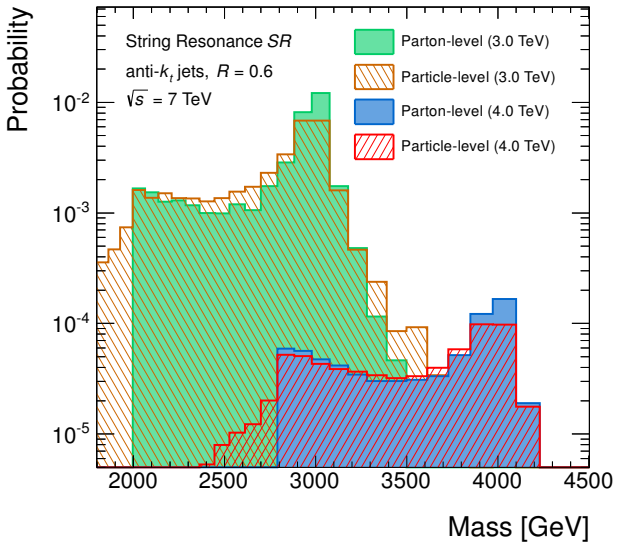

Figure 2.12: The invariant mass distribution at parton-level and the particle-level for string resonant structures at two different string scales: $M_s = 3$ TeV and $M_s = 4$ TeV. The anti-k_T jet algorithm with the distance parameter $R = 0.6$ was used in order to reconstruct jets at particle-level. At the parton-level a cut was applied at 2 TeV and 2.8 TeV, respectively.

top-quarks. Thus the branching ratio of the $q\bar{q}$ decay channels and the total decay width are different compared to the $W^{\pm}$ boson. This model does not arise from theoretical considerations and is therefore arbitrary. As other models, it is used as benchmark to determine the discovery reach of the experiment. In addition to the hadronic channels, the leptonic decay channels were used to search for the W' using the same experimental data records [40]. This allows the comparison of the sensitivity to this model in different decay channels. The combination of leptonic and hadronic channels might be used as a distinguishing properties compared to other new physics models as e.g. the excited states of quarks.

The generated W' events include the hadronic decay channels only. For this purpose Pythia 6 was used. Instead of the cross-section at LO accuracy provided by Pythia, the NNLO electroweak-corrected cross-section was used for the limit setting procedure presented in Chap. 9. The cross-sections were calculated using the MSTW2008 PDF [24]. The invariant mass distribution for two different W' masses $M_{W'}$ are shown at parton-level and particle-level in Fig. 2.11. The cross-sections for masses shown in this figure are: 1.19 pb at 1.4 TeV and 0.03 pb at 2.4 TeV. The cross-section at 3 TeV is approximately 0.008 pb, which is around 3 times smaller compared to q^* at the same mass.

2.3.3 Low-Scale String Resonance

One of the main theoretical issues in the context of the Standard Model is the fact that it does not incorporate the gravitational force. The attempt to describe gravity in terms of quantum field theory leads to a non-renormalizable theory [41]. One candidate for the quantum theory of gravitation is the so-called String Theory. The elementary particles

of quantum field theories as for example the QCD are assumed to be point-like. In string theory these objects are extended and are called strings. A consequence of this theory is the existence of a massless spin-2 particle, which is assumed to be the graviton [42]. By analogy with the force carriers of the electromagnetic, weak and strong interactions, the hypothetical graviton is assumed to be the mediator of the gravitational force. The scale hierarchy problem is additionally one of the questions the Standard Model is confronted with in explaining the large difference of many orders of magnitude between the Planck scale $M_p \approx 10^{19}$ GeV and the electroweak $M_{\mathrm{EW}} \approx 250$ GeV scale. The string scale M_s, which is the fundamental scale of the string theory, could be of the order of few TeV and thus orders of magnitude smaller than the Planck scale M_p in case of the existence of so-called large extra dimensions. Therefore low-scale string resonances are candidates in order to solve the scale hierarchy problem.

Low-scale string models predict colored excited states in the TeV range, which could be observed in events with two jets in the final state. The calculated scattering amplitudes exchanging string excited states are functions of the string scale M_s only. The invariant mass of the first resonance is expected to be at the string scale M_s. A unique property of the string models compared to other new physics models is the existence of a number of independent states with degenerate masses. The mass for the n^{th} string excited state is given as $M_n = \sqrt{n}M_s$ with the highest spin $J_{\max} = j_0 + n$, where j_0 is the spin of the corresponding Standard Model particle [43]. For instance, the first string excited states of quarks q^*s have a mass equal to the string scale M_s with $J = 1/2$ and also $J = 3/2$. q^*s are expected to be produced in processes $qg \to qg$ which are dominant in the kinematic region covered by the search as discussed in Chap. 9. Another possible string excited states are color octets g^*s, which can be produced in processes as $gg \to q\bar{q}$ with $J = 0$, $J = 1$ and $J = 2$. The above mentioned states contribute to a single resonant structure. The second string resonance structure is expected to appear at the mass of $\sqrt{2}M_s$, where the factor $\sqrt{2}$ is a distinguishing property of the low-scale string models compared to other new physics models with large extra dimensions. For example, second string excited states of quarks q^{**}s can be produced with spins $J = 1/2$, $J = 3/2$ and $J = 5/2$. The appearance of excited states with different spins makes it possible to use angular distributions as a sensitive and discriminating tool. Furthermore, the invariant mass distribution can be used for the search of a second resonance, even though it is expected to become significant at much larger integrated luminosities, if the decay mode $q^{**} \to q^*g$ should be realized in nature [44].

The events were generated using CalcHEP 2.5.6 [43, 45] with the MRSTMCal PDF [46] interfaced with Pythia 6 [18] in order to provide a simulation at particle-level. The invariant mass distribution of the first string resonances for two different string scales M_s are shown at parton-level and particle-level in Fig. 2.12. The cross-sections for masses shown in this figure are: 0.085 pb at 3 TeV and $1.6 \cdot 10^{-3}$ pb at 4 TeV. The cross-section at 3 TeV is approximately 3 times larger compared to that of q^* at the same mass.

2.3.4 Color-Octet Scalar

The initial-state hadrons in pp collisions carry color-charge and thus provides an environment for the production of possible new colored resonances. An example for colored states is the excited quark q^*, which is briefly discussed in Sec. 2.3.1. The q^* is a color-triplet

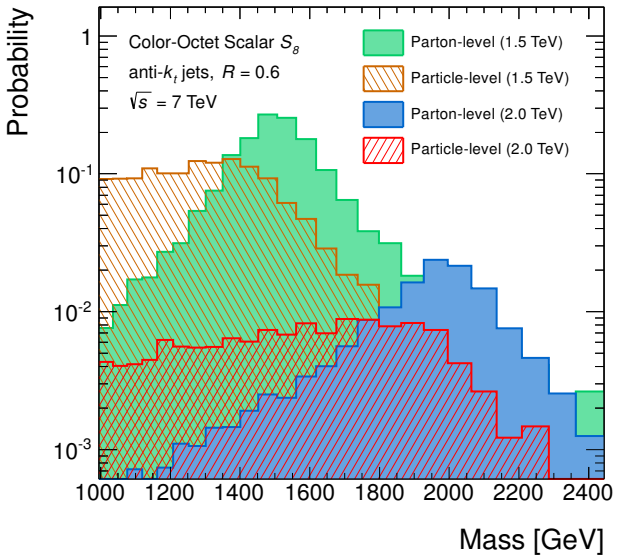

Figure 2.13: The invariant mass distribution at parton-level and the particle-level for two different Color-Octet Scalar S_8 masses: $M_{S_8} = 1.5$ TeV and $M_{S_8} = 2.0$ TeV. The anti-k_T jet algorithm with the distance parameter $R = 0.6$ was used in order to reconstruct jets at particle-level.

fermion which can be produced via quark-gluon fusion and arise in composite models. Another possibility is the production of color-octet scalars S_8, which can arise e.g. in technicolor models[14] [49].

In the model considered, the color-octet scalars are produced via gluon-gluon fusion. The new physics scale Λ was chosen to be the S_8 mass M_{S_8}, where the production cross-section scales with Λ^{-2}. Due to the nature of the momentum distribution of gluons inside the protons, the production cross-sections falls rapidly by more than five orders of magnitude from 0.5 TeV to 2.5 TeV at a center-of-mass energy of 7 TeV [49]. The only decay channel of color-octet scalars is $S_8 \to gg$. This fact allows the enhancement of the signal-to-background ratio at high energies within the LHC environment, because qq and qg interactions are dominant in the regime of interest. For this purpose quantities which are sensitive to the jet substructure can be used.

The color-octet scalar parton-level events were generated at LO accuracy using MadGraph 5 [50] with the CTEQ6L1 PDF [51] and were interfaced to Pythia 6 in order to simulate showering and hadronization. The invariant mass distribution for two different S_8 masses M_{S_8} are shown at parton-level and particle-level in Fig. 2.13. The S_8 decay widths for masses shown in this figure are[15]: 224 GeV at 1.5 TeV and 290 GeV at

[14] In technicolor models a new strong interaction is introduced acting on a new degree of freedom called technicolor. The technicolor interaction is used to realize the electroweak symmetry breaking, providing the gauge bosons $W^{\pm}$ and Z^0 with masses [47]. The discovery of a Higgs boson with a mass of around 125 GeV with couplings consistent with the Standard Model predictions, exclude the simplest technicolor models. However, the odds are that new strong dynamics contribute to the electroweak symmetry breaking. For example, bosonic technicolor models include both a Higgs and the technicolor sector [48].

[15] Calculated using the formula provided in Ref. [52].

2 TeV. Thus, for a given mass, this model provides a 4 times larger decay width compared to the width of q^*. The cross-sections are: 3.9 pb at 1.5 TeV and 0.3 pb at 2 TeV. For $M_{S_8} = 3$ TeV the cross-section is 0.004 pb, which is approximately 7 times smaller compares to that of q^* at the same mass.

3 Theoretical Predictions

In this chapter techniques used to produce theoretical predictions and uncertainties for the inclusive jet and dijet spectra are discussed. These predictions are compared to the measurements in Sec. 8. The software tool and methods to produce QCD prediction at next-to-leading order are briefly discussed in Sec. 3.1. The methods used to derive theoretical uncertainties are described in Sec. 3.2. Additional corrections applied to the QCD spectra which enable the possibility to make comparisons between the measurements and predictions, are detailed in Sec. 3.3. In addition to the predictions produced as described in Sec. 3.1-3.3, predictions using the so-called POWHEG BOX were generated. This method and its results are discussed in Sec. 3.4.

3.1 Next-to-leading Order Cross-section

The predictions of the inclusive jet and dijet cross-section were determined at next-to-leading order (NLO) using the NLOJET++ [53, 54] software. For this purpose the following PDF sets were used (cf. Sec. 2.1.4): CT10, MSTW 2008, NNPDF 2.3. NLOJET++ performs an integration of Eq. 2.6 using Monte Carlo (MC) techniques. For this purpose events of initial-state and final-state partons are generated and the cross-section at tree-level is calculated which is used as event weight. As the next step NLO corrections and the corresponding weights to the event at tree-level are generated iteratively changing the kinematics. To provide a reasonable cancellation of real and virtual NLO contributions, $1.2 \cdot 10^{10}$ events were generated. In case of the inclusive jet cross-section up to three jets can be reconstructed, where two parton final-states are provided at tree-level and a third parton from real emissions originating from NLO contributions. The jets were reconstructed using the anti-k_T jet finding algorithm (cf. Sec. 2.2) using two different distance parameters: $R = 0.4$ and $R = 0.6$. The double-differential inclusive jet cross-section is calculated as the sum of all generated events k as follows:

$$\frac{d^2\sigma(p_T, y)}{dp_T dy} = \frac{\sum_k N_{\text{jets},k}(p_T, y) w_k}{N_{\text{tree}} \Delta p_T \Delta y}, \tag{3.1}$$

where $N_{\text{jets},k}(p_T, y)$ is the number of jets reconstructed in a given bin (p_T, y) in the k^{th} event with the corresponding weight w_k, N_{tree} is the number of events at tree-level, and Δp_T (Δy) is the width of the corresponding p_T (y) bin. The dijet cross-section is an event based observable and is calculated as follows:

$$\frac{d^2\sigma(m_{12}, y^*)}{dm_{12} dy^*} = \frac{\sum_k N_{\text{evt},k}(m_{12}, y^*) w_k}{N_{\text{tree}} \Delta m_{12} \Delta y^*}, \tag{3.2}$$

where $N_{\text{evt},k}(m_{12}, y^*)$ is the number of events reconstructed in bin (m_{12}, y^*), and Δm_{12} (Δy^*) is the width of the corresponding m_{12} (y^*) bin. The quantity y^* is the rapidity separation

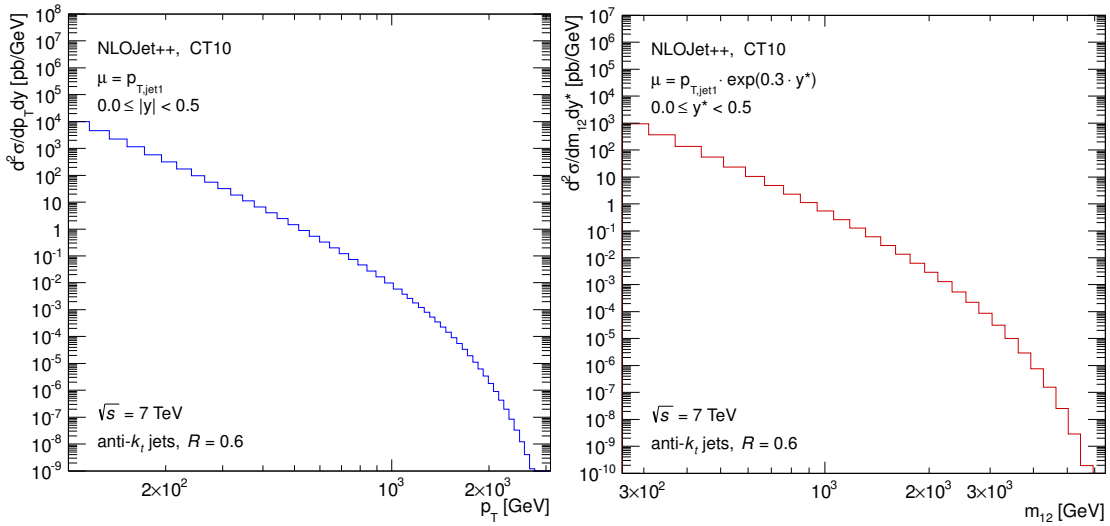

Figure 3.1: Inclusive jet (left) and dijet (right) cross-section spectra produced using NLOJET++ in the region $0.0 \leq |y| < 0.5$ (resp. $0.0 \leq y^* < 0.5$). The jets were reconstructed using the anti-k_T algorithm with disctance parameter $R = 0.6$.

of the two leading jets and is defined as:

$$y^* = \frac{1}{2}|y_1 - y_2|, \tag{3.3}$$

where y_1 and y_2 is the rapidity of the leading and second-leading jets, respectively. For brevity y^* is called rapidity in the following[1]. The invariant mass of the two highest p_T jets is defined as:

$$m_{12} = \sqrt{(E_{\text{jet1}} + E_{\text{jet2}})^2 - (\vec{p}_{\text{jet1}} + \vec{p}_{\text{jet2}})^2}, \tag{3.4}$$

where E is the energy and $\vec{p}$ the momentum of the jet.

For the inclusive jet cross-section the factorization and renormalization scales (cf. Sec. 2.1.3) were chosen to be the highest jet transverse momentum $p_{T,\text{jet1}}$ in a given event k:

$$\mu = \mu_F = \mu_R = p_{T,\text{jet1}}. \tag{3.5}$$

For the dijet cross-section the scale was chosen to be dependent on the rapidity separation y^*:

$$\mu = \mu_F = \mu_R = p_{T,\text{jet1}} \cdot e^{0.3y^*} \tag{3.6}$$

This scale choice (Eq. 3.6) is motivated by the choice $\mu = \frac{m_{12}}{2\cosh(0.7y^*)}$ given in Ref. [55], which has a similar dependence as function of the rapidity separation y^*. This choice was made because of instability of the NLOJET++ cross-section calculation for large rapidity separations y^*, when using the jet p_T as scale. To allow comparison between the theoretical predictions and data in case of the dijet cross-section, asymmetric cuts were

[1] A Lorentz boost applied to the rapidity y parallel to the z-axis with the velocity β results in a rapidity $y\prime = y + \ln\sqrt{\frac{1-\beta}{1+\beta}} = y + \kappa$. The rapdity y is Lorentz invariant except the additive term κ. The difference of rapidities as given in Eq. 3.3 is then $y_1\prime - y_2\prime = (y_1 - \kappa - (y_2 - \kappa)) = y_1 - y_2$. Thus the quantity y^* is the rapidity of both jets in the dijet reference frame.

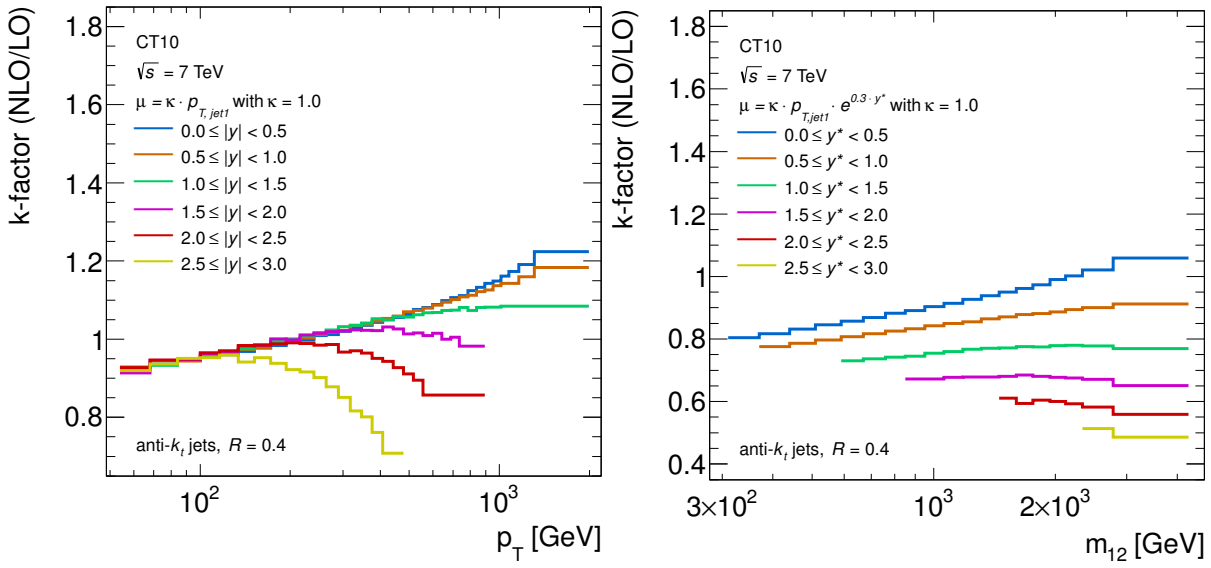

Figure 3.2: k-factors for the inclusive jet and dijet cross-sections for various rapidity regions of the covered phase-space. The jets were reconstructed using the anti-k_T jet finding algorithm with the distance parameter $R = 0.4$. The k-factor is defined as the ratio of the cross-section obtained form fixed-order NLO calculations and the cross-section calculated at LO.

applied to the transverse momenta p_T of the two leading jets. The events were included in the cross-section calculation if the $p_{T,\text{jet1}} > 100$ GeV and $p_{T,\text{jet2}} > 50$ GeV. The inclusive jet (left) and dijet (dijet) cross-section spectra determined using NLOJET++ in the rapidity region $0.0 \leq |y| < 0.5$ (resp. $0.0 \leq y^* < 0.5$) are exemplary shown in Fig. 3.1.

The k-factor is defined as the cross-section calculated at next-to-leading order (NLO) divided by the cross-section determined at leading-order (LO). Fig. 3.2 shows the k-factors as function p_T (left) and m_{12} (right) for jets reconstructed using the distance parameter $R = 0.4$ in all rapidity bins covered by the cross-section measurements detailed in Sec. 8. The k-factors are below unity at low-p_T (-m_{12}) and become greater than unity in the high-energy regime. Furthermore a dependence on the rapidity y (rapidity separation y^*) can be observed. With increasing rapidity the negative correction to the cross-section at LO increases. For jets found with $R = 0.6$ the k-factors are shifted towards higher values by approximately 15% in all covered phase-space regions. The dependence on the PDF choice was found to be small, where the maximum difference was observed in the high-p_T (-m_{12}) regime and is of the order of few percent.

3.2 Theoretical Uncertainties

Due to the neglection of higher-order terms in the NLO calculations, an uncertainty was derived for the inclusive jet and dijet cross-section predictions. Three different uncertainty types which contribute to the total theoretical systematic uncertainty are the choice of the factorization μ_F and renormalization μ_R scale, PDF, and the strong coupling α_s. The uncertainties were derived by varying the inputs for the cross-section calculations inde-

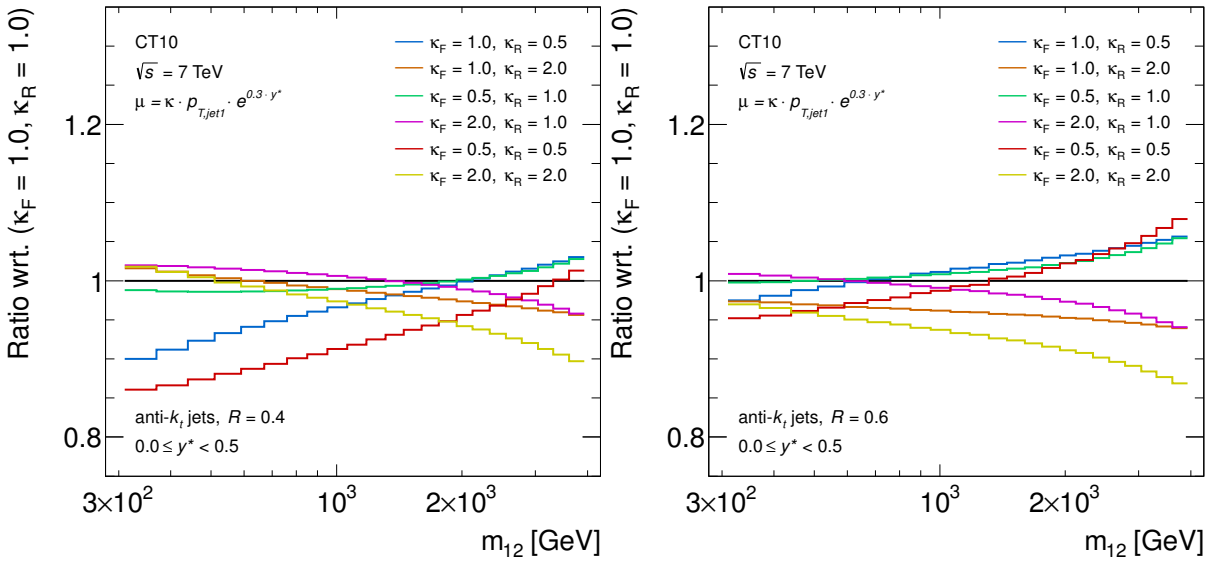

Figure 3.3: Ratios of dijet cross-sections produced with scale choices given in the legend and the nominal scale choice are shown exemplary. The jets were reconstructed using the anti-k_T algorithm with distance parameters $R = 0.4$ (left) and $R = 0.6$ (right) in the regime $y^* < 0.5$.

pendently. Instead of performing the full calculation for each set of theoretical parameters, the APPLGRID [56] software interfaced with NLOJET++ was used to determine the uncertainties. The cross-section factorizes into perturbative and non-perturbative parts as discussed in Sec. 2.1.3. The PDFs are non-perturbative inputs of the cross-section calculation, where the perturbative coefficients are independent of the choice of the PDF. The perturbative coefficients are stored as function of x_1, x_2, and Q^2 in a look-up table denoted as *grid*, where the quantities x_1 and x_2 are Bjorken's scaling variables of the incoming partons and $Q^2 = \mu^2$ is the scale chosen as given in Eq. 3.5 and Eq. 3.6. The choice of the strong coupling α_s and $\mu_{F/R}$, as well as the convolution with the PDF can be done posteriori. The relative uncertainty components as function of p_T (m_{12}) are derived from the ratio between the cross-sections calculated using different sets of theoretical parameters and the nominal cross-section.

The scale uncertainties were determined by varying μ_F and μ_R by factors κ of 0.5, 1, and 2 independently, which results in nine combinations. The combinations (0.5, 2) and (2, 0.5) were excluded in order to avoid instability of the calculations. Therefore cross-section spectra for seven scale combinations (μ_F, μ_R) were considered. Dijet cross-section ratios for various choices of the scales (μ_F, μ_R) with respect to the nominal cross-section as function of m_{12} for anti-k_T $R = 0.4$ (left) and $R = 0.6$ (right) are shown in Fig. 3.3. In case of the inclusive jet predictions the behavior of the cross-section ratios due to the scale choice is similar and results in slightly lower uncertainties as function of p_T. The cross-section for a given scale pair (μ_F, μ_R) depends on the distance parameter R. In the low-p_T (-m_{12}) region a large deviation for $R = 0.4$ jets can be observed for scale choice combinations where κ_R is reduced compared to the nominal choice. This effect leads to an asymmetric uncertainty and is the dominant uncertainty component in this phase space regime for jets reconstructed with the distance parameter $R = 0.4$. At parton-level, the dependence on R can only originate from real gluon emission contributions with three

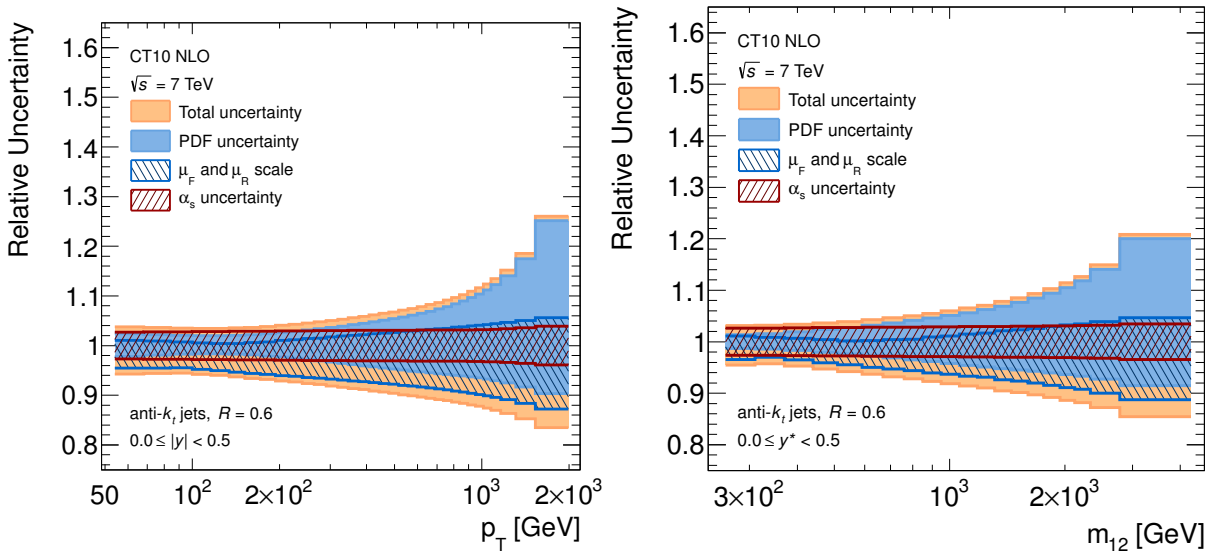

Figure 3.4: Total uncertainty and the individual components for the inclusive jet (left) and dijet (right) predictions using the CT10 PDF set. The jets were reconstructed using the anti-k_T algorithm with $R = 0.6$ within the rapidity range $0.0 \leq |y| < 0.5$ (left) and the rapidity separation range $0.0 \leq y^* < 0.5$ (right).

partons in the final-state. In this configuration, it is possible to reconstruct three jets if using $R = 0.4$ and two jets in case of $R = 0.6$. A decreased renormalization scale μ_R increases the strong coupling α_s and thus increases the probability for a three final-state parton configuration. The cross-section for a given bin in the low-p_T (-m_{12}) regime for jets reconstructed with $R = 0.4$ is lower, because more jets with a lower transverse momentum are reconstructed in case of $R = 0.4$ compared to jet final-states reconstructed with $R = 0.6$. The asymmetric scale uncertainties were derived from the envelope of the different cross-section spectra. The stability of the cross-section against the variation of the factorization and normalization scales can be interpreted as indication for a reasonable scale choice given in Eq. 3.5 and Eq. 3.6 or as non-importance of higher order contributions.

The PDF uncertainties were calculated following the recommendations of the individual groups. For the predictions produced with CT10 and MSTW2008 the CTEQ group recommendations were followed, which use the Hessian method [57]. The PDF uncertainty of the cross-section σ in a given phase-space bin (p_T, $|y|$) or (m_{12}, y^*) can be calculated as follows [58]:

$$\Delta\sigma_{\max^+} = \sqrt{\sum_{i=1}^{N} [\max(\sigma_i^+ - \sigma_0, \sigma_i^- - \sigma_0, 0)]^2} \tag{3.7}$$

$$\Delta\sigma_{\max^-} = \sqrt{\sum_{i=1}^{N} [\max(\sigma_0 - \sigma_i^+, \sigma_0 - \sigma_i^-, 0)]^2}, \tag{3.8}$$

where σ_0 is the cross-section obtained using the central PDF, $\sigma_i^{+/-}$ are the cross-sections calculated using the PDF corresponding to the eigenvector i in positive (+) and negative

(-) directions, and N the number of eigenvector sets for each direction, respectively. Due to occasionally shift of σ_i^+ and σ_i^- in the same direction with respect to σ_0, the most positive and the most negative terms are taken. Each PDF set provides different numbers of member PDFs. CT10 has 52 member PDFs: 26 eigenvector sets for the positive and 26 for the negative direction. The resulting uncertainties for CT10 are at 90% CL and are scaled down by the factor 1.64485 to be able to compare with other PDFs, whereas the uncertainties for MSTW 2008 were determined at 1σ. For the NNPDF 2.3 set PDF uncertainties were calculated as follows [27]:

$$\Delta\sigma_{\max} = \sqrt{\frac{1}{N_{\text{rep}} - 1} \sum_{i=1}^{N_{\text{rep}}} (\sigma_i - \sigma_0)^2}, \tag{3.9}$$

where N_{rep} is the number of PDF replicas provided, where in case of NNPDF 2.3 $N_{\text{rep}} = 100$. The PDF used to calculate σ_0 is an average calculated using the PDF replicas. As a consequence the PDF uncertainties are symmetric. The relative PDF uncertainties for the inclusive jet (left) and dijet (right) cross-section spectra are indicated as blue bands in Fig. 3.4 for predictions using the CT10 PDF set. The shape and the width of the uncertainty bands in the covered rapidity range are similar for the inclusive jet and dijet spectra. The PDF uncertainties are the dominant source of the total theoretical uncertainty at high-p_T (-m_{12}) and amount to up to approximately $^{+25\%}_{-10\%}$ in the central rapidity region for the last p_T (-m_{12}) bin of the covered phase space. The PDF uncertainties increase up to approximately $^{+60\%}_{-12\%}$ in the most forward rapidity region. In the low-p_T (-m_{12}) regime the uncertainties are of the order of around 3% and decrease slightly to around 2% with increasing y (y^*). In case of MSTW2008 the PDF uncertainties are at the few percent level over the entire phase space covered with the maximum of around 4% at high-p_T (-m_{12}). The PDF uncertainties for predictions produced with NNPDF 2.3 are similar to that of MSTW 2008 in the low-p_T region and amount to up to 20% in the most forward region at high-p_T, where these are the dominant uncertainty components.

The result of the PDF fitting procedure depends on the choice of the QCD coupling constant $\alpha_s(M_Z)$. Therefore the considered PDFs are valid only for fixed values of α_s. In order to estimate the relative uncertainty the cross-sections for two additional $\alpha_s^{+/-}$ values around the nominal value were determined. For each variation of $\alpha_s(M_Z)$ an alternative PDF set is provided. The uncertainty on the cross-section has a small dependence on the phase-space region and is around 4%.

The uncertainty bands for each component contributing to the total theoretical uncertainty are shown in Fig. 3.4 for central rapidity y (y^*) jets reconstructed using the jet parameter $R = 0.6$. Furthermore the inclusive jet and dijet cross-section predictions for various PDFs with respect to the prediction determined using the CT10 PDF set are shown in Fig. 3.5. This figure indicates a sensitivity of the considered observables to PDFs.

3.3 Non-perturbative and Electroweak corrections

The cross-section predictions determined using NLOJET++ as detailed in the previous sections are at parton-level. The comparison between the predicted jet cross-sections and

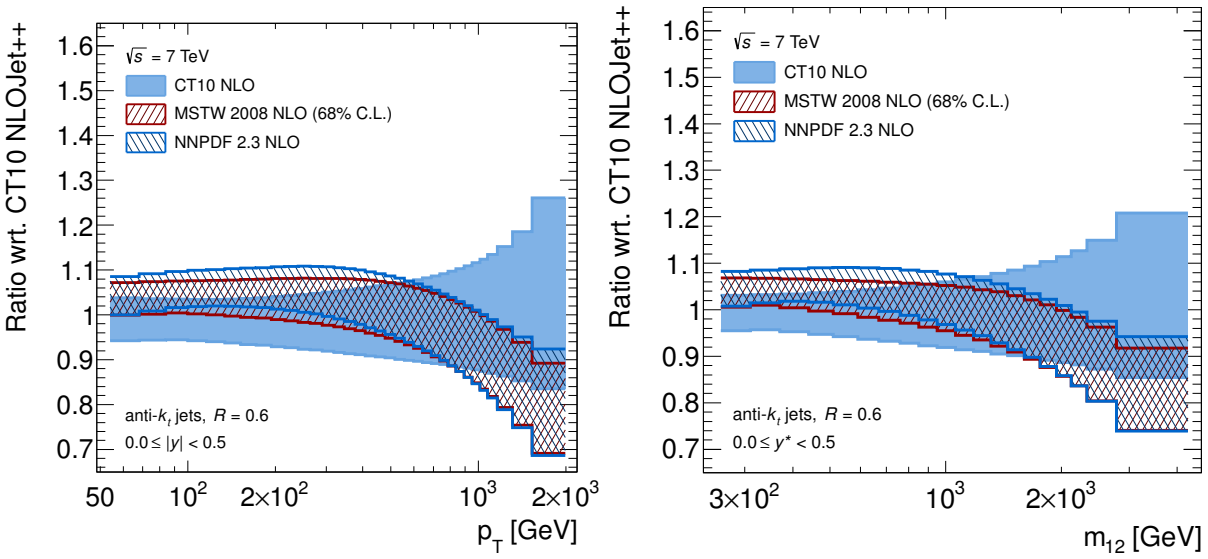

Figure 3.5: Comparison of inclusive jet (left) and dijet (right) cross-section predictions for different PDF sets. As an example three different PDFs are shown: CT10, MSTW2008, NNPDF 2.3. As reference the cross-section determined using the CT10 PDF was used. The uncertainty bands correspond to the total theoretical uncertainty determined using α_s, scale, and PDF uncertainties. The jets were reconstructed using the anti-k_T algorithm with $R = 0.6$ within the rapidity range $0.0 \leq |y| < 0.5$ or $0.0 \leq y^* < 0.5$, respectively.

data is done at particle-level[2]. The cross-section at this level comprises effects caused by hadronization (HAD) and the underlying event (UE), which are not included in the cross-section predictions at parton-level. In order to estimate these effects for a given jet distance parameter R, bin-by-bin factors $F(p_T, y)$ ($F(m_{12}, y^*)$) are applied to the cross-section spectra at parton-level. The double-differential cross-section prediction can be written as:

$$\frac{d^2\sigma(p_T, y)}{dp_T dy} = \frac{d^2\sigma_{\text{part}}(p_T, y)}{dp_T dy} \times F(p_T, y) \tag{3.10}$$

$$\frac{d^2\sigma(m_{12}, y^*)}{dm_{12} dy^*} = \frac{d^2\sigma_{\text{part}}(m_{12}, y^*)}{dm_{12} dy^*} \times F(m_{12}, y^*), \tag{3.11}$$

where $\frac{d^2\sigma_{\text{part}}(p_T,y)}{dp_T dy}$ and $\frac{d^2\sigma_{\text{part}}(m_{12},y^*)}{dm_{12} dy^*}$ are the partonic cross-sections in the corresponding bins. The multiplicative correction factors F were derived using the leading-order Monte Carlo event generators Herwig++ and Pythia 6 (cf. Sec. 2.1.2). In these cases, the NLO contributions are estimated through parton showers and thus this approach is an approximation. A proper treatment is provided e.g. by the so-called Powheg method, where the parton showers are matched to the full NLO calculations (cf. Sec. 3.4). For the inclusive jet cross-section spectra produced with Pythia 6, three different UE tunes were used: AUET2B [59], AMBT2B [59], and Perugia2011 [60]. For the non-perturbative corrections derived using Herwig++ the UE-EE3 CTEQ6L [61] tune was used. The simulations were performed with two different configurations: simulation of non-perturbative

[2]Also denoted as hadron-level. At this level, jets are reconstructed using stable particles which have a lifetime of $\tau > 10$ ps (cf. Sec. 5.3).

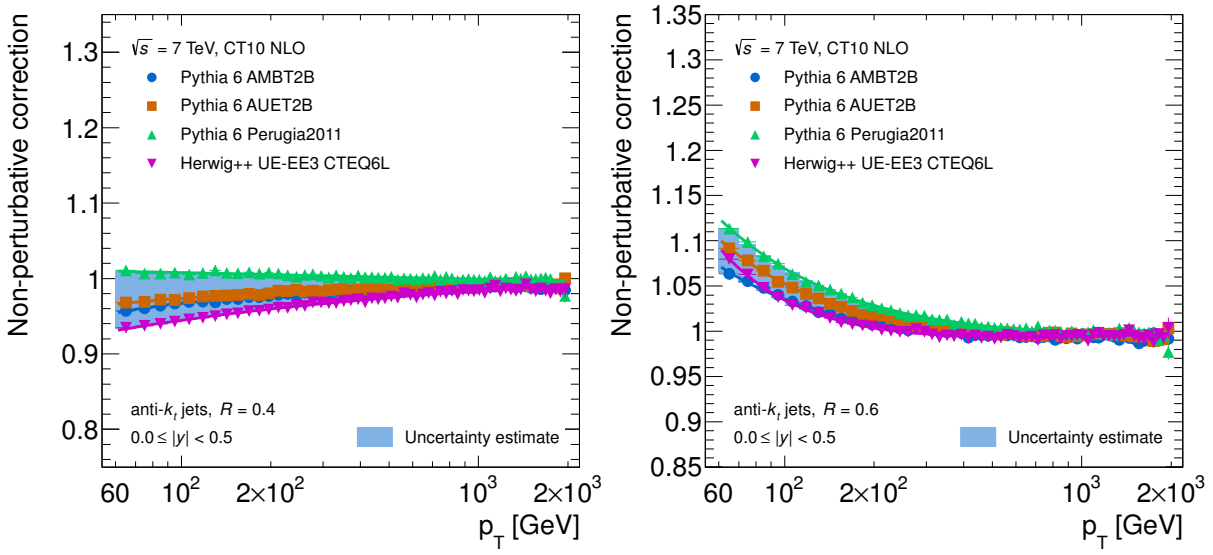

Figure 3.6: Non-perturbative corrections for the inclusive jet cross-section spectrum in the central rapidity region for various UE tunes and generators. The jets are found using the distance parameter $R = 0.4$ (left) and $R = 0.6$ (right). The blue band indicates the uncertainty estimate on the non-perturbative corrections.

effects enabled (w/ UE+HAD) and disabled (w/o UE+HAD). The factor F for a given (p_T, y) or (m_{12}, y^*) bin is then calculated as follows:

$$F = \frac{\tilde{\sigma}^{\text{w/ UE+HAD}}}{\tilde{\sigma}^{\text{w/o UE+HAD}}}, \tag{3.12}$$

where $\tilde{\sigma} \equiv \frac{d^2\sigma(p_T,y)}{dp_T dy}$ ($\tilde{\sigma} \equiv \frac{d^2\sigma(m_{12},y^*)}{dm_{12}dy^*}$) are the LO cross-section predictions using the considered leading-order generators for a given (p_T, y) ((m_{12}, y^*)) bin. The resulting non-perturbative correction factors F as function of p_T for two different jet parameter R are shown exemplary for the inclusive jet cross-section in Fig. 3.6. The largest deviation of the factors F from unity can be observed in the low-p_T region, while with increasing transverse momentum, F converge to unity. As discussed in Sec. 2.1.3, the UE leads to higher reconstructed jet energies and thus increases the number of reconstructed jets (events) in a given (p_T, y) ((m_{12}, y^*)) bin. Because of the steeply falling shape of the cross-section spectra, this effect is enhanced with decreasing p_T (m_{12}) and is expected to be larger for jets reconstructed using $R = 0.6$, which cover a larger area compared to jets found using $R = 0.4$. In case of the hadronization (HAD) the opposite behavior is expected, where the jet energy is lowered due to out-of-cone effects and therefore a lower cross-section is observed in a given (p_T, y) ((m_{12}, y^*)) bin. For jets reconstructed using $R = 0.4$ this effect is expected to be more pronounced compared to $R = 0.6$, because of the smaller area covered by this jet definition. Hence the non-perturbative correction depends on the jet distance parameter R. The largest impact can be observed in the low-p_T regime, where in case of the distance parameter $R = 0.4$ the non-perturbative corrections tend to be below unity, while for $R = 0.6$ the correction is greater than one. The final correction factors were derived as average of the considered setups. To avoid large fluctuations for lack of statistics, the results were smoothed by fitting the following

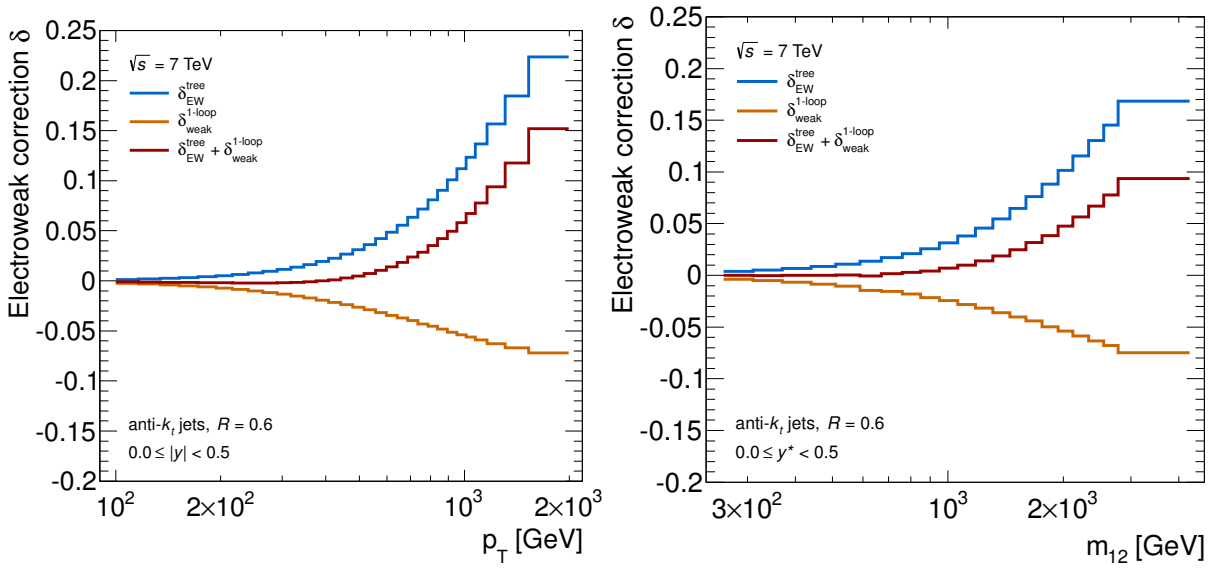

Figure 3.7: Shown the electroweak corrections $\delta_{\text{EW}}^{\text{tree}}$ and $\delta_{\text{weak}}^{\text{1-loop}}$ for the inclusive jet (left) and dijet (right) cross-sections in the first rapidity bin y (y^*), where the largest impact is observed. The jets were reconstructed using the distance parameter $R = 0.6$. The corrections were provided by the theory group given in Ref. [62].

function:

$$F(x) = p_0 + p_1 \cdot x^{p_2} + \log^{p_3}(x), \tag{3.13}$$

where $x \equiv p_T$ ($x \equiv m_{12}$) for a given rapidity range $|y|$ (y^*). An estimate of the symmetric uncertainties were determined from the envelope which is shown as blue band in Fig. 3.6. For $R = 0.4$ jets, the largest difference can be observed between Herwig++ interfaced with the UE-EE3 CTEQ6L tune and Pythia 6 using the Perugia2011 tune at low-p_T. The maximum deviation is approximately 6% in the first bin and decreases with increasing p_T. For jets reconstructed using the parameter $R = 0.6$, the largest deviation is around 8% in the first transverse momentum bin.

The influence of electroweak (EW) corrections on the inclusive jet and dijet cross-sections become significant at high-p_T (-m_{12}) due to the occurrence of Sudakov and other subleading logarithms originating from virtual exchange of massive gauge bosons. The corrections are dominated by Sudakov logarithms with the leading term $\propto \alpha_W \ln^2(Q^2/M_{\text{W}}^2)$, where $\alpha_W = \alpha/\sin^2(\theta_W)$ is the weak coupling constant, Q is the energy scale of the hard scatter, and M_{W} is the mass of the W-boson. The quantities appearing in the definition of α_W are the electromagnetic coupling constant α and the Weinberg angle θ_W. For $Q^2 \gg M_{\text{W}}^2$ the Sudakov logarithms can lead to large negative corrections. The electroweak corrections have a negligible impact on the total cross-section, but can lead to large corrections in certain phase-space regions.

The methods used to calculate the EW corrections are described in Ref. [62] and the corrections were provided by the authors. The corrections applied consist of electroweak tree-level $\delta_{\text{EW}}^{\text{tree}}$ and purely weak virtual $\delta_{\text{weak}}^{\text{1-loop}}$ corrections. The correction factor $\delta_{\text{EW}}^{\text{tree}}$ is defined to correct the QCD cross-section at LO σ_{QCD}^{0} to the full Standard Model (SM)

LO cross-section σ^0 as follows:

$$\sigma^0 = \sigma^0_{\text{QCD}} \cdot (1 + \delta^{\text{tree}}_{\text{EW}}). \tag{3.14}$$

These corrections comprise the remaining tree-level EW contributions of the order $O(\alpha_s\alpha)$ and $O(\alpha^2)$, which are not included in the calculations of the cross-section σ^0_{QCD} including QCD diagrams only. The NLO corrections $\delta^{\text{1-loop}}_{\text{weak}}$ are defined to correct the full SM LO cross-section σ^0 as follows:

$$\sigma^{\text{NLO(EW)}} = \sigma^0 \cdot (1 + \delta^{\text{1-loop}}_{\text{weak}}). \tag{3.15}$$

At NLO the corrections were obtained as purely weak corrections and are defined by diagrams at the order $O(\alpha_s^2\alpha_W)$. The impact of photonic corrections is expected to be at a few percent-level and the corrections were neglegted. The total correction can then be written as follows:

$$\sigma^{\text{NLO(EW)}} \approx \sigma^0_{\text{QCD}} \cdot (1 + \delta^{\text{tree}}_{\text{EW}} + \delta^{\text{1-loop}}_{\text{weak}}). \tag{3.16}$$

The corrections are applied to the NLO QCD cross-section calculated at the order $O(\alpha_s^3)$ using NLOJet++, as well as to the predictions produced using the Powheg BOX (see Sec. 3.4). Using QCD NLO diagrams as additional contributions to the pure weak corrections $\delta^{\text{1-loop}}_{\text{weak}}$ result in corrections of the order $O(\alpha_s^3\alpha_W)$ and thus are neglected.

The corrections for the central rapidity region are shown in Fig. 3.7 . The largest corrections of up to approximately 20% (15%) are applied to the cross-section predictions at high-p_T (-m_{12}) calculated in the first rapidity bin covering the region $0.0 \leq |y|$ (y^*) < 0.5. The dependence on p_T (m_{12}) is due to the flavor composition in the different phase-space regions. In the high-x regime qq-initiated interactions dominate and result in larger EW tree-level corrections $\delta^{\text{tree}}_{\text{EW}}$ compared to the low-x region, where gg-initiated processes becomes dominant. The negative weak corrections $\delta^{\text{1-loop}}_{\text{weak}}$ are also dependent on p_T (m_{12}). This behavior is due to large logarithms $\propto \ln^2(Q^2/M^2_{\text{W}})$ (among others) appearing at high Q^2. Because no uncertainty estimates were provided for this correction, no uncertainty was assigned. The full discussion can be found in Ref. [62].

3.4 NLO and Parton Shower

Powheg is a tool, which allows to match next-to-leading order (NLO) calculations and parton showers. It is interfaced to the Pythia event generator to simulate parton shower, hadronization and UE. This enables the possibility to produce predictions at particle-level without correcting for non-perturbative effects (cf. Sec. 3.3) and is expected to provide predictions with smaller theoretical uncertainties. Because of the inclusion of the parton shower simulation, the cross-section spectra determined using Powheg comprise an all order approximation and are at hadron-level already, whereas the predictions obtained using NLOJet++ are calculated at fixed-order NLO.

As a first step the Powheg algorithm produces the so-called underlying Born configuration (QCD $2 \to 2$ hard scatter) for each event. Additionally the hardest partonic emission in the event is generated. The fixed-order NLO predictions are obtained using the factorization and normalization scales equal to the transverse momentum of the final-

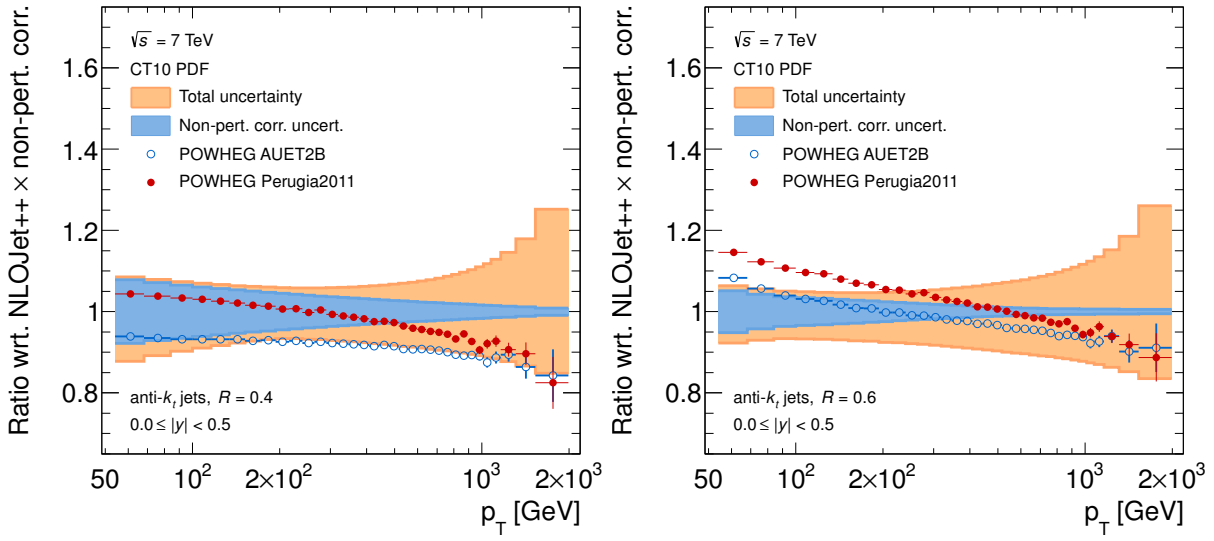

Figure 3.8: Ratios of the inclusive jet cross-sections predicted using POWHEG with respect to the NLOJET++ predictions discussed in Sec. 3.1 and Sec. 3.2. The NLOJET++ predicted cross-section spectra are corrected for non-perturbative effects which are derived as detailed in Sec. 3.3. Additionally the uncertainty due to the non-perturbative effects and the total uncertainty are shown as bands. The jets were reconstructed in the rapidity range $0.0 \leq |y| < 0.5$ using the jet finding algorithm anti-k_T with the distance parameters $R = 0.4$ (left) and $R = 0.6$ (right).

state partons p_T^{born}. To suppress collinear and soft divergent leading-order contributions to the cross-section, events with $p_T^{\text{born}} < 5$ GeV were rejected, which is far below the covered phase-space of the measurements. The difference between cross-sections at low-p_T (-m_{12}) and high-p_T (-m_{12}) is several orders of magnitude in the covered phase-space. To produce predictions of the cross-section over the entire phase-space within a reasonable amount of computation time, an event-based weighting method is used. The events are distributed according to the differential cross-section multiplied by a factor $S(k_T)$ [63]:

$$S(k_T) = \left(\frac{k_T^2}{k_T^2 + k_{T,\text{supp}}^2} \right)^3 ,$$

where k_T is the transverse momentum of the final-state partons and k_T^{supp} is the dimensionful quantity used to control the event weighting, which was set to 200 GeV. The predictions of the inclusive jet and dijet spectra using POWHEG[3] with the CT10 PDF set for the Perugia2011 and AUET2B tunes are exemplary shown for the inclusive jet cross-section for two different anti-k_T distance parameters R in Fig. 3.8. The difference between the cross-section spectra produced using Perugia 2011 and AUET2B depends on p_T (m_{12}) and decreases with increasing p_T (m_{12}). Thus it behaves in the same way, as the estimate of the uncertainty due to non-perturbative effects. The slope of the spectra

[3]To avoid problems due to large event weights, the POWHEG version given in Ref. [64] was used. The folding parameters were set to 5-5-2 (foldsci=5, foldy=5, and foldphi=2), and doublefsr=1. For the cross-section predictions the same POWHEG generation parameters as provided in Ref. [65] were used. A detailed description of the POWHEG generation parameters can be found in Ref. [66].

compared to NLOJET++ produced spectra corrected for non-perturbative effects deviates resulting in a 20% shift of the ratio over the covered phase-space. The same behavior can be observed in all rapidity $|y|$ (resp. y^*) bins and for both distance parameters R.

3.5 Baseline Predictions

The inclusive jet and dijet cross-section spectra determined using NLOJET++ were used as baseline predictions. For these spectra non-perturbative corrections were applied in order to provide predictions at particle-level, where they are compared to measurement results. Additionally, EW corrections were applied aiming to improve the description of the cross-section spectra. For these predictions theoretical uncertainties were estimated, which enables the possibility to assess the comparisons between measurements and NLOJET++ predictions. In case of POWHEG predictions, no theoretical uncertainty estimates were calculated and thus a meaningful comparison to measurements is not possible. The NLOJET++ predictions exploiting the CT10 PDF set were used as reference for other predictions. All predictions are compared with respect to the measured cross-sections as detailed in Sec. 8. The predicted inclusive jet (top) and dijet (bottom) cross-section spectra for jets reconstructed using the anti-k_T algorithm with distance parameters $R = 0.4$ (left) and $R = 0.6$ (right) are shown in Fig. 3.9. The phase-space shown in these figures reflects the kinematic coverage of the measurements in the upcoming analyses. In case of the inclusive jet cross-section spectrum the transverse momentum ranges from 100 GeV up to 2000 GeV. The rapidity $|y|$ is subdivided in six intervals covering the regime $0 \leq |y| < 3$. The range of the transverse momentum depends on the rapidity y, because it is the transverse projection of the jet momentum, which for a given jet energy decreases as $|y|$ increases. The spectra were scaled as function of the y bins in order to avoid overlapping. The difference of the cross-sections at the lowest transverse momentum and the phase space limit at high-p_T amounts to approximately eight orders of magnitude. The dijet cross-section spectra cover the dijet mass region 260 GeV $< m_{12} <$ 5000 GeV. The rapidity separation y^* is subdivided in six intervals and covers the regime $0 \leq y^* < 3$ [4]. The lower dijet mass boundary depends on the rapidity separation y^*. The lower edge is chosen such that the dijet cross-section is not biased due to kinematic cuts. The difference between dijet cross-sections in the low-m_{12} region and the high-m_{12} amounts to approximately eight orders of magnitude.

[4] The rapidity separation bin $2.5 \leq y^* < 3.0$ was not included in the cross-section measurement.

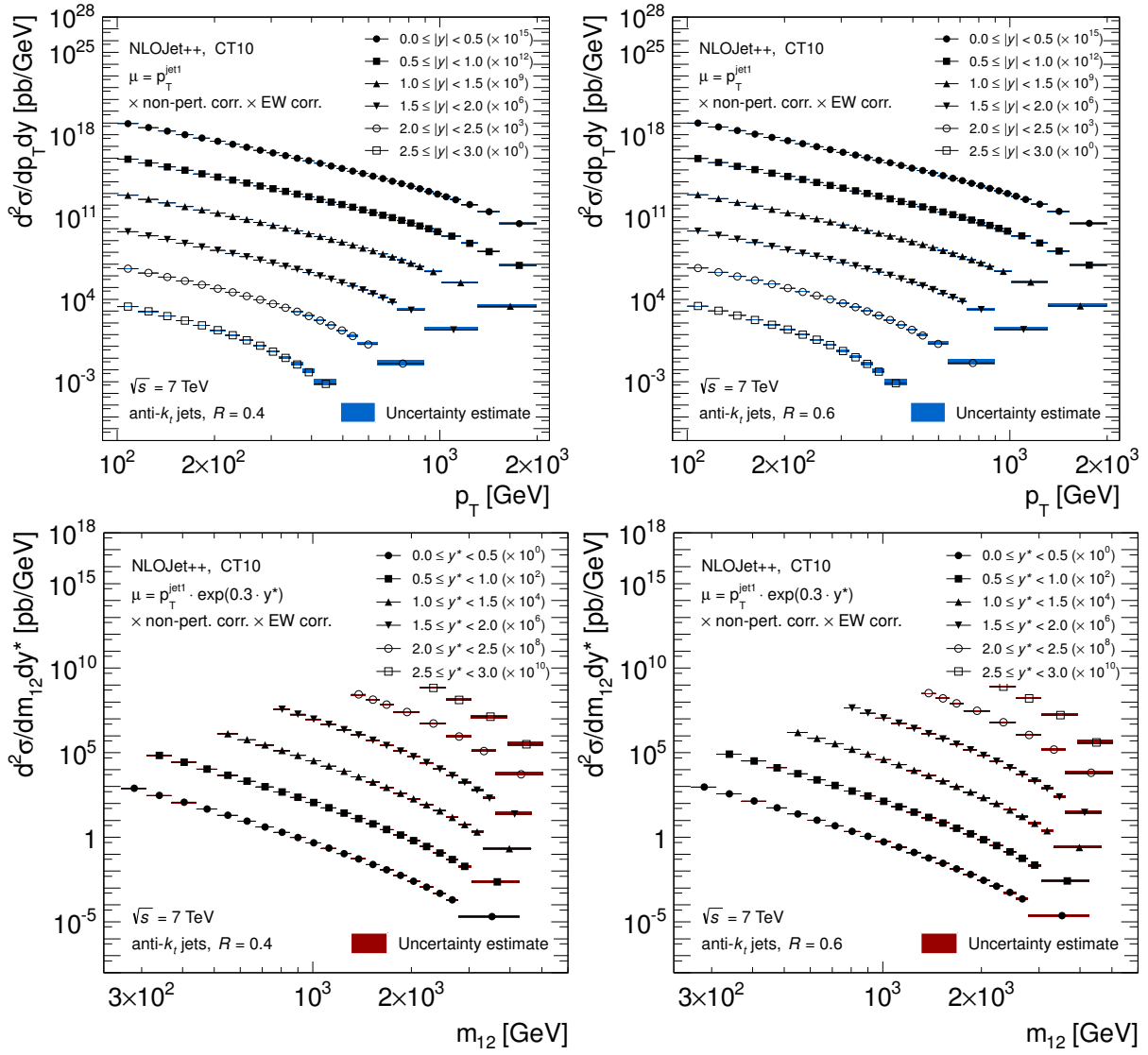

Figure 3.9: Inclusive jet (top) and dijet (bottom) cross-section predictions obtained with NLOJET++ using the CT10 PDF set in various rapidity y (resp. y^*) bins. The spectra are scaled. The jets were reconstructed using the anti-k_T algorithm with distance parameters $R = 0.4$ (left) and $R = 0.6$ (right). Shown is the entire phase-space covered by the measurement as detailed in Sec. 8. The estimated uncertainty (blue rectangle) includes the theoretical uncertainties as discussed in Sec. 3.2 and uncertainties due to non-perturbative effects (cf. Sec. 3.3).

4 The ATLAS Experiment at LHC

In this chapter the Large Hadron Collider (LHC) and the ATLAS (A Toroidal LHC ApparatuS) experiment are introduced. The LHC at CERN[1] is currently the most powerful accelerator. It was installed in the former Large Electron Positron (LEP) tunnel, which is located around 50 m to 175 m underground. The LHC and the associated experiments are briefly discussed in Sec. 4.1. The ATLAS experiment is a multi-purpose detector installed at LHC and the data used in this thesis were recorded using ATLAS. The aspects of the ATLAS experiment are detailed in Sec. 4.2.

4.1 The Large Hadron Collider

The LHC is a synchrotron collider, which is able to store protons or heavy-ions, where the former is used for studies in context of this thesis. Two proton beams, circulating in opposite directions in two adjacent vacuum pipes are brought to a collision at the center of four experiments. The accelerating protons are bend using approximately 1200 superconducting dipole magnets of around 8.3 T. Additionally, various other magnet types are used, serving different purposes as e.g. focusing the proton beams by quadrupole magnets. The LHC stores non-continuous beams, which consist of proton bunches. The LHC as well as the experiments were designed to operate at a bunch spacing of 25 ns (≈ 7.5 m at speed of light). The circumference of the circular tunnel is around 27 km which allows to store up to 3564 proton bunches with the 25 ns configuration, which results in a bunch-crossing rate of 40 MHz. Nevertheless the LHC fill pattern contains gaps and is designed to store up to 2808 proton bunches. The particle-free gaps were introduced to allow the extraction kicker magnets of the beam dumping system to achieve the nominal field-strength and for beam cleaning purposes [67].

The size of the proton bunches is of the order of 10 μm in the transverse and around 1 cm in the longitudinal direction containing each about 10^{11} protons. The high number of protons within a bunch causes multiple proton-proton (pp) interactions per bunch-crossing referred to as in-time pile-up. The LHC was designed to provide pp collisions at a center of mass energy $\sqrt{s}$ of 14 TeV and peak instantaneous luminosities $\mathcal{L}_{\text{peak}}$ of the order of $10^{34}\text{cm}^{-2}\text{s}^{-1}$. The number of events N_{exp} is by definition correlated with the instantaneous luminosity $\mathcal{L}$ as follows:

$$N_{\text{exp}} = \sigma_{\text{exp}} \times \int \mathcal{L}(t)dt, \tag{4.1}$$

where σ_{exp} is the cross-section of interest and the time integral $\int \mathcal{L}(t)dt$ is denoted as integrated luminosity[2]. Given an inelastic pp cross-section[3] of approximately 60 mbarn

[1] European Organization for Nuclear Research

[2] If not explicitly mentioned, the integrated luminosity is simply called luminosity.

[3] The total pp cross-section is approximately 100 mbarn at $\sqrt{s} = 7$ TeV [68] and additionally consists of

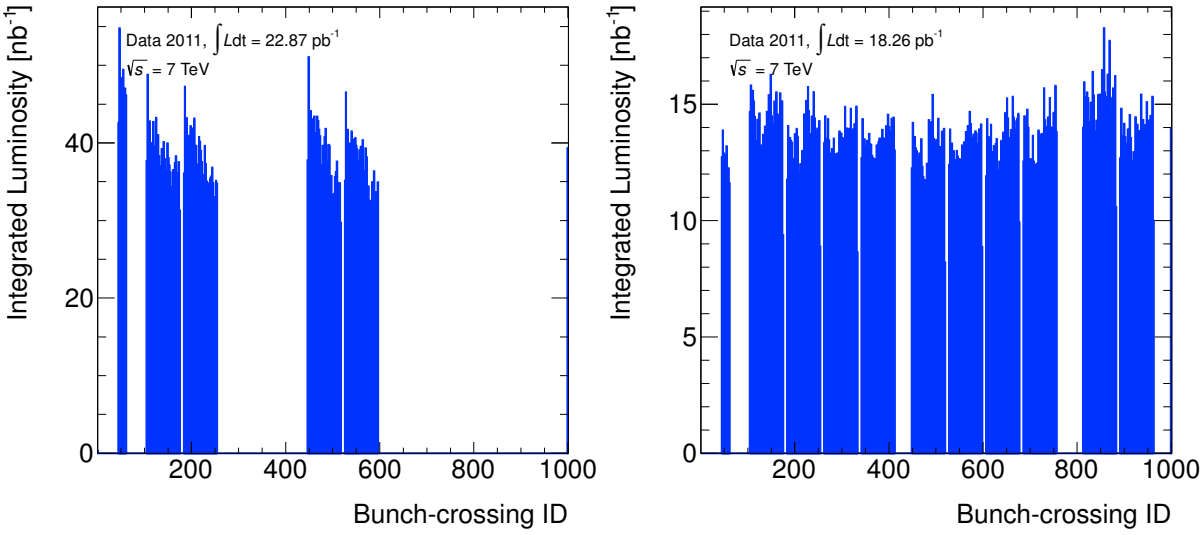

Figure 4.1: Two different bunch train configurations in the early (left) and late phase (right) of data-taking. On the y-axis the integrated luminosity in nb^{-1} and on the x-axis the bunch-crossing identification number (BCID) in the interval $[1, 1000]$ are shown. The distance between consecutive BCIDs amounts to 25 ns.

[69] at $\sqrt{s} = 7$ TeV, $600 \cdot 10^6$ inelastic events per second and 19 inelastic events per bunch-crossing are expected.

The main experiments installed at the four interaction points are LHCb (LHC beauty) [70], ALICE (A Large Ion Collider Experiment) [71], CMS (Compact Muon Solenoid) [72] and ATLAS [73]. LHCb and ALICE are special-purpose experiments. Additional experiments located at LHC covering specific physics purposes are LHCf (LHC forward) [74], TOTEM (TOTal Elastic and diffractive cross-section Measurement) [75], and MoEDAL (Monopole and Exotics Detector At the LHC) [76], where the interaction points are shared with ATLAS, CMS and LHCb, respectively. CMS and ATLAS are the two general-purpose detectors.

In 2011 the LHC was configured to provide bunch-crossings with a minimum spacing of 50 ns. The colliding bunches were organized in so-called trains, where the maximum train length was chosen to be approximately 1.5 μs. Bunch train configurations in the early phase (left) and the late phase (right) of data-taking are exemplary shown in Fig. 4.1. The maximum number of bunch-crossings per full LHC revolution was 1331, with a typical bunch population of $1.2 \cdot 10^{11}$ protons. The achieved instantaneous peak luminosity was $3.6 \cdot 10^{33} \mathrm{cm}^{-2}\mathrm{s}^{-1}$ with a maximum number of inelastic interactions per bunch-crossing of around 20. The integrated luminosity delivered by the LHC is approximately 5.5 fb^{-1} [78]. The evolution of the integrated luminosity (left) and the peak average number of interactions per bunch-crossing[4] (right) are shown in Fig. 4.2 per day for the data-taking

contributions from diffractive and elastic cross-sections.

[4]The average number of interactions per bunch-crossing was determined for all bunch-crossings over the time range of typically 60 s defined by the so-called luminosity-block (cf. Sec. 4.2.7). Only the maximum average values are shown in Fig. 4.2 (right).

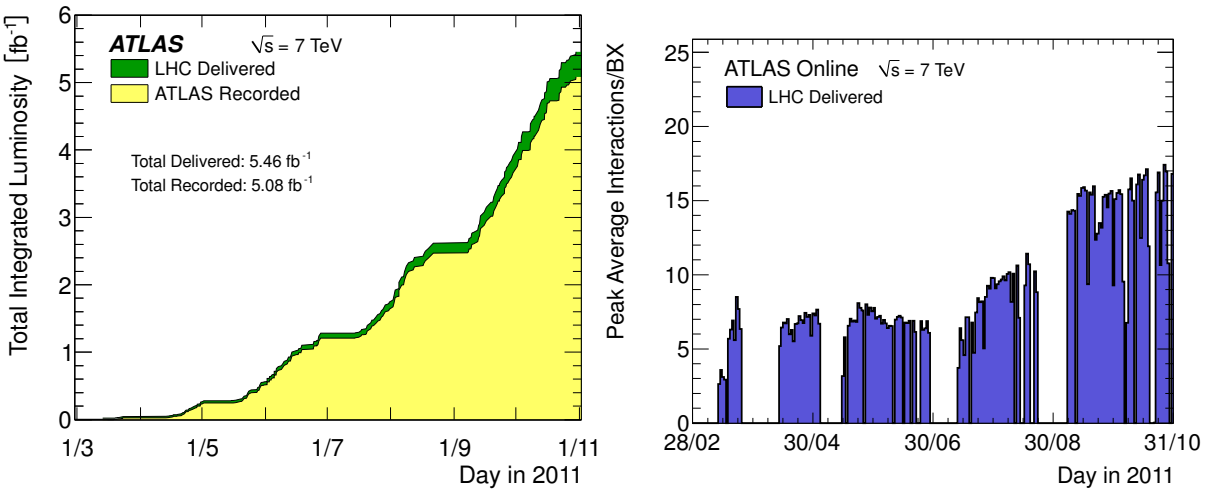

Figure 4.2: Left: evolution of the integrated luminosity during the data-taking in 2011 as function of day. Right: The peak average number of *pp* collisions per bunch-crossing (BX) per day. [77]

in 2011.

4.2 The ATLAS detector

The aim of the ATLAS detector is to cover the rich physics potential provided by LHC. The main benchmark was the search for the Standard Model Higgs boson covering many predicted decay channels and a wide range of masses. It is also used for Standard Model measurements, as well as to search for new phenomena predicted beyond the Standard Model such as for example massive exotics particles introduced in Sec. 2.3. ATLAS was fully operational for almost four years between 2008 and 2012 and is being prepared for the next run period starting in 2015.

An overview of the sub-components of the ATLAS detector are shown in Fig. 4.3. To be able to cover as much of the wide range of physics as possible, various sub-detectors and technologies were used. The detector consists of several layers, which can be grouped according to their purpose. The pixel detector, transition radiation tracker, and semiconductor tracker form the tracking system and are components of the inner detector. The inner detector is located within the magnetic field of 2 T created by the solenoid magnet. The tracking system is surrounded by the electromagnetic and hadronic calorimeters measuring the energy of incident particles. The most outer sub-detectors form the muon system, which is embedded within the magnetic field produced by the superconducting toroid magnets. The solenoid magnet is located in front and the toroid magnets lie outside of the calorimeter system.

The tracking system has to provide a good timing resolution to allow distinction between particle tracks from subsequent bunch-crossings as well as a high granularity to be able to separate multiple *pp* collisions per bunch-crossing. The calorimeter system has to provide a good energy resolution in the TeV region. All detector sub-components were also designed in order to fulfill the requirements on radiation hardness.

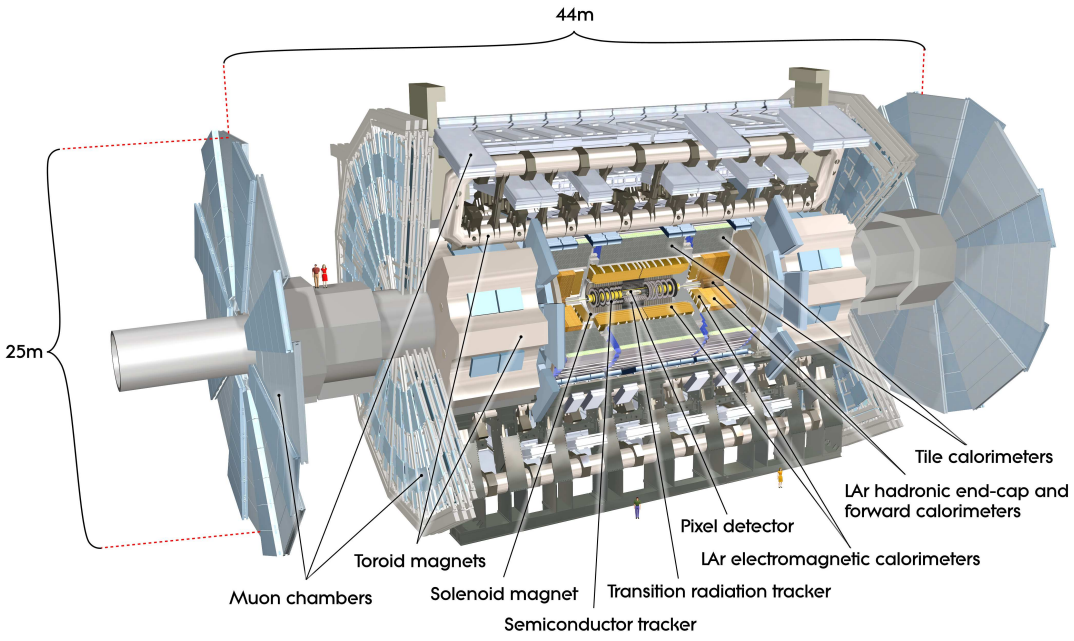

Figure 4.3: Cut-away view of the ATLAS detector showing the main sub-detectors and components. [73]

4.2.1 Coordinate System

For ATLAS a right-handed Cartesian coordinate system is used. The nominal interaction point (IP) which is at the center of the detector was chosen as origin. The z-axis was chosen to be along the beam pipe. The direction of the x-axis points to the center of the LHC ring and the y-axis points upwards.

More convenient coordinates are used in ATLAS to describe the kinematic condition of physics objects which are summarized in the following. In the transverse plane cylindrical coordinates (r, ϕ) are used, where $r = \sqrt{x^2 + y^2}$ is the radial distance to the beam, $\phi = \arctan(y/x)$ is the azimuthal angle around the z-axis relative to the x-axis. The rapidity is defined as $y = \frac{1}{2}\ln(\frac{E+p_z}{E-p_z})$, where E is the energy and p_z the longitudinal component of the three-momentum. The pseudorapidity[5] is defined as $\eta = -\ln(\tan(\theta/2))$, where the polar angle $\theta = \operatorname{arccot}(z/r)$ is measured from the z-axis. The relation between the polar angle θ and the pseudorapidity is illustrated in Fig. 4.4. Distances in the η-ϕ-plane are measured in ΔR which is given as: $\Delta R = \sqrt{\Delta\phi^2 + \Delta\eta^2}$. Quantities indexed with T, such as p_T, are projections to the x-y-plane of the quantity considered.

4.2.2 The Inner Detector

A computer-rendered cut-away image of the inner detector (ID) and its sub-components is shown in Fig. 4.5. The detector consists of three high-resolution sub-detectors which complement each other. The outermost sub-components form a cylinder of radius ≈ 1.2 m

[5]The pseudorapidity can be expressed in terms of the momentum p: $\eta = \frac{1}{2}\ln(\frac{|p|+p_z}{|p|-p_z})$. For high energies $E \gg m$ (massless four-momentum) the absolute value of the three-momentum is $|p| \approx E$ and thus $y \approx \eta$.

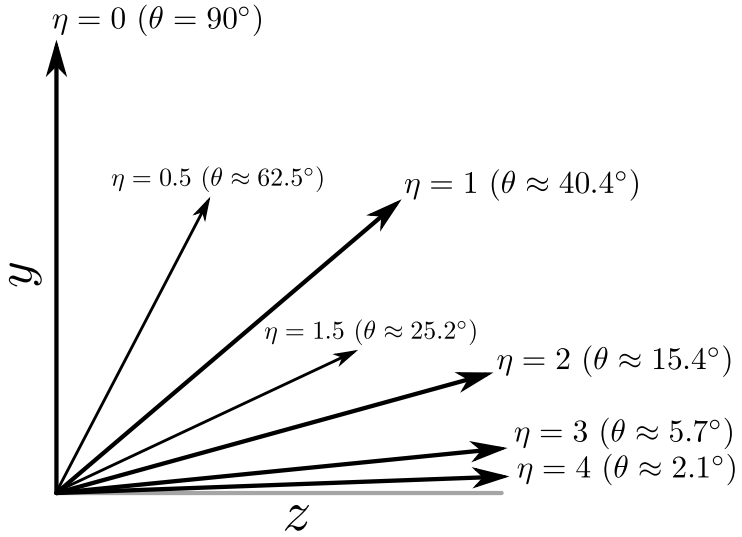

Figure 4.4: The relation between the pseudorapidity η and the angle θ with respect to the z-axis.

and length ≈ 7 m. The ID is located within the axial magnetic field of 2 T, which bends the trajectory of charged particles and thus allows precise measurements of the transverse momentum p_T. The achieved relative p_T resolution is $\sigma_{p_T}/p_T = 0.05\% \cdot p_T \oplus 1\%$ (p_T in GeV) and the space resolution is around 10 μm. The ID covers a region of up to $|\eta| = 2.5$ which corresponds to an angle of 9.4° with respect to the beam axis.

The sub-component closest to the interaction point, where the largest track density is created, is the silicon-pixel detector [79] with a minimum pixel size of 50×400 μm^2 in R-$\phi \times z$. The minimum radial distance to the beam axis is around 46 mm. The silicon pixel sensors function as solid-state ionization chambers. A particle traversing the doted semiconductor produces electron positron pairs, which can be detected by the read-out electronics. The pixel detector is arranged in three cylindric layers in the barrel and three disks in the end-caps. An intrinsic accuracy of 10 μm in the R-ϕ plane and 115 μm in z (barrel) or R (end-caps) is achieved.

The silicon microstrip detector (SCT) [80] is situated around the pixel detector. It consists of four double layers in the barrel and nine double disks in the end-caps. Because of the lower track density, silicon strips instead of pixels are used. This reduces the resolution and the number of readout-channels. The SCT has a binary readout, which registers whether a strip was hit or not. This limits the single strip accuracy to about 23 μm. The pixel detector as well as the SCT covers particles traversing the detectors within $|\eta| < 2.5$.

The outermost sub-detector of the ID is the transition radioation tracker (TRT) [81]. It is composed of straw tubes, which have an anode wire in the center and are filled with a Xenon/CO_2-based binary gas mixture with an additional small amount of O_2. The gas is ionized by transversing charged particles and low-energy transition radiation photons. The TRT is used in the proportional counting region and measures the drift-time of the ionization clusters to the wire. The drift-time is converted to the radial distance between the wire and the track of the charged particle. In the barrel the straw tubes are aligned

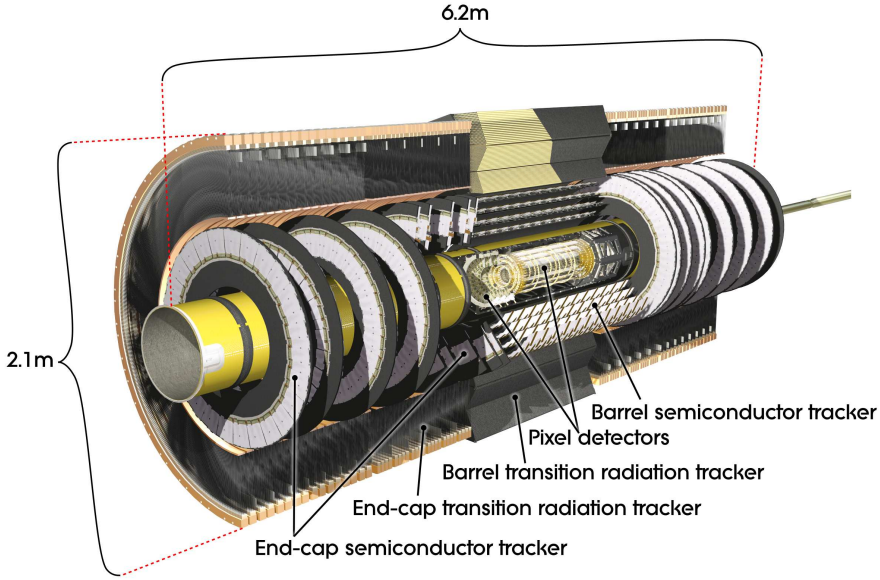

Figure 4.5: Cut-away drawing of the ATLAS inner detector and its sub-systems. [73]

parallel and the end-caps orthogonal to the beam-pipe. Due to the alignment and form, the TRT is able to provide measurements of the position in the R-ϕ plane (barrel) and z-ϕ plane (end-caps). The achieved drift-time accuracy is around 130 μm. The TRT provides an average of 36 hits per track and thus improves the momentum resolution and allows electron identification[6] over a wide range of energies.

The total number of read-out channels of the inner detector is $\sim 87 \cdot 10^6$, which can be broken down in contributions of $\sim 80 \cdot 10^6$ channels by the pixel detector, $\sim 6 \cdot 10^6$ channels by the SCT, and $\sim 3.5 \cdot 10^5$ channels by the TRT. Combined measurements of the three sub-detectors provide a robust pattern recognition and high accuracy. Particles that traverse the tracking system interact with the material. This causes energy losses and perturbance of the particle trajectory. Therefore the material budget of the inner detector is designed to be minimal. The readout windows in case of the pixel and SCT detectors are below the distance of 50 ns between consecutive bunch-crossings. The TRT has the largest read-out window of 75 ns and thus the signal is potentially affected by the subsequent bunch-crossing [83].

Charged Particles and Collision Vertex Reconstruction

For track reconstruction purposes different algorithms are used. At the first stage an inside-out algorithm is used as baseline algorithm. Hits detected by the pixel and SCT detectors are converted into three-dimensional space-points. Track seeds are found using

[6]The TRT provides the possibility to discriminate electrons from pions in the energy regime between 1 and 200 GeV exploiting transition radiation (TR). As discriminating quantity the high threshold (HT) fraction is used. HT is the energy threshold at about $6-7$ keV. For a given TRT tube a HT hit is present, if the HT is exceeded at least one of three times within the readout window of 75 ns. The HT fraction is defined as the fraction of hits on track that exceed the high threshold. For particle momenta of 4 GeV $< p <$ 20 GeV, the average HT fraction is approximately 0.25 for electrons and 0.05 for pions [82].

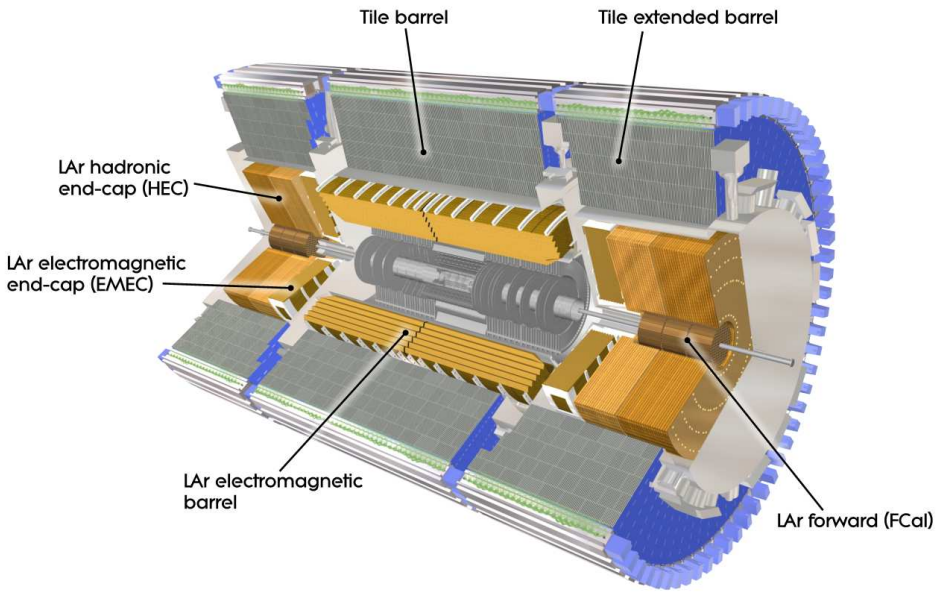

Figure 4.6: Cut-away view of the ATLAS calorimeter system. [73]

three space-points in adjacent layers, which also provide a rough estimate of the track direction. Hits in the surrounding layers located in the estimated area are added to the track. As the outermost detector the TRT is used for reconstruction. At the second stage the track reconstruction starts from the information povided by the TRT and extends to the silicon detectors. The back-tracking algorithm is primarily designed to reconstruct secondaries. In the final stage tracks are reconstructed using the TRT with no extension into the pixel and SCT detectors, which are denoted as TRT-standalone tracks. After the track reconstruction, tracks are associated with vertex candidates. These vertex seeds are determined from the z-position of the reconstructed tracks. An χ^2 fit is performed using the vertex seed and tracks in the vicinity. Tracks with too large distance to the vertex candidate are used to seed a new vertex. This step is repeated until no further vertex candidates can be found. Because of the short readout time of the detectors, the primary vertex reconstruction is robust against out-of-time pile-up. The achieved vertex resolution depends on the number of reconstructed tracks fitted to the vertex. For events with 10 reconstructed tracks the vertex resolution in z is around 200 μm and decreases with an increasing number of tracks. For events with 70 tracks the resolution is around 50 μm in the longitudinal direction [84]. A detailed description of the ATLAS track and vertex reconstruction can be found in Ref. [85].

4.2.3 The Calorimeter System

Particles that traverse the calorimeter deposit their energy by interacting with the detector material. Different calorimeter types and technologies are used in ATLAS to fulfill the requirements given at LHC. An overview of the calorimeter system and its sub-components are shown in Fig. 4.6.

ATLAS calorimeters are designed as sampling calorimeters, which consist of alternating layers of absorber and active material. The absorber material is chosen such that the probability for a particle to deposit energy is high. The active layer is used to measure the

energy of the incident particles and secondary particles, which are produced in cascades the so-called showers.
The ATLAS calorimeter system consists of two different calorimeter types, the electromagnetic and hadronic calorimeters. The electromagnetic calorimeter uses liquid argon (LAr) as active material and lead (Pb) as absorber. The hadronic calorimeter uses different technologies and is realized as iron-scintillator and LAr-copper and -tungsten sampling calorimeter. The calorimeter system covers the energy measurement of particles within $|\eta| \approx 4.9$, which corresponds to angle with respect to the beam-axis of 0.9°. Over the large η-range different technologies are used to fulfill the requirements aroused by physics processes of interest and the radiation environment provided by LHC. A high coverage in pseudorapidity is especially required to improve the accuracy of the missing transverse energy reconstruction, which is an essential constituent of many final states predicted by physics beyond the Standard Model.

The relative energy resolution of the electromagnetic calorimeter of the incident particles is $\sigma_E/E = 10\%/\sqrt{E/\mathrm{GeV}} \oplus 0.7\%$. This allows for instance a measurement of the Higgs boson mass in the $\gamma\gamma$ final state with an accuracy of 1% [7]. The search for the Higgs boson as well as other heavy particles decaying in hadronic final states, manifest as jets, define also the requirements for the performance of the hadronic calorimeter. The achieved relative energy resolution is $\sigma_E/E = 50\%/\sqrt{E/\mathrm{GeV}} \oplus 3\%$ in the barrel and end-cap region. The measurement of the invariant masses depends additionally on the angular resolution, which is achieved by a high granularity in η and ϕ.

In addition to the granularity, the calorimeter thickness is important to provide a good resolution e.g. for high energetic jets. A sufficient thickness allows the measurement of the full electromagnetic and hadronic showers caused by particles carrying energy at the TeV scale and hence reduces punch-through into the muon system. Therefore the calorimeter system was designed e.g. to measure electron energies up to 1.5 TeV [87]. In order to quantify the depth of a calorimeter two different measures are used. The radiation length X_0 is defined as follows: $E(x) = E_0 e^{-x/X_0}$, where $E(x)$ is the energy of an electron as function of the traversed distance x in detector material, E_0 is the initial energy of the particle, and X_0 the radiation length. Hence X_0 is the average distance over which an electron loses $1/e$ of its energy on average by bremsstrahlung[8]. In contrast to electrons more material is required to stop hadrons. For hadronic calorimetry the hadronic interaction length λ is used to quantify the depth of the calorimeter. It is defined as the mean distance a particle traverses the detector material before an interaction takes place. For material with high Z as Pb and Cu, which are used in the ATLAS calorimeter as absorber the hadronic interaction length λ is factor 10-30 larger compared to the radiation length X_0 [9]

[7] The significance of the Higgs signal in the $H \to \gamma\gamma$ channel depends on the energy resolution and thus also on the mass resolution. The dominant systematic uncertainty in this channel was found to be the uncertainty due to the mass resolution [86].

[8] The radiation length X_0 is also relevant for high energetic photons which split to e^+e^- pairs. In this case X_0 is 7/9 of the mean free path of a photon for pair production. Effects like ionization and others lead to further energy loss which can be described by a more complex formalism. The radiation length X_0 is also used to describe the length of electromagnetic cascades. [17]

[9] For Cu (Pb) $\lambda \approx 15.3$ (17.6) cm and $X_0 \approx 1.4$ (0.6) cm. The numbers were derived from properties given in Ref. [17].

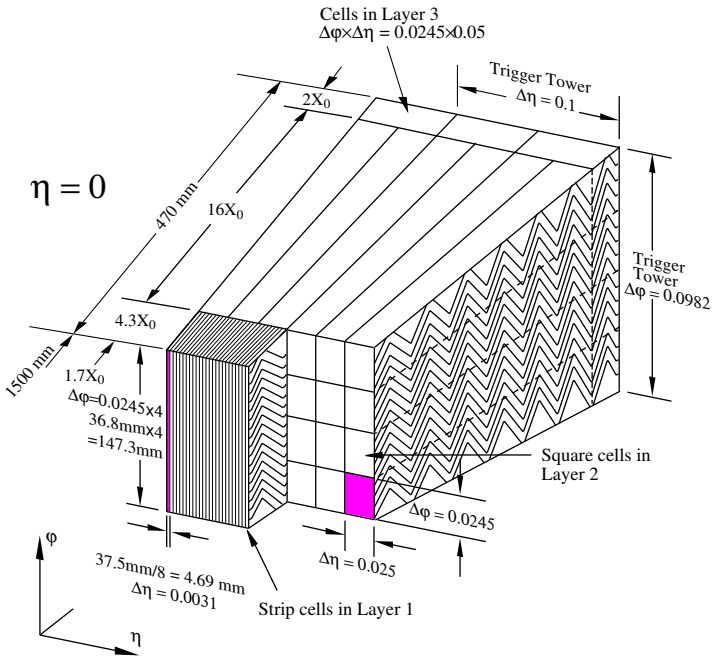

Figure 4.7: Slice of the barrel electromagnetic calorimeter. Indicated are the accordion structure with the three layers, the granularity of the cells in η and ϕ, and the trigger towers (cf. Sec. 4.2.6). [73]

An additional aspect in the calorimeter design is the linearity of the energy scale. The detector linearity is a measure of how accurate a particular energy measurement can be transfered to any energy. For the electromagnetic calorimeters the achieved linearity is below 0.5% and for hadronic calorimeters below 2% [88].

The Electromagnetic Calorimeters

The electromagnetic barrel calorimeter consists of two structurally identical sub-components centered around $\eta = 0$. It is based on technology using LAr as active layer and is therefore embedded in the centrally located cryostat. The electromagnetic barrel calorimeter covers pseudorapdities up to $|\eta| < 1.475$ which corresponds to an angle with respect to the beam-axis of $\theta \approx 26°$. A schematic drawing of the inner structure is shown in Fig. 4.7. The alternating calorimeter layers are accordion-shaped. This design provides complete ϕ symmetry without any cracks and a fast extraction of the signal at the rear or at the front of the electrodes. In the barrel the accordion waves run along the R-axis. To ensure a constant active layer width the folding angles of the waves vary as function of R. The electromagnetic barrel consists of 3 layers covering different purposes. The first layer provides high granularity in η. The second layer provides the largest radiation length and therefore measures the largest energy fraction of the electromagnetic cascade. The third layer is designed to collect the tail of the cascades and therefore provides a coarser granularity in η. The total depth in units of radiation length X_0 of the electromagnetic calorimeter increases with η from 22 to 33, which aim to cover the entire electromagnetic shower originating from electromagnetic interacting particles at TeV scale.

The end-cap electromagnetic calorimeters (EMEC) consist of two wheels installed on

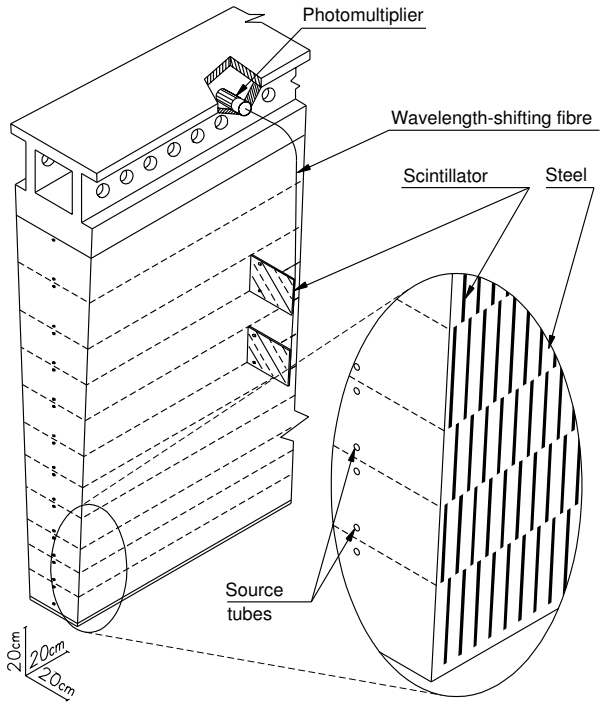

Figure 4.8: A module of the tile calorimeter and its optical readout. Also shown is the position of photomultipliers, and a zoom-in to illustrate the alignment of the absorber/scintillator layers and the location of the Cs sources. [73]

each side of the detector. The outer wheels cover $1.375 < |\eta| < 2.5$ and the inner wheels up to $|\eta| < 3.2$. The accordion geometry was also realized in the EMEC wheels. The accordion waves are aligned parallel to the radial direction. The same segmentation as in the electromagnetic barrel calorimeter was used. The granularity of $\Delta\eta \times \Delta\phi$ is 0.025×0.025. The depth of the electromagnetic calorimeter in terms of radiation length X_0 is approximately $23X_0$ in the barrel and above $25X_0$ for $|\eta| > 1.5$.

The electromagnetic barrel has two locations in η, where uniformity of the energy measurement is interrupted. One is located at $\eta = 0$, where the two half-barrels are joined and at $\eta \approx 0.8$, where the thickness of the absorber material changes. The transition region from the electromagnetic barrel to the EMEC is located around $|\eta| \approx 1.45$, which also causes a non-uniformity in the energy measurement. The total number of electromagnetic calorimeter channels is around 160000.

The Hadronic Calorimeters

The tile calorimeter is installed outside the cryostats, which contain the electromagnetic calorimeter. It consists of two components on each side of the detector called the tile barrel and the tile extended barrel. The former covers pseudorapidities up to $|\eta| < 1.0$ and the latter the region $0.8 < |\eta| < 1.7$. A cut-away drawing of one tile calorimeter module is shown in Fig. 4.8. By analogy with the electromagnetic calorimeter, the tile barrel is splitted into three layers, where the second layer provides the largest thickness of 4.1 interaction length λ. The total thickness of the instrumented part at the outer edge of the tile calorimeter including other detector components like the electromagnetic calorimeter

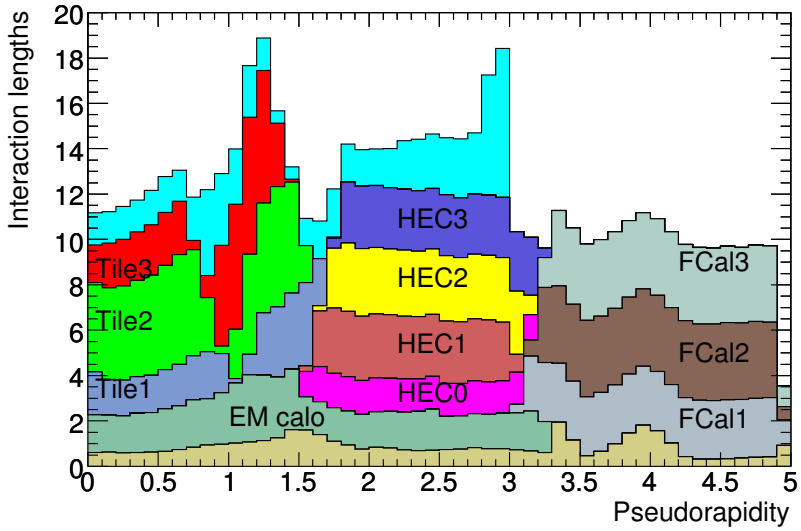

Figure 4.9: Interaction length λ as function of $|\eta|$, in the electromagnetic calorimeters, the sub-layers of the hadronic calorimeters and the total active calorimetry. Also shown is the material in front of the first layer of the muon system. [73]

in the central region at $\eta = 0$ is 9.7λ. In contrast to the barrel the layer thickness of the extended barrel increase with R, where the third layer provides the largest depth of around 3.3λ. The tile calorimeter is realized as a sampling calorimeter, which uses steel for the passive layer and scintillating tiles as active material.

The hadronic calorimeter in the end-cap (HEC) consists of two cylindrical wheels, the front wheel (HEC1) and the rear wheel (HEC2), on each detector side which are located behind the EMEC. It uses the LAr in the active layer and copper as absorber. The HEC wheels and the EMEC wheels share the same cryostats. Both wheels cover the pseudorapidity region $1.5 < |\eta| < 3.2$, which overlaps with the tile calorimeter to reduce the decrease of the interaction length in the transition region. The HEC wheels are constructed from wedge-shaped modules in the r-ϕ plane with alternating parallel copper flat plates along the beam-axis. Each HEC wheel is segmented in two longitudinal layers resulting in four layers on each side, where the thickness of the copper plates for each layer increases as function of the distance from the interaction point. The distance between the plates is independent of the position and orientation. The inter-plate gaps are sub-divided into four equidistant drift zones. The cells are defined by a set of consecutive read-out electrode pads. They are staggered such that the same η range is covered by each pad within the cell. The pre-amplified signals from the pads are actively summed and form one output signal.

The granularity $\Delta\eta \times \Delta\phi$ of the HEC is 0.1×0.1 up to $|\eta| = 2.5$ and is fourfold reduced in the more forward region. In total 5632 read-out channels are realized on both sides of the detector. The thickness up to the end of the HEC including all previous material is around 12λ (cf. Fig. 4.9).

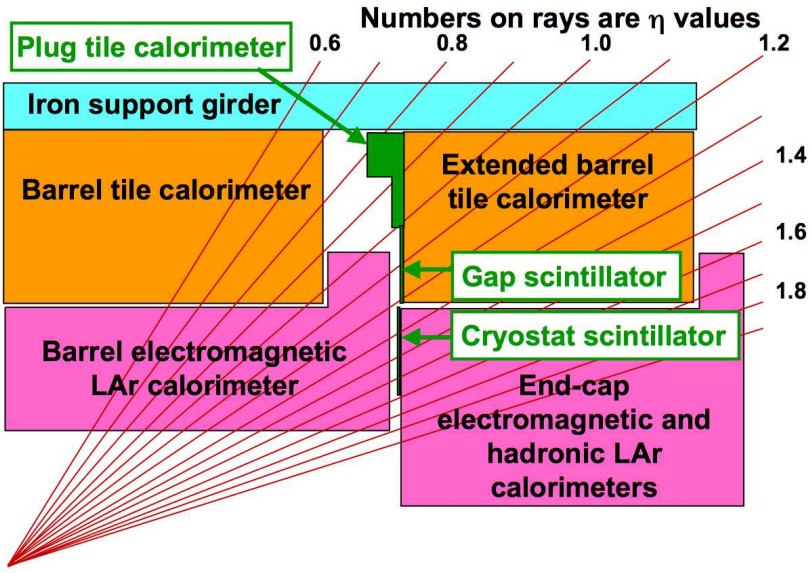

Figure 4.10: Locations of the gap detectors in the r-z-plane. [73]

Transition region between Barrel and End-Cap

In the transition region between the barrel and end-cap calorimeters service structures, such as cables, for the inner detector and the LAr calorimeters are installed. In Fig. 4.10 the gap region in r-z-plane is shown. To provide additional coverage in the transition region and compensate for losses in the dead material, several detectors are installed. The outermost detector in this region is a tile sub-module of reduced size, denoted as plug. In addition to the energy measurement it reduces the particle flux to the muon system. The gap scintillators which cover the pseudorapidity range $1.0 < |\eta| < 1.2$ provide information which can be used to derive corrections for energy losses in the gap. The cryostat scintillators which cover the region $1.2 < |\eta| < 1.6$ are installed between the electromagnetic barrel and end-cap and serve the same purpose.

The Forward Calorimeters

The forward calorimeters (FCal) provide energy measurement in the range $3.2 < |\eta| < 4.9$. The FCAL share the outmost cryostats with EMEC and HEC to achieve a better uniformity. Due to the small angle with respect to the beam-axis the FCal operates in a high radiation environment. Thus one of the main design requirement is radiation hardness. As consequence the thickness of the active layer is reduced compared to other calorimeters, which leads to shorter electron drift times.

The FCAL is subdivided in three layers in longitudinal direction. The first layer consists of consecutive copper plates as absorber and is optimized for electromagnetic energy deposits. The electrode structures were installed in holes drilled in the plates parallel to the beam-axis. Rods with a smaller diameter are inserted, where LAr in between is filled. The second and third layers are hadronic calorimeters, where tungsten is used to increase the interaction length λ. The layers use similar architectures. A detailed description of the FCal calorimeter is given in Ref. [89].

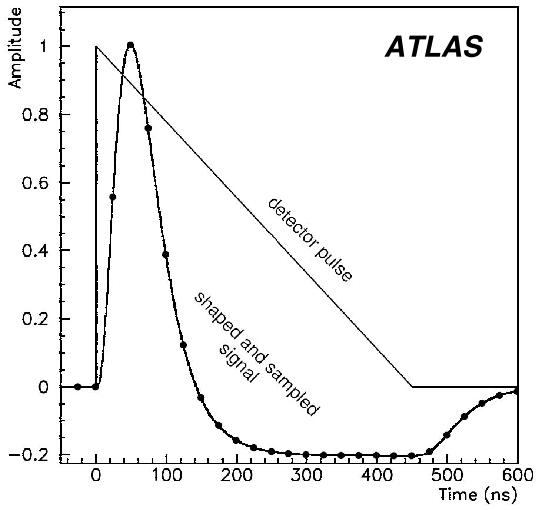

Figure 4.11: The detector pulse and the bi-polar signal at the output of the shaper. The dots indicate the points in time of digitization. [90]

Calibration of the Calorimeter Signal

Charged particles traversing the active layer of the LAr calorimeters produce electron-ion pairs, which drift to the electrodes driven by an electric field. The pulse height of the measured triangular shaped ionization current is proportional to the deposited energy within the active material. The analogue signal is shaped and digitized with 5 samples at 25 ns intervals. In Fig. 4.11 the pulse of the current in the LAr cell and the signal after the bi-polar shaping procedure is shown. The peak current of the triangular signal corresponds to the maximum of the signal $A_{\max}$ after the bi-polar shaping. Therefore the maximum of the shaped pulse $A_{\max}$ is proportional to the energy deposited by the particle. The typical signal time is around 600 ns in the central region and is reduced to approximately 300 ns in the forward region, which is large compared to the time between consecutive bunch-crossings of 25 ns. Therefore particles from different bunch-crossings traversing the same calorimeter cell would cause superimposed signals. This behavior is referred to as out-of-time pile-up. Particles from different pp collisions (in-time pile-up) which deposit energy in the same cell would cause a higher amplitude $A_{\max}$. The shaping time t_p of the shapers affects the electronics and out-of-time pile-up noise level. The electronic noise is increasing with a decreasing t_p, whereas the impact of out-of-time pile-up is increasing with the time constant of the shaper. The time constant is carefully optimized, which leads to a peaking time[10] between 30 ns and 45 ns [92]. This method is based on the assumption that previous and subsequent bunch-crossings exist. Energy deposits of particles originating from bunch-crossings with no previous or subsequent bunch-crossings are overestimated or underestimated, respectively. As the first step the counts are converted to the signal current in units of μA for each individual cell. The conversion factors are derived using a precise charge-injection system by injecting a precise calibration signal at the input of the detector cells. The calibration from μA to a signal in GeV is determined from test-beam measurements.

An illustration of a signal shape obtained from a tile calorimeter cell in presence of

[10] $A_{\max}$ as well as the peaking time are determined using the so-called Optimal Filtering Method [91].

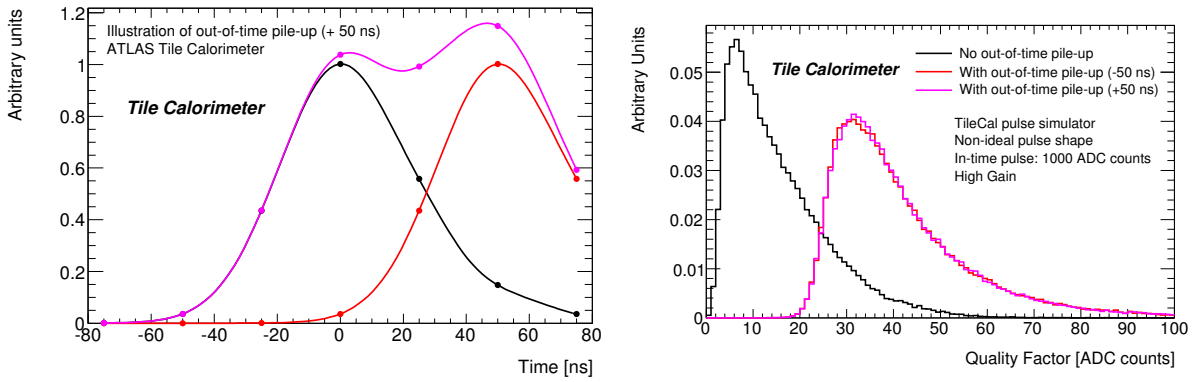

Figure 4.12: Left: sketch of the pulse shape generated in the tile-calorimeter in presence of out-of-time pile-up. Right: Quality Factor (QF) distribution in different out-of-time pile-up environments and with no out-of-time pile-up. [94]

out-of-time pile-up is shown in Fig. 4.12 (left). The distorted shape of the signal can be detected using the so-called Quality Factor (QF), which is a measure for the compatibility between the known and the observed pulse shapes. The distributions of QF with different out-of-time pile-up configurations are shown in Fig. 4.12 (right). A similar quantity is also calculated for each LAr cell which is a measure of the difference between the shapes of the predicted and observed pulses (cf. Sec. 6.1.2). The energy reconstruction algorithm was shown to be robust against out-of-time pile-up with the 50 ns bunch spacing configuration in 2011 [93]. The calibration of the tile calorimeter can be sub-divided in three parts. A charge-injection system is used to calibrate the shaping and digitizing electronics in order to obtain conversion factors form ADC counts to pC. The photomultipliers are calibrated and monitored using a laser system. For the calibration and monitoring of the scintillator and optical system, a ^{137}Cs γ-source, which is moved within the calorimeter, is used. The method allows to calibrate the entire chain. The absolute calibration from the collected charge in pC to the energy in GeV is obtained from test-beam measurements using electrons.

4.2.4 The Luminosity Detectors and Measurement

The luminosity of a pp collider can be calculated as follows [95]:

$$\mathcal{L} = \frac{\mu_{\text{vis}} n_{\text{b}} f_{\text{r}}}{\sigma_{\text{vis}}}, \tag{4.2}$$

where $\sigma_{\text{vis}} = \epsilon\sigma_{\text{inel}}$ is the total inelastic cross-section and $\mu_{\text{vis}} = \epsilon\mu_{\text{inel}}$ the average number of inelastic interactions per bunch-crossing multiplied by the efficiency ϵ of the luminosity detector. f_{r} is the revolution frequency of the LHC and n_{b} is the number of bunch pairs colliding per revolution. To determine the luminosity scale, the visible cross-section σ_{vis} is calibrated for each luminosity detector separately. For this purpose dedicated beam separation scans were performed referred to as van der Meer (vdM) scans. The absolute luminosity can be derived from accelarator parameter measurements and is given as:

$$\mathcal{L} = \frac{n_{\text{b}} f_{\text{r}} n_1 n_2}{2\pi \Sigma_x \Sigma_y}, \tag{4.3}$$

where n_1 and n_2 are the number of protons per bunch in the clockwise and counterclockwise beam respectively, and Σ_x and Σ_y are the horizontal and vertical convolved beam widths. The widths Σ_x and Σ_y are measured by moving the beams in stages with respect to each other in the x-y-plane and are combined with external measurements of the population product $n_1 n_2$ to obtain the total luminosity for calibration. Several sub-detectors are used for luminosity measurements. The detectors can be sub-divided in two categories. The detectors which measure the luminosity on bunch-by-bunch basis and detectors which measure the total luminosity integrated of all bunch-crossings.

The instantaneous luminosity is proportional to the measured number of interactions per bunch-crossing μ_{vis} (see Eq. 4.2), where the latter is measured by two main luminosity detectors: LUCID [96] and BCM [97]. LUCID (LUminosity measurement using Cerenkov Integrating Detector) is primarily designed for luminosity measurements. It detects inelastic pp scattering in the forward region, and is therefore able to measure the integrated luminosity and provide online monitoring of the instantaneous luminosity. The two detectors are located on each side at the distance of ± 17 m from the interaction point. It consists of 16 aluminium tubes filled with C_4F_{10} gas. The tubes surround the beam-pipe and cover pseudorapidity in the range $5.6 < |\eta| < 6.0$. An incident charged particle that traverses the tube creates Cherenkov light in the gas that is reflected by the tube walls and is detected by the photomuliplier tubes (PMT) located at the back end of the tubes. The signal is digitized and processed by hardware-based algorithms, which provide luminosity measurements for each bunch-crossing. The processing electronics run independent from the main data acquisition system and are not affected by the deadtime of the trigger system (cf. Sec. 4.2.6).
The Beam Conditions Monitor (BCM) consists of diamond sensors which surround the beam-pipe at a distance of ± 184 cm from the IP and are alligned as vertical (BCMV) and horizontal pairs (BCMH). The BCM was originally designed to monitor the background level and is able to request a beam-abort in case the probability of damaging the ID becomes high. The good time resolution of around 0.7 ns and the fast read-out allow a bunch-by-bunch luminosity measurement at $|\eta| = 4.2$. BCMV and BCMH are treated as independent devices and are both used for the luminosity measurement.

The inner detector is described in Sec. 4.2.2. It is used to reconstruct the number of primary vertices (N_{PV}), which are produced in inelastic pp collisions within $|\eta| < 2.5$. The determination of N_{PV} behaves non-linear with increasing number of interactions per bunch-crossing due to vertex masking and fake vertices. The former is due to the inefficiency to resolve nearby vertices in an in-time pile-up environment, the latter occur due to wrongly assigned tracks of adjacent vertices. Data-driven corrections were applied to be able to determine the luminosity using the ID.

The tile calorimeter (cf. Sec. 4.2.3) and the FCal (cf. Sec. 4.2.3) are also used for luminosity determination. The methods are based on measuring detector currents. The Tile and FCal do not provide independent luminosity measurements, because the calibration was performed using LUCID. Therefore these sub-systems were used as tool to check stability and linearity of other techniques.

4.2.5 The Muon Spectrometer

The muon system is the outermost set of sub-detectors which surrounds the calorimeter system and covers the pseudorapidity range $|\eta| < 2.7$. A computer-rendered image of muon detector components is shown in Fig. 4.3. Its purpose is to measure muon trajectories which are deflected by a magnetic field and provide charge identification. Muons are minimum ionizing particles, which have a small probability to deposit energy by ionization across their way trough the detector. In contrast to the inner detector, where the particles are deflected in the r-ϕ plane, the charged particles in the muon detector are bend in the r-z-plane. The magnetic deflection is caused by the toroid magnets. Among others the main performance goal is a good momentum resolution over a wide range which is required to be $\sigma/p_T = 10\%$ at $p_T = 1\text{TeV}$.

The muon system consists of two detector types. The Monitored Drift Tubes (MDT's) allow a precision measurement of the muon tracks over a large η-range in the central region. For measurements in the end-cap Cathode Strip Chambers (CSC's) are used. The MDT'S are tubes with a diameter of 30 mm, which are filled with a Ar/CO_2 gas mixture. They work as drift tubes, where electron and ion clusters are produced along the incident charged partical trajectory. The electrons drift due to the electric field towards the anode wire creating an avalanche and induce a signal on the wire. The CSC's are multiwire proportional chambers with cathode planes subdivided into strips aligned perpendicular to anode wires. The muon system is instrumented with separate detectors for trigger purposes, which provide a good timing resolution of few nanoseconds. A detailed description of the muon system is given in Ref. [98].

4.2.6 The Trigger System

As discussed in the previous section, the LHC is designed to provide bunch-crossing rates of up to 40 MHz with many pp interactions on average, whereas only a subset of the resulting final states is of interest. Due to the limited band-width and a large data size of a detector read-out, events can be recorded with a rate of around 200 Hz. The reduction of the rate is achieved by a fast and efficient event pre-selection, which is realized in a multilevel trigger system.

The ATLAS trigger system is organized in three levels: the Level-1 (L1) trigger, the Level-2 (L2) trigger, and the third level trigger, called event filter (EF). The L2 and EF trigger are denoted as high-level trigger (HLT). The amount of information used for trigger decisions increases with the level, where EF uses more complex algorithms and largest amount of information. The usage of different trigger stages, which use different levels of detail allow the reduction of the average decision time. The largest reduction of the event rate is achieved by the L1 trigger. Thus the L1 trigger is a hardware-based trigger, which provides trigger decisions within 2.5 μs with a maximum accepted event rate of 75 kHz. As input for the decision the calorimeter with reduced granularity and dedicated sub-detectors of the muon system are used. The output provided by the L1 trigger and forwarded to the L2 trigger. This output contains region of interests (ROI) in the detector, where signatures of interest were detected. The L2 trigger algorithms are implemented in software running on high-performance computing clusters. At this level fast algorithms are used to process partial high-granularity event data within the ROIs.

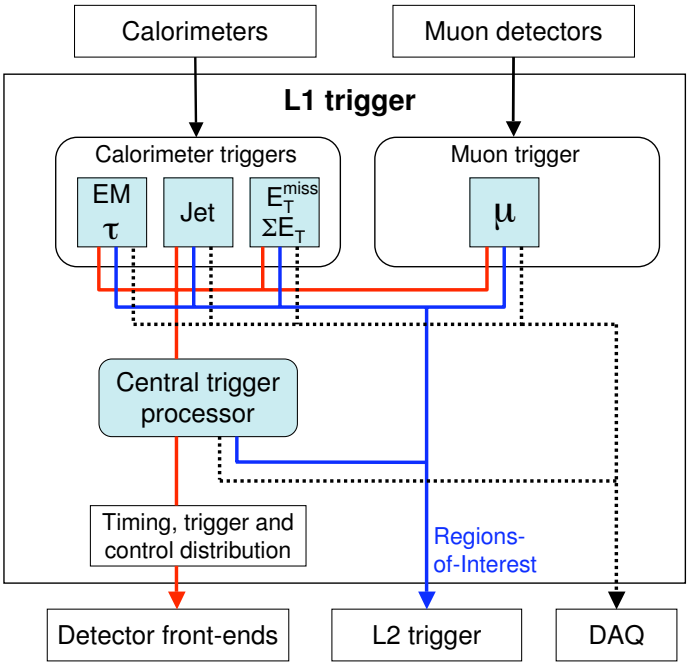

Figure 4.13: Reduced block diagram of the L1 trigger system. The calorimeter and muon trigger results are provided as input for the central trigger processor (CTP). The connections to the DAQ (dotted black), the detector front-ends (red), and L2 trigger (blue) are indicated. [100]

The computation of a trigger decision takes up to 40 ms. The event rate was reduced to $4-5$ kHz. The events passing the L2 trigger are forwarded to the EF. The EF uses more complex algorithms which take the full event information as input for the trigger decision. Due to the large amount of processed information the trigger decision can take up to four seconds. The output rate of the EF was in the range between 300 Hz and 400 Hz. [99]

Trigger requirements are usually fixed during the entire year of data taking. If the trigger rates exceed constrains due to the available computational power and band-width, some trigger decisions are down-scaled by a factor d, which is adjusted dynamically according to the instantaneous luminosity during a run. That means that only the d^{th} decision is forwarded to the next trigger or is recorded. The down-scale of the trigger decision is done at all three levels, which are taken into account when reconstructing e.g. spectra as function of p_T. During the processing of an event by the triggers at different levels, the measured detector data is stored in the pipelines within the Data Acquisition (DAQ) system and is finally recorded, when the event passed the trigger requirements. In the following a more detailed discussion focusing on jet trigger is presented.

The Level-1 Trigger

To fulfill the latency requirements for a single trigger decision the granularity was reduced and a compact design was realized. Informations from the inner detector are not included in the trigger decision. The architecture of the L1 trigger is illustrated in Fig. 4.13. The trigger consists of two sub-components, the calorimeter trigger and the muon

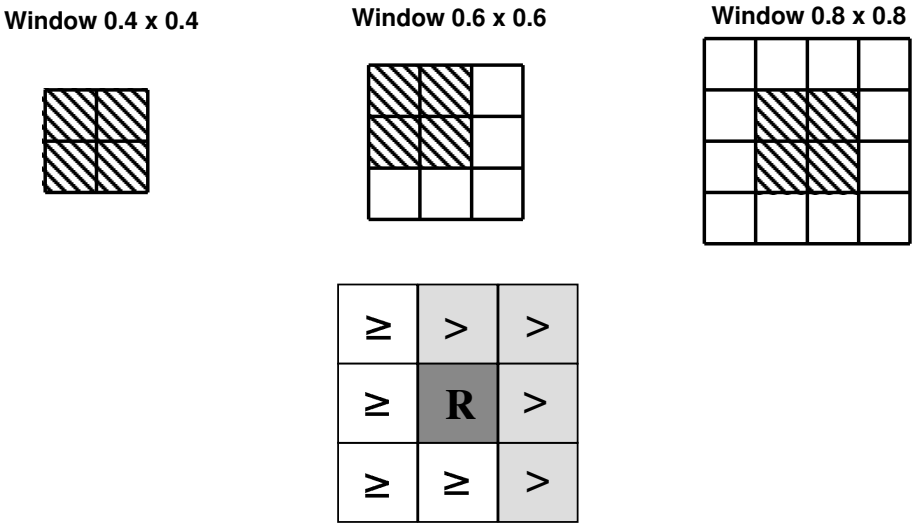

Figure 4.14: Function principle of the jet trigger algorithm. [100]

trigger. They determine the multiplicity of objects, such as jets, which exceed defined transverse energy E_T thresholds. Additionally the calorimeter trigger determines the sum of transverse energies E_T^{sum} and missing transverse energy E_T^{miss}, which are transmitted to the Central Trigger Processor (CTP), where the trigger decision is generated. The muon trigger is not used in this thesis, therefore only the calorimeter trigger and in particular the jet trigger are discussed in the following.

The Level-1 Calorimeter trigger: The L1 calorimeter trigger (L1Calo) uses around 7200 analogue trigger towers (TT's) with reduced granularity. A trigger tower build from calorimeter cells in the barrel is indicated in Fig. 4.7. It is a set of calorimeter cells located within $\Delta\eta \times \Delta\phi$ of at least 0.1×0.1 in most parts of the calorimeter system [11]. The signals for each TT are determined by summing up to 60 individual analogue calorimeter cell signals. The analogue TT signals are digitized every 25 ns by the pre-processor (PP). Additionally, the PP converts ADC counts to transverse-energy and generates the so-called jet elements. To avoid triggering on a mixture of objects originating from different bunch-crossings (BC), it is essential to identify the original BC, which is also done within the PP. As detailed in Sec. 4.2.3 the width of the signal from the electromagnetic and hadronic calorimeter cells covers several bunch-crossings, which complicate the identification of the bunch-crossing. Algorithms used for bunch-crossing identification (BCID) are required to be efficient for a wide range of energy deposits and simple, to reduce the contribution to the total latency. Thus several algorithms are used for this purpose, which exploit the signals provided by the TTs [101]. The data are then sent in parallel to the Cluster Processor (CP) and Jet/Energy-sum Processor (JEP). The JEP processes jet trigger elements of the size of 2×2 TT's in electromagnetic and hadronic calorimeters, to find jets using a sliding window algorithm. The received electromagnetic and hadronic jet elements, are summed up by the JEP. The function principle of the jet finding algorithm is illustrated in Fig. 4.14. The algorithm runs over all possible overlapping windows consisting of 2×2, 3×3 or 4×4 jet elements and calculates the transverse energy sums $\sum E_T$,

[11] As described in the previous sections a coarser minimum granularity is provided by the calorimeter system at higher pseudorapidity.

which are compared to pre-defined thresholds. To avoid multiple-counting the window is required to surround 2 local maximum jet elements, which are found by comparing the $\sum E_T$ to that of the eight nearest non-overlapping 2×2 jet element neighbors. In case of the 3×3 window, four windows are possible, where the window with the maximum $\sum E_T$ is used as indicated in Fig. 4.14 (left). The calculated E_T values of jet elements are transmitted as 9 bit digital numbers. This leads to comparisons of identical digital values. Therefore the comparisons to the 2×2 jet element neighbors are split into 'greater than' and 'greater than or equal to' as shown in Fig. 4.14 (right). The region of interest (ROI) is defined by the position of the 2×2 local maximum. The jets found by the L1 trigger algorithm are square objects in η-ϕ, with sizes of 0.4×0.4, 0.6×0.6, and 0.8×0.8. The largest window size was configured for the triggers used in the upcoming analyses, which corresponds the area of a jet with the distance parameter $R \approx 0.45$ (cf. Sec. 2.2). The CP provides electron/photon and τ-lepton identification, which has a transverse energy above a pre-defined threshold. A sliding window algorithm with finer granularity and further isolation criteria is used to find the ROIs. Both processors count also the number of objects of interest and send these information to the CTP. A full description of the L1 trigger system is given Ref. [102].

High level trigger: The L2 trigger and the EF trigger are both referred to as High Level Trigger (HLT) and are both software-based running on high-performance computers. When an event is accepted by the CTP at L1, data containing the full calorimeter information at the location of the ROIs are sent to the L2 trigger. This data covers typically around 1-2% of the full event record. For jet finding a simplified cone algorithm [103] with cone radius $R = 0.4$, which uses the full calorimeter granularity within a window around the ROI. At L2 a noise suppression method was used, which takes electronics noise and noise due to pile-up into account. A measured calorimeter cell energy is required to be above $3 \times \sigma_{\text{noise}}$ within the ROI and the L2 window, where σ_{noise} is the noise level. The trigger rate is reduced to $4 - 5$ kHz, where the processing time is below 40 ms. The decision generated by the L2 trigger is finally transmitted to the EF, where the full event record is available. At this level, reconstruction and calibration methods similar to the ones in the offline reconstruction can be used. In contrast to the offline reconstruction the final correction required due to the non-compensating nature of the detector, was not applied at EF level. At both stages tracking information from the inner detector is available, whereas only provided for a fraction of events at L2 due to the limited band-width. The upcoming analyses use jet triggers of different threshold configurations at EF. The requirements on E_T and information about jet reconstruction are coded in the trigger name. The triggers used in this thesis are denoted as EF_jX_a4tc_EFFS, where X is the E_T threshold in GeV, *a4tc* means that the jets were found using the anti-k_T algorithm with the distance parameter $R = 0.4$ and topological clusters as input, which provide a pile-up noise suppression. The expression 'EFFS' stands for Event Filter Full Scan and indicates that the full detector information was used for the jet finding. This EF trigger are simply called 'EF Jet $E_T > X$ GeV' in the following. The triggers used are inclusive jet triggers, thus no requirements on the jet multiplicity are made[12].

For the EF triggers with low-E_T threshold requirements, random triggers were used as seed called L1_RD0_FILLED and L2_rd0_filled_NoAlg. The RD0 is a down-scaled high-

[12]Jet triggers requiring N jets are denoted e.g. as EF_NjX_a4tc_EFFS

rate random trigger implemented in the CTP, which selects colliding (FILLED) bunch pairs. At L2 no algorithms were used to process event data. Instead a randomly selecting algorithm was used. For the sake of completeness, the EF triggers and the corresponding chain used in this thesis are shown in Tab. 4.1. The configured E_T thresholds increase with the trigger level within a trigger chain. The lower threshold at L1 (L2) was chosen to reduce the loss of events at HLT due to trigger inefficiencies. Exemplary are also shown the down-scale factors for a randomly selected run and luminosity block (cf. Sec. 4.2.7).

Level 1		Level 2		Event Filter	
Name	down-s.	Name	down-s.	Name	down-s.
L1_RD0_FILLED	468800	L2_rd0_filled_NoAlg	1.0	EF Jet $E_T > 10$ GeV	18.6
L1_RD0_FILLED	468800	L2_rd0_filled_NoAlg	1.0	EF Jet $E_T > 15$ GeV	4.3
L1_RD0_FILLED	468800	L2_rd0_filled_NoAlg	1.0	EF Jet $E_T > 20$ GeV	1.2
L1_J10	44200	L2_j25	1.0	EF Jet $E_T > 30$ GeV	1.0
L1_J15	28500	L2_j35	1.0	EF Jet $E_T > 40$ GeV	1.0
L1_J30	4430	L2_j50	1.8	EF Jet $E_T > 55$ GeV	1.0
L1_J50	2140	L2_j70	1.0	EF Jet $E_T > 75$ GeV	1.0
L1_J75	1	L2_j95	1.0	EF Jet $E_T > 100$ GeV	595.0
L1_J75	1	L2_j95	1.0	EF Jet $E_T > 135$ GeV	153.0
L1_J75	1	L2_j95	1.0	EF Jet $E_T > 180$ GeV	35.8
L1_J75	1	L2_j95	1.0	EF Jet $E_T > 240$ GeV	1.0

Table 4.1: The full chains for triggers used in this thesis. Also shown are the down-scale factors for a randomly chosen run and luminosity block.

4.2.7 Data acquisition

The recorded data is organized in so-called *runs*, which is a time period of a stable beam lasting up to several hours. The runs are sub-divided in so-called luminosity blocks (LB's). LB's are subsequent periods within a run assigned by the trigger hardware. A typical duration in the data under consideration was around one minute. Changes in the configuration like a trigger down-scale adjustment cause the start of a new luminosity block. The instantaneous luminosity is considered to be constant in context of a LB. This fact is used to calculate the integrated luminosity by using the information on duration of the LB. [104]

Events which receive an L1A accept decision are written to disk storage system located at CERN. In order to provide the data to all ATLAS members, the data is distributed via a distributed multilevel computing architecture. The first level is the so-called Tier-0, which is the computing facility at CERN storing the data in the raw format. This data is used for reconstruction purposes at Tier-0. Derived formats of the raw data are then distributed to different Tier-1 facilities. The following formats are distributed: Event Summary Data (ESD), Analysis Object Data (AOD), primary Derived Physics Data (DPD), TAG files, various n-tuple and histogram files, and log files [105]. ESD contain detailed information of the event reconstruction and sufficient information in order re-fit tracks, re-done the calibration etc. The size of ESD is around 35% with respect to size of

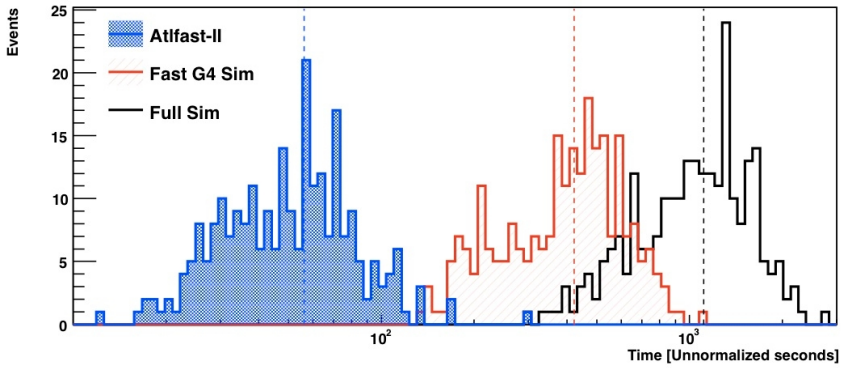

Figure 4.15: CPU time needed for detector simulation using $t\bar{t}$ events [106]. The Fast G4 simulation is not used in context of this thesis. A description of this method can be found in Ref. [106].

the raw data. In case of AOD the size is further reduced to 5% of the raw data and below for DPD and n-tuples. In general, these data are further reduced in size according to different requirements and are distributed to various Tier-2 and Tier-3 high performance computing clusters, where the user analysis code is executed.

4.2.8 Detector and Pile-Up Simulation

The simulation software for ATLAS consists of several components grouped together as ATLAS simulation infrastructure [106]. Final state particles simulated using MC generators, are propagated through the ATLAS detector simulation. Two different approaches were used to simulate the detector: the full GEANT4 based and Atlfast-II (AF-II) detector simulation. The full ATLAS detector simulation is based on highly detailed description of the sub-detector components. It uses the GEANT4 particle simulation toolkit [107], which simulates the interactions of traversing particles with the detector materials. The energies deposited in the sensitive regions of the detector are recorded as "hits" containing information as the total energy, position etc. The digitization takes the "hit" information as input. At this step e.g. background events and detector noise can be overlaid before the detector signal is generated [106]. The outcome of the simulation process has the same structure as data and can be used to apply the same reconstruction algorithms. GEANT4 provides phenomenological models and parameterizations for physics processes. The so-called *physics list* which consists of a set of models, is used to describe the different types of interactions. For hadronic interactions the so-called QGSP_BERT physics list was chosen, which uses the Quark Gluon String Precompound (QGSP) model for the hadron-nucleon interactions and the Bertini cascade model to describe the interactions of hadrons below 10 GeV. The *physics list* was validated from data recorded during the test beam runs by comparing the results with GEANT4 predictions for various calorimeter sub-components. Good agreement between data and prediction was found for pion and proton beams. Further validation tests were performed by identifying single particles e.g. from kaon decays, which were produced in pp collisions [108]. With the increasing number of recorded event statistics in data a higher number of simulated Monte Carlo (MC) events is required. During the full simulation of an event around 80% of time is spent to simulate particle showers traversing the calorimeter. To reduce the amount of time to

simulate the ATLAS detector a fast simulation has been developed called AF-II, which uses *FastCaloSim* for the calorimeter [109]. This is realized by parameterizing the longitudinal and lateral energy profiles of single particle showers and is therefore less accurate compared to the full simulation. Nevertheless the parametrization can be tuned against data and has been validated against the full simulation [106]. The CPU time spent to simulate events in ATLAS exploiting different methods is shown in Fig. 4.15. The simulation using AF-II is processed approximately one order of magnitude faster compared to the full simulation. The samples for the new physics models introduced in Sec. 2.3 were produced using AF-II. All other MC simulation were produced using the full detector simulation.

Several pile-up background types can be identified in ATLAS: In-time pile-up, out-of-time pile-up, cavern background, beam halo and beam gas events [106]. In-time and out-of-time pile-up are introduced in Sec. 4.1 and Sec. 4.2.3, respectively. In case of in-time pile-up additional collisions are generated and passed through the full detector simulation. These collisions are overlaid at a rate, which corresponds to that in data. In order to improve the performance and save disk space a large portion of this background is removed. The sample is divided into events with and events without a jet with $p_T > 35$ GeV. The events without such a jet are re-used, and the events with such a jet are only used once. Out-of-time pile-up is treated in a similar way, overlaying collisions that originate from different bunch-crossings. The sensitive time window of each sub-detector to previous and sub-sequent bunch-crossings is taken into account. Cavern background consists mainly of slow neutrons, long-lived neutral kaons and low-energy photons escaping the calorimeter and the forward shielding elements. The most affected detector component is the muon system. Beam halo events originate from machine-induced secondary particles which can be caused by interactions e.g. in the collimators located outside of the detector. Halo particles cross the detector from side to side leaving energy deposits in the calorimeter system. Beam gas events originate from collisions between the proton bunch and gas within the evacuated beam-pipe. Cavern background, beam halo and beam gas events were typically not simulated [110], because a cleaning procedure is applied in physics analyses in order to reject such events as discussed in Sec. 6.1.3.

5 Jet Reconstruction and Monte Carlo Based Energy Calibration

Jets can be reconstructed using different physics objects as input for the jet finding algorithms. The different inputs required for the analyses presented in this thesis are discussed in Sec. 5.1 - 5.3. The correction and calibration of reconstructed jets at detector-level using Monte Carlo based techniques are introduced in Sec. 5.4.

5.1 The Topological Cluster Algorithm

The topological cluster algorithm uses calorimeter cells which are calibrated at the electromagnetic scale including corrections for energy losses optimized for photons and electrons [112]. An incident particle deposits energy in several calorimeter cells in longitudinal and lateral directions. The aim of the topological clustering algorithm is to group the affected cells and to determine the total deposited energy within each cluster and to achieve as close as possible correspondence between clusters and particles. The result of the clustering procedure is a three-dimensional object within the calorimeter system. The basic strategy of the algorithm is to add cells in an iterative procedure around a seed cell to the cluster, provided that the signal-to-noise ratio of the new cell is above a defined threshold. Thus, this approach leads to noise suppression.

Finding seed cells: As the first step the seed cells (also denoted as proto-cluster) are identified by requiring the energy-to-noise to be greater than a threshold t_{seed}:

$$\frac{|E_{\text{cell}}|}{\sigma_{\text{cell}}} > t_{\text{seed}}, \tag{5.1}$$

where $|E_{\text{cell}}|$ is the absolute value of the energy measured in each cell and $\sigma^2_{\text{cell}} = \sigma^2_{\text{elec.}} + \sigma^2_{\text{pile-up}}$ the expected RMS of the electronics and pile-up noise distribution. In Fig. 5.1 (left) exemplary shown are seed cells ($t_{\text{seed}} = 4\sigma_{\text{cell}}$) in the first layer of the forward calorimeter.

Neighbors finding: The list of seed cells determined in the seed finding procedure are sorted in descending order according to their signal-to-noise ratio. The adjacent cells of each proto-cluster which are not included in the seed cells list, and have a signal-to-noise ratio above $t_{\text{neighbor}} = 2\sigma_{\text{cell}}$ are added iteratively to the proto-cluster. Proto-clusters sharing the same neighbor cells are merged. The seed cells list is discarded after each iteration and the neighbor cells are treated as seed cells in the next step. All eight surrounding cells located within the same calorimeter layer are considered as well as adjacent layers and calorimeter systems. All adjacent cells which have a signal-to-noise ratio between $t_{\text{cell}} = 0\sigma_{\text{cell}}$ and $t_{\text{neighbor}} = 2\sigma_{\text{cell}}$ are attached to the proto-cluster. In case this type of cell shares proto-clusters, the cell is added to the proto-cluster which provides the most

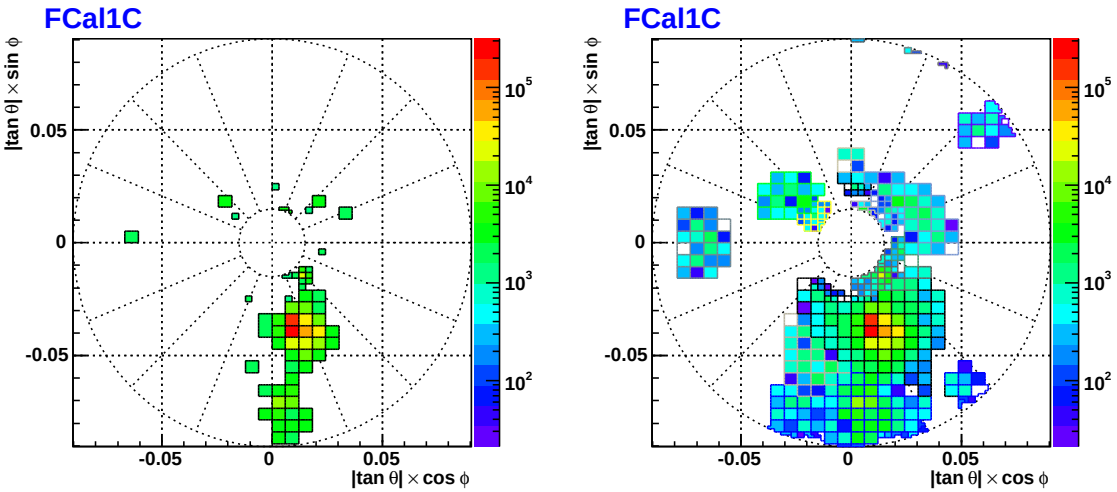

Figure 5.1: Simulated deposition of energy in the forward calorimeter. Seed cells in the first layer of the forward calorimeter with energy deposits above $4\sigma_{\text{cell}}$ (left) and the resulting clusters (right) are shown in the polar coordinate system. The color indicates the amount of energy measured which is coded in units of MeV. The seed cells of several clusters shown are located in other calorimeter layers. [111]

significant adjacent cell. The resulting proto-clusters are sorted in descending order in E_T and are converted to clusters. The cell-by-cell noise σ_{cell} as function of the pseudo rapidity for each calorimeter layer is shown in Fig. 5.2. Shown are distributions of pure electronics noise and cell noise in presence of pile-up for various LAr detector components. The cell noise varies by many orders of magnitude over the entire detector especially in presence of pile-up. The largest impact due to pile-up on σ_{cell} can be observed in the end-caps and the forward region of the calorimeter system. In the central region electronics noise is the dominant source.

Splitting Algorithm: Using the procedure described above could lead to clusters covering large areas of the calorimeter in case of more than one incident particle. The cluster splitting algorithm is designed to split clusters constructed by the topological cluster algorithm in order to separate the energy deposits of the individual particles. As the first step local maximum cells are found. They are located by requiring a measured cell energy to be above 500 MeV and greater than that of adjacent cells. Furthermore a minimum number of neighboring cells within the parent cluster is required. For clusters with at least two local maxima a modified clustering algorithm is performed using the local maxima as seed cells. For this procedure only cells within the parent cluster are considered. In case of neighboring cells which share proto-clusters merging is not performed. Instead adjacent cells are added to the local maximum which provides the best energy-to-noise ratio. The outcome of this procedure is exactly one cluster around each local maximum. In Fig. 5.1 (right) exemplary shown are clusters in the first layer of the forward calorimeter. The noise suppression mechanism leads to an improved performance of the calorimeter system in presence of pile-up.

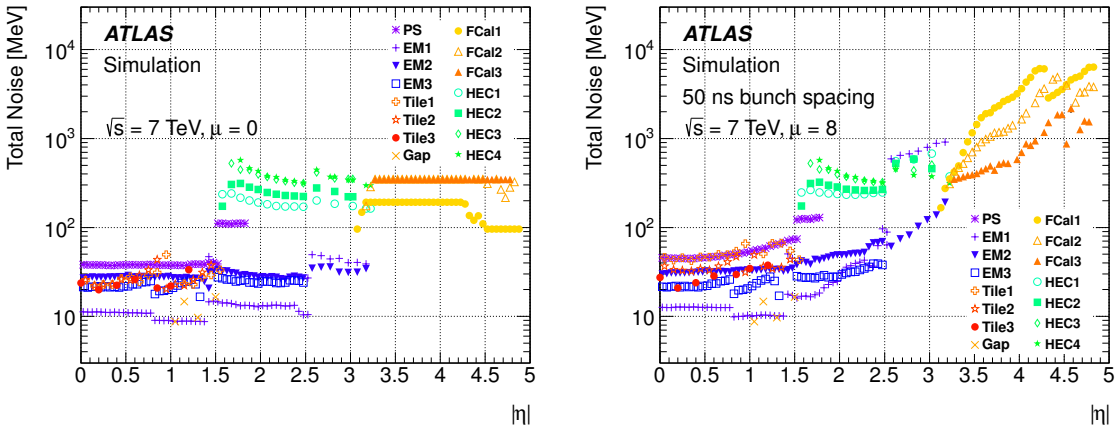

Figure 5.2: Total noise (left) and total noise in presence of pile-up (right) for different LAr calorimeter layers as function of the absolute value of pseudo-rapidity $|\eta|$. The average number of interactions per bunch-crossing is $\mu \equiv \mu_{\text{avg}} = 8$. [113]

5.2 Local Cluster Weighting

The local cluster weighting (LCW) calibrates the topological clusters independent of the jet finding algorithms. The aim is to provide cluster energies which corresponds to stable particle energies. The correction factors were derived using detailed simulations of randomly distributed single neutral and charged pions in the ATLAS detector. This calibration procedure consists of four steps: classification of clusters, cell-based weighting, correction for out-of-cluster effects and dead material.

As a first step the topological clusters are tagged as electromagnetic or hadronic. As discriminating quantities, cluster shape variables are used. Because clusters are associated with particles, the electromagnetic clusters correspond to electrons, photons, and neutral pions, whereas hadronic clusters correspond to charged hadrons and neutrons. Two cluster shape variables are used, the avarege cell energy density $\langle\rho\rangle$ and the longitudinal depth of the shower center λ_{center}. For both particle types a four-dimensional histogram is constructed containing pseudorapidity $|\eta|$, the cluster energy E_{cluster}, $\log_{10}(\lambda_{\text{center}})$, and $\log_{10}(\langle\rho\rangle) - \log_{10}(E_{\text{cluster}})$. The histogram was filled using simulated pions. From this a probability of observing a neutral pion w_i is calculated:

$$w_i = n_i^{\pi^0}/(n_i^{\pi^0} + 2 \cdot n_i^{\pi^\pm}), \tag{5.2}$$

where $n_i^{\pi^{0,\pm}}$ is the fraction of clusters for a given bin i in the four-dimension histogram. A cluster is tagged as electromagnetic for $w_i > 0.5$. Exemplary shown in Fig. 5.3 (left) is the probability of observing a π^0 (color coded z-axis) for cluster energies 8 GeV $< E_{\text{cluster}} <$ 16 GeV in the calorimeter region $0.2 < |\eta| < 0.4$. In contrast to the electromagnetic clusters, the hadronic clusters are characterized by a lower energy density and a larger longitudinal cluster depth.

The clusters tagged as hadronic are calibrated using a cell-based method weighting within the hadronic cluster to correct for the lower calorimeter response to hadrons. At this step no corrections are applied to clusters which are tagged as electromagnetic. The

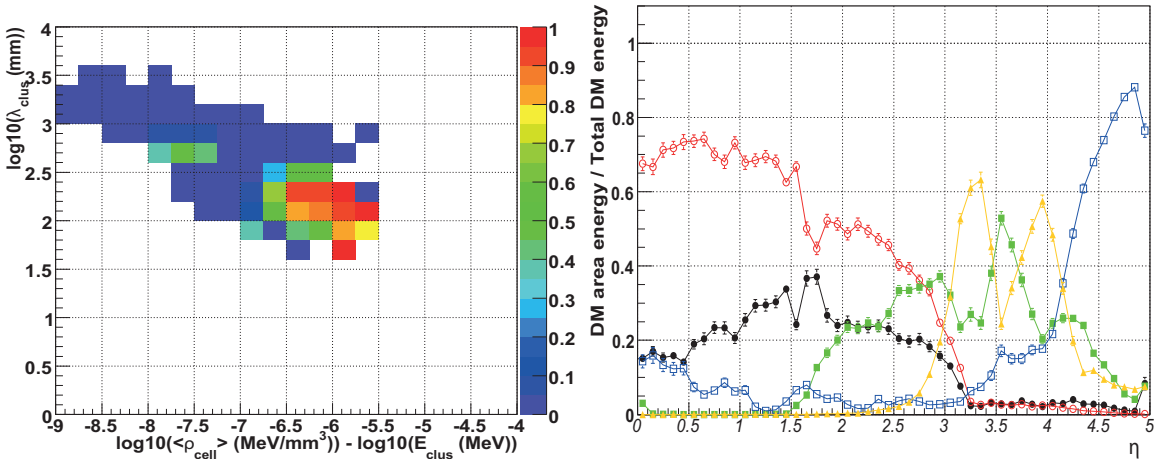

Figure 5.3: Left: probability map to observe a neutral pion for two shower shape sensitive quantities used to distinguish electromagnetic and hadronic clusters for cluster energies in the range 8 GeV $< E_{\text{cluster}} <$ 16 GeV. Right: energy fraction deposited by a charged pion of 200 GeV in dead material (DM) as function of η. Dead material: before the electromagnetic calorimeter (black), between the electromagnetic and hadronic calorimeters (red), regions between calorimeter modules (green), material behind calorimeter system (blue), and before forward calorimeter (yellow). [114]

average weights for each cell are defined as:

$$w_{cell} = \frac{E_{\text{cell}}^{\text{calib}}}{E_{\text{cell}}^{\text{reco}}}, \tag{5.3}$$

where $E_{\text{cell}}^{\text{reco}}$ is the measured energy in the active layers and $E_{\text{cell}}^{\text{calib}}$ the sum of energy deposits in active and inactive parts of the cell. The weights are stored as function of E_{cluster}, the energy density $\rho_{\text{cell}} = E_{\text{cell}}^{\text{reco}}/V_{\text{cell}}$ and $|\eta|$.

As the next step the out-of-cluster corrections are applied. This correction aims to account for low-energy deposits in tails of the hadronic showers, which are not included in the clusters due to noise suppression. To avoid an overestimation of energies in case of adjacent clusters in multi-particle events, this method takes the degree of isolation of the clusters into account.

As the final step the so-called dead material (DM) corrections are applied at the cluster level. The aim is to compensate energy losses due to energy deposits in material outside the calorimeter volume. The ratio of energy deposits in different DM regions and the total DM energy deposits for a charged pion carrying the energy of 200 GeV as a function of pseudorapidity $|\eta|$ is shown in Fig. 5.3 (right). DM includes the material before the electromagnetic calorimeter (black), between the electromagnetic and hadronic calorimeters (red), calorimeter cracks (green), behind the calorimeter system (blue), and before the forward calorimeter (yellow). Different methods are used to derive corrections for DM regions shown. A more detailed description and discussion on the performance can be found in Ref. [115] and Ref. [114].

5.3 Jet Finding

The anti-k_t algorithm with the distance parameters $R = 0.4$ and $R = 0.6$ (cf. Sec. 2.2) was used to reconstruct jets. Jets reconstructed from four different types of inputs are used in the context of jet analyses in ALTAS: calorimeter jets, track jets, truth jets, and parton-level jets. All jet types are reconstructed using the same jet finding configuration.

The calorimeter jets, which are also denoted as reconstruction-level or detector-level jets, are found using topological cluster at the electromagnetic scale (EM) and LCW scale. For the jet finding, clusters with a total energy above 0 are considered. The algorithm requires four-vector objects as input, where each cluster is treated as massless. The energy is the sum of the cell energies E_k and the position is the center of energy in the detector frame of reference:

$$E_{\text{cluster}} = \sum_k E_k \quad \text{and} \quad m_{\text{cluster}} = 0, \tag{5.4}$$

$$\eta_{\text{cluster}} = \frac{1}{E_{\text{cluster}}} \sum_k E_k \eta_k \quad \text{and} \quad \phi_{\text{cluster}} = \frac{1}{E_{\text{cluster}}} \sum_k E_k \phi_k. \tag{5.5}$$

The so-called track jets use the information provided by the inner detector (cf. Sec. 4.2.2). As input four-vectors of reconstructed charged particle tracks are used which are associated with the primary collision vertex. The mass is assumed to be that of $\pi^{\pm}$. The reconstruction of primary vertices is summarized Sec. 4.2.2. The primary collision vertex is defined as the vertex with the maximum $\sum(p_T^{\text{track}})^2$, where p_T^{track} is the transverse momentum of a track associated with given primary vertex. The tracks are required to have a transverse momentum of $p_T^{\text{track}} > 500$ MeV, a transverse impact parameter with respect to the primary vertex of $|d_0| < 1.5$ mm, and $|z_0 \sin\theta| < 1.5$ mm, where z_0 is the longitudinal impact parameter and θ the polar angle[1]. Since tracks from the hardest scatter vertex are used for the jet reconstruction, track jets are kinematically stable against pile-up. Therefore track jets are used as reference objects for calorimeter jets. The inner detector covers the pseudorapidity region $|\eta| < 2.5$, whereas due to the large dimensioning of jets the full acceptance is achieved for the geometric region $|\eta_{\text{jet}}^{\text{track}}| < 2.5 - R$, where R is the anti-$k_t$ distance parameter.

Jets found using simulated stable particles are referred to as truth jets or particle-level jets. These are particles with a lifetime τ constrained by $c\tau > 10$ mm, which corresponds to $\tau \approx 30$ ps. Neutrinos and muons are not included in the truth jet reconstruction in context of the calibration and performance studies. Neutrinos do not leave an observable signal in the calorimeter and muons are able to deposit a small amount of measurable energy in some parts of the calorimeter, which is usually not proportional to the muon energy. The occasionally occurring muons can have a large impact on the truth jet energy and can cause tails in the response function. For the correction of detector effects which is performed in the cross-section measurement (cf. Sec. 8), these particle types were included in the truth jet reconstruction procedure.

[1] d_0, z_0, and θ are parameters of the so-called *perigee parametrization* around the point of closest approach to the z-axis [116]. This parametrization is used as representation of charged particle tracks in ATLAS.

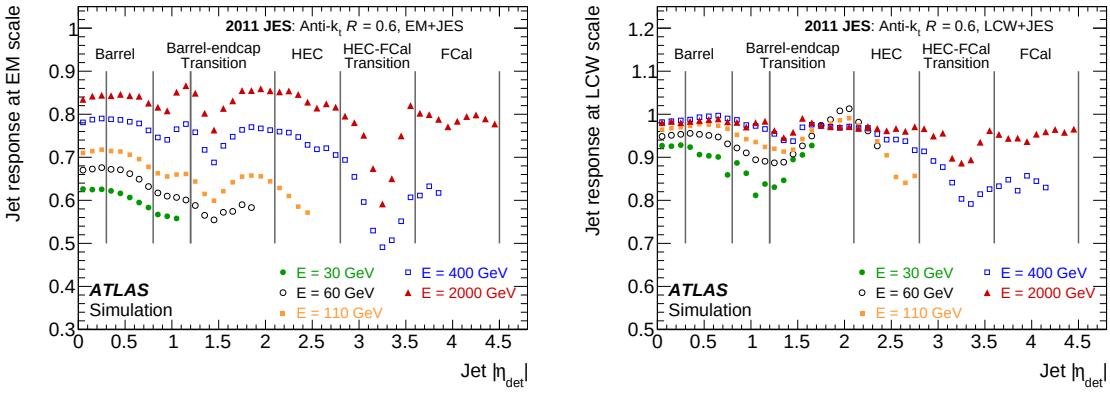

Figure 5.4: Jet energy response as function of the pseudorapidity in the detector frame of reference $|\eta_{\text{det}}|$ for jets reconstructed at EM (left) and LCW (right) scale. Shown are jet responses for different jet energies E. [113]

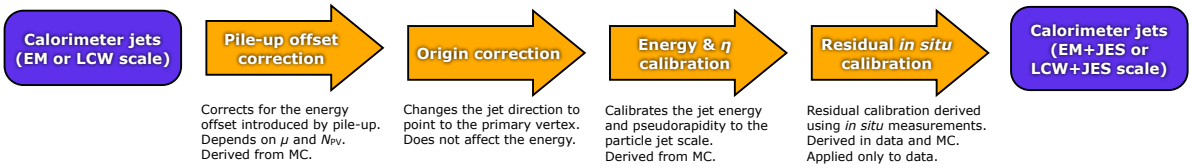

Figure 5.5: Overview of the ATLAS calibration chain. [113]

5.4 Monte Carlo Based Jet Calibration

The topological clusters at electromagnetic scale (EM) are three-dimensional objects composed of calorimeter cells which measure energy deposits of particles produced in electromagnetic showers. The topological clusters at the EM scale can be calibrated further (at the jet constituents level) before jet finding as detailed in the previous section. The correction of signals from hadronic deposits reduces the measured energy fluctuations and therefore improves the energy resolution. The calibration method used for the cross-section measurements is LCW (cf. Sec. 5.2). In Fig. 5.4 the average jet response for various energies as function $|\eta_{\text{det}}|$ determined using Monte Carlo simulation is shown. The response is defined as the reconstructed jet energy at EM (LCW) scale divided by the jet energy at particle-level. The left plot shows the jet response determined using topological clusters at EM scale. The right figure shows the jet response using topological clusters, which were calibrated using the LCW method. The reconstructed jet energy at LCW scale is improved compared to jet energy at EM scale. Due to effects, such as energy loss from particles not reaching the calorimeter (out-of-cone), the jet energy scale at LCW is still lower than the energy scale obtained at particle-level. Therefore a jet-based calibration is additionally applied.

The calibration of the jet energy and direction is performed in several steps. An overview of the calibration chain is shown in Fig. 5.5. Jets are found using topological clusters at the EM or LCW scale as described in the previous section. As the first step the pile-up correction is applied, which compensates the energy offset caused by in-time and out-of-time pile-up (cf. Sec. 5.4.1). The correction is based on Monte Carlo simulations and

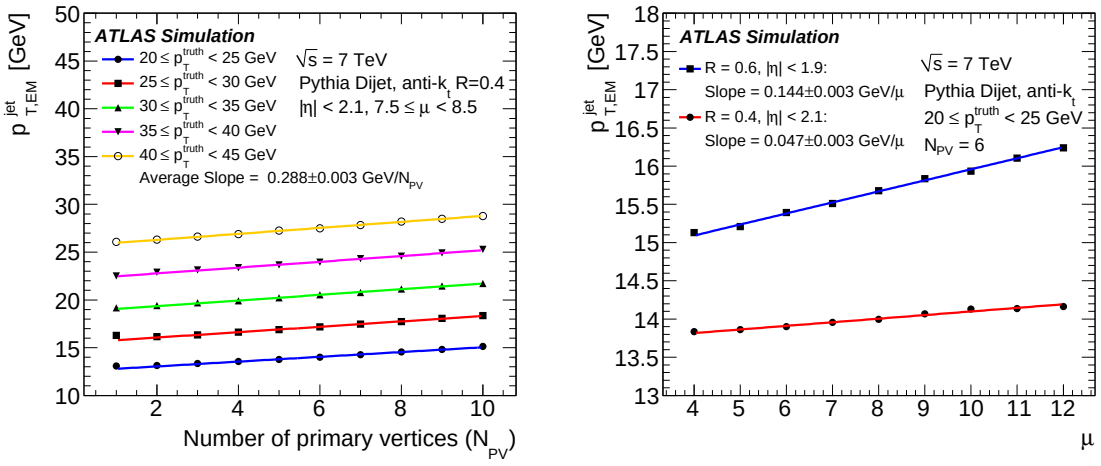

Figure 5.6: Dependence of the jet transverse momentum at EM scale as function of N_{PV} (left) and μ_{avg} (right). [113]

was derived as function of the reconstructed number of primary vertices N_{PV} and the average number of interactions μ_{avg} per bunch-crossing within a luminosity block (cf. Sec. 4.2.4) in a given jet p_T and η bin. As second step the direction of the jet is corrected. The assumed origin of the jets before this correction is the nominal center of the ATLAS detector. The direction is corrected such that the jets point back to the primary vertex of the hardest scattering process. In the next step the jet energy and η is calibrated based on Monte Carlo simulation. As reference the truth jet energy and direction at particle-level is used. The correction is derived as function of the jet pseudorapidity η_{det} determined in the detector frame of reference. Calibrated jets at this step are denoted as EM+JES or LCW+JES dependent on the type of topological cluster used for the jet finding. The last step of the calibration procedure is the so-called in-situ correction of the jet transverse momentum p_T. This correction was applied to take effects not captured by the Monte Carlo based calibration into account. In-situ corrections are derived from data and are described in Chap. 6. In the following a more detailed description of each MC-based calibration step is given.

5.4.1 Pile-up correction

The pile-up correction is based on Monte Carlo simulations and is validated with in-situ methods, which are described in Chap. 6. The aim is to calculate the offset $\mathcal{O}$ added to the jet transverse momentum p_T in a pile-up environment characterized by the quantities μ_{avg} and N_{PV}. This information is used to subtract the calculated offset from reconstructed jet p_T at the EM (LCW) scale.

Because of the small signal read-out window (cf. Sec. 4.2.2) of the inner detectors compared to the proton bunch spacing, tracks and primary vertices from the same bunch-crossing are reconstructed only. Thus the number of reconstructed primary vertices N_{PV} is used as a measure for in-time pile-up activity. As discussed in Sec. 4.2.3 the LAr calorimeter is designed to operate in an environment with energy deposits from previous and subsequent bunch-crossings. For a single calorimeter cell this can only be achieved if

in-time activity over a large time window is available. Deposited energies with no deposits from previous bunch-crossings are overestimated and underestimated, if no deposits from subsequent bunch-crossings occur. Therefore the average number of interactions per bunch-crossing μ_{avg} was used to estimate the out-of-time pile-up activity. It is an average over all bunch-crossings within a luminosity block and is therefore a measure for the in-time activity over a time window of typically 1 minute. For the pile-up correction events at the beginning of the proton bunch trains within 600 ns were excluded, because no previous filled bunches exist and in order to avoid mis-modeling issues in MC. The bias introduced at the beginning of the train is covered by the systematic uncertainty. Additionally the distortion by pile-up depends on the pseudorapidity of the jets due to the energy flow distribution and various calorimeter technologies used in different regions.

The correction $\mathcal{O}$ is determined for jets reconstructed at the EM and LCW scale and is applied to the transverse momentum $p_{T,\text{EM/LCW}}$ as follows:

$$p_{T,\text{EM/LCW}}^{\text{corr}} = p_{T,\text{EM/LCW}} - \mathcal{O}_{\text{EM/LCW}}(N_{\text{PV}}, \mu_{\text{avg}}, \eta_{\text{det}}),$$

where $p_{T,\text{EM/LCW}}^{\text{corr}}$ is the corrected transverse momentum, $\mathcal{O}$ the correction for a given pile-up condition, which aims to make the jet p_T independent of N_{PV} and μ_{avg}. $\mathcal{O}$ is derived for a given reference pile-up environment such that $\mathcal{O}(N_{\text{PV}} = N_{\text{PV}}^{\text{ref}}, \mu_{\text{avg}} = \mu_{\text{avg}}^{\text{ref}}) = 0$ in a given bin η_{det}. The reference working point is arbitrary and was chosen to be $\mu_{\text{avg}}^{\text{ref}} = 5.4$ and $N_{\text{PV}}^{\text{ref}} = 4.9$. A linear relation between the pile-up signal added to the transverse momentum of the jet and the amount of pile-up is assumed and the correction $\mathcal{O}$ is modeled as follows [113]:

$$\begin{aligned}
\mathcal{O}(N_{\text{PV}}, \mu_{\text{avg}}, \eta_{\text{det}}) &= p_T(N_{\text{PV}}, \mu_{\text{avg}}, \eta_{\text{det}}) - p_T^{\text{truth}} && (5.6)\\
&= \frac{\partial p_T}{\partial N_{\text{PV}}}(\eta_{\text{det}})(N_{\text{PV}} - N_{\text{PV}}^{\text{ref}}) + \frac{\partial p_T}{\partial \mu_{\text{avg}}}(\eta_{\text{det}})(\mu_{\text{avg}} - \mu_{\text{avg}}^{\text{ref}}) && (5.7)\\
&= \alpha(\eta_{\text{det}})(N_{\text{PV}} - N_{\text{PV}^{\text{ref}}}) + \beta(\eta_{\text{det}})(\mu_{\text{avg}} - \mu_{\text{avg}}^{\text{ref}}). && (5.8)
\end{aligned}$$

The reconstructed jet $p_{T,\text{EM}}$ ($\equiv p_{T,\text{EM}}^{\text{jet}}$) in bins of the truth jet p_T^{truth} as function of N_{PV} is shown in Fig. 5.6 (left). Only jets found using anti-k_T $R = 0.4$, pointing to the central region within $|\eta_{\text{det}}| < 2.1$ in the range $7.5 \leq \mu_{\text{avg}} < 8.5$ are shown. The average slope α was found to be independent of the truth jet p_T^{truth}, but has a dependence on the jet distance parameter R due to different areas covered by the jets, where $\alpha_{R=0.6} > \alpha_{R=0.4}$. Fig. 5.6 (right) shows the jet $p_{T,\text{EM}}$ as function of μ_{avg} for truth jets within $20 \leq p_T^{\text{truth}} < 25$ GeV and $N_{\text{PV}} = 6$. The dependence on out-of-time pile-up was found to be smaller than that on in-time pile-up with a linear behavior in both cases, which confirms the assumption. The slopes α and β were determined by averaging the fit results for various bins in μ_{avg} and N_{PV}, respectively.

5.4.2 Origin correction

The direction of a jet and its constituents is determined in the detector frame of reference (cf. Sec. 4.2.1). The polar angle corresponding to particle associated with topological cluster in a given event is corrected such that it points back to the primary collision vertex, keeping the cluster energy unaffected. The four-momenta of the jets are then re-calculated using the origin corrected topological cluster. The corrected pseudorapidity of

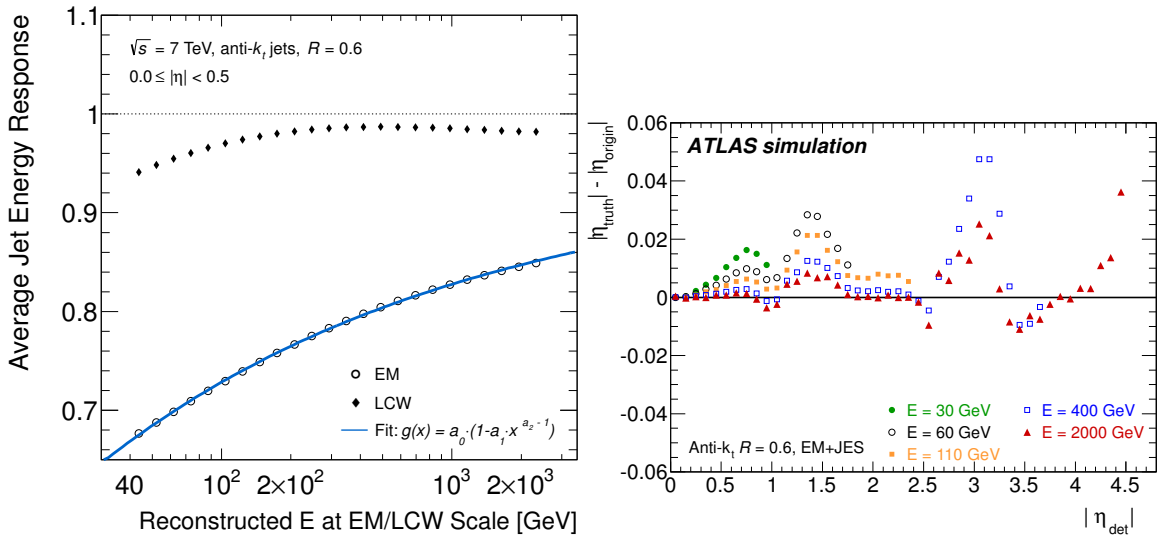

Figure 5.7: Left: average jet response as the function of the jet energy in the pseudorapidity region $0.0 \leq |\eta| < 0.5$. The reciprocal of the jet response was used as correction. The function given in Eq. 5.9 with an additional parameter was fit to the jet response at the EM scale. Right: deviation between the pseudorapidity after origin correction η_{origin} and jet pseudorapidity at particle-level η_{truth} as function of η_{det} for various jet energies E at EM+JES scale [113].

the jets is denoted as η_{origin}. The origin correction yields an improvement in the angular resolution and jet p_T response. [117]

5.4.3 Monte Carlo based jet energy and η calibration

Particles carrying the largest fraction of energy within jets are charged pions $\pi^{\pm}$ and photons γ originating mainly from neutral pions π^0 decaying into $\gamma\gamma$. Photons deposit energy via e^+e^- pair production, which is already calibrated as discussed in Sec. 4.2.3. The largest contribution to the jet calibration is due to the hadronic constituents of the jets, which can be calibrated before jet finding using the LCW technique.

The efficiency of measuring energy deposits of electromagnetic and hadronic particles in the calorimeter are denoted as e and h, respectively. The ATLAS calorimeter system is non-compensating with a ratio of $h/e < 1$, which is used as a measure for the degree of non-compensation. In each hadronic interaction within a shower a significant part of the energy is lost due to effects such as binding energy losses, which can not be measured due to the non-compensating nature of the calorimeter. As high-energy secondary particles, mainly pions are produced within the shower. The main contribution to the behavior of the jet response as function of the jet energy is because of the transfer of energy from the hadronic to the electromagnetic sector via π_0 production. On the other hand a negligible amount of energy is transferred to the hadronic sector [118]. With increasing incident particle energy the number of secondaries increase and therefore a larger total energy fraction is transferred to the electromagnetic sector. The average fraction of the energy in the electromagnetic sector f_{π^0} as function of the energy E of the incident particle can be parametrized as follows: $f_{\pi^0}(E) = 1 - (E/E_0)^{m-1}$, where E_0 and m are parameters. The charged pion calorimeter response π with respect to that of the electron e can be

then written as [118]:

$$\pi/e = 1 - a \cdot E^{m-1}, \tag{5.9}$$

where the parameter $a = (1 - h/e) \cdot E_0^{1-m}$. Assuming an idealized environment, where effects caused by dead material, the magnetic field, etc. are ignored, the jet response can be approximately described using the functional form given in Eq. 5.9.

The aim is to calibrate the energy and direction of the calorimeter jets using truth jets as reference. The calorimeter jets as well as truth jets used were isolated. An isolated jet is defined as a jet with no adjacent jets of the same type within the distance $\Delta R = 2.5 \cdot R$ and $p_T > 7$ GeV, where R is the anti-k_t distance parameter. The isolation is required to reject jets which are reconstructed as two jets or two adjacent jets are merged into one jet, which would yield very low or large response, respectively. For each calorimeter jet, a truth jet was searched for using the distance ΔR between the jets. The matching distance was chosen to be $\Delta R = 0.3$.

The calibration was derived and applied as function of the reconstructed jet energy at EM/LCW scale $E_{\mathrm{EM/LCW}}$ and pseudorapidity in the detector frame of reference η_{det}. The response $\mathcal{R}_{\mathrm{EM/LCW}}$ can not be derived in bins of $E_{\mathrm{EM/LCW}}$ directly. This is a consequence of the steeply falling jet energy spectrum (cf. Sec. 3.5). For a given $E_{\mathrm{EM/LCW}}$ bin the calorimeter jets with a high response migrate from the left into the bin considered. On the other hand the number of jets with a low response migrating from the right is smaller. Thus the response distribution in bins of $E_{\mathrm{EM/LCW}}$ is asymmetric with a shifted mean. Therefore the jet response $\mathcal{R}_{\mathrm{EM/LCW}}$ is calculated in bins of the jet energy at particle-level E_{truth} and the pseudorapidity η_{det}, which results in a Gaussian shaped distribution. The distribution is fitted using a Gaussian function and average jet response $\bar{\mathcal{R}}_{\mathrm{EM/LCW}}$ is defined as the most probable value of the resulting Gaussian fit. Additionally, the average jet energy at EM/LCW scale $\bar{E}_{\mathrm{EM/LCW}}$ is determined for each pair of bins (E^{truth}, η_{det}). This information was used to construct jet response curves in each η_{det} bin. The jet response as function of the reconstructed jet energy $E_{\mathrm{EM/LCW}}$ was parametrized using the following function:

$$f_{\mathrm{calib}}(E_{\mathrm{EM/LCW}}) = \sum_{i=0}^{N} a_i \cdot (\ln\, E_{\mathrm{EM/LCW}})^i, \tag{5.10}$$

where a_i are parameters and N the order of the polynomial. The fit is performed for all orders N ranging from 1 to 6 and the polynomial is chosen according to the best fit. This function is used to correct each jet at the EM scale to the true energy as follows:

$$E_{\mathrm{EM/LCW+JES}} = 1/f_{\mathrm{calib}}|_{\eta_{\mathrm{det}}} \cdot E_{\mathrm{EM/LCW}}, \tag{5.11}$$

where the jet energy $E_{\mathrm{EM/LCW+JES}}$ is the calibrated energy at EM+JES or LCW+JES scale. The jet response in the central rapidity region as function of the jet energy at EM/LCW scale is shown in Fig. 5.7 (left). A modified version of Eq. 5.9 was used to perform a fit to the jet response at EM scale. This function provides a good description of the jet response, despite idealized conditions assumed to derive the response analytically.

In addition to the energy, the direction of the jets is affected due to gaps in the transition regions of the calorimeter system. The topological clusters within a jet are subject to different energy responses in the vicinity of poorly instrumented regions, which cause a bias of the jet direction. This bias is corrected starting from origin corrected pseu-

dorapidity η_{origin}. As reference the truth jet pseudorapidity η_{truth} is used. The correction was derived as the mean difference $\Delta\eta = \eta_{\text{truth}} - \eta_{\text{origin}}$ in bins of E_{truth} and η_{det}. The parametrization is done as function of the corrected jet energy $E_{\text{EM/LCW+JES}}$ [2] and the pseudorapidity η_{det}. The correction is applied as follows:

$$\eta_{\text{corr}} = \eta_{\text{origin}} + \Delta\eta.$$

The difference between $|\eta_{\text{truth}}|$ and $|\eta_{\text{origin}}|$ for various jet energies $E_{\text{EM/LC+JES}}$ as function of η_{det} is shown in Fig. 5.7 (right). The largest corrections are applied in the transition regions and are small for most calorimeter regions. A more detailed description can be found in Ref. [113].

[2] The transformation from E_{truth} to $E_{\text{EM/LCW+JES}}$ was done by analogy with the jet energy calibration method.

6 Jets in ATLAS and Data-Based Calibration

The first part of this Chapter covers the basic components and tools which are essential for the data, event, and jet selection. It is the basis for the in-situ calibration methods, which are used to apply further correction using MC-calibrated jets as input. These data-based calibration techniques are briefly introduced. Additionally some important aspects of the performance of jets measured with the ATLAS detector as e.g. in a pile-up environment are discussed. Furthermore it is important that the MC simulation, which is used as input for the unfolding procedure in Chap. 8, reflects the measurement up to a certain degree. This aspect is covered throughout the entire Chapter.

6.1 Data and Jet Quality

6.1.1 Data Quality Assessment

From the physics analysis point of view it is important to know the degraded conditions and isolate data recorded in presence of detector problems, which inevitably affect measurements. In ATLAS, a set of tools provide an infrastructure to monitor the data, assess the data quality and propagate the information to the physics analysis. The main aspects of this infrastructure are the Data Quality Monitoring Framework (DQMF) [119], the Detector Control System (DCS) [120], and the defects database [104, 121].

The DQMF provides tools in order to monitor data quality and produce plots during the data taking (online) and after the run (offline). For the purpose of detector status monitoring, events are reconstructed immediately and plots are produced, which are used as input for automated checks performed by the offline DQMF. In addition manual checks are performed by detector experts and physicist shifters in order to improve the assessment of the detector status. The DCS uses the information stored in the conditions database in order to automatically determine the status of the sub-detectors and calculate the so-called primary defects. A defect is a representation of a particular detector problem and has two possible states for a given luminosity block: *absent* or *present*. Two different types of defects are defined: *primary defects* and *virtual defects*. Primary defects[1] are derived from detector conditions and are stored in the defects database. Virtual defects are the result of logical combinations of primary defects and other virtual defects. The definition of virtual defects is stored in the defects database and the state of a specific virtual defect is computed on access. Virtual defects are applied to the entire data and can

[1] An example of primary defects usage is the analysis of the high-voltage trip problem in the LAr calorimeter. It can be divided in two phases: high-voltage breakdown and re-ramp up to the nominal voltage. If for example the high-voltage is in the ramp-up state the so-called HVRAMPUP defect is present, otherwise it is absent [121].

be modified as the knowledge of the impact of detector issues on physics analysis improves.

The final result of the data quality assessment process is stored in the so-called good runs list (GRL). The GRL is a file, which contains a list of luminosity blocks passed the data quality requirements. The virtual defects are used to generate the GRL. Each class of physics analysis requires a set of sub-detector components to be in a state tagged as *good* during the data recording phase. Therefore several GRL files were produced covering different analyses requirements on the operability of the individual sub-detectors. Two different GRL versions were used in the context of the analyses detailed in Chap. 8 [2] and Chap. 9 [3].

6.1.2 Event and Jet Quality: Measures and Quantities

In addition to the quality requirements on the operability of essential sub-detectors, each event and jet is required to fulfill further quality criteria. In this context a set of quantities called cleaning variables is used to classify the quality of an event or jet. In the following the quantities and the classification criteria for the quality of jets are introduced. Additionally the predicted distributions are compared to data. A good agreement between MC simulation and data is essential for detector unsmearing purposes in the analyses presented in Chap. 8.

LAr Calorimeter Error Flag

In order to achieve further improvement of data-quality the so-called LArError-flag is used. This flag indicates noise bursts and data integrity errors on event-by-event basis [122]. It is used in case of collision data only. The measured luminosity, which is an essential ingredient of the cross-section measurements, is corrected for events excluded due to bad LAr calorimeter conditions indicated by the LArError-flag. The number of rejected events covered by the GRLs amounts to approximately 0.3%.

Jet Vertex Fraction

The jet vertex fraction (JVF) is used in order to separate jets coming from the hard scattering vertex from jets originating from pile-up vertices. JVF is based on the information obtained from the track and vertex reconstruction. For each jet the sum of transverse momenta $\sum p_T^{\text{track}}$ of the associated tracks[4] is calculated for each vertex i. JVF is defined as $\sum p_T^{\text{track}}$ for tracks associated with hard scattering vertex divided by the $\sum p_T^{\text{track}}$ for all primary vertices. A jet is tagged as 'vertex confirmed', if JVF > 0.6 [113]. In data, approximately 85% of all jets with $p_T > 50$ GeV covered by the tracking system carry a JVF above 0.6. This quantity is used in the context of jet in-situ calibration methods briefly introduced in Sec. 6.3. The JVF distribution obtained using data and Monte Carlo (MC) simulation is shown in Fig. 6.1. As can be observed in this figure, data and MC simulation are in a good agreement. For jets reconstructed in a detector region not covered by the tracking system JVF $= -1$.

[2] data11_7TeV.periodAllYear_DetStatus-v36-pro10-02_CoolRunQuery-00-04-08_All_Good.xml
[3] data11_7TeV.periodAllYear_DetStatus-v36-pro10_CoolRunQuery-00-04-08_JetEtMiss.xml
[4] A track is matched to a jet if the distance with respect to the jet axis $\Delta R < 0.4$. ΔR is measured in (η, ϕ). [113]

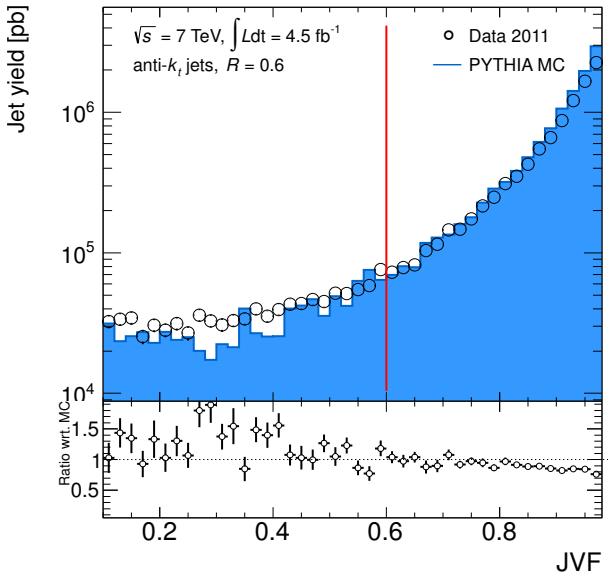

Figure 6.1: Jet vertex fraction (JVF) distribution obtained from data and Monte Carlo simulation is shown in the upper figure. All jets with a transverse momentum above 50 GeV within $|y| < 3.0$ were considered. The red vertical line indicates the threshold, above which a jet is tagged as 'vertex confirmed'. The ratio of data with respect to the MC prediction is shown in the lower part of the figure. The jet yield (y-axis) is the trigger-downscale and luminosity weighted number of jets determined at detector-level.

Jet Energy Distribution within the Calorimeter

The maximum energy fraction $f_{\max}$ is defined as:

$$f_{\max} = \frac{E_{\max}}{\sum_i E_i}, \tag{6.1}$$

where E_i is the energy measured by the calorimeter sampling[5] (cf. Sec. 4.2.3) i and $E_{\max} = \max\{E_i\}$ is the maximum measured energy. The purpose of this measure is to filter out jets with proportionally large energy deposits shared by just one calorimeter sampling, which could originate e.g. from calorimeter noise bursts. The $f_{\max}$-distribution obtained from data and MC simulation is shown in Fig. 6.2 (left). On average approximately 45% of the jet energy is deposited in one calorimeter sampling.

The electromagnetic fraction is defined as:

$$f_{\mathrm{EM}} = \frac{E_{\mathrm{EM}}}{(E_{\mathrm{EM}} + E_{\mathrm{HAD}})}, \tag{6.2}$$

where $E_{\mathrm{EM}} = \sum_i^{N_{\mathrm{EM}}} E_i$ with the number of electromagnetic calorimeter sampling layers N_{EM} and E_i the energy measured by the electromagnetic calorimeter sample i. By analogy with the electromagnetic part of the calorimeter, E_{HAD} is defined as the sum of energies

[5]The total energy in one calorimeter sample is calculated using calorimeter clusters (see Sec. 5.1) inside the jet. In case no clusters are available, the energies measured by the individual cells inside the jet are taken as input for this calculation.

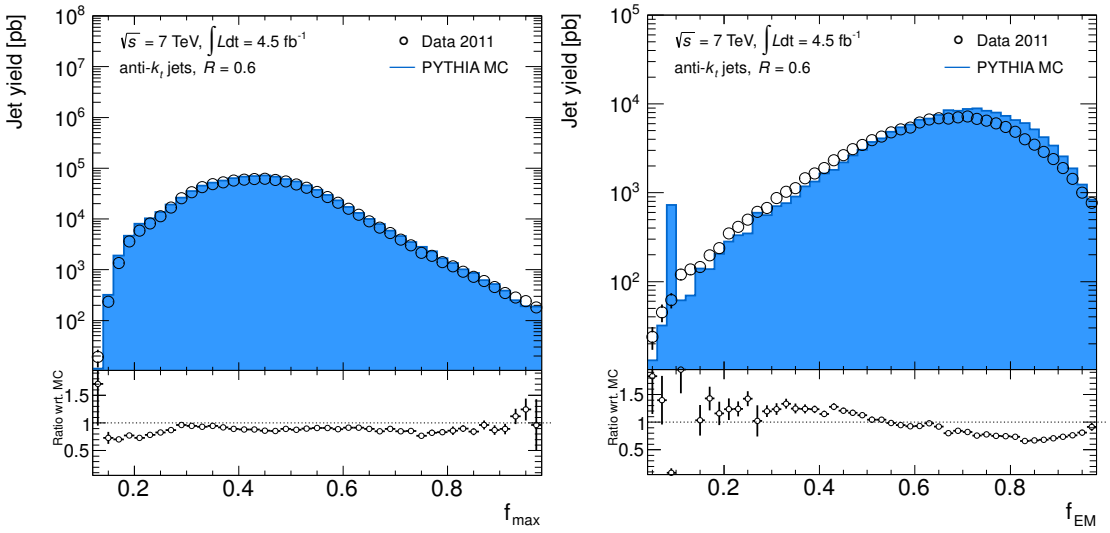

Figure 6.2: Left: distribution of jets according to the fraction of maximum energy deposited in a single calorimeter sampling f_{max} (Eq. 6.1). Right: distribution of the electromagnetic fraction f_{EM} (Eq. 6.2). The distributions were produced using collision data (circle) and MC simulation (blue filled area).

measured by the individual sampling layers of the hadronic calorimeter for a given event. This feature is used in order to filter out jets with energy deposits originating from coherent noise within the electromagnetic calorimeter. The distribution of the electromagnetic fraction f_{EM} is shown in Fig. 6.2 (right) for data and MC. On average around 70% of the jet energy is deposited in the electromagnetic calorimeter.

The energy fraction f_{HEC} is defined as follows:

$$f_{\mathrm{HEC}} = \frac{E_{\mathrm{HEC}}}{E_{\mathrm{jet}}} \tag{6.3}$$

where E_{jet} is the energy of the jet at EM scale (cf. Sec. 5.4) and E_{HEC} the sum of energies measured by the four hadronic end-cap calorimeter (HEC) sampling layers. The purpose of this feature is to exclude jets measured in presence of randomly distributed pulses in the HEC. The hadronic end-cap calorimeter covers the pseudorapidity region $1.5 \leq |\eta_{\mathrm{det}}| < 3.2$ and thus around 60% of jets within $0.0 \leq |y| < 3.0$ are not affected. f_{EM} and f_{HEC} were used in combination with the signal quality measures f_Q^{LAr} and f_Q^{HEC} as discussed in the next sub-sections. For all three distributions (f_{max}, f_{EM}, and f_{HEC}) a reasonable agreement between collision data and MC simulation is achieved.

Signal Quality Measures

The liquid argon quality f_Q^{LAr} is the fraction of energy measured by LAr calorimeter cells with a $Q_{\mathrm{cell},i}$ greater than 4000. $Q_{\mathrm{cell},i}$ is a measure for the discrepancy between the measured and predicted response of a LAr calorimeter cell. It is defined as [123]:

$$Q_{\mathrm{cell},i} = \sum_{k}^{N_{\mathrm{samples}}} (a_k^{\mathrm{meas}} - a_k^{\mathrm{pred}})^2, \tag{6.4}$$

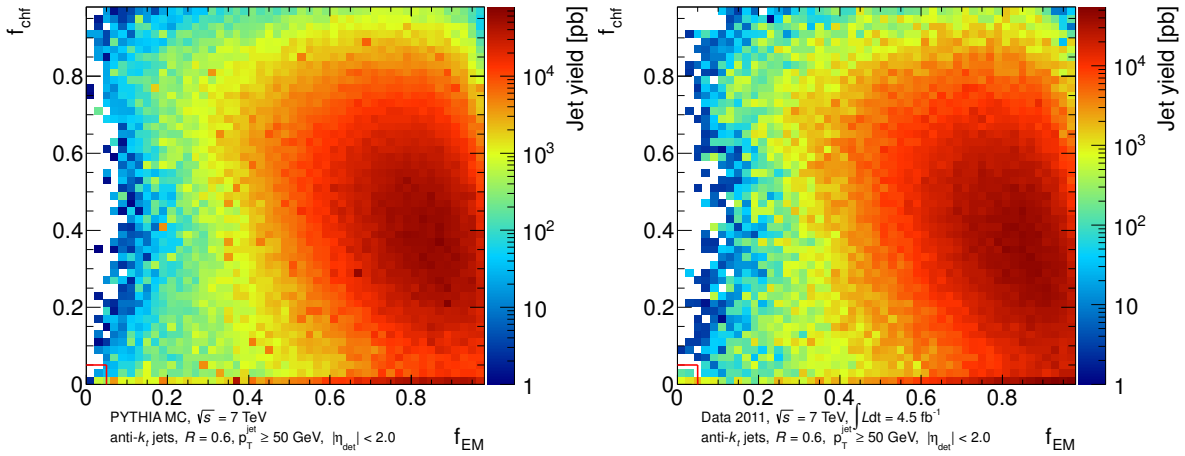

Figure 6.3: Distribution of jets according to the electromagnetic energy fraction f_{EM} (Eq. 6.2) and the charge fraction f_{chf} in MC simulation (left) and collision data (right). The red rectangle indicates the region rejected by the quality cuts as listed in Tab. 6.2.

where a_k^{meas} are the measured and a_k^{pred} the predicted samples of the pulse shape (cf. Sec. 4.2.3), and N_{samples} the number of samples recorded. This quantity is used to estimate the fraction of the jet energy originating from cells with a measured pulse shape deviating from the predicted one, which can be caused by out-of-time pile-up effects. The HEC quality f_Q^{HEC} is defined equivalently to f_Q^{LAr}. In case of f_Q^{HEC} only calorimeter cells belonging to the HEC are used. The distribution of jets according to the quality measures f_Q^{LAr} (f_Q^{HEC}) in combination with f_{EM} (f_{HEC}) is shown in Fig. 6.4 (Fig. 6.5). As can be observed from Fig. 6.4 the distribution determined using MC simulation (left) deviates from that obtained using data (right). The distributions in Fig. 6.5 show a reasonable agreement between MC (left) and data (right). Nevertheless, especially in the high-f_Q^{HEC} region a disagreement can be observed. The mismodelling has a negligible impact on the uncertainty, because, within the kinematic region of interest, only few jets are affected. Another variable used in this context is the average cell-energy weighted jet quality $\langle Q \rangle$, which is defined as:

$$\langle Q \rangle = \frac{\sum_{\mathrm{LAr\ cells}} w_i |w_i| E_i^2 \cdot Q_{\mathrm{cell},i}}{\sum_{\mathrm{LAr\ cells}} w_i |w_i| E_i^2}, \tag{6.5}$$

where E_i is the energy and w_i the corresponding weight of the LAr calorimeter cell i. The quantity $Q_{\mathrm{cell},i}$ is defined in Eq. 6.4. In context of the jet selection, $\langle Q \rangle$ was scaled as follows: $Q_{\mathrm{mean}}^{\mathrm{LAr}} = \langle Q \rangle / 65535$. The impact due to out-of-time pile-up effects on the signal quality is briefly discussed in App. A.4. In the region within a bunch train with the largest impact due to out-of-time effects the quantity $Q_{\mathrm{mean}}^{\mathrm{LAr}}$ is a factor of two larger compared to an unaffected regime. The $Q_{\mathrm{mean}}^{\mathrm{LAr}}$ distribution produced using data and MC simulation is shown in Fig. 6.6 (left). In data, the jet yield tends to be systematically above of that determined using MC simulation for $Q_{\mathrm{mean}}^{\mathrm{LAr}} > 0.02$. Around 15% of jets in data with $p_{T,\mathrm{jet}} \geq 50$ GeV fall into the region $Q_{\mathrm{mean}}^{\mathrm{LAr}} > 0.02$. This fraction decreases to around 5% for jets with $p_{T,\mathrm{jet}} \geq 100$ GeV. Around 1% of the jets with $p_{T,\mathrm{jet}} \geq 50$ GeV carry $Q_{\mathrm{mean}}^{\mathrm{LAr}} > 0.8$. This portion decreases to a sub-per mil level, if the jet transverse momenta are constrained to be above 100 GeV. In the low-$Q_{\mathrm{mean}}^{\mathrm{LAr}}$ region below 0.02, MC simulation overestimates the jet yield obtained from data.

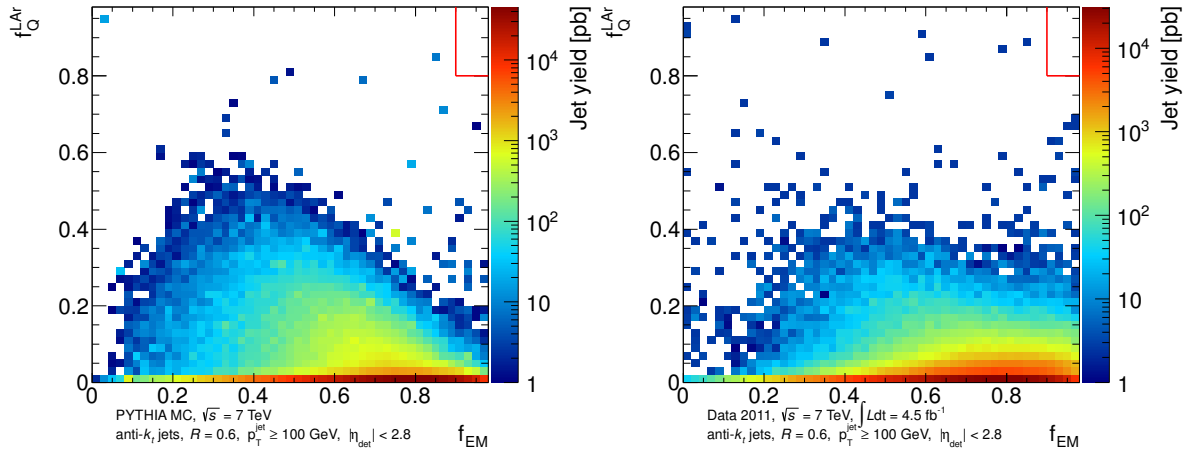

Figure 6.4: Distribution of jets according to the energy fraction f_{EM} (Eq. 6.2) and the quality variable f_Q^{LAr} in MC simulation (left) and collision data (right). The red rectangle indicates the cuts applied in context of the jet cleaning procedure listed in Tab. 6.2.

Negative Energy and Jet Charged Fraction

The measured cell energy E_i could be measured as negative due to electronic noise or out-of-time pile-up effects. The negative energy is defined as the sum of measured calorimeter cell energies below -2.5 GeV:

$$E_{\mathrm{neg}} = \sum_{\text{Cells w/}E<-2.5\text{ GeV}} E_i, \tag{6.6}$$

where E_i ist the energy measured by a single calorimeter cell i. The E_{neg} distribution for collision data and MC simulation is shown in Fig. 6.6 (right). The MC simulation provides a reasonable description of the E_{neg} distribution.

The jet charge fraction f_{ch} is the sum of transverse momenta of tracks associated with the jet $\sum p_T^{\mathrm{trk}}$ divided by the calibrated transverse momentum p_T^{jet} of the jet. This quantity is used in combination with f_{EM}. The two dimensional distribution is shown in Fig. 6.3. The figures show a reasonable agreement between MC (left) and data (right).

Jet Time

The jet time t_{jet} is defined as follows:

$$t_{\mathrm{jet}} = \frac{\sum_{\text{Calo. cells}} w_i |w_i| E_i^2 \cdot t_i}{\sum_{\text{Calo. cells}} w_i |w_i| E_i^2},$$

where w_i is a predetermined weight and E_i is the energy measured by the ith calorimeter cell inside the jet. The time t_i is the estimated time difference between the start of ionization inside the cell and the corresponding bunch-crossing (cf. Sec. 4.2.3). This quantity is used to estimate the out-of-time energy portion within the jet. Around 99% of all jets are withing the interval -10 ns $< t_{\mathrm{jet}} < 10$ ns and thus have an energy content associated with the bunch-crossing of interest.

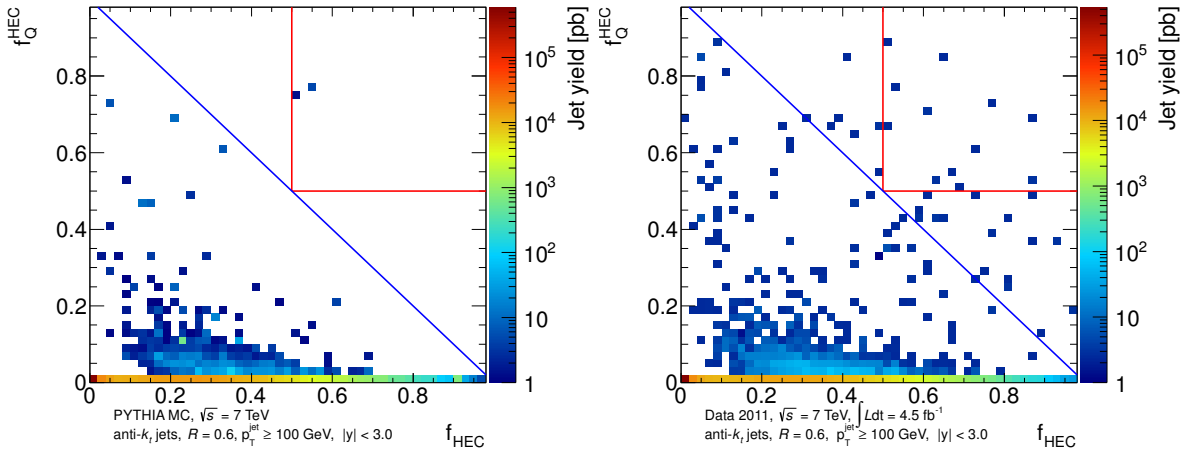

Figure 6.5: Distribution of jets according to the energy fraction f_{HEC} (Eq. 6.3) and the quality variable f_Q^{HEC} in MC simulation (left) and collision data (right). The red rectangle indicates the cuts applied in context of the jet cleaning procedure listed in Tab. 6.2.

Non-operational Cells and the Non-instrumented Regions

Type	Cut
Non-operational cells	$\mathrm{BCH}_{\mathrm{corr,cell}} > 0.5$
Poorly instrumented regions	$f_{\mathrm{gap}} > 0.5$

Table 6.1: A list of cuts applied in order to remove jets in collision data. The jet is removed if one of the listed criteria is fulfilled. The quantities $\mathrm{BCH}_{\mathrm{corr,cell}}$ and f_{gap} are defined in Eq. 6.7 and Eq. 6.8, respectively.

In the following two variables are introduced to discriminate jets reconstructed using non-operational cells or the non-instrumented region of the calorimeter (cf. Sec. 4.2.3). In order to estimate the fraction of energy originating from non-operational cells the following variable is used [113]:

$$\mathrm{BCH}_{\mathrm{corr,cell}} = \sum_{\text{non-op. cells}} \frac{E_{\mathrm{corr},i}}{E_{\mathrm{jet}}}, \tag{6.7}$$

where $E_{\mathrm{corr},i}$ is the estimated energy for the i^{th} non-operational Tile calorimeter cell and E_{jet} the jet energy at EM scale obtained using topologigal clusters. The energy $E_{\mathrm{corr},i}$ is estimated exploiting the energy density of adjacent well-functioning cells in the same calorimeter layer. As discribed in Sec. 4.2.3 the transition region between the Barrel and End-Cap covering $1.0 < \eta < 1.6$ is poorly instrumented. The fraction of jet energy measured in this region is given as follows:

$$f_{\mathrm{gap}} = \frac{E_{\mathrm{gap}}}{E_{\mathrm{jet}}}, \tag{6.8}$$

where E_{gap} is the jet energy measured in the transition region and E_{jet} the jet energy

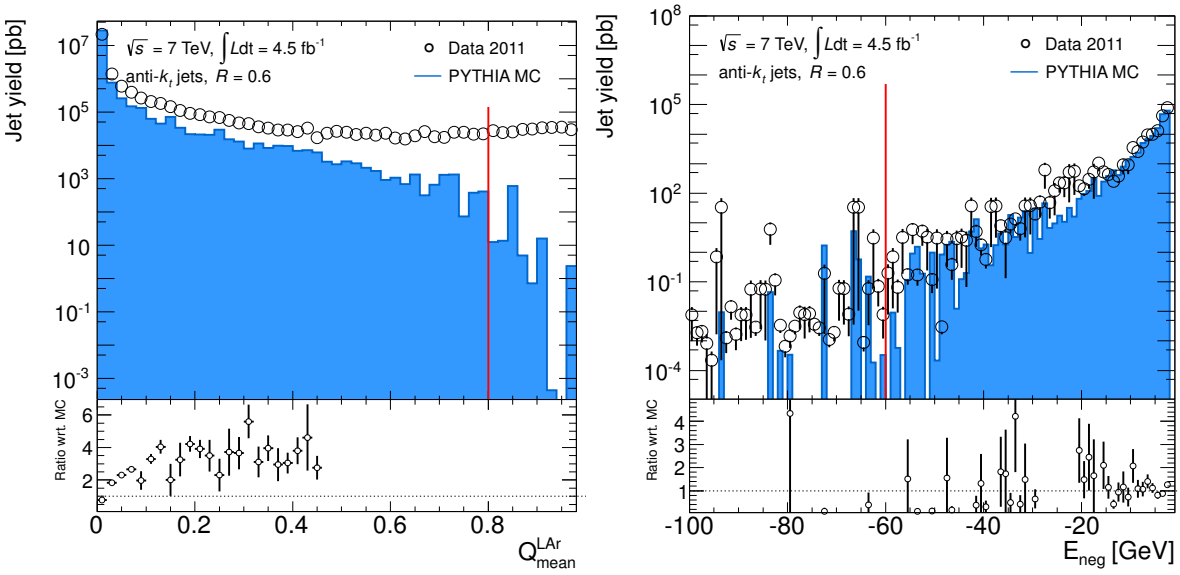

Figure 6.6: Left: $Q^{\mathrm{LAr}}_{\mathrm{mean}}$ distribution. Right: E_{neg} (Eq. 6.6) distribution. In the lower panel the ratio with respect to the distribution determined using MC is shown. The missing points are out-of-range and thus are not shown. The covered kinematic region is 50 GeV $\leq p_{T,\mathrm{jet}} <$ 3500 GeV. The red lines indicate the cuts applied for the purpose of jet quality classification and are listed in Tab. 6.2.

at EM scale. The average $\mathrm{BCH}_{\mathrm{corr,cell}}$ and f_{gap} as function of ϕ_{det} and η_{det} are shown in Fig. 6.7. These quantities were used to reject jets with high correction factors due to non-operational cells and non-instrumented regions. The cuts were applied to jets in data only and are listed in Tab. 6.1.

In approximately 20% of the recorded data, the jet energy measurement is distorted in the detector region $-0.10 < \eta_{\mathrm{det}} < 1.50$ and $-0.88 < \phi_{\mathrm{det}} < -0.50$ due to a LAr calorimeter hardware problem. On average, most of the jet energy is deposited within the electromagnetic LAr calorimeter as can be seen in in Fig. 6.2 (right) and therefore this defect has a significant impact on the the jet energy measurement. The impact on the jet yield in the affected region is shown in Fig. 6.8. The LAr calorimeter defect is modeled well in the detector simulation as indicated in Fig. 6.8 (right). Also the calibration compensates for this problem. Nevertheless, jets were removed pointing to the affected region in the upcoming analyses. Dependent on the analysis this issue was treated differently. A dedicated discussion can be found in Chap. 8 and Chap. 9.

6.1.3 Jet Quality Classification

The jet quality classification can be subdivided in two categories: Background and Instrumentation. In the following the jet quality criteria applied in the context of the cross-section measurement and the search for new phenomena are introduced. The goal is to remove jets not originated from the hard scattering process which are referred to as fake-jets acting as background. Two different selection criteria were used dependent on the analysis. The aim is to keep balance between rejection of fake-jets and the selec-

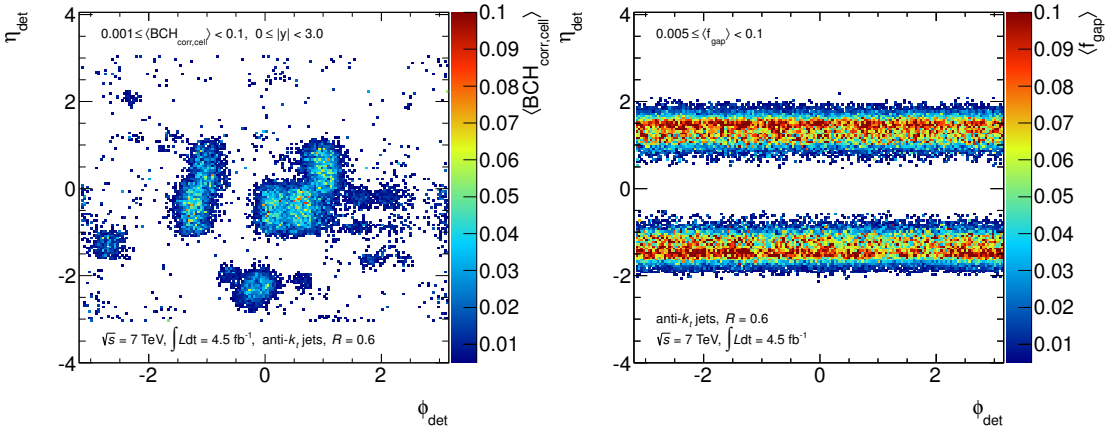

Figure 6.7: Left: trigger down-scale factor weighted mean energy fraction $\mathrm{BCH}_{\mathrm{corr,cell}}$ (see Eq. 6.7) as function of ϕ_{det} and η_{det}. Right: trigger down-scale factor weighted mean energy fraction f_{gap} (see Eq. 6.8) as function of ϕ_{det} and η_{det}. The covered kinematic region is 50 GeV $\leq p_T <$ 3500 GeV.

tion efficiency for jets produced in proton-proton collisions as high as possible. The main contributions to the measured jet energy can originate from various sources listed in the following [113]:

Beam-gas: Secondary particle fluxes are mainly due to elastic and inelastic scattering of beam-protons on the residual, partly beam-induced, gas within the evacuated beam-pipe [123].

Beam-halo: Machine-induced secondary particles which can be caused by interactions e.g. in the collimators located outside of the detector. Halo particles cross the detector from side to side leaving energy deposits in the calorimeter system [123].

Cosmic-ray muons: High-energy cosmic muons can deposit energy in the calorimeter which is usually not in-time with energy deposits originating from proton-proton collision [117].

HEC spikes: "HEC spikes" are randomly distributed pulses overlapping with the useful signals in the HEC, which can have a large impact on the jet energy measurement [124].

EM coherent noise: electromagnetic interference affecting coherently a large amount of calorimeter cells. The coherent noise can originate from various different sources, as power supplies, digital noise and external electromagnetic sources [125].

Two different cut sets were used in order to classify fake-jets and thus reduce the background contributions. The cut sets are labeled Looser and Medium and are listed in Tab. 6.2. The impact of these cuts on the jet selection efficiency is shown in Fig. 6.9. The efficiency is measured using a tag-and-probe in dijet events. The jet selection efficiency is defined as the fraction of selected probe jets as function of and p_T of the probe jets [113]. A study with an out-of-time and fake-jet sample showed that in case of the Looser cut set 37.8% of the jets with $p_T > 150$ GeV are rejected. This portion increases

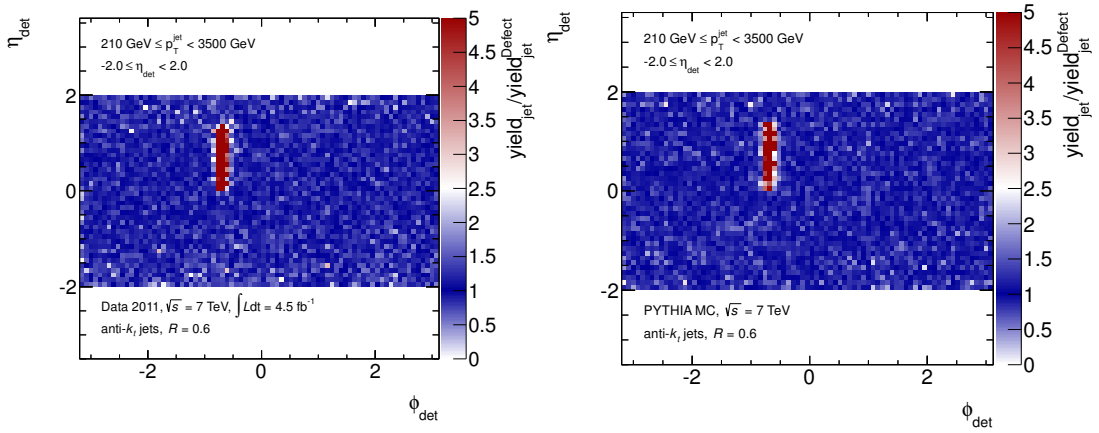

Figure 6.8: Left: ratio of the jet yields $\text{yield}_{\text{jet}}$ and $\text{yield}_{\text{jet}}^{\text{Defect}}$ as function of ϕ_{det} and η_{det}. For this purpose uncalibrated jets at LC scale (cf. Sec. 5.2) reconstructed using the anti-k_T jet algorithm with the distance parameter $R = 0.6$ were used. $\text{yield}_{\text{jet}}^{\text{Defect}}$ was measured using data in presence of the LAr calorimeter defect with an integrated luminosity of $\mathcal{L} = 924\ \text{pb}^{-1}$. The jet yield $\text{yield}_{\text{jet}}$ was determined using data where the LAr calorimeter defect was absent. This data amounts to $\mathcal{L} = 3584\ \text{pb}^{-1}$. As can be observed in this figures, the impact on the jet yield due to the LAr defect is modeled well in MC.

for high-p_T jets and amounts to 68.6%, if the jet transverse momenta are required to be above 500 GeV. The loss of jets of interest due to these cuts is negligible. The selection efficiency is better than 99.8% for jets with a transverse momentum above 20 GeV. In case of the MEDIUM cut set, around 99.5% of the out-of-time and fake-jets are rejected for jets with $p_T > 150$ GeV. This fraction increases slightly as the lower limit on the jet p_T increases. The selection efficiency is better than 99% for jets with $p_T > 50$ GeV. [123] As can be observed from the lower panel of Fig. 6.9 a good agreement between data and MC is achieved.

6.2 Trigger Efficiencies and Combination

In order to cover a wide range of the phase space and simultaneously enhance the statistical power several triggers were combined. For this purpose high-level triggers covering the rapidity range up to $|y| \approx 3.0$ were used in the upcoming analyses only[6]. These central single-jet triggers are listed in Sec. 4.2.6 and are fully efficient in the rapidity region $|y| < 3.0$ as discussed in Ref. [55]. Therefore no angle dependent trigger efficiencies have to be considered. However, these high-level triggers are not fully efficient over the entire kinematic range covered by the jet measurements. The aim is to find the kinematic region, where the individual triggers are fully efficient and thus operating unbiased. The boundary separating these regions is denoted as X_{min}, where X is a kinematic variable as e.g. p_T. All triggers in the upcoming analyses were used in the fully efficient kinematic region in order to avoid the correction for trigger inefficiencies. The trigger efficiency as function of a certain kinematic variable is calculated using the so-called bootstrap

[6] An exception are data-based calibration techniques which exploits jet measurements done with sub-detector in the forward region (cf. Sec. 6.3).

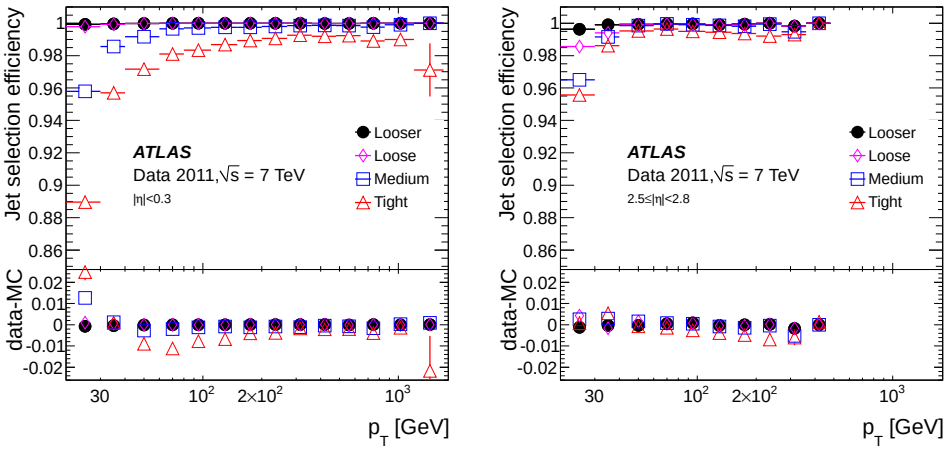

Figure 6.9: Jet selection efficiency as function of the transverse momentum p_T of the jet for different quality criteria and two different pseudorapidity regions. The ratio between of the selection efficiencies calculated using data and Monte Carlo simulations is shown in the lower panel of the figures [113]. The jets were reconstructed using the anti-k_T jet finding algorithm with the distance parameter $R = 0.4$. The LOOSER and MEDIUM cut sets were used in the context of the analyses presented in Chap. 8 and Chap. 9, respectively. The cut sets LOOSE and TIGHT were not considered in this thesis. The definitions can be found in Ref. [113].

method. The efficiency of a trigger of interest (INT) as function of a kinematic variable X is determined using a reference trigger (REF), which is assumed to fulfill the relation $X_{\text{min}}^{\text{REF}} < X_{\text{min}}^{\text{INT}}$. The trigger efficiency in a given bin k of a kinematic variable X can be calculated as follows:

$$\epsilon_k = \frac{N_{k,\text{INT\&REF}}}{N_{k,\text{REF}}},$$

where $N_{k,\text{INT\&REF}}$ is the number of events in bin k selected by both triggers, and $N_{k,\text{REF}}$ is the number of events selected by the reference trigger in the same bin. In Fig. 6.10 (left) the single-jet trigger efficiencies as function of the calibrated jet p_T are shown exemplary for the relevant central jet triggers in the pseudorapidity regime $1.2 < |\eta| < 2.1$. The trigger efficiency for the 'EF Jet $E_T > 240$ GeV' trigger (cf. Sec. 4.2.6 Tab. 4.1) as function of the dijet mass m_{jj} for dijets reconstructed within $y^* < 0.6$ is shown in in Fig. 6.10 (right). The trigger efficiency was required to be above 99.5%, which The trigger was used in the mass region $m_{jj} > 847$ GeV, where this trigger starts to be fully efficient.

In case of the inclusive jet cross-section measurement (cf. Chap. 8) the triggers were combined using the so-called division method. For this purpose the p_T spectrum is segmented in slices separated by $p_{T,\text{min}}$ of the triggers, which are the lower edges of the regions, where the triggers are assumed to be fully efficient. Thus, each trigger is uniquely associated with a p_T-slice constrained by these boundaries. For each trigger t a weight w_t was calculated as follows:

$$w_t = \sum_{k=1}^{N_{\text{LB}}} \frac{\mathcal{L}_k}{d_{kt}}, \tag{6.9}$$

Background type	LOOSER	MEDIUM
HEC spikes	($f_{\mathrm{HEC}} > 0.5$ and $\lvert f_Q^{\mathrm{HEC}}\rvert > 0.5$ and $Q_{\mathrm{mean}}^{\mathrm{LAr}} > 0.8$) or ($\lvert E_{\mathrm{neg}}\rvert > 60$ GeV)	($\lvert E_{\mathrm{neg}}\rvert > 60$ GeV) or ($f_{\mathrm{HEC}} > 0.5$ and $\lvert f_Q^{\mathrm{HEC}}\rvert > 0.5$) or ($f_{\mathrm{HEC}} > 1 - \lvert f_Q^{\mathrm{HEC}}\rvert$)
EM coherent noise	($f_{\mathrm{EM}} > 0.95$ and $\lvert f_Q^{\mathrm{LAr}}\rvert > 0.8$ and $Q_{\mathrm{mean}}^{\mathrm{LAr}} > 0.8$ and $\lvert\eta_{\mathrm{det}}\rvert < 2.8$)	($f_{\mathrm{EM}} > 0.9$ and $\lvert f_Q^{\mathrm{LAr}}\rvert > 0.8$ and $\lvert\eta_{\mathrm{det}}\rvert < 2.8$)
Non-collision background and cosmic-ray muons	($f_{\mathrm{EM}} < 0.05$ and $f_{\mathrm{ch}} < 0.05$ and $\lvert\eta_{\mathrm{det}}\rvert < 2.0$) or ($f_{\mathrm{EM}} < 0.05$ and $\lvert\eta_{\mathrm{det}}\rvert \geq 2.0$) or ($f_{\mathrm{max}} > 0.99$ and $\lvert\eta_{\mathrm{det}}\rvert < 2.0$)	($f_{\mathrm{EM}} < 0.05$ and $\lvert\eta_{\mathrm{det}}\rvert \geq 2.0$) or ($f_{\mathrm{max}} > 0.99$ and $\lvert\eta_{\mathrm{det}}\rvert < 2.0$) or ($\lvert t_{\mathrm{jet}}\rvert > 10.0$) or ($f_{\mathrm{EM}} < 0.05$ and $f_{\mathrm{ch}} < 0.1$ and $\lvert\eta_{\mathrm{det}}\rvert < 2.0$) or ($f_{\mathrm{EM}} > 0.95$ and $f_{\mathrm{ch}} < 0.05$ and $\lvert\eta_{\mathrm{det}}\rvert < 2.0$)

Table 6.2: A list of cuts (LOOSER and MEDIUM) applied in order to remove fake-jets originating from different background types. These cuts were introduced in Ref. [123]. The jet is tagged as a fake-jet if the listed criteria are fulfilled. The quantities are defined in Sec. 6.1.2.

where N_{LB} is the number of luminosity blocks (LB) of the entire data sample, d_{kt} is the down-scale factor for a given LB k and trigger t, and $\mathcal{L}_k$ is the integrated luminosity of the luminosity block (LB) k. For each jet, the calibrated transverse momentum p_T^{jet} is used to identify the corresponding trigger and therefore the weight w_t. The inverse of this weight was used to scale the number of jets on jet-by-jet basis. The boundaries of the trigger slices are not necessarily overlapping with the bin edges, therefore several triggers can contribute to the same p_T and y bin.

In order to eliminate statistically significant deficits caused by trigger inefficiencies and to maximize the amount of statistics an iterative procedure was used to determine the optimal trigger boundaries $p_{T,\mathrm{min}}$, which are not necessarily coincident with the bin edges of the histogram[7]. As the first step inclusive jet p_T spectra were produced, where the initial trigger thresholds $p_{T,\mathrm{min}}$ were chosen such that the trigger efficiencies were above 99%. The thresholds were shifted from −15% to +15% relative to the initial boundaries. The spectra produced with trigger thresholds shifted by +15% were assumed to have the smallest bias due to trigger inefficiencies and were therefore used to fit a smooth function, which is used as reference. The following function was used to fit the spectra:

$$f(x) = p_1(1-x)^{p_2}x^{p_3+p_4\ln x}, \tag{6.10}$$

where $x \equiv 2p_T/p_5\sqrt{s}$ and the p_i are the fit parameters. Eq. 6.10 is a modification of the function used to estimate the background in the search for new resonant-like phenomena with dijets detailed in Sec. 9. The inclusive p_T cross-section tends to zero at the phase space limit constrained by the center-of-mass energy of $\sqrt{s} = 7$ TeV. In the rapidity central region at $y = 0$ the jet p_T limit is 3.5 TeV and is below 3.5 TeV for more forward

[7]The bin widths used for this study are based on the fractional transverse momentum resolution and were derived as described in Sec. 8.3.2.

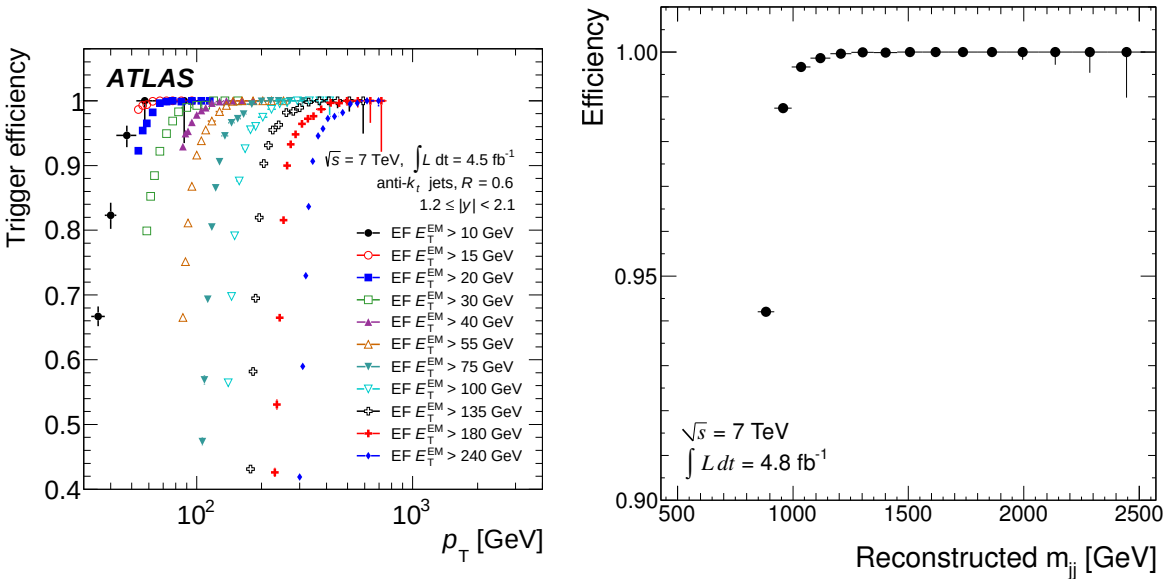

Figure 6.10: Left: single jet trigger efficiency as a function of the reconstructed jet p_T^{jet} for jets with $1.2 < |y| < 2.1$, shown for different high-level triggers [126]. The jets were reconstructed using anti-k_t with the distance parameter $R = 0.6$. Right: trigger efficiency of the 'EF Jet $E_T > 240$ GeV' trigger as function of the invariant dijet mass m_{jj}. For this purpose jets where reconstructed using the anti-k_t algorithm with the distance parameter $R = 0.6$. The dijets were restricted to the rapidity region $y^* < 0.6$ (cf. 9.1).

regions. That was taken into account by the factor 2 and the 5th parameter p_5 in the definition of x. The functional form of 6.10 is phenomenologically motivated by the steeply falling shape of the cross-section as function of p_T. By constraining parameter p_3 to negative values the function is forced to increase with lower p_T. At high-p_T it becomes zero for $x \to 1$, when reaching the phase space limit. A Gaussian distribution does not provide a proper description of the underlying probability density function (p.d.f.) for a given p_T bin in the high-p_T region due to low statistics. Using Gaussian p.d.f. in the fitting procedure causes biased results in the high-p_T tail. To get the best description of the data a so called Log-Likelihood fit was performed based on the Poisson probability density function. Each jet was weighted with the weight w_t (cf. Eq. 6.9) dependent on the trigger t modifying the underlying Poisson distribution. In order to recover the underlying p.d.f. for a given p_T and y bin, the effective number of events was calculated as follows:

$$N^b_{\text{eff}}(p_T, y) = \left(\frac{N^b_{\text{jets}}(p_T, y)}{\Delta N^b_{\text{jets}}(p_T, y)} \right)^2 , \tag{6.11}$$

where $N^b_{\text{jets}}(p_T, y) = \frac{1}{\Delta p_T} \sum w$ is the number of events corrected for down-scale factors and normalized to the bin-width Δp_T, and $\Delta N^b_{\text{jets}}(p_T, y) = \frac{1}{\Delta p_T^2} \sum w^2$ is the corresponding statistical uncertainty. The bin-width normalization was performed to take effects due to non-equidistant binning into account. For a given rapidity bin y, the goal of the fitting

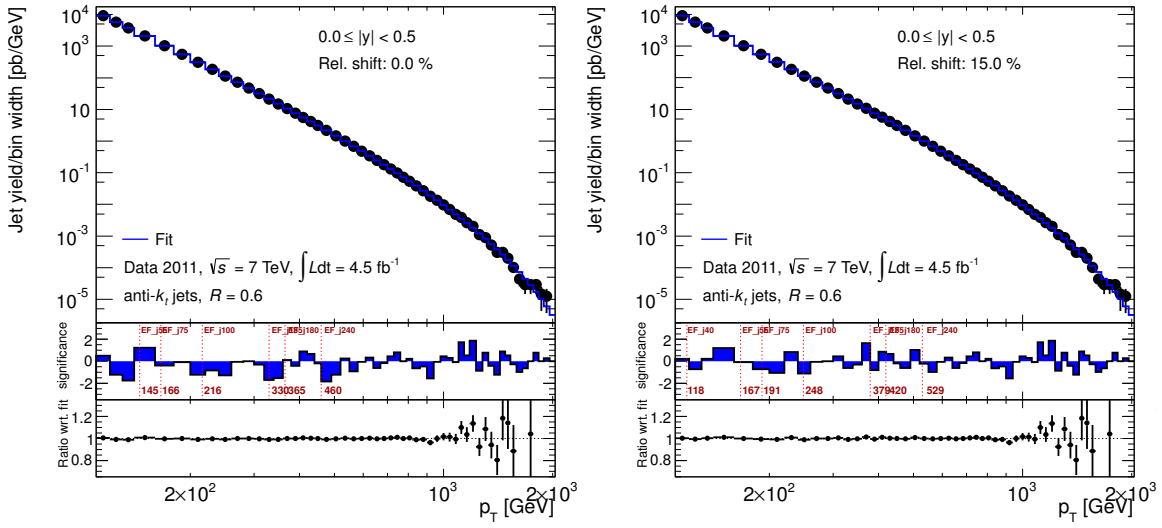

Figure 6.11: Left: luminosity and trigger-downscale factor corrected jet yield as function of the transverse momentum p_T of the jet in the range 100 GeV $\leq p_T <$ 3500 GeV. The spectrum was constructed using trigger thresholds listed in Tab. 6.3. Right: luminosity and trigger-downscale factor corrected jet yield as function of the transverse momentum p_T of the jet in the range 100 GeV $\leq p_T <$ 3500 GeV. The spectrum was constructed using trigger thresholds, which are 15% greater compared to the nominal boundaries. The jets were reconstructed using the anti-k_T algorithm with distance parameter $R = 0.6$ in both cases. The blue line shows the fit result. The bin-by-bin significance and the ratio with respect to the fit are shown in the lower parts of these figures.

procedure is to minimize the sum of Poisson probabilities over all p_T-bins considered:

$$\mathcal{L} = -\sum_{p_T} \log(P(N^b_{\text{eff}}(p_T, y), \nu') \text{ with } \kappa = \frac{N^b_{\text{jets}}(p_T, y)}{N^b_{\text{eff}}(p_T, y)} \text{ and } \nu' = \nu \cdot \Delta p_T / \kappa, \tag{6.12}$$

where $N^b_{\text{eff}}(p_T, y)$ is defined in Eq. 6.11, ν is the fit value which is modified iteratively during the fitting procedure, $P(N^b_{\text{eff}}(p_T, y), \nu')$ is the Poisson probability to observe $N^b_{\text{eff}}(p_T, y)$ characterized by the expectation value ν'. The Minuit2 package [127, 128] was used combining different minimization algorithms to improve the stability of the fits. The result of the fit was used as reference for p_T spectra produced with different trigger threshold configurations. The fit compared to the spectra using the final trigger strategy (left) and the +15% (right) shifted spectrum in the central rapidity region for anti-k_T $R = 0.6$ jets is exemplary shown in Fig. 6.11. The bin-by-bin significance is shown in the middle part. The significance was calculated using the p-value[8] based on the Poisson distribution (cf. Sec. 9.2). The Poisson p-values were translated into significances using the Gaussian distribution which are referred to as z-values. The negative sign was introduced as indication that data is below the fit in a given bin. In the lower part of these figures the ratios of data with respect to the fit are shown. The final trigger slices were chosen

[8]The p-value is the probability for a single measured test statistic t of being greater than or equal to the observed test statistic t_0.

such that the local significance for a given p_T bin is within the interval -2σ and $+2\sigma$. This procdure was also done for all rapidity bins. A spectrum affected by trigger inefficiencies would have a locally significant downward deviation from the smooth function. The iteratively determined trigger thresholds $p_{T,\mathrm{min}}$ were also used in the dijet analysis, where no significant discrepancies were observed between the spectra and a smooth fit. A list of the p_T-slices used is provided in Tab. 6.3. These p_T-slices were also used for spectra determined using anti-k_T jets reconstructed with the distance parameter $R = 0.4$. This can be done, because jets reconstructed using the distance parameter $R = 0.6$ collect more energy on average. This effect causes a shift of the lower limit of the plateau where the triggers are fully efficient to higher values of p_T. Additionally the jet resolution for jets reconstructed using anti-k_T with $R = 0.4$ is better, which gives a steeper slope of the trigger efficiency turn on curve compared to jets reconstructed using $R = 0.6$ at detector-level. The final spectra do not show local statistical significant deficits and as a consequence no additional systematic uncertainty has to be considered. The same holds for spectra produced using the anti-k_T algorithm with $R = 0.4$.

In order to combine triggers for the dijet cross-section measurement the so-called *inclusion method for fully efficient combinations* based on two triggers was used [129]. For this purpose weights were calculated for all trigger pair combinations from the set of high-level triggers listed in Sec. 4.2.6 Tab. 4.1. For the entire data sample one weight per trigger pair was determined. For each event, a pair of triggers is obtained using the calibrated transverse momenta of the leading and second-leading jets. For this purpose the p_T slices listed in Tab. 6.3 were used. At least one of these triggers was required to accept the event. Events not triggered by one of these two triggers were rejected. The weight for a given trigger pair is calculated as follows:

$$w = \sum_{k=1}^{N_{\mathrm{LB}}} \mathcal{L}_k \cdot (1 - \prod_{t}^{N_{\mathrm{trig}}} (1 - \frac{1}{d_{kt}})),$$

where $\mathcal{L}_k$ is the integrated luminosity of the luminosity block (LB) k, N_{LB} is the number of LBs in the entire data set, d_{kt} is the down-scale factor for a given LB k and trigger t, $N_{\mathrm{trig}} = 2$, and the term $(1 - \prod_t^{N_{\mathrm{trig}}}(1 - \frac{1}{d_{kt}}))$ is the probability that at least one of the triggers accepts the event. In cases where both jets were associated with the same trigger, the down-scale factor corrected integrated luminosity as defined in Eq. 6.9 was taken as weight. This method increases the statistical power in cases where both triggers are down-scaled. This is possible because of the random nature of the down-scaling procedure.

In case of the search for new resonant-like phenomena using the dijet mass spectrum (cf. Chap. 9) the 'EF Jet $E_T > 240$ GeV' trigger (cf. Sec. 4.2.6 Tab. 4.1) was used only. The trigger efficiency was determined as function of the invariant mass m_{jj} as shown in Fig. 6.10 (right). This distribution was used directly to determine m_{jj}^{min}, which defines the lower boundary of the spectrum of interest.

6.3 In-Situ Calibration

In the following a summary of the in-situ jet energy scale (JES) calibration techniques used in ATLAS is given [113]. In contrast to the MC-based jet calibration method intro-

High-level trigger	$p_T^{\min}$ [GeV]	$p_T^{\max}$ [GeV]
EF Jet $E_T > 10$ GeV	50	56
EF Jet $E_T > 15$ GeV	56	63
EF Jet $E_T > 20$ GeV	63	84
EF Jet $E_T > 30$ GeV	84	103
EF Jet $E_T > 40$ GeV	103	145
EF Jet $E_T > 55$ GeV	145	166
EF Jet $E_T > 75$ GeV	166	216
EF Jet $E_T > 100$ GeV	216	330
EF Jet $E_T > 135$ GeV	330	365
EF Jet $E_T > 180$ GeV	365	460
EF Jet $E_T > 240$ GeV	460	3500

Table 6.3: A list of trigger thresholds used for the inclusive jet and dijet measurements, where each high-level trigger is associated with an unique slice $p_T^{\min} \leq p_{T,\text{jet}} < p_T^{\max}$. The thresholds were obtained applying an iterative algorithm, which uses the local significance as measure in order optimize the smoothness of the p_T spectra. The thresholds were applied for jets reconstructed using the distance parameter $R = 0.4$ and $R = 0.6$.

duced in Sec. 5.4, the recorded data is used to derive correction factors. The aim is to correct for effects which are not described by the Monte Carlo simulation. The in-situ correction is applied to jets, which are already calibrated using the MC-based calibration techniques. A large part of the systematic uncertainty components are coming from the in-situ calibration techniques. Therefore this summary is the basis for the understanding of individual systematic uncertainty components introduced in Chap. 7.

The in-situ calibration factors are derived in several steps, using the resulting information of the previous steps. The basic strategy is to use the transverse momentum p_T^{ref} of a well-calibrated reference object. Because of the transverse momentum conservation, the transverse momentum p_T^{jet} of the jet is assumed to be in balance with p_T^{ref}. The in-situ correction in the more forward region ($0.8 \leq |\eta_{\text{det}}| < 4.5$) is based on the so-called η-intercalibration, which exploits the transverse momentum balance in events with dijet topologies. The aim is to eliminate the dependence of the jet response on the pseudorapidity by calibrating the response in the more forward region against that in the central region ($|\eta_{\text{det}}| < 0.8$). For the absolute JES calibration three different types of reference objects are exploited: The Z-boson, the photon, and low-p_T jets in multi jet events. The absolute calibration is performed for jets in the central region covering pseudorapidities up to $|\eta_{\text{det}}| < 1.2$ for a transverse momentum p_T of up to 800 GeV.

The Z-boson was used in the context of the so-called direct balance (DB). In this case events with one Z-boson and one jet recoiling against the former were used, and the transverse momenta of these objects were compared directly. For the photon the so-called missing transverse momentum projection fraction (MPF) method was used. The balance of the photon transverse momentum p_T^{γ} and the full hadronic recoil was exploited providing a jet definition independent calibration method. In multi jet events the leading

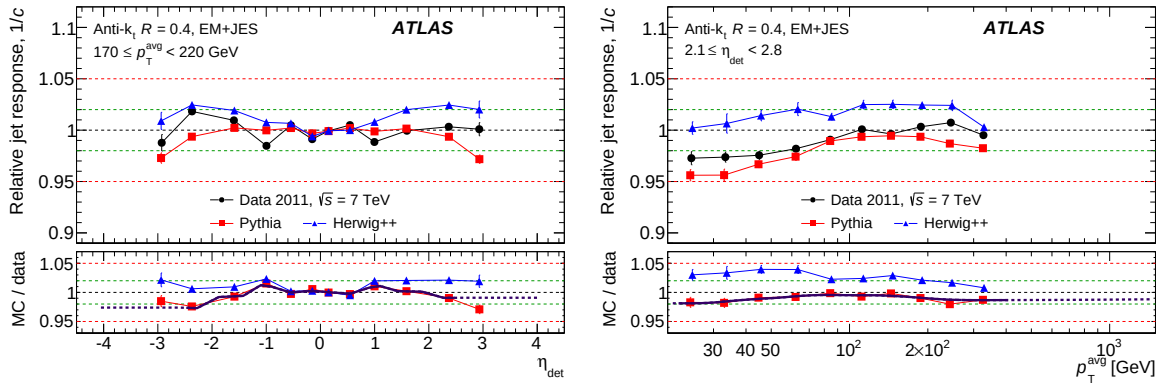

Figure 6.12: Left: relative jet response $1/c$ as function of η_{det} for jets reconstructed using the anti-k_t algorithm with the distance parameter $R = 0.4$ and calibrated with the EM+JES scheme. The jet response is shown for collision data and MC simulation for two different generators: HERWIG++ and PYTHIA. In the lower part of the figure the ratios between $1/c$ derived using Monte Carlo simulations and $1/c$ calculated using data is shown. The correction applied is shown as thick magenta line in the lower part of the figure. The dotted part of the line indicates the η_{det} region where an extrapolation is used. Right: by analogy with left figure the relative response as function of p_T^{avg} for jets pointing to the pseudorapidity regime $2.1 \leq \eta_{\text{det}} < 2.8$ is shown. [113]

high-p_T jet is calibrated utilizing the recoil-system consisting of non-leading[9] low-p_T jets. These low-p_T jets are calibrated using the Z- and photon jet balance methods. This technique is referred to as multi jet balance (MJB). The MJB can be used iteratively to extend the calibrated p_T range for non-leading jets. A more detailed discussion can be found in Ref. [117, 113].

6.3.1 Intercalibration Between the Central and Forward Pseudorapidity Regime

Due to the mixture of technologies used in ATLAS the jet response is dependent on the pseudorapidity η. In order to eliminate differences of the jet response between the central ($|\eta_{\text{det}}| < 0.8$) and forward region ($0.8 < |\eta_{\text{det}}| < 4.5$) the so-called η-intercalibration was used. This technique is used to make the detector jet response independent of the pseudorapidity η. This is achieved by applying a correction to jets reconstructed within the regime $0.8 \leq |\eta| < 4.5$ in order to equalize the response. It is also used to propagate the jet energy scale uncertainty from the central to the more forward region as discussed in Chap. 7.

The η-intercalibration exploits dijet events and uses the so-called matrix method [117]. For this purpose a "left" and a "right" jet is defined as follows: $\eta_{\text{det}}^{\text{left}} < \eta_{\text{det}}^{\text{right}}$. The p_T

[9]The non-leading jets are defined as jets with a p_T that is lower than the p_T of the leading jet in a given event.

balance is quantified using the asymmetry A, which is defined as:

$$A = \frac{p_T^{\text{left}} - p_T^{\text{right}}}{p_T^{\text{avg}}}, \tag{6.13}$$

where $p_T^{\text{avg}} = (p_T^{\text{left}} + p_T^{\text{right}})/2$. The asymmetry defined in Eq. 6.13 is then used to determine the ratio of the jet responses R, which is defined as follows:

$$R = \frac{p_T^{\text{left}}}{p_T^{\text{right}}} = \frac{c^{\text{left}}}{c^{\text{right}}} = \frac{2 + A}{2 - A},$$

where $c^{\text{left/right}}$ are the η-intercalibration factors of the "left"/"right" jet. The response ratio R is calculated in bins of $\eta_{\text{det}}^{\text{left}}$ (i), $\eta_{\text{det}}^{\text{right}}$ (j), and p_T^{avg} (k). The relative correction factor c_{ik} for a jet reconstructed in a given η_{det} and p_T^{avg} bin is determined by minimizing:

$$S(c_{1k}, ..., c_{Nk}) = \sum_{j=1}^{N} \sum_{i=1}^{j-1} \left(\frac{1}{\Delta\langle R_{ijk}\rangle} (c_{ik}\langle R_{ijk}\rangle - c_{ik}) \right)^2 + X(c_{1k}, ..., c_{Nk}),$$

where N is number of η_{det} bins, $\langle R_{ijk}\rangle$ is the average of the R_{ijk} distribution in given bins $(i,\ j,\ k)$ and $\Delta\langle R_{ijk}\rangle$ the corresponding statistical uncertainty. The additional term $X(c_{1k}, ..., c_{Nk})$ was added to prevent the minimizer algorithm to choose the solution $c_{ik} = 0$. The minimization was performed for each p_T^{avg} (k) bin and the average calibration factors c_i determined in each η_{det} bin were scaled in order to force the average calibration factors to unity in the $|\eta_{\text{det}}| < 0.8$ regime.

For the selection of events central and forward triggers were used and the events were corrected for the down-scale factors using the exclusion method. The intervals in p_T^{avg} associated with the triggers were determined such that the trigger efficiency is greater than 99% (cf. Sec. 6.2). The quality requirements described in Sec. 6.1.2 were applied and events were rejected containing at least one jet pointing to the malfunctioning calorimeter region. In order to select clean dijet topologies the azimuthal angle between the leading and second-leading jet was required to be $|\Delta\phi(\text{jet1, jet2})| > 2.5$ rad. Additionally, the following requirements on events containing a third jet in the central ($|\eta_{\text{det}}| < 2.5$) or forward ($|\eta_{\text{det}}| > 2.5$) region were made: $p_{T,\text{jet3}}^{\text{central}} < \max(0.25 \times p_T^{\text{avg}}, 12\ \text{GeV})$ and $p_{T,\text{jet3}}^{\text{forward}} < \max(0.2 \times p_T^{\text{avg}}, 10\ \text{GeV})$. The jets used in the selection above were required to originate from the hard scattering vertex and thus have a JVF > 0.6 (cf. Sec. 6.1.2). The relative jet response $1/c$ as function of η_{det} and the ratios between data and MC are exemplary shown in Fig. 6.12 (left) for dijets in the interval $170 \leq p_T^{\text{avg}} < 220$ GeV. The relative jet response as function of p_T^{avg} in the region $2.1 \leq |\eta_{\text{det}}| < 2.8$ is shown in Fig. 6.12 (right).

6.3.2 Z-jet and γ-jet Techniques

The production of Z bosons together with jets is used to improve the JES calibration for jets in the central pseudorapidity region $|\eta_{\text{det}}| < 1.2$. For this purpose Z bosons decaying in e^+e^- pairs were considered only. In contrast to other in-situ methods, the Z-jet analysis allows to derive correction factors for jets in the low-p_T regime.

As the first step, events used for the Z-jet analysis, were identified using an electron

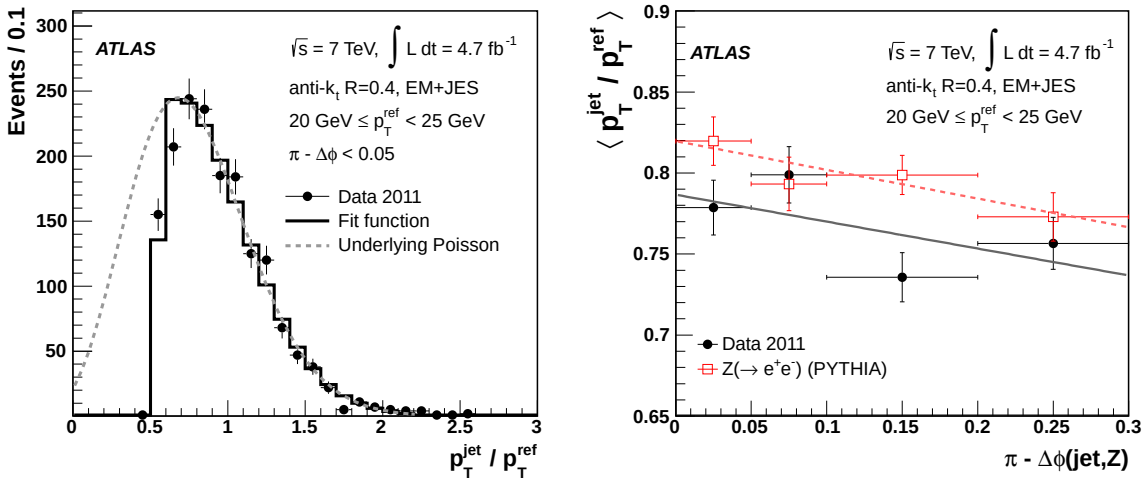

Figure 6.13: Left: $p_T^{\text{jet}}/p_T^{\text{ref}}$ distribution of Z-jet events with the following constraints: 20 GeV $\leq p_T^{\text{ref}} <$ 25 GeV and $\pi - \Delta\phi < 0.05$. The transverse momentum of the reference object p_T^{ref} is defined in Eq. 6.14. The jets were reconstructed using the anti-k_T algorithm with $R = 0.4$ and were calibrated to the EM+JES scale. Right: response $\langle p_T^{\text{jet}}/p_T^{\text{ref}} \rangle$ as function of $\pi - \Delta\phi$. The information extracted in the region shown in this figure was used as input for a linear fit, which is used for extrapolation purposes. [113]

trigger, which selects well-identified electrons according to the strategy described in Ref. [130]. The selected events were required to have a reconstructed primary vertex with at least three tracks. The electron identification cuts labeled 'medium' for the purpose of electron identification quality were applied [131]. Events containing exactly two electron[10] candidates with a transverse energy E_T^e above 20 GeV within $|\eta^e| < 2.47$ are used. The transition region $1.37 < |\eta^e| < 1.52$ and other regions with a distorted energy measurement were excluded. Additionally the two electron candidates were required to have opposite signed charges. Only Z boson candidates which were reconstructed within the invariant mass window of 66 GeV $< M_{e^+e^-} <$ 166 GeV were kept for the further analysis. The leading jet was required to be reconstructed within $|\eta| < 1.2$ and fulfill the jet quality criteria (cf. Sec. 6.1.2) with JVF > 0.5 (cf. Sec. 6.1.2). All jets with a transverse momentum $p_T > 12$ GeV were considered. An event was rejected, if the electron candidates are not isolated from the leading jet. The isolation distance was chosen to be $\Delta R(\text{jet}, e^{+/-}) > 0.35$ and $\Delta R(\text{jet}, e^{+/-}) > 0.5$ for jets reconstructed with the distance parameter $R = 0.4$ and $R = 0.6$, respectively. In order to suppress events which contain high-p_T jets originating from additional parton radiation, the p_T^{jet2} of the second-leading jet was required to be less than $0.2 \cdot p_T^Z$. This cut was applied for jets covered by the tracking system with JVF > 0.75.

Despite the cuts applied to select appropriate event candidates, the p_T-balance is still sensitive to additional parton radiation. In order to achieve further reduction of this effect, the following quantity was used as reference:

$$p_T^{\text{ref}} = p_T^Z \times |\cos(\Delta\phi(\text{jet}, Z))|, \tag{6.14}$$

[10]Electrons and positrons are both called electrons and are not distinguished.

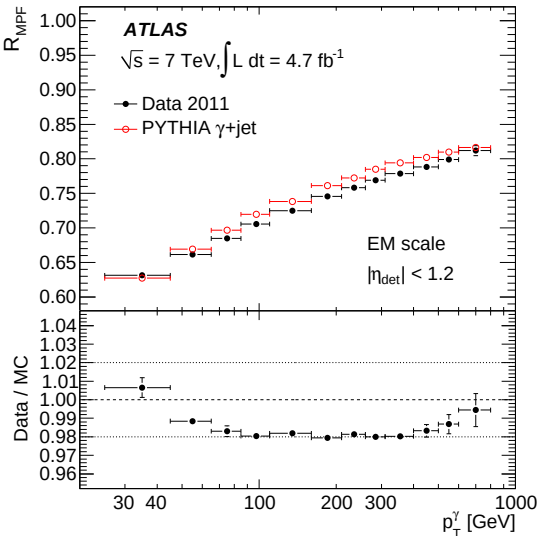

Figure 6.14: Response R_{MPF} as function of p_T^{γ}. In the lower panel the ratio between data and MC is shown. [113]

where p_T^Z is the transverse momentum of the Z boson and $\Delta\phi(\mathrm{jet}, Z)$ the difference between the azimuthal angles of the jet and the Z. In order to determine the response, the distribution of the ratio $p_T^{\mathrm{jet}}/p_T^{\mathrm{ref}}$ was determined in bins of p_T^{ref} and $\Delta\phi(\mathrm{jet}, Z)$. In case of events, where $p_T^{\mathrm{ref}} \geq 35$ GeV, the arithmetic mean was determined. In the low-p_T^{ref} regime below 35 GeV a fit was performed due to the cut of 12 GeV on the jet transverse momentum applied to all jets, which cause an asymmetric distribution as shown in Fig. 6.13 (left). Thus a modified Poisson distribution was used as the fit function. In order to stabilize the fit against statistical fluctuations a two-step fitting procedure was performed in order to compensate for this effect. The least biased region due to additional parton radiation is at $\Delta\phi(\mathrm{jet}, Z) = \pi$. Therefore the determined mean balance $\langle p_T^{\mathrm{jet}}/p_T^{\mathrm{ref}}\rangle$ in a given $\Delta\phi(\mathrm{jet}, Z)$-bin was extrapolated to $\Delta\phi(\mathrm{jet}, Z) = \pi$ using a linear function as shown in Fig. 6.13 (right), where the range for the linear fit was chosen to be $\pi < \Delta\phi(\mathrm{jet}, Z) < \pi - 0.3$. This procedure provides further suppression of the p_T^{jet} sensitivity to additional parton radiation.

The second technique used to estimate the absolute calorimeter jet response exploits γ-jet events. For this purpose the total hadronic recoil was taken into account and the so-called missing transverse momentum projection fraction (MPF) response[11] was defined as follows:

$$R_{\mathrm{MPF}} = 1 + \frac{\vec{p}_T^{\,\gamma} \cdot \vec{E}_T^{\mathrm{miss}}}{|\vec{p}_T^{\,\gamma}|^2}, \tag{6.15}$$

where $\vec{E}_T^{\mathrm{miss}}$ is the vectorial sum of the transverse projections of calorimeter cells included in topological clusters and $\vec{p}_T^{\,\gamma}$ the vectorial transverse momentum of the reference photon. The MPF response is derived from the projection of $\vec{E}_T^{\mathrm{miss}}$ onto the direction of the photon.

[11] By analogy with the Z-jet calibration method, jet response was also derived using the direct balance method, where the transverse momentum p_T^{jet} of the leading jet was compared to the p_T^{γ} of the photon. The systematic uncertainty was shown to be smaller in case of the MPF technique and therefore this method was taken for the in-situ calibration of jets.

The basic assumption of this method is that $\vec{E}_T^{\text{miss}}$ only arises from the non-compensating nature of the calorimeter, energy losses due to the noise-suppression mechanism and non-functioning calorimeter regions[12]. The MPF response depends only on $\vec{p}_T^{\,\gamma}$ and $\vec{E}_T^{\text{miss}}$ and is therefore independent on the choice of the jet algorithm.

The first step in the γ-jet event selection is the requirement of a primary vertex associated with at least five tracks. The events are required to have at least one reconstructed photon, where the leading photon must have $p_T^\gamma > 25$ GeV. Furthermore, the event must pass a single photon trigger [130], where the p_T^γ trigger threshold depends on the p_T^γ of the leading photon. Moreover, the identification criteria for photons described in Ref. [132] must be fulfilled in case of the leading photon and it is also required to be reconstructed in the barrel calorimeter within the pseudorapidity regime $|\eta^\gamma < 1.37|$. In order to suppress the background due to e.g. jets containing a high energetic π^0 decaying into $\gamma\gamma$, the leading photon candidate was required to be isolated. For this purpose the so-called transverse isolation energy $E_T^{\gamma\ \text{Iso}}$ was used, which is calculated around the photon candidate[13] within a cone of radius 0.4 in the η-ϕ-plane and is corrected due to pile-up contributions. The photon candidates were required to have $E_T^{\gamma\ \text{Iso}} < 3$ GeV. Further background contributions come from jets that are misidentified as photons, so-called fake-photons. The aim of the photon reconstruction algorithm is to include unconverted photons and photons converted into a e^+e^- pair. The photons falling into the former category do not have tracks associated with them, while in the latter category tracks are reconstructed. In order to increase the reconstruction efficiency of photons converted into a e^+e^- pair, also photon candidates are taken into account which have only one associated track (single-track conversions). The fake-photons have tracks related to them and produce wider showers within the calorimeter and contribute therefore as background. This background is suppressed using the ratio $E_T^{\gamma\text{cluster}} / \sum p_T^{tracks}$, where $E_T^{\gamma\text{cluster}}$ is the transverse energy of the photon candidate cluster [132] and $\sum p_T^{tracks}$ is the sum of the transverse momenta of the matching tracks. This ratio was required to be between 0 and 2 in case of single-track conversion and between 0.5 and 1.5 for photons, where two tracks were reconstructed. In case of jets the quality criteria introduced in Sec. 6.1.3 were applied and the jets were required to have a transverse momentum of $p_T^{\text{jet}} > 12$ GeV. Moreover, events were required to contain at least one reconstructed jet, with a leading jet within $|\eta^{\text{jet1}}| < 1.2$. Soft radiation affecting γ-jet balance was suppressed by requiring $|\Delta\phi(\text{jet}, \gamma)| > 2.9$ rad between the photon and the leading jet and the second-leading jet was required to have a $p_T^{\text{jet2}} < 0.3 \times p_T^\gamma$. In this case, the second-leading jet was taken from a set of non-leading[14] jets, which have a JVF > 0.75 or are outside of the tracking system. An event which contains a jet with $p_T^{\text{jet}} > 20$ GeV pointing to a malfunctioning calorimeter region (cf. Sec. 6.1.2) was rejected. This criteria was applied to all leading and second-leading jets independent of their transverse momentum.

The distribution of the response R_{MPF} defined in Eq. 6.15 is determined in bins of p_T^γ and fitted using a Gaussian function. The expectation value of the Gaussian function is

[12] The p_T balance can be written as $\vec{p}_T^{\,\gamma} + \vec{p}_T^{\,\text{jet}} = 0$ and the missing transfers momentum vector can be written as $-\vec{E}_T^{\text{miss}} = R^\gamma p_T^\gamma + R^{\text{jet}} p_T^{\text{jet}}$. The response $R^\gamma = 1$, because the photon is well calibrated. The combination of these equations results in a calorimeter jet response given in Eq. 6.15.

[13] The contribution from the photon candidate within 5×7 electromagnetic calorimeter cells around the barycenter of the photon candidate are not included in the calculation of $E_T^{\gamma\ \text{Iso}}$.

[14] All jets whose p_T is less than the p_T^{jet1} of the leading jet.

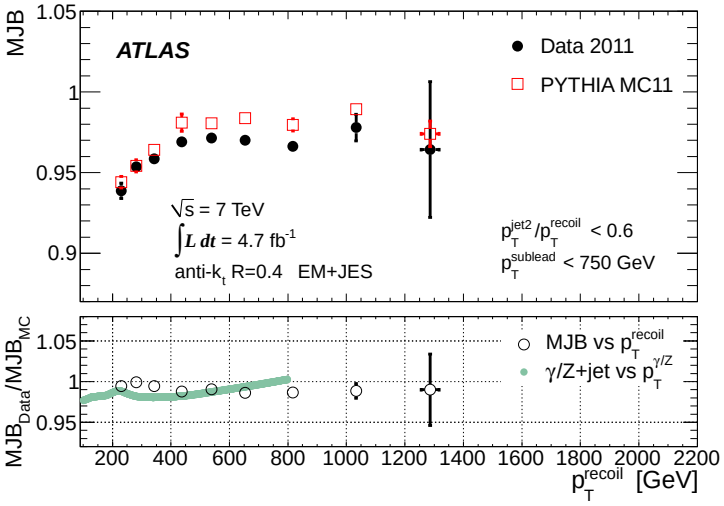

Figure 6.15: MJB as function of p_T^{recoil} for jets reconstructed using the anti-k_T algorithm with the distance parameter $R = 0.4$. The jets were calibrated with the EM+JES scheme. The thick line in the lower part of the figure is the data-to-MC ratio of the the p_T of the jet with respect to p_T^γ or p_T^Z as function of p_T^γ or p_T^Z (cf. Sec. 6.3.2). [113]

taken as the mean response. The average jet response R_{MPF} as function of p_T^γ determined using topological clusters at the EM-scale is shown Fig. 6.14. The relative response is similar to that discussed in Sec. 5.4 obtained with jets at EM scale and jets at particle-level as reference objects. In contrast to the direct jet balance, no explicit use of jets was made in case of the MPF method and thus no further corrections were applied. The lower plot in Fig. 6.14 shows the ratio of the jet response in data with respect to that in MC. The response obtained using data is below that of MC. The ratio between data and MC is around $1 - 2\%$ for $p_T^\gamma > 100$ GeV.

6.3.3 Multijet Transverse Momentum Balance

The calibration of jets reconstructed in the high-p_T region above ~ 800 GeV was improved using the multijet balance method (MJB). As the other in-situ absolute jet energy scale (JES) calibration methods, MJB covers the pseudorapidity regime $|\eta_{\text{det}}| < 1.2$. MJB exploits the p_T balance between the jet with the highest transverse momentum p_T^{jet1} and the p_T^{recoil} of the so-called recoil system. The recoil system consists of non-leading jets which are reconstructed in the lower p_T regime. These jets are corrected using η-intercalibration results (cf. Sec. 6.3.1), as well as absolute JES corrections derived using the γ-jet and Z-jet (cf. Sec. 6.3.2) techniques. Therefore, this method aims to extend the p_T regime covered by the γ-jet and Z-jet methods. The MJB response is defined as follows:

$$\text{MJB} = \frac{|\vec{p}_T^{\,\text{jet1}}|}{|\vec{p}_T^{\,\text{recoil}}|},$$

where $\vec{p}_T^{\,\text{jet1}}$ the transverse momentum of the leading jet and $\vec{p}_T^{\,\text{recoil}}$ is the vectorial sum of the transverse momenta of the jets forming the recoil-system.

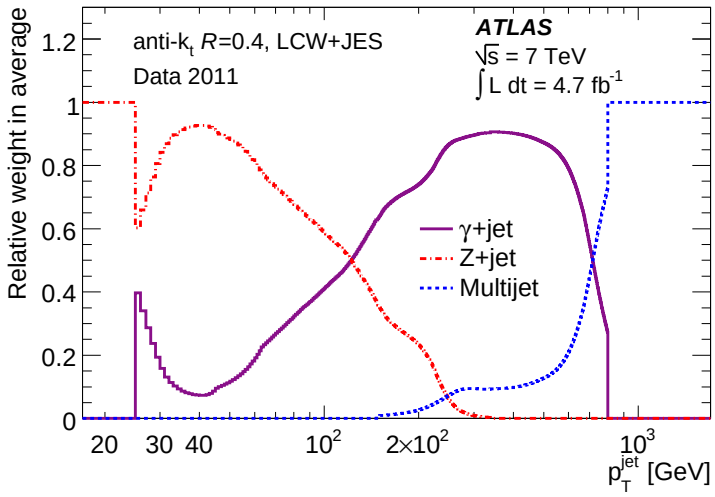

Figure 6.16: Weights of each individual in-situ technique used for the calculation of the average data-to-MC ratio [113].

In order to increase the statistical significance, different single jet triggers were used. The triggers were combined using the division method (cf. Sec. 6.2) by defining non-overlapping intervals in p_T^{recoil} for each single jet trigger. The events were required to have at least one primary vertex associated with at least five reconstructed tracks. Events containing an identified electron, muon or photon were rejected. All jets above $p_T > 20$ GeV were required to pass the quality criteria discussed in Sec. 6.1.3. Events containing jets pointing to a malfunctioning detector region (cf. Sec. 6.1.2) were rejected. Furthermore, events were required to have at least three good quality jets with $p_T > 25$ GeV reconstructed within the pseudorapidity region $|\eta| < 2.8$, whereas the leading jet was required to be within $|\eta| < 1.2$. Moreover, two angular variables were defined to select events containing one jet produced against a well-defined recoil system: α and β. The quantity $\alpha = |\Delta\phi - \pi|$, where $\Delta\phi$ is the azimuthal angle between the leading jet and the recoil system and was required to be less than 0.3 rad. The quantity β is the smallest azimuthal opening angle between the leading jet and the non-leading jets of the recoil system. The angle β was required to be greater than 1 rad. The last category of cuts selects events where non-leading jets are separated from the leading jet in p_T. The non-leading jets are required to be in the regime where the in-situ absolute JES calibration methods are valid. This is achieved by requiring $p_T^{\text{jet2}} < 750$ GeV for the second-leading jet. The leading jet is required to be above the p_T region of the recoil system. This is controlled by the ratio $p_T^{\text{jet2}}/p_T^{\text{recoil}}$ which is chosen to be less than 0.6. Fig. 6.15 exemplary shows MJB as function of p_T^{recoil} and the ratio between MJB derived from MC simulation and that from data.

6.3.4 Combination of the In-Situ methods and Final Calibration

As input for the last calibration step jets corrected using the techniques described in Sec. 5.4 are used. The final correction factors are derived by comparing data and MC in following way:

$$R(p_T^{\text{jet}}, \eta) = \frac{\langle p_T^{\text{jet}}/p_T^{\text{ref}}\rangle_{\text{data}}}{\langle p_T^{\text{jet}}/p_T^{\text{ref}}\rangle_{\text{MC}}}, \tag{6.16}$$

where p_T^{jet} is the corrected transverse momentum using MC-based calibration methods, p_T^{ref} the transverse momentum of the reference object and $R(p_T^{\text{jet}}, \eta)$ is the inverse of the jet energy scale correction factor applied to jets reconstructed using collision data and is the final correction step within the calibration procedure. The data-to-MC response ratios $R(p_T^{\text{jet}}, \eta)$ were determined as function of p_T^{ref}. In general, the choice of the bin widths of the considered in-situ methods is different. In order to combine the methods, fine p_T bins were introduced and interpolating splines were used to evaluate the response ratios for a given p_T bin. The combined data-to-MC ratio is calculated as a weighted average, where the corresponding weights are determined by a χ^2 minimalization of the response ratios. The weights and thus the contribution of each individual in-situ method as function of p_T^{jet} is exemplary shown in Fig. 6.16 for jets at LCW+JES scale. The correction is dominated by Z-jet for low-p_T jets with $p_T^{\text{jet}} < 100$ GeV, whereas the contributions of the γ-jet method ranges between 100 GeV $< p_T^{\text{jet}} <$ 700 GeV. The contribution to the correction of high-p_T jets $p_T^{\text{jet}} > 700$ GeV comes from the multijet transverse momentum balance technique.

6.3.5 Jet Energy Correction Due to Non-Operational cells

Non-operational calorimeter cells distort the jet energy measurement and thus a correction is applied to jets (cf. Sec. 6.1.2). For this purpose the quantities $\text{BCH}_{\text{corr,jet}}$ and $\text{BCH}_{\text{corr,cell}}$ are used, where the latter is defined in Eq. 6.7. $\text{BCH}_{\text{corr,cell}}$ is the energy fraction of non-operational cells, which is estimated using the measured energy of neigbouring cells. In contrast, $\text{BCH}_{\text{corr,jet}}$ is based on simulated average jet shape. By analogy with Eq. 6.7 it is calculated as follows:

$$\text{BCH}_{\text{corr,jet}} = \sum_{\text{non-op. cells}} \frac{E_{\text{corr},i}}{E_{\text{jet}}}, \tag{6.17}$$

where $E_{\text{corr},i}$ is the estimated energy for the non-operational calorimeter cell i within the cone of the jet and E_{jet} the jet energy at EM scale. In order to estimate $E_{\text{corr},i}$, jet profiles were determined using MC, where the Tile cells were fully operational. The energy fraction is calculated as function of the transverse momentum p_T at EM-scale, the distance between the jet axis and the cell centre in the (η, ϕ)-plane, the calorimeter sampling and the pseudorapidity η_{cell} and the azimuthal ϕ_{cell} of the cell [133].

The jet energy E^{uncorr} at the electromagnetic scale, which is used as input for the calibration procedure, was corrected as follows:

$$E^{\text{BCHcorr}} = E^{\text{uncorr}} \cdot \frac{1 - \text{BCH}_{\text{corr,cell}}}{1 - \text{BCH}_{\text{corr,jet}}}. \tag{6.18}$$

This correction step was applied to jets with $E^{\text{BCHcorr}} > m_{\text{origin}}$ only, where m_{origin} is the invariant mass of the origin corrected topological clusters within the jet at the em. scale (cf. Sec. 5.4.2).

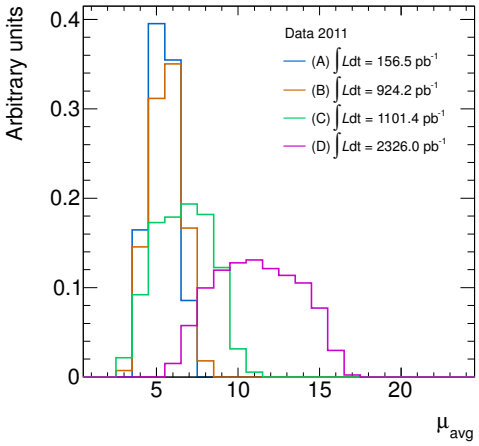

Figure 6.17: Distributions of events according to the average number of interactions per bunch-crossing μ_{avg} in data for different periods. The distributions are normalized to unity. The distributions were normalized to unity. All jets were included falling into the kinematic region covered by the cross-section measurements in Chap. 8.

6.4 Pile-Up in Data and Monte Carlo Simulation

A correction for in-time and out-of-time pile-up is applied in the context of the jet energy scale calibration as discussed in Sec. 5.4.1. In order to characterize pile-up, the average number of interactions per luminosity block μ_{avg} and the number of reconstructed primary vertices N_{PV} was used. N_{PV} is derived using input from the tracking system which is much faster compared to the integration time of the em. calorimeter electronics and thus is expected to be a good measure for in-time pile-up activity. μ_{avg} was chosen as a measure for out-of-time pile-up, because a certain level of in-time pile-up on average is needed by design in order to avoid out-of-time pile-up effects. In this section the impact of in-time and out-of-time pile-up on the jet measurement and the quality of the MC simulation is discussed. For this purpose fully calibrated and pile-up corrected jets were used.

6.4.1 In-Time Pile-Up

The data record can be sub-divided in four periods with different in-time pile-up environments which is indicated in Fig. 6.17. These periods are simulated in MC, which is also sub-divided according to different in-time pile-up conditions reflecting the situation in data as listed in Tab. 6.4. In order to improve the agreement between data and MC the so-called pile-up re-weighting was applied. For this purpose simulated events or jets were re-scaled using weights as function of μ_{avg} and the period of data taking. The aim is to re-weight the simulated spectrum such that the normalized $\mu_{\text{avg}}^{\text{MC}}$ distribution reflects the normalized $\mu_{\text{avg}}^{\text{Data}}$ distribution. The integral over the distributions was normalized to unity, which preserves the number of events in MC simulation. Additionally a correction factor was multiplied in order to reflect the portion of data taken within each period compared to the entire data. The above described procedure can be applied to spectra, where the spectrum of interest is constructed using a single trigger with down-scale factors equal to unity as e.g. done in Chap. 9. In case of trigger combination schemes

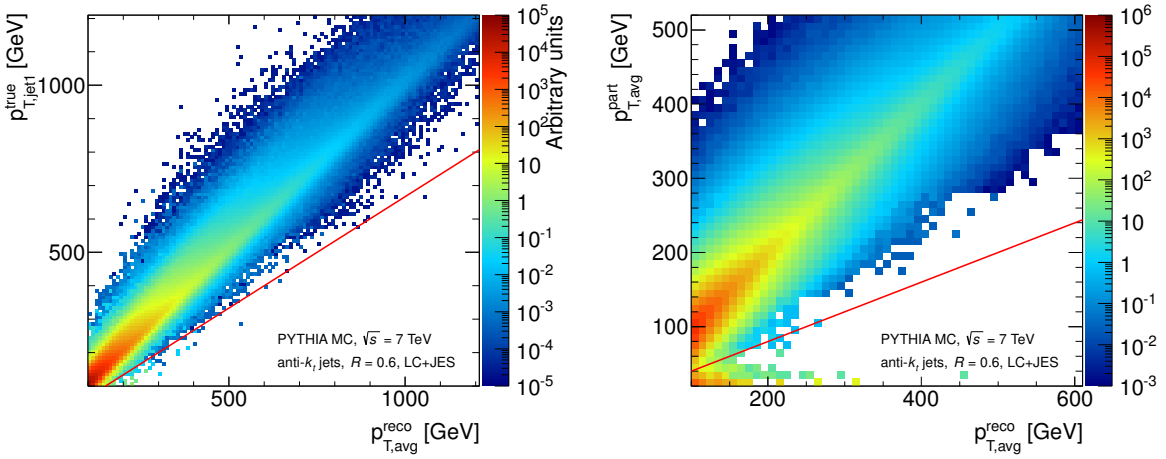

Figure 6.18: Left: distribution of events as function of the transverse momentum of the first leading jet $p^{\text{true}}_{T,\text{jet1}}$ at particle-level and the average transverse momentum of the first two leading jets at detector-level. Right: distribution of events as function of the average transverse momentum of the first two leading partons $p^{\text{part}}_{T,\text{avg}}$ and the average transverse momentum of the first two leading jets at detector-level. The red line in both figures reflects the cuts applied as listed in Tab. 6.5. Events below this line were rejected.

with several triggers as used for the measurements in Chap. 8 a more complex strategy is applied. The down-scale factors of the considered triggers are different and also depend on the pile-up environment, which differs from period to period. Also, for a given trigger, the down-scale factors change slightly within a period. These facts must be taken into account when deriving and applying pile-up weights. In case of an inclusive jet analysis, the simulated jet $p_{T,\text{jet}}$ is used in order to determine triggers, which are associated with unique p_T slices as discussed in Sec. 6.2. The weights are derived using a trigger down-scale factor corrected and normalized $\mu^{\text{Data}}_{\text{avg}}$ distribution for a given trigger as reference. In case of the dijet cross-section measurement two triggers per event were combined. By analogy with inclusive jet trigger combination procedure, trigger pairs were identified using the transverse momenta p_T of the leading and second-leading jets of each simulated event. For each trigger pair a trigger down-scale factor corrected and normalized $\mu^{\text{Data}}_{\text{avg}}$ distribution is used as reference. Due to the complex re-weighting strategy large weights can be introduced which cause artifacts with large statistical uncertainties.

In order to provide MC simulation samples with a high statistical power over the entire kinematic region covered by the measurements, the MC simulation is produced in slices of $p^{\text{part}}_{T,avg}$, which is the average transverse momentum of the leading and second-leading final state partons. Weights are used to re-weight the different samples in order to reconstruct the correct spectra as discussed in greater detail in App. A.3. These weights differ orders of magnitude over the entire $p^{\text{part}}_{T,avg}$ region. An additional offset on the transverse momentum $p_{T,\text{jet}}$ due to in-time pile-up can cause a migration of jets from low-p_T bins to high-p_T bins. This can result in large statistical uncertainties due to the error propagation with large weights. Therefore additional cuts are applied in the selection of simulated events. In order to identify such events, the transverse momentum of leading jet $p^{\text{true}}_{T,\text{jet1}}$ (A) at particle-level and the average transverse momentum of the first two leading partons

Period	Int. lumi. (data)	Fraction f_{Data}	Fraction f_{MC}
(A)	156.5 pb^{-1}	3.5%	4.5%
(B)	924.2 pb^{-1}	20.5%	18.8%
(C)	1101.4 pb^{-1}	24.4%	29.0%
(D)	2326.0 pb^{-1}	51.6%	47.7%

Table 6.4: The portion of different pile-up configurations in collision data (f_{Data}) and Monte Carlo simulation (f_{MC}). The integrated luminosities were determined on the basis of the GRL used for the cross-section measurements (cf. Sec. 6.1.1) and were corrected for events affected by LAr calorimeter errors (cf. Sec. 6.1.2). The total integrated luminosity in data amounts to 4.5 fb^{-1}. In case of MC, the fractions were obtained exploiting the MC samples used for the purpose of cross-section measurements (cf. App. A.3). The total number of events amounts to $1.8 \cdot 10^7$ in MC simulation. The ratio $f_{\text{MC}}/f_{\text{Data}}$ was used as weight in case of simulated events and jets in context of the pile-up re-weighting procedure.

$p_{T,\text{avg}}^{\text{part}} = (p_{T,\text{part1}} + p_{T,\text{part2}})/2$ (B) are compared to the average transverse momentum $p_{T,\text{avg}}^{\text{reco}} = (p_{T,\text{jet1}}^{\text{reco}} + p_{T,\text{jet1}}^{\text{reco}})/2$ at detector-level. The distributions and cuts are shown in Fig. 6.18. The event rejection criteria are indicated as red lines in this figures and are listed in Tab. 6.5. Due to the application of cut A, few events over the entire $p_{T,\text{avg}}^{\text{reco}}$ spectrum are removed. Cut B removes events in the low-$p_{T,\text{avg}}^{\text{reco}}$ regime only. This cut set has no significant impact on the shape of the spectra of interest, but has a large impact on the statistical power. In order to preserve the cross-section of the MC spectra, the number of events used as input for the MC re-weighting procedure, were counted after the application of these cuts.

Type of comparison	Cut
(A) Comparison between detector- and particle-level	$p_{T,\text{avg}}^{\text{reco}} > 2 \cdot p_{T,\text{jet1}}^{\text{true}}$
(B) Comparison between detector- and parton-level	$p_{T,\text{avg}}^{\text{reco}} > 2.5 \cdot p_{T,\text{avg}}^{\text{part}}$

Table 6.5: A list of cuts applied in order to remove events in MC simulation which cause large statistical uncertainties. The event is removed if one of the listed criteria is fulfilled. The cuts (A) and (B) are indicated as red lines in Fig. 6.18

.

6.4.2 Out-of-time Pile-up

As described in section 6.4.2 the LHC bunch train structure is organized in several trains with 50 ns spacing between consecutive proton bunches within a train. The spacing between trains varies from 150 ns to more than 650 ns. In contradiction to the collision data the bunch train structure simulated in Monte Carlo is organized in four equidistant trains with a 50 ns spacing between the proton bunches within trains. The spacing

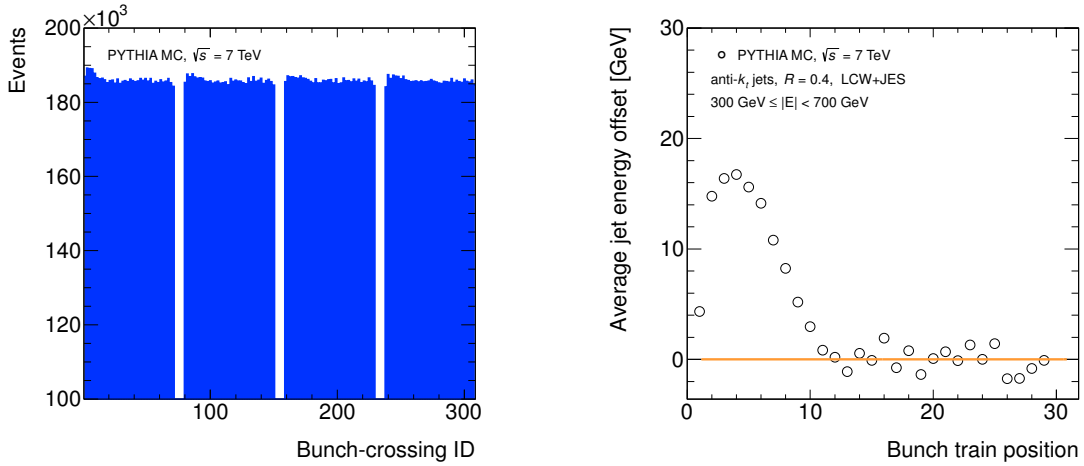

Figure 6.19: Left: bunch train configuration implemented in MC simulation. The spacing between bunch-crossings within the train amounts to 50 ns, which reflects the situation in collision data. A similar configuration of 4 subsequent trains with a spacing at around 200 ns between the trains is realized in approximately 2.3 fb^{-1} (cf. Tab. 6.4 period (D)) of data. Right: jet energy offset as function of the position within the train. For this purpose calibrated jets reconstructed exploiting the anti-k_t algorithm with $R = 0.4$ were used. The maximum jet energy offset in the first 10 bunch-crossings is around 15 GeV.

between the trains amounts to 200 ns. The bunch train configuration simulated in MC is shown in Fig. 6.19 (left). The reconstructed energy in the liquid argon calorimeter (LAr) originated from a certain bunch-crossing depends on the position of the involved proton bunches within the train (BTP) and the distance to the previous and subsequent train. On average, the maximum additional jet energy due to the position within the train amounts up to approximately 15 GeV in the first ten bunch-crossings compared to bunch-crossings in the middle of the train (BTPs between 10 and 30). This can increase the number of jets e.g. in a given p_T-bin due to the single-sided migration of jets caused in combination with the steeply falling nature of the kinematic spectra. The jet energy offset simulated in MC as function of the bunch train position (BTP) is shown in Fig. 6.19 (right). This effect originates from the absence of previous bunches and is not compensated by the pile-up correction, because of the exclusion of the first 600 ns within the train (cf. 5.4.1). In case of jets coming from bunch-crossings at the end of a train less energy is measured, because of the absence of subsequent bunches. This effect has a smaller impact on the jet energy measurement compared to the offset added to jets, which originates from collisions in the first BTPs and amounts to few GeV. The impact due to out-of-time pile-up effects on the cross-section measurements and the implications on the systematic uncertainties are discussed in greater detail in 8.4.2. Further studies focusing on the low-p_T region can be found in App. A.4.

6.5 Jet Resolution

The cross-section measurements comprise corrections for detector effects like the resolution, which is required to be well modeled in Monte Carlo (MC) simulation. The relative

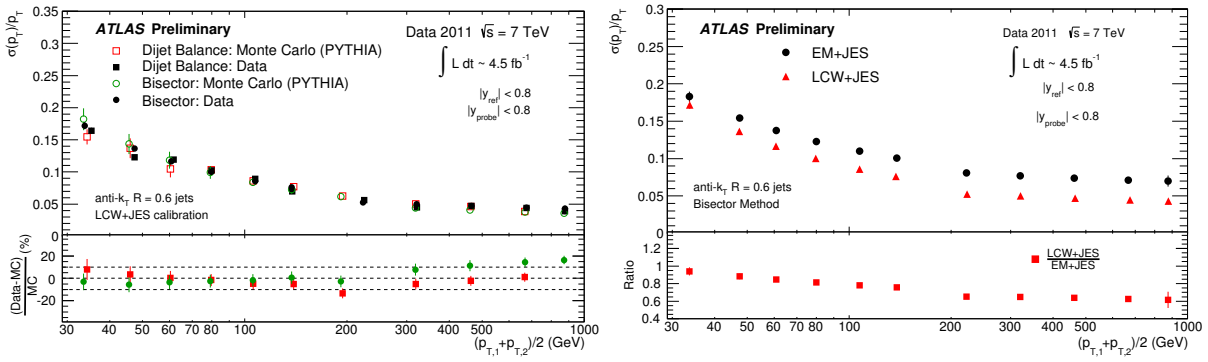

Figure 6.20: Left: relative jet p_T resolution determined using the dijet balance and bisector methods as a function of the average jet $\bar{p}_T$ of the dijet system. The leading and the second-leading jet were required to be in the central rapidity region $|y| < 0.8$. The jets were reconstructed using the anti-k_t algorithm with the distance parameter $R = 0.6$. The lower part of this figure shows the difference between data and MC simulation. The 10% difference is indicated by the black dotted line. Right: comparison of the relative jet p_T resolution obtained using jets calibrated with the EM+JES and LCW+JES schemes. The resolution was determined using the bisector technique. Both leading jets were required to be in the central rapidity region $|y| < 0.8$. The jets were reconstructed using anti-k_t with $R = 0.6$. [134]

resolution on the transverse momentum can be determined exploiting the information at detector- and particle-level provided in MC simulations. It can also be measured in-situ using the *dijet balance* method [135] and the *bi-sector* method [136]. These methods are applied to data and MC simulation in order to estimate the uncertainty on the relative p_T resolution. The cross-section measurements discussed in Chap. 8 are performed as function of the rapidity y and y^*. Due to the limited angular resolution, jets can migrate from one rapidity bin to another and thus affect the cross-section. In order to study the impact on the cross-section, the angular resolution was determined. The resolution is also determined for the invariant dijet mass m_{jj} and was used as basis for exclusion limits based on Gaussian shaped templates as discussed in Chap. 9.

The relative jet resolution of a kinematic variable X can be estimated using events or jets at detector-level (X^{reco}) and particle-level (X^{true}). For this purpose the ratio $(X^{\text{reco}} - X^{\text{true}})/X^{\text{true}}$ is calculated for each event or jet in bins of X^{true}. The resulting distributions can be fitted using a Gaussian function. In this case, the Gaussian parameter σ (standard deviation) provides the relative resolution $\sigma(X)/X$ for each X^{true} bin. In order to compare same jets at detector- and particle-level a matching and isolation algorithm is applied. It is also possible to estimate the relative resolution using in-situ techniques. In ATLAS, this is done for the relative resolution on the jet transverse momentum using two different approaches [137]. The first one is the so-called *dijet balance* method, which exploits the momentum conservation in the transverse plane in order to determine the jet p_T resolution. The resolution measurement is based on the p_T asymmetry of the leading and

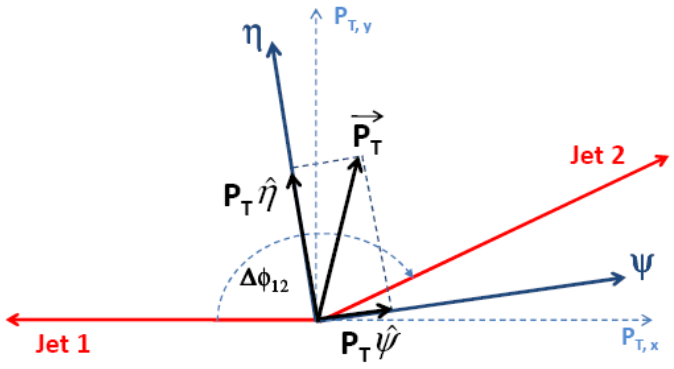

Figure 6.21: Sketch of the bi-sector method [137].

second-leading jet, which is defined as:

$$A(p_{T,\text{jet1}}, p_{T,\text{jet2}}) = \frac{p_{T,\text{jet1}} - p_{T,\text{jet2}}}{p_{T,\text{jet1}} + p_{T,\text{jet2}}} \tag{6.19}$$

The p_T asymmetry distributions were determined as function of the average transverse momentum of the dijet system $\bar{p}_T \equiv (p_{T,\text{jet1}} + p_{T,\text{jet2}})/2$. The distributions were parametrized by fitting a Gaussian function to the distribution of $A(p_{T,\text{jet1}}, p_{T,\text{jet2}})$ in order to extract the standard deviation σ_A, which is correlated with the resolution. On the supposition that the transverse momenta of the jets are balanced on average and the p_T resolution is the same for both jets, which is the case if both jets point to the same rapidity region, the relation between σ_A and the relative jet p_T resolution is given by:

$$\sigma_A = \frac{\sqrt{\sigma^2(p_{T,\text{jet1}}) + \sigma^2(p_{T,\text{jet2}})}}{\langle p_{T,\text{jet1}} + p_{T,\text{jet2}} \rangle} \simeq \frac{1}{\sqrt{2}} \frac{\sigma(p_T)}{p_T} \tag{6.20}$$

In order to reduce the sensitivity to soft radiation effects and thus enhance the back-to-back jet purity, events were removed, where a transverse momentum of the third-leading jet $p_{T,\text{jet3}} > 10$ GeV or azimuthal angle $|\Delta\phi(\text{jet1,jet2})| \geq 2.8$. An additional soft radiation correction was applied, due to presence of soft particles not detected by the calorimeter. For this purpose the presence of third-leading jets with $p_{T,\text{jet3}} < 10$ GeV was allowed. The correction was calculated by extrapolating the relative p_T resolution obtained with different $p_{T,\text{jet3}}$ cut thresholds down to $p_{T,\text{jet3}} \to 0$ GeV. The relative resolution for the dijet topology is worsen around 3-5% for jets at $\bar{p}_T \approx 100$ GeV in presence of soft jets with $p_{T,\text{jet3}} < 10$ GeV. Furthermore, the so-called particle balance correction is applied due to soft QCD effects and out-of-jet losses. For this purpose the detector-level balance, which is the difference between the transverse momenta of the second-leading and leading jet at detector-level, is decomposed in terms of the particle-level balance and other components. The correction is estimated by applying the same correction method as used in case of soft radiation exploiting particle-level jets as input. The correction is applied to data and MC and ranges between 2%-10% depending on the jet p_T.

The second method used to determine the relative jet p_T resolution is the so-called

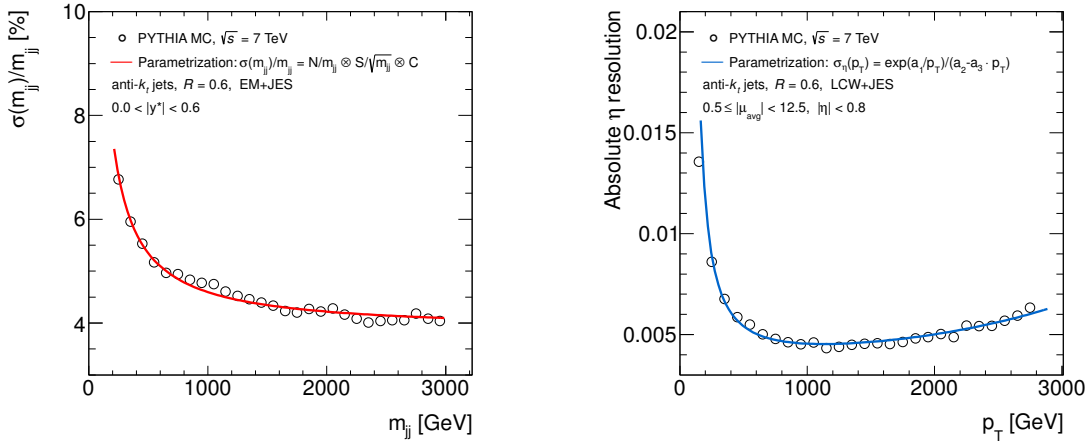

Figure 6.22: Left: relative invariant dijet mass m_{jj} resolution as function of m_{jj}. The jets were reconstructed using the anti-k_T algorithm with the distance parameter $R = 0.6$ and calibrated using the EM+JES scheme. The parametrization is performed using the function given in Eq. 6.22. Right: absolute η resolution as a function of the jet p_T in the pseudorapidity region $|\eta| < 0.8$.

bi-sector method. This technique is based on the transverse vector $\vec{P}_T$ which is defined as the vector sum of the leading and second-leading jet characterizing the imbalance of the dijet system as illustrated in Fig. 6.21. The direction of the η-axis is chosen such that it has an angle of $\Delta\phi_{12}/2 \equiv \Delta\phi(\text{jet1,jet2})/2$ to the first two leading jets in the transverse plane. The Ψ-axis is chosen to be orthogonal to the η-axis. In an ideal back-to-back dijet event all components of the two dimensional vector $\vec{P}_T$ are zero. At particle-level the non-zero variance of $p_{T,\eta}$ and $p_{T,\Psi}$ is mainly due to initial-state gluon radiation which is expected to be isotropic. Therefore, at particle-level, the variations $\sigma_\Psi^{\text{part}}$ and $\sigma_\eta^{\text{part}}$ were assumed to be equal in the (η, Ψ) plane. Other effects like the final-state radiation not included in the reconstruction of the first two leading jets could have a larger impact on $\sigma_\Psi^{\text{part}}$, because such a third-leading jet would be produced close-by. At detector-level $\vec{P}_T^{\text{calo}}$ has non-zero component due to detector-effects, where the $p_{T,\Psi}$ component is most sensitive to the jet energy resolution. For both jets pointing to the same rapidity region the relative p_T resolution is given by:

$$\frac{\sigma(p_T)}{p_T} = \frac{\sqrt{\sigma_\Psi^2 - \sigma_\eta^2}}{\sqrt{2} p_T \sqrt{\langle \cos \Delta\phi(\text{jet1,jet2}) \rangle}} \tag{6.21}$$

By subtracting σ_Ψ^2 for σ_η^2 soft radiation effects are minimized. The σ_Ψ^2 for σ_η^2 were extracted by fitting a Gaussian function around the kernel. In presence of pile-up one of the leading jets can be replaced by a pile-up jet. This introduces tails mainly in the $p_{T,\Psi}^{\text{calo}}$ distributions which are not affecting the Gaussian fits, because the fit range was chosen to be around the kernel and thus effects introduced by pile-up on the resolution measurement were shown to be negligible. The relative p_T resolution determined applying the described techniques with collision data and MC simulation is shown in Fig. 6.20 (left). The methods show consistent results. The relative resolution is at around 14% at $\bar{p}_T$ of 50 GeV and improves down to 4% at an average transverse momentum $\bar{p}_T = 1000$ Gev. The lower panel of the

figure shows the discrepancy between data and MC, which is taken as input in order to estimate the systematic uncertainty. The in-situ methods agree within 10% with the pure MC-based method. The different calibration schemes described in Sec. 5.4, which are both used in the upcoming analyses, lead to different relative jet p_T resolutions as shown in Fig. 6.20 (right). The LC+JES scheme provides a 40% better resolution at high-p_T. The reason for this improvement is mainly due to the correction for calorimeter non-compensation effects and energy deposits in the non-instrumented parts of the detector. The relative resolution can be parametrized using the following function [137]:

$$\frac{\sigma(p_T)}{p_T} = \frac{N}{p_T} \oplus \frac{S}{\sqrt{p_T}} \oplus C, \tag{6.22}$$

where $\frac{N}{p_T}$ is the so-called noise term, $\frac{S}{\sqrt{p_T}}$ the stochastic term, and C the constant term. The noise term is expected to be significant in the low-p_T regime up to 30 GeV and comprises electronics noise, detector noise and contributions from pile-up activity. The stochastic term, which describes the impact of statistical fluctuations on the resolution, is dominant in the region between 30 GeV and 400 GeV. The constant term is the limiting factor in the high-p_T region above approximately 400 GeV and encompasses the dependence of the jet response on η, energy losses due to non-instrumented calorimeter regions, etc. The function given in Eq. 6.22 reflects the determined curvature of the relative resolution and is used in order to evaluate $\sigma(p_T)/p_T$ for a given jet p_T. For instance, the relative p_T resolution for jets, which are reconstructed using the distance parameter $R = 0.6$ and are calibrated with the LCW+JES scheme, is parametrized as follows[15]: $N = 5.79$, $S = 0.69$, and $C = 0.03$.

In order to estimate the relative m_{jj} resolution and the absolute η resolution, jets reconstructed at detector-level were compared to jets at particle-level. The technique is described in the previous part of this sub-section. The relative m_{jj} resolution as function of m_{jj} is shown in Fig. 6.22 (left). $\sigma(m_{jj})/m_{jj}$ as function of m_{jj} has a similar shape compared to $\sigma(p_T)/p_T$ as function of p_T and can also be described using Eq. 6.22. This is indicated by the red line in this figure. The relative resolution amounts to 5% at $m_{jj} = 1$ TeV and decreases to around 4% at $m_{jj} = 3$ TeV. By analogy with m_{jj} the relative η resolution was determined by using pseudorapidities η of jets at detector- and particle-level. The absolute η resolution as function of p_T for jets pointing to the central-region of the detector is shown in Fig. 6.22 (right). The minimum relative resolution is achieved at around 1 GeV and increases with increasing p_T.

[15]Numbers were taken from the ATLAS jet resolution tool version 'JetResolution-01-00-00'.

7 Systematic Uncertainties

The jet energy scale (JES) calibration methods are introduced in Sec. 5.4 and in Sec. 6.3. In this chapter the uncertainties due to the JES calibration procedure are briefly summarized. This summary is based on the information published in Ref. [113]. The systematic uncertainties are covered by a set of 63 components, which are listed in Tab. 7.1. JES uncertainties were determined by varying the selection cuts and comparing resulting response ratios in data and MC simulations. Uncertainties due to selection, modeling of the reference objects, and calibration are included as well. Only statistically significant differences between data and MC are taken as systematic uncertainties. In case of a non-significant deviation bins are combined iteratively to reduce the statistical uncertainty. This treatment reduces the contribution of statistical uncertainties to systematic uncertainties. Approximately half of the JES uncertainty components are statistical uncertainties of the in-situ calibration methods.

7.1 Relative Forward Jet Calibration

The η-intercalibration technique is described in Sec. 6.3.1. This method is used to propagate the calibration and uncertainties to the forward region. Several systematic uncertainties are considered in this context. The dominant uncertainty component of the η-intercalibration method is due to the large deviation between the predictions using Pythia and Herwig++ in the more forward region. Additionally negligible systematic uncertainties due to the modeling of the relative jet p_T-resolution, the trigger strategy, and the selection criteria of the dijet topology were studied. The uncertainty from this source is dominant in the more forward region above $\eta \approx 1.5$. For jets with transverse momenta of 25 GeV it amounts to approximately 2.5% at $\eta = 2.5$ with no contributions in the central pseudorapidity region up to $\eta = 1.2$. For jets with $p_T = 300$ GeV it is around 2% at $\eta = 2.5$.

7.2 Z-jet Balance

The Z-jet balance calibration method is described in Sec. 6.3.2. The individual contributions to the uncertainty from this source are summarized in the following:

- The uncertainty due to the electron energy scale was estimated by shifting the energy of the electron up and down according to the uncertainty evaluated in Ref. [112].

- To reduce the bias due to additional parton radiation, $\Delta\phi(\text{jet}, Z)$ was extrapolated to $\Delta\phi = \pi$. The uncertainty on the extrapolation procedure was estimated by applying the procedure for different fit ranges.

Name	Description
Common sources	
Electron/photon E scale	Electromagnetic energy scale
Z-jet p_T balance (DB)	
MC generator	MC generator difference between Alpgen/Herwig and Pythia
Radiation suppression	Radiation suppression due to second jet cut
Extrapolation	Extrapolation in $\Delta\phi(\text{jet}, Z)$ between jet and Z boson
Pile-up jet rejection	Jet selection using jet vertex fraction
Out-of-cone	Contribution of particles outside the jet cone
Width	Width variation in Poisson fits to determine jet response
Statistical components	Statistical uncertainty for each of the 11 bins
γ-jet p_T balance (MPF)	
MC Generator	MC generator difference Herwig and Pythia
Radiation suppression	Sensitivity to radiation suppression second jet cut
Jet resolution	Variation of jet resolution within uncertainty
Photon Purity	Background response uncertainty and photon purity estimation
Pile-up	Sensitivity to pile-up interaction
Out-of-cone	Contribution of particles outside the jet cone
Statistical components	Statistical uncertainty for each of the 12 bins
Multijet p_T balance	
α selection	Angle between leading jet and recoil system
β selection	Angle between leading jet and closest sub-leading jet
Dijet balance	Dijet balance correction applied for $\lvert\eta\rvert < 2.8$
Close-by, recoil	JES uncertainty due to close-by jets in the recoil system
Fragmentation	Jet fragmentation modelling uncertainty
Jet p_T threshold	jet p_T threshold
p_T asymmetry selection	p_T asymmetry selection between leading jet and sub-leading jet
UE,ISR/FSR	Soft physics effects modelling: underlying event and soft radiation
Statistical components	Statistical uncertainty for each of the 10 bins
Other components	
η-intercalibration	Propagation of calibration and uncertainties to the forward region
Single hadron response	Single particle response uncertainty propagated to the jet-level
Pile-up	Additional uncertainty due to pile-up correction
Close-by	Additional uncertainty from close-by jets
Flavor composition	Quark vs. gluon composition difference between Pythia and Herwig
Flavor response	Quark vs. gluon response difference between Pythia and Herwig

Table 7.1: Summary of the different jet energy scale uncertainty components discussed in this chapter. [113]

- The uncertainty due to pile-up was estimated by relaxing the JVF cut on the leading jet. The difference between the variation and the nominal result was taken as systematic uncertainty.

- The transverse momentum p_T^Z of the Z-boson is used as the reference for the jet calibration. However, this is only an approximation of the truth jet p_T^{truth} due to out-of-cone radiation and underlying event (UE). The former effect is due to the limited cone size of the truth jet, where not all particles recoiling from the Z might be included. The latter is hardly affecting p_T^Z of the Z-boson, but the transverse

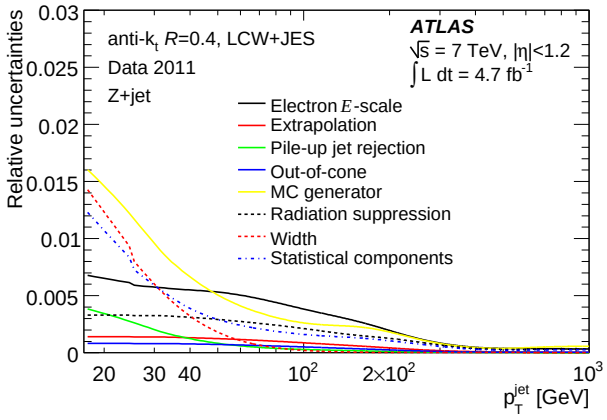

Figure 7.1: Uncertainty components introduced by the Z-jet in-situ calibration method [113].

momentum p_T^{jet} of the jet due to particles originating from the UE. In order to estimate the impact of these effects the measure k_{OOC}[1] was introduced exploiting track jets. For jets reconstructed using the distance parameter $R = 0.4$, k_{OOC} is around 0.93 in the low-p_T and 0.99 in the high-p_T region. For jets found with $R = 0.6$, it is around unity independent of p_T. The uncertainty due to out-of-cone effects and UE is estimated by changing the transverse momentum p_T^Z of the Z-boson with the factor k_{OOC}. The altered data-to-MC ratio is compared to the nominal ratio and the difference is taken as systematic uncertainty.

- The uncertainty due to the choice of the MC generators was studied using Pythia and Alpgen [138]. This was estimated as the difference between the data-to-Pythia and data-to-Alpgen ratios.

- To reduce additional radiation effects not corrected by the $\Delta\phi(\text{jet}, Z)$ extrapolation procedure, events were rejected, where the transverse momentum $p_{T,\text{jet2}}$ of the second-leading jet exceeds a threshold. An uncertainty was estimated by varying this threshold up and down.

- In order to determine the mean of the ratio $p_T^{\text{jet}}/p_T^{\text{ref}}$ a fit was performed for $p_T^{\text{ref}} < 35$ GeV. The sensitivity of the fit to statistical fluctuations was reduced by fixing the width of the fit function. The uncertainty due to this fitting procedure was estimated by varying the width up and down.

The relative uncertainty for the individual components is exemplary shown in Fig. 7.1 for jets reconstructed using the distance parameter $R = 0.4$. The dominant component in the low-p_T regime is the uncertainty due to the choice of the MC generator. The relative uncertainty due to the electron energy scale dominates in the jet transverse momentum region above 50 GeV. It amounts to approximately 0.5% at 60 GeV and decreases as p_T increases. In the transverse momentum regime above 400 GeV all uncertainty components from this source are negligible.

[1] k_{OOC} is defined as $k_{\text{OOC}} = p_T^{\text{IC, ALL}}/(p_T^{\text{IC+OC, ALL}} - p_T^{\text{IC+OC, UE}})$, where $p_T^{\text{IC, ALL}}$ is the average scalar p_T sum of all tracks inside (IC) a jet cone with radius R, $p_T^{\text{IC+OC, ALL}}$ is the average scalar p_T sum of all tracks inside and outside (OC) the cone, and $p_T^{\text{IC+OC, UE}}$ is the average contribution from UE to $p_T^{\text{IC+OC, ALL}}$.

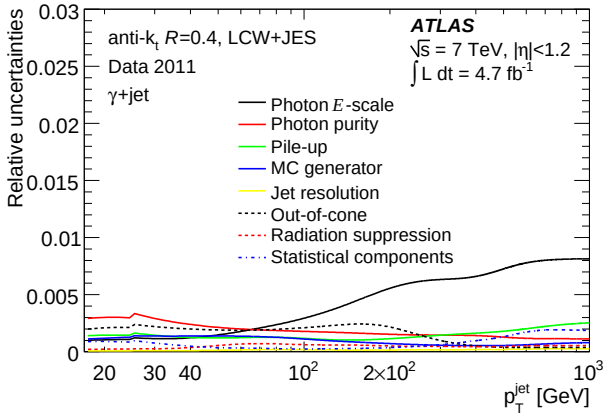

Figure 7.2: Uncertainty components of the γ-jet in-situ calibration technique [113].

7.3 γ-jet Balance

The γ-jet balance method exploits the transverse momentum balance between a jet and a photon and is described in Sec. 6.3.2. The uncertainty components from this source are summarized in the following:

- The energy of electrons is calibrated exploiting $Z \to e^+e^-$ decays. The photon energy was also corrected using the electron energy calibration. Due to the differences of the photon energy scale compared to the electron energy scale, the systematic uncertainty is increased in case of photons. The photon energy scale uncertainty was propagated to the jet response.

- The uncertainty due to jets that are misidentified as photons was estimated by calculating responses using two different Pythia MC samples: the default γ-jet sample and the inclusive jet samples enriched with narrow jets, which has a higher probability to be identified as photons.

- To determine the impact of pile-up on the γ-jet analysis, the response of different types of events was compared. In order to cover in-time pile-up, the events were separated using the reconstructed number of primary vertices: $N_{\mathrm{PV}} \leq 2$ and $N_{\mathrm{PV}} \geq 6$. Furthermore, the effect of out-of-time pile-up was estimated using the average number of interactions per bunch-crossing μ_{avg}. Two different out-of-time pile-up samples were selected: $3.5 < \mu_{\mathrm{avg}} < 5.5$ and $\mu_{\mathrm{avg}} > 7$. The uncertainty on pile-up was estimated as the maximum difference of the responses obtained from the four event samples.

- The uncertainties due to the modeling of parton shower, fragmentation and MPI are evaluated using two different MC generators: Pythia and Herwig++. The difference between the two responses are used as systematic uncertainty.

- The measurement of the jet p_T resolution using data and MC is described in Sec. 6.5. The uncertainty on the resolution was propagated using the method detailed in Sec. 8.4.2. The difference between the nominal response and the response obtained with the degraded resolution is taken as systematic uncertainty.

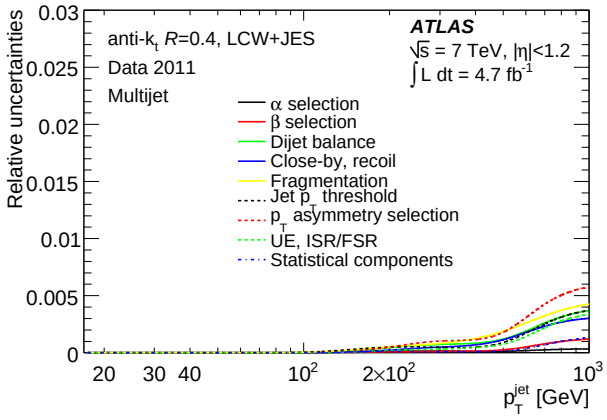

Figure 7.3: Uncertainty components of the multijet balance in-situ calibration method [113].

- The largest impact on the p_T balance is due to the UE, which adds additional energy to the jet, and out-of-cone radiation. This uncertainty was estimated by analogy with the Z-jet analysis.
- The effect of soft radiation to the data-to-MC response ratio was evaluated by varying the p_T cut of the second leading jet and $\Delta\phi(\text{jet}, \gamma)$ resulting in two different events samples which were compared to the data-to-MC response ratio produced with the nominal sample.

The relative uncertainty components as function of the jet transverse momentum p_T are shown in Fig. 7.2. In the low-p_T region below 50 GeV the uncertainty due to the photon purity is dominant. In the region above 50 GeV the dominant component is the uncertainty due to the photon energy scale, which is around 0.8% at 1 TeV. The second dominant uncertainty component in the high-p_T region is due to the impact of pile-up.

7.4 Multijet Balance

The multijet balance (MJB) method is used for the absolute jet calibration and is described in Sec. 6.3.3. The uncertainty components are briefly summarized in the following:

- The relevant selection cuts were varied individually and the ratio of MJB between data and MC was determined. In order to estimate the uncertainty due to event selection cuts, this ratios determined with modified cuts were compared to the default selection.
- The uncertainty due to close-by jets was incorporated, which has an impact on jets within the recoil-system. The impact of close-by jets is discussed in Sec. 7.8.
- In order to evaluate the impact of the mis-modeling of fragmentation the Herwig++ generator was used. This systematic uncertainty was estimated by comparing to Pythia MC results.
- To obtain the uncertainty due to ISR/FSR and UE, MJB predicted using the default MC was compared to that determined using Pythia with the Perugia2011 UE tune.

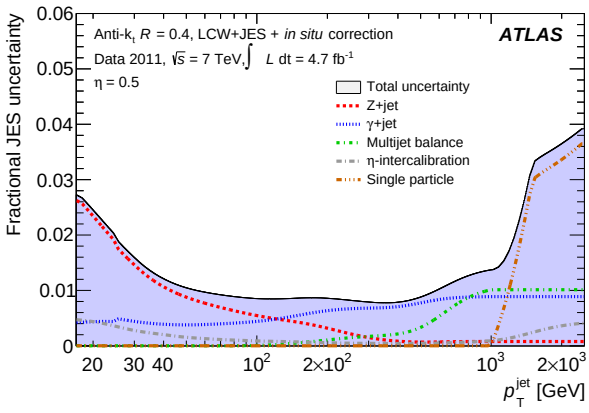

Figure 7.4: The individual contributions to the total uncertainty from different calibration techniques in the central rapidity region: Z-jet (cf. Sec. 7.2), γ-jet (cf. Sec. 7.3), Multijet balance (cf. Sec. 7.4), and single particle response [113].

- The reference transverse momentum of jets forming the recoil-system is calibrated using the in-situ γ-jet and Z-jet methods as well as the η-intercalibration technique. Therefore different contributions to the uncertainty due to the absolute JES calibration were propagated. The JES of the non-leading jets is also affected by the uncertainty on the η-intercalibration, which provides a relative calibration. The propagation of the individual uncertainty components was performed by varying the jet energy and momentum scale of the reference jets.

The uncertainty components from this source are exemplary shown in Fig. 7.3. The uncertainties are negligible in the low-p_T regime and increases with increasing transverse momentum of the jet. The dominant uncertainty is due to the p_T asymmetry selection and is approximately 0.6% at $p_T^{\text{jet}} = 1$ TeV.

7.5 Single Hadron Response

Due to the low statistical significance of the in-situ techniques above 1 TeV, the JES uncertainty derived exploiting the single particle response measurement was used for jets with a transverse momentum of $p_T > 1$ TeV. The uncertainty on the response to jets is determined for jets reconstructed in the central region within $|\eta| < 0.8$. The single particle energy response uncertainty was determined exploiting various measurements and comparing data and MC predictions.

For low-momentum particles the ratio between the calorimeter energy deposition E and the momentum p of the corresponding isolated track was measured using data from ATLAS. In case of higher particle momenta, the Combined Test Beam (CTB) measurements were included. For this purpose a slice of the central region of ATLAS was exposed to single charged pions with momenta of up to 350 GeV. Due to the fact that not exactly the same calorimeter was used for CTB measurements additional uncertainties covering the differences were taken into account [139]. On average around 10-12% of the jet energy is carried by neutral hadrons as e.g. K_S, K_L and neutrons. In case of K_S which mainly decay into pions before reaching the calorimeter the CTB and E/p measurements were

used. For the other neutral particles no test beam measurements are available and the GEANT4 simulation with different hadronic physics models were compared to the default ATLAS model (cf. Sec. 4.2.8) to determine the uncertainty. In case of single particle momenta $p > 400$ GeV, no in-situ and direct test beam measurements are available. In order to account for potential effects due to non-linearities at high-energy densities and longitudinal leakage, an additional 10% uncertainty was convolved with the uncertainty determined at 350 GeV [140]. For particles not covered by the measurements mentioned above which deposited energy in the LAr calorimeters as e.g. π^0, the uncertainty on the electromagnetic energy scale calibrated in-situ using $Z \to e^+e^-$ events was used. This uncertainty amounts to around 1.5%. For particles with momenta $p > 20$ GeV, which deposit energy in the hadronic calorimeter and are not covered by the CTB measurements, an uncertainty of 3% is used [141].

The MC simulation provides the constituents and their contribution to the total energy of the jet. Therefore MC is used to propagate the single particle energy response uncertainty of the individual jet constituents to uncertainty on the JES. For this purpose pseudo-experiments were performed by changing the single particle energy response according to the corresponding uncertainty. The width of the resulting JES distribution is taken as the final JES uncertainty. Additional effects, which potentially affect the propagation were also taken into account. In order to determine the total uncertainty in the high-p_T regime, the uncertainties of the in-situ absolute calibration methods were fixed at $p_T = 1$ TeV and subtracted in quadrature from the single hadron response uncertainty for jets with $p_T > 1$ TeV. The contributions to the total uncertainty from the single hadron response and the individual in-situ calibration techniques discussed in previous sub-sections are shown in Fig. 7.4. The single hadron response uncertainty is the dominant contribution in the high-p_T regime and amounts up to 4% in the central rapidity region.

7.6 Pile-Up Correction

The MC based correction of the reconstructed jet p_T for pile-up effects is detailed in Sec. 5.4.1. As reference objects jets at particle-level were taken. To estimate the systematic uncertainty on the correction for pile-up effects, pile-up independent reference objects were used: photons in γ-jet events and track jets. The photon transverse momentum p_T^γ is used as reference quantity exploiting the transverse momentum balance. Additionally track jets originating from the primary vertex were used to evaluate this systematic uncertainty component, because track jets were shown to be insensitive to pile-up. The total systematic uncertainty due to pile-up is estimated from the difference of the pile-up correction O derived using data and MC:

$$\Delta O = O(N_{\mathrm{PV}}, \mu_{\mathrm{avg}})|_{\mathrm{data}} - O(N_{\mathrm{PV}}, \mu_{\mathrm{avg}})|_{\mathrm{MC}},$$

where N_{PV} is the number of primary vertices and μ_{avg} the average number of interactions per bunch-crossing. The combined uncertainty from the considered in-situ techniques, was calculated as a weighted RMS of ΔO. In the central region the pile-up uncertainty is less than 1% as function of N_{PV} and μ_{avg} in the covered phase-space and is larger in the very forward region. A detailed discussion is given in Ref. [142].

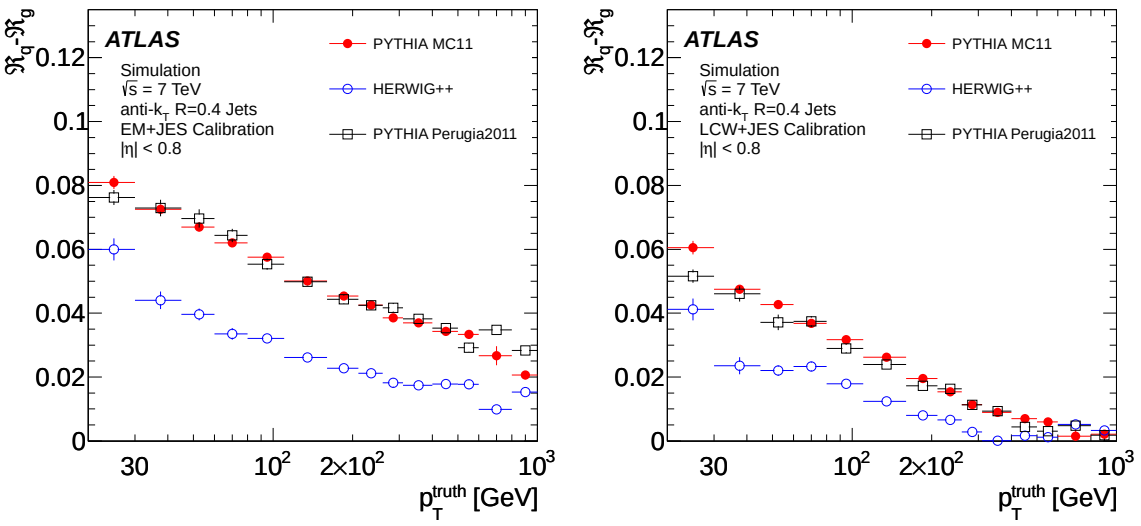

Figure 7.5: Jet response difference $\Delta\mathcal{R} = \mathcal{R}_q - \mathcal{R}_g$ between light-quarks and gluons as function of jet transverse momentum at particle-level. It is shown for three different MC simulation samples for EM+JES (left) and LCW+JES (right) calibrated jets. [113]

7.7 Flavor Composition and Response

The probability for a gluon initiated jet to contain more particles is higher compared to a light-quark jet[2]. As a consequence the average transverse momentum p_T of the particles within a gluon jet is lower. Additionally, the energy distribution within the jet is broader in case of gluon jets. Due to the higher average p_T of particles within light-quark jets the depth of the shower tends to be larger and therefore the probability to reach the hadronic calorimeter system is higher. The response of gluon jets is lower compared to the light-quark jets. This is due to the fact that the response of the calorimeter to low-p_T particles is lower. Therefore the JES is affected by this effect. Jets reconstructed using the distance parameter $R = 0.4$ are more sensitive to the initial flavor than $R = 0.6$ jets, because of the larger area covered and thus less energy is loss in case of broader jets.

The response of calibrated jets is around unity after the application of calibration techniques detailed in Sec. 5.4 and in Sec. 6.3. The flavor dependence was studied using MC, where the information on the final state partons are available. In data the flavor studies were performed for the purpose of validation using the inclusive jet, γ-jet and Z-jet analyses. The impact of the jet flavor on the JES was studied using light-quark and gluon tagging methods described in Ref. [143]. Fig. 7.5 shows the difference between the responses to light-quark jets and gluon jets $\Delta\mathcal{R} = \mathcal{R}_q - \mathcal{R}_g$ jets as function of particle-level jet p_T^{truth} for different MC simulation samples. The jets were reconstructed using the anti-k_t algorithm with the distance parameter $R = 0.4$ for the EM+JES (left) and LCW+JES (right) calibration scheme. The response difference ΔR is around 8% in the low-p_T region and decreases with increasing p_T. Jets calibrated using the LCW+JES scheme are less dependent to the initial parton flavor, because this scheme utilizes shower

[2]The flavor of jets is categorized in light quarks and gluon in this context. The light-quark initiated jets originate from u-,d-, or s-quarks.

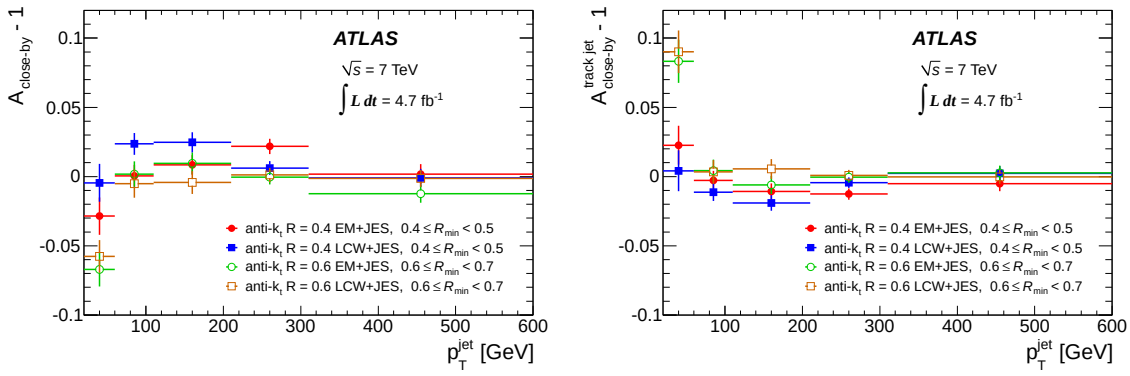

Figure 7.6: Data-to-MC ratios $A_{\text{close-by}}$ (left) and $A^{\text{track jet}}_{\text{close-by}}$ (right) as function of the jet transverse momentum p_T^{jet}. The distributions were determined using different calibration schemes and jet distance parameters. [113]

variables as discussed in Sec. 5.2 .

The uncertainty is determined using differences obtained using different MC samples. The impact on the response difference ΔR due to the choice of the UE tune was estimated using Pythia interfaced with two different UE tunes. The largest impact on ΔR can be observed due to the modeling of the parton shower and fragmentation, which was estimated using two different MC generators: Pythia 6 and Herwig. In the analyses presented in this thesis, the flavor composition was assumed to be unknown. That means, the probability to find a light-quark or a gluon is 50%. This assumption was chosen to provide the most conservative estimate of the corresponding JES components.

7.8 Close-by Jets

To study the impact on the jet energy response due to the presence of nearby jets, track jets originating from the primary primary vertex were exploited as reference objects, which were matched to the closest calorimeter jet within the distance of $\Delta R < 0.3$. The uncertainty was estimated using data and MC simulation.

The estimate on the total close-by JES uncertainty consists of two components, which are added in quadrature. In order to determine the first component the relative response r is defined as follows:

$$r = p_T^{\text{jet}} / p_T^{\text{track jet}}. \tag{7.1}$$

The relative response was determined in bins of R_{min}, which is defined as the distance between the matched calorimeter jet and the closest other jet with $p_T > 7$ GeV at the EM scale. The response defined in Eq. 7.1 was determined for non-isolated calorimeter jets with $R_{\text{min}} < 2.5 \times R$ as well as for isolated jets with $R_{\text{min}} > 2.5 \times R$, where R is the anti-k_T distance parameter. To estimate the uncertainty the data-to-MC ratio $A_{\text{close-by}}$ was defined as follows:

$$A_{\text{close-by}} = \frac{r^{\text{non-iso/iso}}|_{\text{data}}}{r^{\text{non-iso/iso}}|_{\text{MC}}}, \tag{7.2}$$

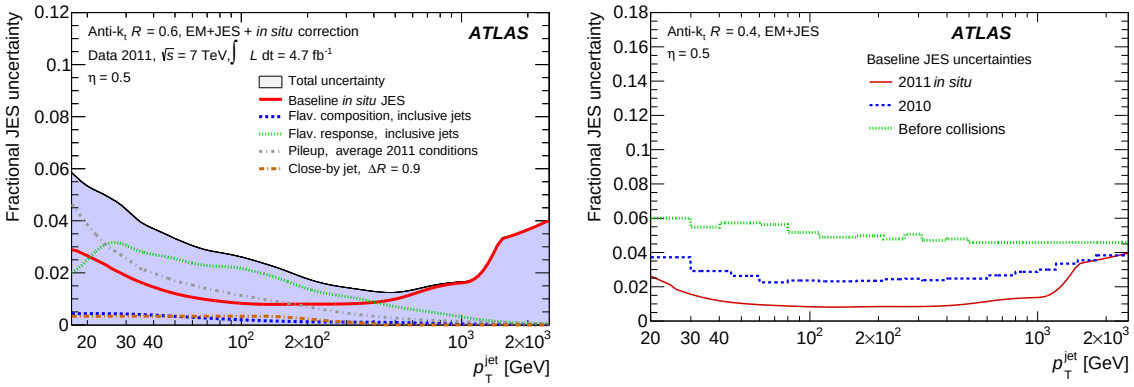

Figure 7.7: Left: relative JES uncertainty as function of p_T for different components in the central pseudorapidity region $\eta = 0.5$. Right: comparison of the total in-situ JES uncertainty obtained using 2010 data (blue dotted) and 2011 data (red) in the central pseudorapidity regime. The green line indicates the uncertainty estimated before LHC collision data. The jets were reconstructed using the distance parameter $R = 0.4$. [113]

where $r^{\text{non-iso/iso}} = r^{\text{non-iso}}/r^{\text{iso}}$ is the ratio between the response $r^{\text{non-iso}}$ obtained for a non-isolated condition and the response r^{iso} for isolated jets. The second uncertainty component is due to the behavior of the track jet response in presence of a nearby jet. In order to determine this uncertainty the ratio $A^{\text{track jet}}_{\text{close-by}}$ was defined as follows:

$$A^{\text{track jet}}_{\text{close-by}} = \frac{p_T^{\text{non-iso}}/p_T^{\text{iso}}|_{\text{data}}}{p_T^{\text{non-iso}}/p_T^{\text{iso}}|_{\text{MC}}}, \tag{7.3}$$

where p_T is the average track jet transverse momentum in case of isolated (p_T^{iso}) and non-isolated ($p_T^{\text{non-iso}}$) track jets. By analogy with the data-to-MC ratio defined in Eq. 7.2, $A^{\text{track jet}}_{\text{close-by}}$ was determined in bins of the calorimeter jet p_T in slices of R_{min}.

The ratios defined in Eq. 7.2 (left) and Eq. 7.3 (right) as function of the jet p_T for different calibration schemes and jet definitions are shown in Fig. 7.6. The largest total close-by uncertainty of about 10% at $R_{\text{min}} < 0.7$ can be observed for jets at low-p_T reconstructed using the distance parameter $R = 0.6$. The uncertainty decreases with increasing jet p_T and is smaller for $R = 0.4$ jets. For distances of $R_{\text{min}} > 0.8$ the total close-by jet uncertainty is less than 1%. A more detailed description of this approach is given in Ref. [117, 113].

7.9 Combined Jet Energy Scale Uncertainty

The individual sets of components contributing to the total jet energy scale uncertainty are summarized in Sec. 7.1 - Sec. 7.8. and are exemplary shown in Fig. 7.7 (left). In this figure the relative uncertainties in the central pseudorapidity regime at $\eta = 0.5$ for jets reconstructed using the anti-k_T algorithm with $R = 0.4$ at EM+JES scale are shown. In the low-p_T region, the uncertainty due to the flavor response is the dominant contribution to the total JES uncertainty. In the high-p_T regime above transverse momenta of approxim-

ately 400 GeV, the contribution from in-situ calibration techniques dominates. The total uncertainty is up to 6% in the low-p_T regime and 4% in the high-p_T regime. A similar picture is obtained for jets reconstructed using the distance parameter $R = 0.6$ and for jets using LC weighed input for calibration. In the more forward region the uncertainty from the in-situ calibration is dominant in the entire p_T region. At $\eta = 2.0$ the total JES uncertainty is up to 7% in the low-p_T regime and 2% for $p_T = 1$ TeV. In Fig. 7.7 (right) the total JES uncertainty from in-situ techniques is shown for data sets recorded in 2010 (blue) and 2011 (red). The green line shows the uncertainty estimate before collision data was available. As can be observed from this figure, the in-situ uncertainty is improved up to jet transverse momenta of approximately 1.2 TeV. In the high-p_T region the same method was used to estimate the uncertainty an thus no improvements were made in this regime compared to the analysis performed in 2010.

7.10 Resolution

The relative energy resolution was determined using methods described in Sec. 6.5. For the dijet balance technique the total uncertainty consists of differences in resolution for various $\Delta\phi$ cuts (around 3% at $p_T = 60$ GeV) and uncertainties from differences in the modeling of soft radiation (up to 6% at $p_T = 30$ GeV). The uncertainty on the assumption $\sigma_{\Psi}^{\text{part}} = \sigma_{\eta}^{\text{part}}$ in case of the bi-sector method, were obtained by varying the $p_{T,\text{jet3}}$ cut. The dependence of the p_T resolution due to the jet energy scale uncertainties was shown to be within 1-2%. The overall uncertainty from in-situ techniques is around 4% at $p_T =$ 500 GeV. Due to the non-closure between the resolution modeled in MC and that obtained from data, an additional uncertainty of 10% was added in quadrature. The resolution using the 'truth' method was determined for different generator models, tunes and cut-off parameters with a maximum deviation of 4% in resolution. The total uncertainty from these sources was calculated as sum of individual contributions in quadrature. In addition to the jet energy resolution, the angular resolution was determined in Sec. 6.5. The uncertainty on the angular resolution was estimated using in-situ techniques and amounts to approximately 10% [144].

8 Jet Cross Section Measurement

Jets produced via QCD processes have orders of magnitude larger cross-section compared to other physics processes. The inclusive jet transverse momentum and dijet mass double-differential cross-sections were measured using the 2011 collision data at center of mass energies of 7 TeV delivered by the LHC. The total integrated luminosity collected by the ATLAS detector used in this analysis is $L = (4.51 \pm 0.08)\ \mathrm{fb}^{-1}$. In case of the inclusive jet analysis, the jet transverse momenta ranges between 100 GeV and 2 TeV covering absolute values of the jet rapidity between 0 and 3. The dijet analysis covers a dijet mass region between 260 GeV and 5040 GeV in the rapidity separation regime between 0 and 2.5. The comparison between theoretical predictions and the measurement probes QCD. In this chapter the cross-section measurements are presented. These analyses were performed independently and parallel to the official ATLAS analyses, which were published in Ref. [126] and Ref. [145]. The analyses in context of this thesis were used for cross-check purposes and important contributions to the ATLAS analyses.

8.1 Measured Quantities

The inclusive jet p_T and dijet double-differential cross-sections[1] are defined as follows:

$$\frac{d^2\sigma}{dp_T dy} = \frac{1}{L}\frac{N_{\mathrm{jets}}(p_T, y)}{\Delta p_T \Delta y} \tag{8.1}$$

$$\frac{d^2\sigma}{dm_{12} dy^*} = \frac{1}{L}\frac{N_{\mathrm{evts}}(m_{12}, y^*)}{\Delta m_{12} \Delta y^*}. \tag{8.2}$$

In Eq. 8.1, $N_{\mathrm{jets}}(p_T, y)$ is the number of jets in a given p_T and y bin, Δp_T and Δy are the corresponding bin widths, and L is the integrated luminosity. In Eq. 8.2, $N_{\mathrm{evts}}(m_{12}, y^*)$ is the number of events in a given m_{12} and y^* bin with the corresponding bin widths Δm_{12} and Δy^*. As described in Sec. 6.2 the triggers were down-scaled due to the limited bandwidth and large jet cross-sections in the low-p_T regime. Therefore the number of jets $N_{\mathrm{jets}}(p_T, y)$ and the number of events $N_{\mathrm{evts}}(m_{12}, y^*)$ in Eq. 8.1 and 8.2 were determined by correcting the measured number of jets and events using the corresponding trigger down-scale factors. Technically, each jet and each event was weighted with the reciprocal of the down-scale corrected integrated luminosity L_t derived for each trigger or trigger pair. In case of the inclusive jet analysis L_t^{incl} was calculated as follows:

$$L_t^{\mathrm{incl}} = \sum_i^{N_{\mathrm{LB}}} \frac{\mathcal{L}_i \cdot \Delta t_i}{d_{t,i}}, \tag{8.3}$$

[1] In this chapter the expression *cross-section measurement* is used as a synonym for both, the inclusive jet p_T and dijet mass double-differential cross-section measurement.

where N_{LB} is the total number of luminosity blocks (LB) considered, $\mathcal{L}_i$ is the instantaneous luminosity measured for each LB i, Δt_i is the duration of the LB i, and d_{ti} is the down-scale factor for each LB i and trigger t. To combine triggers, the covered p_T space was divided into distinct regions. Each trigger was associated with a p_T slice with boundaries chosen to reduce statistical uncertainties and to avoid the necessity of correcting for trigger inefficiencies (cf. Sec. 6.2). A jet was included in the spectra if the decision of the corresponding trigger was positive. In case of the dijet analysis both leading jets were used to derive the trigger decision for each event. An event contributed to the cross-section spectra, if the trigger corresponding to the leading or the second-leading jet has fired. This approach reduces the statistical uncertainty in scenarios where both leading jets were associated with down-scaled triggers. Thus the down-scale corrected integrated luminosities L_t^{dijet} for a given trigger pair t is calculated as follows (cf. Sec. 6.2):

$$L_t^{\mathrm{dijet}} = \sum_i^{N_{\mathrm{LB}}} \frac{\mathcal{L}_i \cdot \Delta t_i \cdot (d_{t_1 i} + d_{t_2 i} - 1)}{d_{t_1 i} \cdot d_{t_2 i}}, \tag{8.4}$$

where $d_{t_1 i}$ and $d_{t_2 i}$ are the down-scale factors of triggers associated with the leading and second-leading jet in LB i, respectively. In order to connect triggers and jets the same method and p_T-slice configuration as used in the inclusive jet analysis was applied. The components N_{LB}, $\mathcal{L}_i$, and Δt_i are equal to the quantities discussed in context of Eq. 8.3. Eq. 8.4 holds for trigger pairs where $t_1 \neq t_2$. In cases, where $t_1 = t_2$, Eq. 8.3 was used to calculate L_t^{dijet}. The total number of luminosity blocks N_{LB} is approximately $61 \cdot 10^3$. This corresponds to a total data-taking duration of around 1000 hours. The trigger selection is the last step in the event and jet selection procedure, which is discussed in the next section.

8.2 Event and jet selection

To ensure the quality of the events and jets contributing to the cross-section spectra, a set of cuts was applied to the collision data and to Monte Carlo simulation in an analogous way. Topological clusters were used as input for the anti-k_t jet clustering algorithm with distance parameters $R = 0.4$ and $R = 0.6$. Calibrated jets at LC scale were used in this analysis. The calibration methods are described in Sec. 5.4 and Sec. 6.3. In the following the event and jet selections are briefly discussed. The cuts are summarized in Tab. 8.1 and Tab. 8.2. These tables provide detailed information on the number of rejected events and jets in data using jets reconstructed with $R = 0.6$. The remaining jets and events were used to construct the final inclusive jet and dijet mass spectra, respectively.

Data quality: The data quality assessment procedure is summarized in Sec. 6.1.1. It was required that important detector components which are essential for the jet measurements were functioning properly. Events recorded in presence of problems in essential detector components were rejected. This selection is used in context of data only.

Pile-up cut: As described in Sec. 6.4.1 and App. A.3 the MC simulation is split into sub-samples with different weights. This treatment ensures a low statistical uncertainty in high-p_T (-m_{12}) regions. The pile-up is simulated in MC, which might lead to jets at detector-level which have a p_T much greater compared to the p_T of the initial parton- or

Event selection (A)	N_{evts}	f_{total}	r_{prev}
Total number of events	431277638	100%	
Data quality	400583113	92.9%	7.1%
LAr noise burst and corrupted data	399290017	92.6%	0.3%
Vertex selection	392127137	90.9%	1.8%
Jet selection (B)	N_{jets}	f_{total}	r_{prev}
Total number of jets after (A)	5192228790	100.0%	
Kinematic selection: $\lvert y\rvert < 3.0$	4469721703	86.1%	13.9%
Kinematic selection: $p_T \geq 50$ GeV	692439261	13.3%	84.5%
Jet quality: MEDIUM scheme	680397977	13.1%	1.7%
Non-operational cells and non-instrumented regions	680390272	13.1%	< 0.1 %
LAr calorimeter issue	665624994	12.8%	2.2 %
Trigger selection	3700670	0.7‰	99.4%
Number of events after trigger selection	2849914		

Table 8.1: List of cuts used in context of the inclusive jet analysis applied on data. The cut set is subdivided in an event selection (A) and jet selection (B). The individual cuts are discussed in Sec. 8.2. The trigger selection is briefly discussed in Sec. 8.1. N_{evts} (N_{jets}) is the number of remaining events (jets) after the application of a cut. f_{total} is the fraction of N_{evts} (N_{jets}) with respect to the total number of events (jets). The quantity r_{prev} is the fraction of rejected events (jets) with respect to the remaining number of events (jets) after the application of the previous cut. The jets were reconstructed using the anti-k_t algorithm with distance parameter $R = 0.6$.

particle-level jet. This can introduce spikes with large statistical uncertainties due to the MC re-weighting procedure. The criteria used to identify this type of events is described in Sec. 6.4.1. It is the first step in the event selection procedure applied on MC simulation. To get the correct cross-section at detector-level the total number of events, which is needed to calculate the weights, was counted after the application of these cuts.

LAr noise burst and corrupted data: The LArError-flag was introduced in Sec. 6.1.2. It indicates noise bursts and data integrity errors and was applied on data only.

Vertex selection: The collision candidates were selected by requiring the presence of at least one reconstructed primary vertex which is consistent with the position of the collision point and which has at least two associated charged particle tracks with a reconstructed $p_T > 400$ MeV. This requirement removes contributions from beam-backgrounds like contributions from beam-gas collisions and other non-collision sources [117].

Kinematic selection: All calibrated jets at detector-level below 50 GeV were excluded from the inclusive jet and dijet analyses. Because of the impact of out-of-time pile-up on the inclusive jet measurement in the region between 50 GeV and 100 GeV (cf. App. A.4) for jets reconstructed with the distance parameter $R = 0.6$, the final results at particle-level are derived for jets transverse momenta above $p_T \geq 100$ GeV. Nevertheless, to account for bin-by-bin migrations in the unfolding procedure, all spectra were

Event selection (A)	N_{evts}	f_{total}	r_{prev}
Total number of events	431277638	100%	
Data quality	400583113	92.9%	7.1%
LAr noise burst and corrupted data	399290017	92.6%	0.3%
Vertex selection	392127137	90.9%	1.8%
Jet selection (B)	N_{jets}	f_{total}	r_{prev}
Total number of jets after (A)	5192228790	100.0%	
Kinematic selection: $\lvert y\rvert < 3.0$	4469721703	86.1%	13.9%
Kinematic selection: $p_T \geq 50$ GeV	692439261	13.3%	84.5%
Event selection (C)	N_{evts}	f_{total}	r_{prev}
Total number of events after (B)	308466800	100.0%	
Jet multiplicity	230843411	74.8%	25.2%
Kinematic selection: $p_{T,\text{jet1}} > 100$ GeV	165108316	53.5%	28.5%
Jet quality: MEDIUM scheme	162955174	52.8%	1.3%
Non-operational cells and non-instrumented regions	162954230	52.8%	< 0.1 %
LAr calorimeter issue	142966301	46.3%	12.3%
Trigger selection	2105650	0.7%	98.5%

Table 8.2: List of cuts used for the event and jet selection in case of the dijet analysis applied on data. The cut set is subdivided in an event selection (A), jet selection (B) and event selection (C). The individual cuts are discussed in Sec. 8.2. The trigger selection is briefly discussed in Sec. 8.1. N_{evts} (N_{jets}) is the number of remaining events (jets) after the application of a cut. f_{total} is the fraction of N_{evts} (N_{jets}) with respect to the total number of events (jets). The quantity r_{prev} is the fraction of rejected events (jets) with respect to the remaining number of events (jets) after the application of the previous cut. The jets were reconstructed using the anti-k_t algorithm with distance parameter $R = 0.6$.

produced above $p_T > 84$ GeV. The region 84 GeV $\leq p_T < 100$ GeV is hardly affected by out-of-time pile-up effects. Inclusive jet spectra produced using $R = 0.4$ jets were not constrained by this cut. In case of the dijet measurement, all events are contributing to the final spectrum where the leading jet has $p_{T,\text{jet1}} \geq 100$ GeV and the second-leading jet has $p_{T,\text{jet2}} \geq 50$ GeV. The choice of asymmetric jet p_T cuts ensures consistent treatment with the theoretical predictions as discussed in Chap. 3. In addition to the cut on the transverse momentum the rapidity cut $|y| < 3.0$ was applied to the jets, which ensures to select jets in a rapidity region, where the central trigger are fully efficient (cf. Sec. 6.2). In the dijet measurement the cut $y^* < 3.0$ was applied.

Jet quality: In addition to the data quality requirements and the vertex selection, which ensures the selection of hard scattering events and therefore removes events triggered by cosmic muons and non-collision background, jet quality cuts were applied. The set of cuts in question was described in Sec. 6.1.2. The aim of the jet quality cuts is to remove jets not originating from the hard scattering events such as cosmic muons and other sources. For the cross-section measurements, the quality classification called MEDIUM was used. The cut set was applied on data and MC simulation.

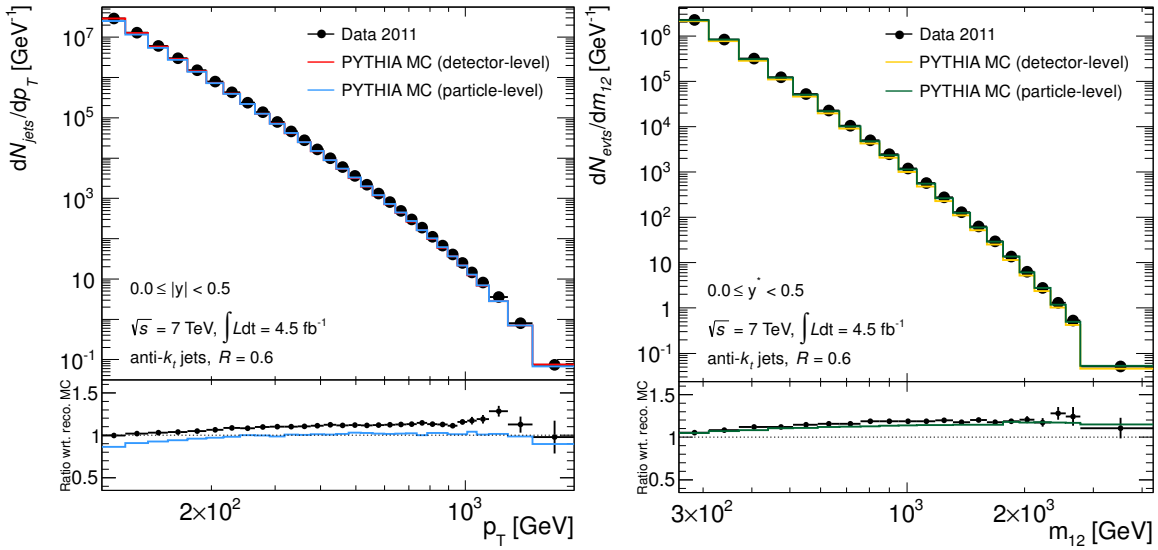

Figure 8.1: Left: inclusive jet p_T spectra in the central rapidity region $0.0 \leq |y| < 0.5$ obtained using data (black dots), MC simulation at detector-level (red lines), and MC simulation at particle-level (blue lines). The quantity $\mathrm{d}N_{\mathrm{jet}}/\mathrm{d}p_T$ (vertical axis) is the down-scale factor corrected number of jets divides by the width of the individual p_T-bins. Right: dijet m_{12} spectra in the central rapidity regime $0.0 \leq y^* < 0.5$ determined using data (black dots), MC simulation at detector-level (orange lines), and MC simulation at particle-level (green lines). $\mathrm{d}N_{\mathrm{evts}}/\mathrm{d}m_{12}$ is the down-scale factor corrected number of dijet events divided by the width of the individual m_{12}-bins. In the lower panel of these figures, ratios with respect to the MC spectra at detector-level are shown. The jets were reconstructed with the anti-k_t $R = 0.6$ algorithm.

Non-operational cells and non-instrumented regions: The cuts due to non-operational cells and non-instrumented regions are discussed in Sec. 6.1.2. The jet energy within these regions was estimated and was used to determine jet energy fractions which were used to tag affected jets. In case of the inclusive jet analysis jets were removed, which were tagged. In the dijet cross-section analysis events were removed, where either of the two leading jets are tagged according to this classification and therefore are affected by non-operational cells and non-instrumented regions.

LAr calorimeter issue: As detailed in Sec. 6.1.2 a defect of LAr calorimeter components in approximately 1 fb^{-1} of the data affected the jet measurement. This issue is modeled in the Monte Carlo simulation. Nevertheless, to avoid effects due to mismodeling and to simplify the treatment of the LAr defect in MC simulation a veto on the entire collision data and MC was applied. This approach allows to avoid a trigger based re-weighting of the MC predicted spectra as discussed in Sec. 6.4.1, which introduces unphysical structures in the shape of the inclusive jet and dijet spectra. The affected region is localized between $-0.88 < \phi < -0.5$ and $-0.1 < \eta < 1.5$. In case of the inclusive jet analysis any jet at detector-level that points to that region is not considered in the spectra at detector-level. In case of the dijet analysis events were rejected if either the leading or second-leading jet falls in the region $-0.88 < \phi < -0.5$ independent of η. These cuts are applied to jets in data and MC and the effect is corrected in the unfolding procedure (cf.

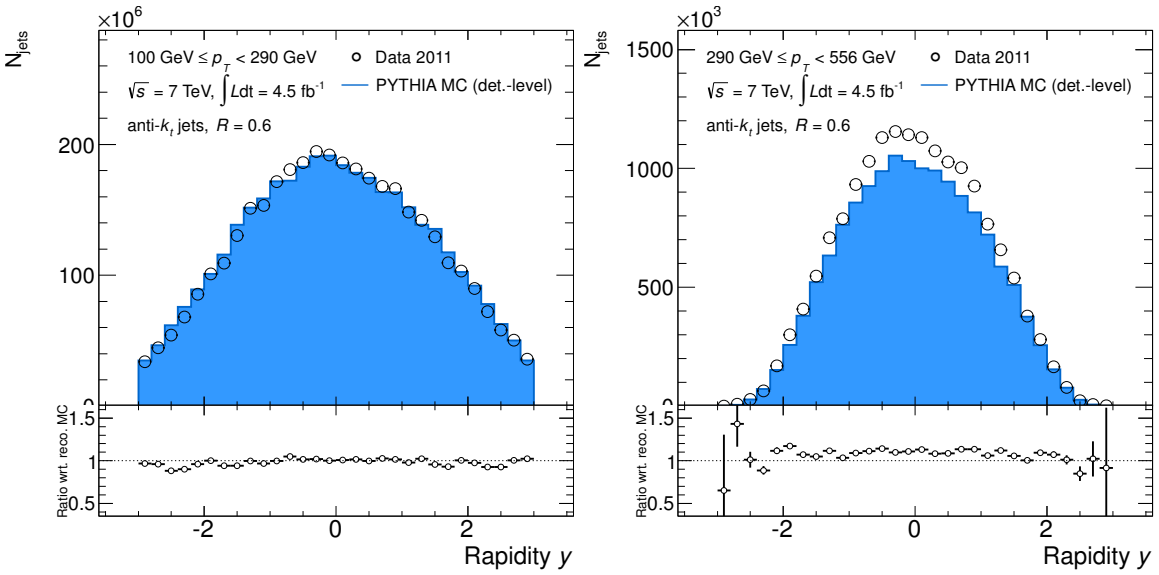

Figure 8.2: Inclusive jet rapidity distributions in the regions 100 GeV $\leq p_T <$ 290 GeV (left) and 290 GeV $\leq p_T <$ 556 GeV (right). The distributions were obtained using collision data and MC simulation at detector-level. In the lower panel the ration between data and MC is shown. The jets were reconstructed using the anti-k_t algorithm with $R = 0.6$.

Sec. 8.3).

Examples of basic distributions at detector-level after the application of the event and jet selection are shown in Fig. 8.1, 8.2, and 8.3. In Fig. 8.1 the inclusive p_T (left) and m_{12} (right) spectra produced using data and MC simulation in the central rapidity region are shown. The spectra produced using MC are shown at detector- and particle-level. In the lower panel of these figures the ratios with respect to the spectra determined using MC at detector-level are shown. The distributions in Fig. 8.2 show the inclusive jet distributions according to the rapidity y in the jet transverse momentum regions 100 GeV $\leq p_T <$ 290 GeV (left) and 290 GeV $\leq p_T <$ 556 GeV (right). In Fig. 8.3 the rapidity distribution of the leading jets in intervals $0.0 \leq y^* < 0.5$ (left) and $1.5 \leq y^* < 2.0$ (right) are exemplary shown. As can be observed from the figures exemplary shown, a good agreement in the shape between data and MC is achieved. The discrepancies in the number of jets N_{jets} (resp. events N_{evts}) are due to the fact, that leading-order Pythia MC was used.

8.3 Correction for Detector Effects

To be able to compare between the cross-section measurements and theoretical predictions at particle-level, it is essential to correct the measured spectra for detector effects. They cause migrations of events between bins due to detector resolution, geometrical acceptance and miscellaneous systematic effects. The detector effects are simulated in MC, which is used as basis to unfold the spectra measured at the reconstruction-level. The goal of the correction procedure is to provide a cross-section spectrum, which deviates as little as possible from the cross-section spectrum at particle-level.

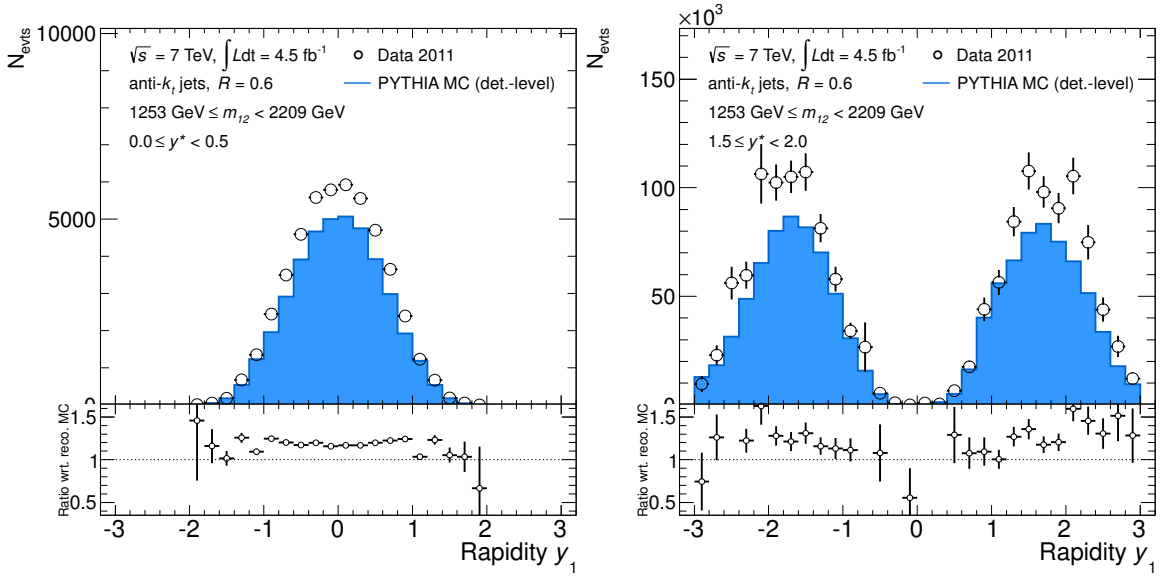

Figure 8.3: Distributions of dijet events according to the rapidity of the leading jet y_1 in the regions $0.0 \leq y^* < 0.5$ (left) and $1.5 \leq y^* < 2.0$ (right). The dijet mass was constrained to be within the interval 1253 GeV $\leq m_{12} <$ 2209 GeV. The distributions were obtained using collision data and MC simulation at detector-level. The jets were reconstructed with the anti-k_t $R = 0.6$ algorithm.

8.3.1 The Unfolding Principle

Definition of the transfer matrix A_{ij}

The information on jet smearing described by MC simulation is stored in the transfer matrix, which describes the correlation between events (jets) at the detector-level and the corresponding events (jets) at the particle-level. For this purpose all available[2] events (jets) at particle-level were considered. Events (jets) reconstructed at detector-level passed the selection criteria discussed in Sec. 8.2. The definition of the transfer matrix differs between the inclusive jet and the dijet measurement. The former is jet-based and the latter is event-based. In case of the inclusive jet measurement, only detector-level jets with a particle-level jet found within $\Delta R < 0.3$ were used to construct the transfer matrix. If more than one particle-level jet was found, the closest jet was considered. This procedure is called matching. Jets at detector-level where no particle-level jets were found and particle level jets with no corresponding detector-level jets were stored separately to determine the matching inefficiency which is used in the unfolding procedure for correction purposes. Furthermore jets were included in the matching inefficiency calculation, where the corresponding particle-level jets were reconstructed in different $|y|$ bins. The inclusive jet transfer matrix produced using the anti-k_T jet finding algorithm with the distance parameter $R = 0.6$ for the central rapidity region $0.0 < |y| < 0.5$ is exemplary shown in Fig. 8.4. By analogy with the inclusive jet analysis, dijet events at detector-level which were reconstructed in different y^* bins compared to the particle-level events, were not included in the transfer matrix and were considered for the calculation of the matching inefficiency. Events at a given level with no corresponding events at the other level were also included in the calculation of the matching inefficiency. In Fig. 8.4 (right) the

[2] At particle-level jets with $p_T < 7$ GeV were already excluded during the MC production.

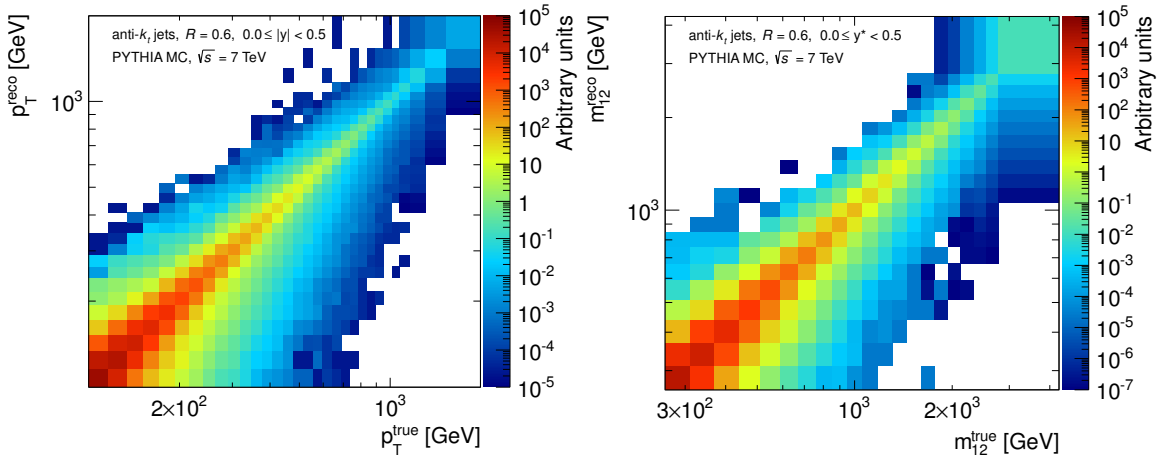

Figure 8.4: Initial transfer matrices determined using the PYTHIA MC simulation. The matrices were used to correct for detector effects in case of the inclusive jet cross-section (left) and the dijet cross-section (right) measurements. The jets were reconstructed using the anti-k_t jet finding algorithm with the distance parameter $R = 0.6$.

dijet transfer matrix is shown for the region $0.0 < y^* < 0.5$ produced using the anti-k_T jet finding algorithm with the distance parameter $R = 0.6$. In order to account for migrations of events (jets) from outside of the kinematic regions covered by the measurements, the transfer matrices were produced with the full kinematic range.

Unfolding procedure

The *iterative dynamically stabilized* (IDS) method was used to unfold the spectra obtained from data. This technique was introduced in Ref. [146, 147]. In this section a summary of the IDS unfolding procedure is given.

As discussed in the previous sub-section, the transfer matrix only comprises events (jets) where a matching between the particle-level and detector-level events (jets) is possible. In order to account for events (jets) at detector-level with no matching at particle-level, the spectra determined using data are corrected. This is realized by multiplying the so-called matching efficiency to the trigger down-scale and luminosity weighted spectra. The matching efficiency is defined as the ratio of the detector-level spectrum constructed using matched events (jets) only and the spectrum determined using all events (jets). The resulting spectra are used as input for the unfolding procedure. The number of events (jets) at particle-level N_j^{tMC} in bin j and detector-level N_k^{rMC} in bin k are related through:

$$N_j^{\mathrm{tMC}} = \sum_{k=1}^{N_{\mathrm{bins}}} \bar{P}_{kj} \cdot N_k^{\mathrm{rMC}} \text{ with } \bar{P}_{ij} = \frac{A_{ij}}{\sum_{k=1}^{N_{\mathrm{bins}}} A_{ik}}, \tag{8.5}$$

where A_{ij} is the transfer matrix defined in the previous sub-section, N_{bins} the number of bins in spectra at particle-level and detector-level, and $\bar{P}_{ij}$ is called unfolding matrix and is the probability for a particle-level event (jet) reconstructed in bin i to be located in bin j. The transfer matrix A_{ij} is an approximation of the real transfer matrix, because the spectra at particle-level for collision data are unknown. The aim of the IDS procedure is

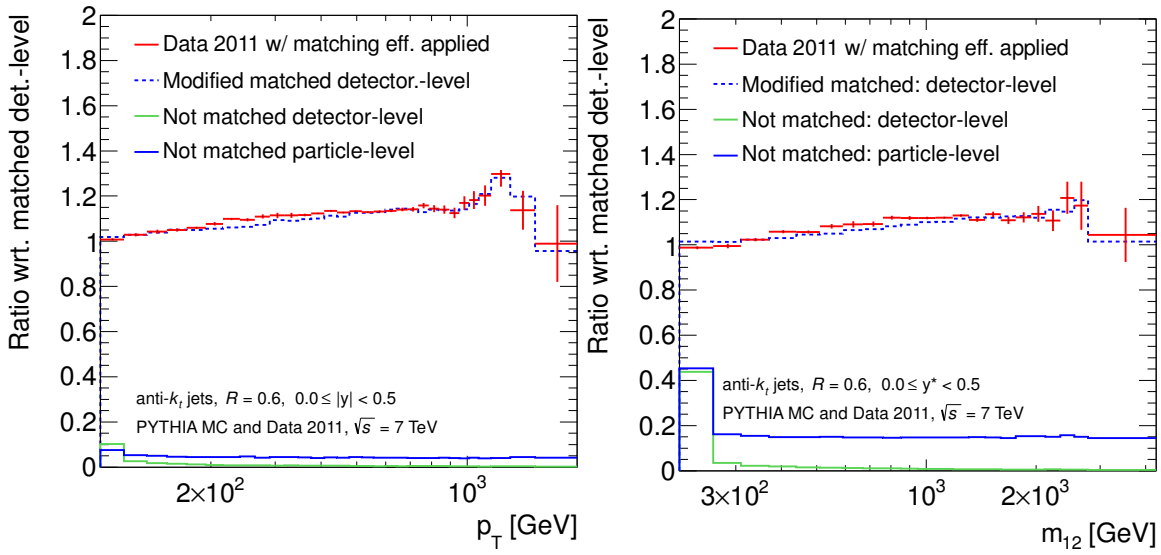

Figure 8.5: Ratios of intermediate spectra used in the IDS unfolding procedure with respect to p_T (left) and m_{12} (right) spectra at detector-level in the rapidity range $0.0 \leq |y| < 0.5$ (left) and $0.0 \leq y^* < 0.5$ (right), respectively.

to improve the transfer matrix A_{ij} in a series of iterations and use the improved transfer matrix to unfold the data spectra using Eq. 8.5. The iterative improvement of the transfer matrix A_{ij} not only improves the description of detector effects, but also the quality of the model used to generate the MC spectra at particle-level. This is done by re-weighting the number of simulated events (jets) N_j^{tMC} at particle-level in bin j to the shape of the intermediate unfolded data spectrum with the number events (jets) N_j^{uData} in the same bin. The iterative procedure is based on the comparison between data and MC spectra. Structures, which are presented in data and are not well simulated in MC could introduce fake-differences. To avoid these effects a regularization function was used, which is defined as follows:

$$f(|\Delta N_k|, \sigma_k, \lambda) = \frac{2}{\sqrt{\pi}} \int_0^x e^{-t^2}\, \mathrm{d}t \text{ with } t = \frac{\Delta N_k}{\sqrt{2}\lambda\sigma_k}, \tag{8.6}$$

where ΔN_k is equal to $\Delta N_k^{\mathrm{t}} = N_k^{\mathrm{uData}} - \kappa \cdot N_k^{\mathrm{tMC}}$, if e.g. comparing the MC particle-level spectra and intermediate unfolded data spectra, σ_k is the corresponding statistical uncertainty, λ a regularization parameter, and and κ is a normalization factor. The normalization factor is defined as $\kappa = N^{\mathrm{uData}^*}/N^{\mathrm{tMC}}$, where N^{uData^*} is the number of events (jets) in data without including events (jets), which correspond to significant new structures and N^{tMC} the total number of events (jets) included in the MC spectrum at particle-level. Eq. 8.6 was introduced to distinguish real differences between data and MC spectra from differences due to statistical fluctuations. The improved transfer matrix $A_{ij}^{'}$ exploits the regularization function and is given as:

$$A_{ij}^{'} = A_{ij} + f(|\Delta N_j^{\mathrm{t}}|, \sigma_j^{\mathrm{t}}, \lambda_{\mathrm{M}}) \cdot \frac{\Delta N_j^{\mathrm{t}}}{\kappa} \cdot P_{ij}, \tag{8.7}$$

where $f(|\Delta N_j^{\mathrm{t}}|, \sigma_j^{\mathrm{t}}, \lambda_{\mathrm{M}})$ is the function defined in Eq. 8.6 and $P_{ij} = \frac{A_{ij}}{\sum_{k=1}^{N_{\mathrm{bins}}} A_{kj}}$ is the so-called folding matrix. The unfolded spectrum characterized by N_j^{uData} was determ-

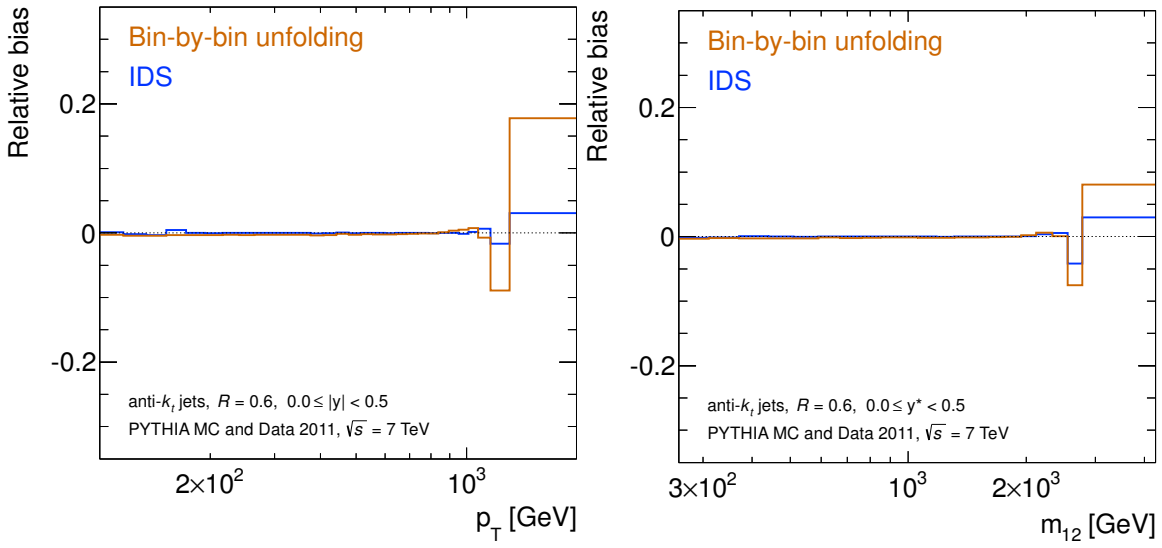

Figure 8.6: The relative bias obtained using two different unfolding techniques: bin-by-bin and IDS. The IDS unfolding leads to the smallest relative bias over the covered kinematic range. The relative bias is shown for the inclusive jet (left) and dijet (right) analysis in the regimes $0.0 \leq |y| < 0.5$ and $0 \leq y^* < 0.5$, respectively.

ined from the sum of three contributions: events (jets) $\kappa \cdot N_j^{\mathrm{tMC}}$, the unfolded fraction of events (jets) obtained from the difference between the data and normalized MC spectrum at detector-level, and the fraction of events (jets) that remain in same bin. The fractions are determined using Eq. 8.6. In the last step of the unfolding procedure, a correction to the final unfolded spectrum is applied to account for events (jets) at particle-level, with no matching at detector-level.

The shape of the spectra determined using data is not described by the MC simulation as shown in the lower panels of Fig. 8.1. In order to quantify the shape bias introduced in the unfolding procedure a smooth function is used to re-weight the particle-level MC spectrum encoded in the transfer matrix such that the detector-level MC spectrum, which is obtained by projection of the transfer matrix, is similar to the data spectrum with matching efficiency applied. The ratios of the matching efficiency corrected data spectrum (red) and the modified spectrum (dashed blue) with respect to the MC spectrum at detector-level determined using matched events (jets) only are exemplary shown in Fig. 8.5. The modified MC spectrum at detector-level is unfolded using the initial transfer matrix. This procedure is repeated using pseudo experiments (cf. Sec. 8.4.1). The mean difference between the unfolding results and the re-weighted particle-level spectra is called *relative bias*. The relative bias determined using IDS and the bin-by-bin correction method are exemplary shown in Fig. 8.6 for the central rapidity region. In case of the bin-by-bin correction, the ratio of the number of events (jets) at particle-level with respect to the number of events (jets) at detector-level is multiplicatively applied to the measured number of events (jets) in a given bin. This technique depends on the shape of the spectra determined using MC. As can be observed from this figures, the IDS technique provides the smallest relative bias below 5%. The number of iterations has an impact on the unfolding bias. Four iterations were performed in case of the inclusive analysis

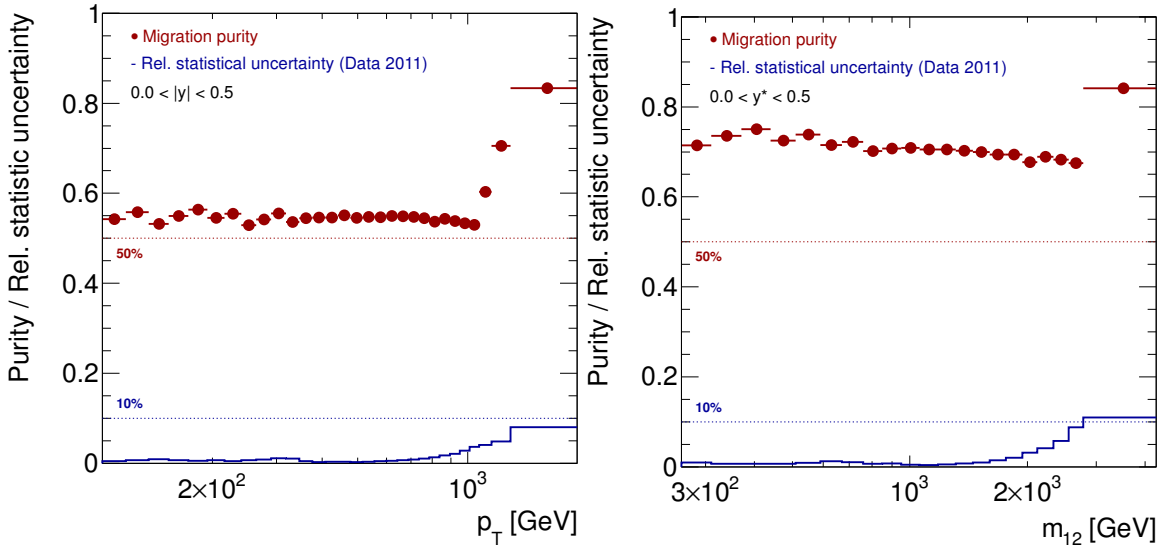

Figure 8.7: Migration purity (red dots) and statistical uncertainties in data (blue lines). The distributions are shown for inclusive jets (left) and the dijets (right) in the central rapidity (resp. rapidity separation) regime. The jets were reconstructed using the anti-k_t algorithm with $R = 0.6$. In theses figures, the final binning is shown. The increase of the migration purity for $p_T > 1$ TeV is due to merging of bins forced by the constraints described in Sec. 8.3.2.

and one iterations was found to be optimal for the dijet analysis. The unfolding bias also depends on the choice of the bin widths, which were optimized using an iterative procedure exploiting the IDS unfolding method. The procedure is described in the next section.

8.3.2 Optimization of the bin widths

The goal of the optimization of the bin widths is to preserve as much information on the shape of the spectra as possible. The choice of the bin widths is based on several quantities competing the amount of information on the shape. The optimization was performed for the inclusive jet analysis only. The resulting bin widths were used in Ref. [126]. In case of the dijet analysis the same bin widths as used in Ref. [126] were taken as basis. The reference for the lower limit of the bin widths in all measured rapidity regions was chosen to be the transverse momentum resolution at $y = 0$ (cf. Sec. 6.5), which is the worst p_T resolution as function of y in the rapidity region covered by the measurement. The resolution was taken from the MC simulation which is assigned with an uncertainty due to mis-modeling compared to the resolution derived using in-situ techniques. To cover the uncertainty on the resolution, the widths were derived such that they are equal to the resolution plus 80% safety margin rounding to an integer number[3]. This approach was applied in the region below 1 TeV. To be more flexible in the bin merging procedure, the binning above 1 TeV was derived from the resolution plus 20% margin. This binning is the smallest binning, which is used as basis for further optimization steps.

[3]The width was measured in units of GeV.

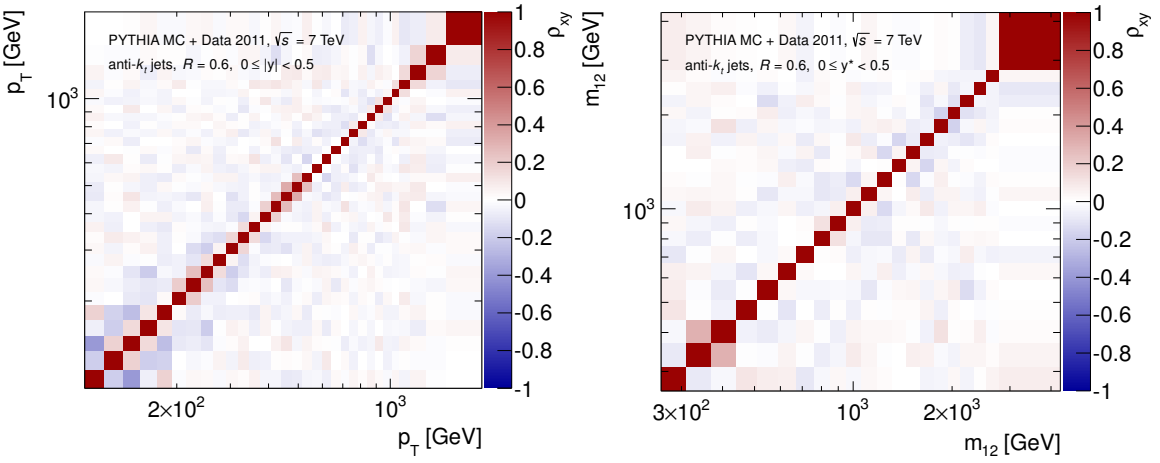

Figure 8.8: Correlation coefficient matrices ρ_{xy} determined using pseudo-experiments derived from data and MC as described in 8.4.1 are shown exemplary in the rapidity interval $0.0 \leq |y| < 0.5$ (right) and . Each pseudo-experiment was unfolded using the IDS unfolding technique. The correlation coefficients $|\rho_{xy}|$ of adjacent bins are below 0.35 in the covered kinematic region. This quantity is used in context of the binning optimization discussed in Sec. 8.3.2.

Several quantities were used to constrain the bin widths. The relative statistical uncertainty in data was required to be below 40% of the systematic uncertainty due to the jet energy scale on jet yield spectra (cf. Sec. 8.4). To check the independence of the measurements in each individual bin the *migration purity* was used. The migration purity is defined as the number of matched reconstruction-level jets (events) divided by the total number of particle-level jets in a given p_T (m_{12}) bin and was required to be at least 50%. The matched detector-level events (jets) used to calculate the purity are contributing to the transfer matrix used to correct data spectra for detector effects. The number of particle-level events (jets) additionally comprises events (jets) where no reconstructed jets were found within a matching distance of $\Delta R < 0.3$. The purity is fluctuating around 55% in the central rapidity region as shown in Fig. 8.7 (left). Because the relative p_T resolution in the more forward region is better compared to the resolution in the central region, the migration purity increases as function of y. The latter was used as basis for the choice of the bin widths. This leads to better migration purity in the more forward rapidity regime. In kinematic regions where the statistical uncertainty is about 10% a purity of around 80% was required, because of non-Gaussian effects due to the low statistical power. Furthermore, the correlation coefficients ρ_{xy} between neighboring bins introduced due to the unfolding procedure, were required to be below 95%, which is fulfilled in all rapidity bins. The correlation coefficient matrix is exemplary shown in the rapidity interval $0.0 \leq y < 0.5$ in Fig. 8.8 for the inclusive jet (left) and dijet (right) analysis. Additionally, the unfolding bias (cf. Sec. 8.3.1), which depends on the bin width is used to constrain the binning. It was required to be below 5%. The relative bias is exemplary shown in Fig. 8.6 for the inclusive jet (left) and dijet (right) analysis.

8.4 Assessment of Uncertainties

8.4.1 Statistical Uncertainties

In order to take correlations into account and propagate the statistical errors correctly, the so-called bootstrap technique was used. For each event, random numbers were generated according to the Poisson distribution around the expectation value $\nu = 1$. The random numbers were used as event weights to generate pseudo-experiments and determine a number of fluctuated spectra. Data and MC are fluctuated such that they are statistically independent. This method was used to produce a set of spectra and transfer matrices, which were used to propagate the uncertainties through the unfolding procedure. The fluctuated spectra from data and Monte Carlo were also used to determine the correlation coefficient matrices to quantify the statistical correlations introduced by IDS as discussed in Sec. 8.3.2.

For each fluctuated data and MC spectrum the unfolding was performed resulting in a covariance matrix, which is constructed using the IDS results. The final statistical uncertainty was calculated using the diagonal elements of the covariance matrix. This treatment ensures the propagation of statistical fluctuations in data and MC. The relative uncertainties are shown as black vertical lines e.g. in Fig. 8.24. The statistical uncertainty is of the order of few percent and below in almost all kinematic regions covered by the cross-section measurements. It is similar for $R = 0.4$ and $R = 0.6$ jets with slightly smaller uncertainty in case of jets reconstructed using the distance parameter $R = 0.6$. The largest statistical uncertainty can be observed in case of the dijet analysis in the rapidity separation interval $2.0 \leq y^* < 2.5$. It amounts up to approximately 12%.

8.4.2 Systematic Uncertainties

The individual sources of systematic uncertainties on the jet measurement are briefly introduced in Sec. 7. Potential modifications of the unfolded spectra due to the event and jet selection or other effects are covered by the unfolding procedure if a good description in MC is provided. The uncertainties were determined according to the discrepancy between collision data and MC simulation. In the following the impact of systematic uncertainties on the cross-section measurements are discussed.

Jet Energy Scale

The systematic uncertainty on the jet energy scale has the largest impact on the measurements. It consists of 63 sub-components, which are briefly discussed in Sec. 7. A summary of the sub-components is given in Tab. 7.1. Each sub-component was treated as independent and as fully correlated in the transverse momentum p_T (resp. dijet mass m_{12}) and pseudorapidity η (resp. rapidity separation y^*). Each component was propagated to the unfolded inclusive jet p_T (resp. m_{12}) spectra separately. For this purpose MC simulation was used, because of the smaller statistical uncertainty in the high-p_T (-m_{12}) region compared to data. For a given sub-component and rapidity (resp. rapidity separation) bin, three spectra were produced: the nominal spectrum, which was used as reference, one spectrum with the transverse momentum p_T of each jet shifted up by 1σ according to the relative uncertainty, and one spectrum with p_T of each jet shifted down

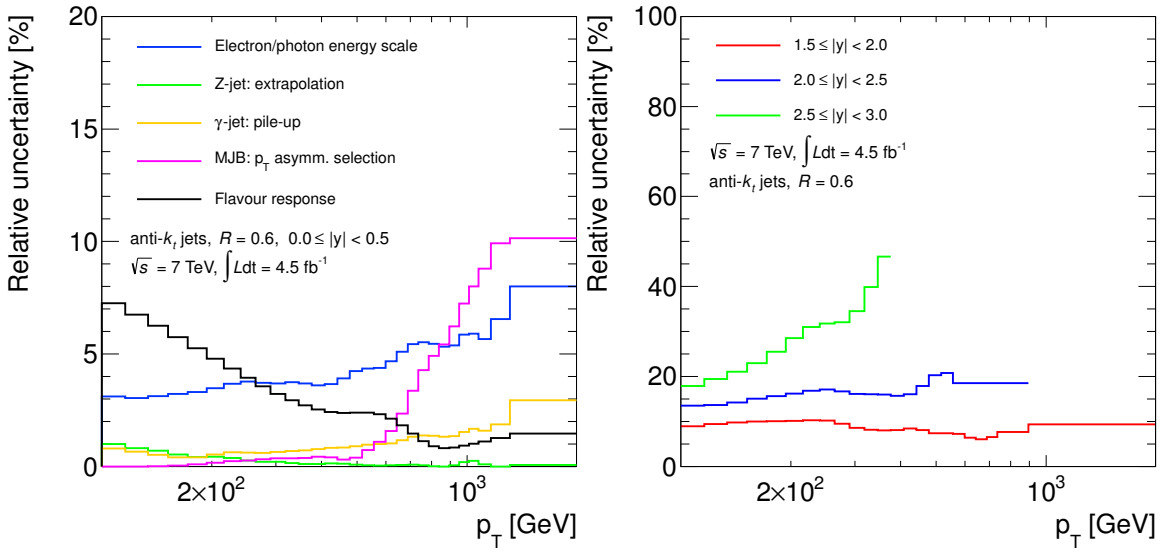

Figure 8.9: Left: selection of five dominant jet energy scale uncertainty components propagated to the inclusive jet cross-section spectrum. Right: relative η-intercalibration uncertainty for three different rapidity regions. This uncertainty originates from the large deviation between the predictions generated using Pythia and Herwig++ (cf. Sec. 7.1).

by 1σ. Each of these spectra was unfolded using the initial transfer matrix. The resulting asymmetric relative uncertainty as function of p_T (resp. m_{12}) in slices of $|y|$ (resp. y^*) were determined by calculating the ratio with respect to the nominal unfolded MC spectrum.

The relative uncertainty of a selection of five dominant JES uncertainty sub-components propagated to the inclusive cross-section spectrum is exemplary shown in Fig. 8.9 (left). In this case the positive component is shown only. In the more forward rapidity region the uncertainty from η-intercalibration is dominant. The relative uncertainty on the inclusive cross-section from this source is shown for three different rapidity intervals in Fig. 8.9 (right).

In case of the inclusive cross-section measurement the relative JES uncertainty on the cross-section is approximately 10% in the low-p_T regime and 35% in the high-p_T region for jets pointing to $0.0 \leq |y| < 0.5$. In the most forward region covered by this measurement the relative uncertainty amounts to 25% in the low-p_T region and is approximately 55% at high-p_T. In the dijet analysis the uncertainty is approximately 10% in the low-m_{12} and 25% in the high-m_{12} region for the rapidity separation interval $0.0 \leq y^* < 0.5$. In the rapidity separation bin $2.0 \leq y^* < 2.5$, which is the most forward region covered by this measurement, the relative JES uncertainty is approximately 25% in the low-p_T region and 40% in the high-p_T region. The relative JES uncertainty is slightly larger for jets reconstructed using the distance parameter $R = 0.4$.

Jet Energy and Angular Resolution

The finite detector resolution introduces bin-to-bin migrations which were corrected using the IDS unfolding technique. The information on the resolution is stored in the transfer

matrices, which are derived exploiting MC simulation. As detailed in Sec. 7.10 the uncertainty on the relative jet energy resolution was derived by comparing the resolution modeled in MC and the resolution obtained using in-situ methods. The resolution derived from data and MC agree within $5\% - 15\%$ dependent on the transverse jet momentum p_T.

In order to account for the mis-modeling of the detector resolution the jet energy resolution (JER) was degraded according to the corresponding uncertainty. The p_T of each jet at reconstruction-level was smeared by σ_s:

$$\sigma_s = \sigma_n \cdot \sqrt{(1 + \Delta\sigma_n/\sigma_n)^2 - 1},$$

where $\sigma_n \equiv \sigma_n(p_T, \eta)$ is the nominal relative p_T resolution and $\Delta\sigma_n \equiv \Delta\sigma_n(p_T, \eta)$ the corresponding uncertainty. σ_s was used to define a Gaussian probability density function with an expectation value around 1, which was used to generate random numbers. The p_T and energy E of each jet was multiplied by the generated random number. The transfer matrices derived using the described method were used to unfold the data spectra. The systematic uncertainty is the ratio of the unfolded result using the smeared transfer matrix with respect to that using the nominal transfer matrix. The relative uncertainty on the cross-sections from this source is estimated to be of the order of few percent. It increases as $|y|$ (resp. y^*) increases. The largest uncertainty can be observed in the high-p_T (-m_{12}) regime in the most forward region covered by the measurements, where it ranges from approximately 10% to 25%. This uncertainty component depends on the jet distance parameter R. This relative uncertainty is larger for jets reconstructed using $R = 0.6$. The JER uncertainty is shown together with other uncertainties in 8.13.

In addition to the energy resolution the uncertainty due to the angular resolution on the cross-section was considered. The angular resolution was determined using MC simulation and the uncertainty was evaluated using an in-situ methods (cf. Sec. 6.5 and Sec. 7.10). To propagate the uncertainty on the angular resolution the above described method was used. The uncertainty is at the per-mill level in the central region and increases as $|y|$ (resp. y^*) increases. In the most forward region it is of the order of few percent.

Trigger Efficiencies

The method to determine the intervals, where the triggers are fully efficient is described in Sec. 6.2. The results produced in context of this thesis were used to construct the cross-section spectra in Ref. [145]. The trigger intervals were adjusted such that no statistically significant local discrepancies between the jet yield spectra and a smooth reference function exist. Therefore, no systematic uncertainties were included from this source.

Jet Reconstruction Efficiencies

The reconstruction efficiency is defined as the number of jets at detector-level where a matching to a particle-level jet is possible divided by the total number of particle-level jets. The reconstruction efficiency is correlated with the matching efficiency which is used for corrections in the unfolding procedure. The ability of the Monte Carlo to correctly simulate the jet reconstruction efficiency in collision data was examined using jets reconstructed from tracks. The comparison between results from collision data and Monte Carlo simulation show no difference in the p_T range covered by the measurement and

therefore no systematic uncertainty was assigned from this source [117]. The reconstruction efficiency using particle-level jets is approximately 100% for jets with $p_T > 50$GeV.

Jet Quality Selection

A detailed description of the quality selection is given in Section 6.1.2. The efficiency was derived using an in-situ tag-and-probe method and MC simulation. The comparison between collision data and MC simulation show an agreement within 0.25%. Therefore a systematic uncertainty of 0.25% to the final cross-section was assigned. In case of the dijet cross-section measurement an uncertainty of 0.5% was used. The uncertainties were treated as fully correlated in p_T and y (resp. m_{12} and y^*).

Luminosity

The luminosity weights were applied in the same way to all bins within the phase space of the measurements and were therefore treated as fully correlated in p_T and y (resp. m_{12} and y^*). The relative uncertainty estimate of the luminosity is $\Delta\mathcal{L}_{\text{int}}/\mathcal{L}_{\text{int}} \pm 1.8\%$ for the analyzed collision data [78].

Impact of Pile-up on Measurements

The impact of pile-up on the measurements was studied using collision data and Monte Carlo simulation, because the detector response simulation provided in the Monte Carlo is used to correct the spectra for detector effects. On average, each bunch-crossing (BC) leads to several proton-proton collisions. Thus the amount of energy deposition originated from the collision of interest are overlapped with energy depositions from other simultaneous proton-proton interactions. This effect is referred to as in-time pile-up and is discussed in Sec. 6.4.1. A correction due to in-time pile-up is applied to jets and methods to determine the uncertainty due to the pile-up correction are briefly summarized in Sec. 7.6. This uncertainty is a sub-component of the JES uncertainty. The impact of in-time pile-up on the inclusive jet p_T spectra are exemplary shown in Fig. 8.10. The jets were reconstructed using the antik-k_T algorithm with distance parameter $R = 0.4$ (left) and $R = 0.6$ (right). Two different data-taking periods with different in-time pile-up conditions were compared to the nominal spectrum at detector-level. The maximum deviation from the nominal spectrum was found to be of the order of few percent.

As described in section 6.4.2 the LHC bunch train structure was organized in several trains with 50 ns spacing between consecutive proton bunches within a train. The spacing between trains vary from 150 ns in the forward to more than 650 ns in the central rapidity region. The bipolar shape of the LAr cell response was designed such that contributions from previous or subsequent bunch-crossings cancel out on average. This is only the case of continuous and uniform bunch trains. The effect due to the absence of previous or subsequent bunch-crossings within the width of the liquid argon calorimeter cell response is called out-of-time pile-up.

The out-of-time pile-up dependence was studied as function of the position of a bunch-crossing within a train called *bunch train position* (BTP). For this purpose the luminosity for a given LB j, BTP k and trigger t is used:

$$L_{k,j,t} = \delta \cdot \sum_{\forall \mu_j^{act} \in k} \mu_j^{act} \text{ with } \delta = \frac{L_{j,t}}{\sum \mu_i^{act}}. \tag{8.8}$$

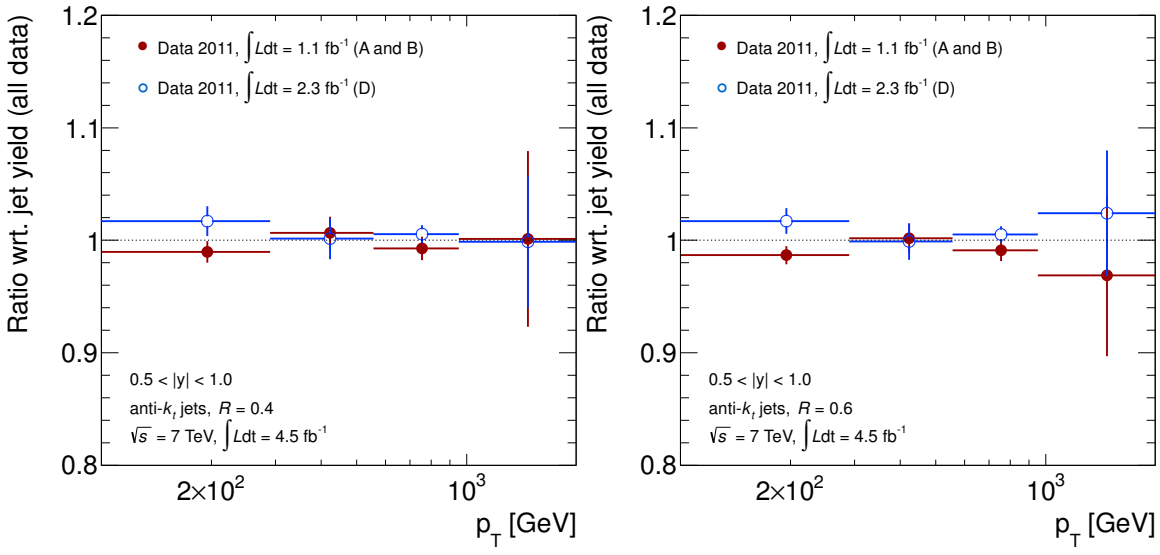

Figure 8.10: Ratios of the luminosity and trigger down-scale factor corrected spectra determined using data recorded in different in-time pile-up scenarios with respect to the jet yield obtained using the full data set. The first period (A and B, red) contains 1.1 fb^{-1} of data. The mean of the average interaction per bunch-crossing μ_{avg} is approximately 6. In case of the second period (D, blue), 2.3 fb^{-1} of the data record were used. In this case, the mean μ_{avg} is approximately 11 (cf. Sec. 6.4.1). The ratios are shown for the rapidity regime $0.5 < |y| < 1.5$. The jets were reconstructed using the anti-k_T algorithm with distance parameters $R = 0.4$ (left) and $R = 0.6$ (right). The stability of the measurement is similar for $R = 0.4$ and $R = 0.6$, where jets reconstructed with the distance parameter $R = 0.4$ provide a slightly better performance. The maximum discrepancies as function of p_T and $|y|$ were found to be of the order of few percent and are covered by the systematic uncertainties discussed in Sec. 7.6. The same conclusions hold for the dijet analysis.

The integrated luminosity $L_{i,t}$ for a given μ^{act} bin i and trigger t results from the sum over all luminosity blocks $\sum_{LB} L_{j,i,t}$. The requirement of a continuous train is fulfilled between bunch train position 11 and 20 (BTP11-20) and was taken as *control region*. The selected trains were required to have a minimal train length of 1250 ns (corresponds to 25 BTPs) and a minimal distance to the previous train of 250 ns (5 BTPs). Both requirements are intended to suppress the influences on the control region from the absence of previous or subsequent bunch-crossings. The above mentioned definition covers around 3.7fb^{-1} of data. The ratios of yields using the full sample with respect to the sub-sample 'BTP11-20' are shown for the dijet analysis in Fig. 8.11 and for the inclusive jet analysis in Fig. 8.12. The ratios are shown for MC and data. In case of the dijet analysis the nominal spectrum determined in the interval $0.0 \leq y^* < 1.0$ (left) is approximately 2% above the spectrum obtained from the control sample in the low-m_{12} region. This behavior is simulated in MC. Data and MC are in a good agreement within the statistical uncertainties. The same statement holds for jets reconstructed using the distance parameter $R = 0.4$. The agreement is also good in the more forward regions as demonstrated in Fig. 8.11 (right). In case of the inclusive jet analysis a discrepancy between data and MC can be observed

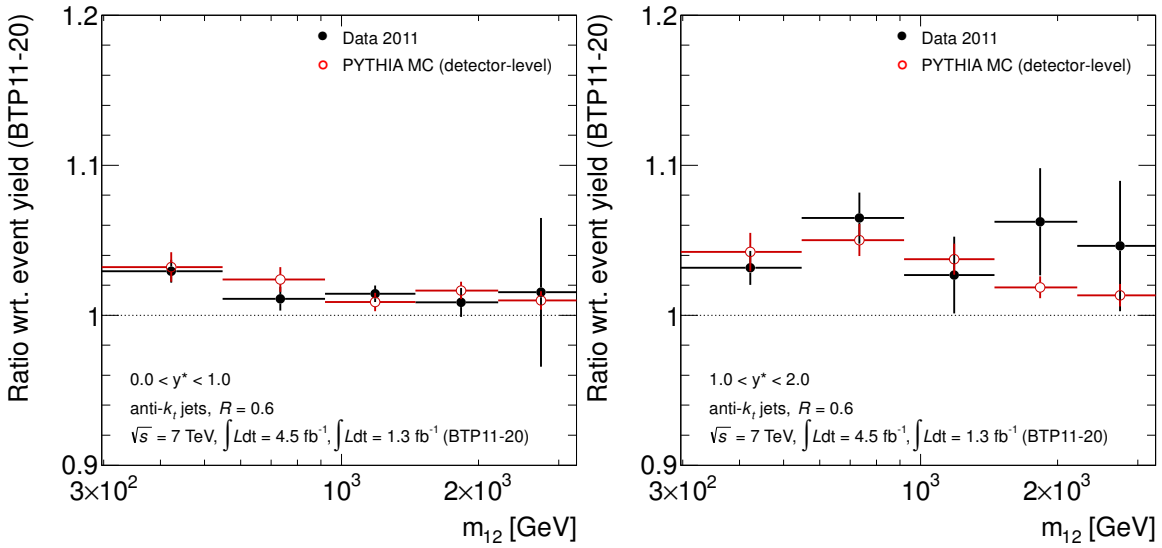

Figure 8.11: Event yield of the full data set with respect to that obtained from the control sample (BTP11-20) as function of the dijet mass m_{12} for jets reconstructed using $R = 0.6$ in $0.0 \leq y^* < 1.0$ (left) and $1.0 \leq y^* < 2.0$ (right).

in the low-p_T region for jets reconstructed with $R = 0.6$ pointing to the rapidity forward region as shown in Fig. 8.12 (right). In case of jets reconstructed using $R = 0.4$ a good agreement was found. The disagreement is observed outside the phase space covered by the measurement (cf. App. A.4). The difference between data and MC is not significant and is already covered by the JES pile-up uncertainty. Therefore no additional systematic uncertainty from this source was assigned. The decision to exclude this uncertainty component in Ref. [126] and Ref. [145] is based on the study performed in context of this thesis.

Unfolding Procedure

The systematic uncertainty introduced by the unfolding procedure due to the difference on the shape between data and reconstructed MC spectra was estimated using a data-driven method. The calculated quantity is called relative bias and was used as unfolding uncertainty estimate. The technique is described in Sec. 8.3.1 and was used in order to derive the p_T bin widths in case of the inclusive jet analysis (cf. Sec. 8.3.2). The maximum relative unfolding uncertainty is approximately 4% in the high-p_T (-m_{12}) regime. The relative uncertainty (relative bias) is shown exemplary in Fig. 8.6 for the central rapidity regions $0.0 \leq |y| < 0.5$ (left) and $0.0 \leq y^* < 0.5$ (right).

Matching Efficiency

In the inclusive jet analysis a matching procedure was performed to find jet pairs at particle-level and reconstruction-level to construct the transfer matrix. The procedure is described in Sec. 8.3.1. The matching distance ΔR was chosen to be 0.3 for the nominal transfer matrix. Two additional transfer matrices were produced using $\Delta R = 0.2$ and $\Delta R = 0.4$. These matrices were used unfold the measured inclusive jet p_T spectra. The estimate of the systematic uncertainty on the choice of ΔR was determined by comparing the spectra unfolded using the modified transfer matrices to the nominal unfolded spectra.

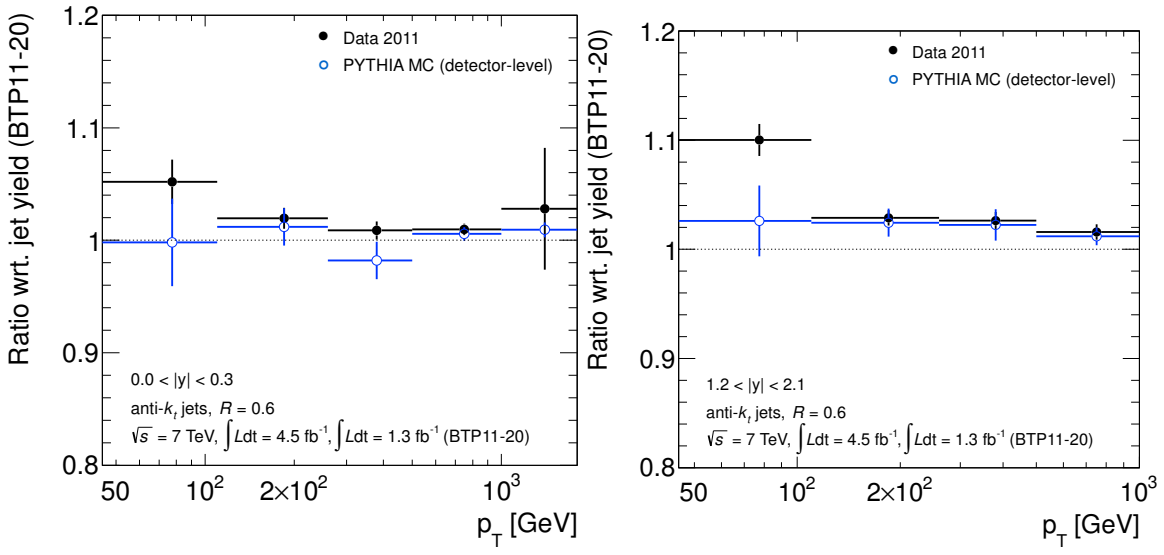

Figure 8.12: Jet yield of the full data set with respect to that obtained from the control sample (BTP11-20) as function of the jet transverse momentum p_T for jets reconstructed using $R = 0.6$ in $0.0 \leq |y| < 0.3$ (left) and $1.2 \leq |y| < 2.1$ (right).

The maximal deviation from the nominal spectrum was observed in the high-p_T region using the matching parameter $\Delta R = 0.2$. The estimated relative uncertainty is at the per-mill level. In case of the dijet analysis no matching procedure was used and thus no matching uncertainty was assigned.

The two dominant uncertainties, the remaining uncertainties, and the total systematic uncertainty are exemplary shown for two different rapidity intervals in 8.13. The JES uncertainty is the dominant uncertainty followed by the JER uncertainty. The remaining uncertainty labeled as 'Others' in these figures comprises the following components: uncertainty due to jet quality, integrated luminosity, jet angular resolution, and matching efficiency.

8.5 Results

In the following the results of the cross-section measurements are discussed. The theoretical predictions are shown with respect to the unfolded data and agree within the experimental and theoretical uncertainties.

8.5.1 Inclusive Cross-Section Measurement

The double-differential cross-section was measured as function of jet p_T for different $|y|$ bins ranging from 0 to 3. The jet finding algorithm anti-k_t with distance parameters $R = 0.4$ and $R = 0.6$ was used to define jets. The cross-section measurement starts at 100 GeV and extends to 2 TeV in the central rapidity region spanning eight orders of magnitude. The measurement was corrected for detector effects using the unfolding procedure described in Sec. 8.3.1. The resulting cross-sections are compared to POWHEG

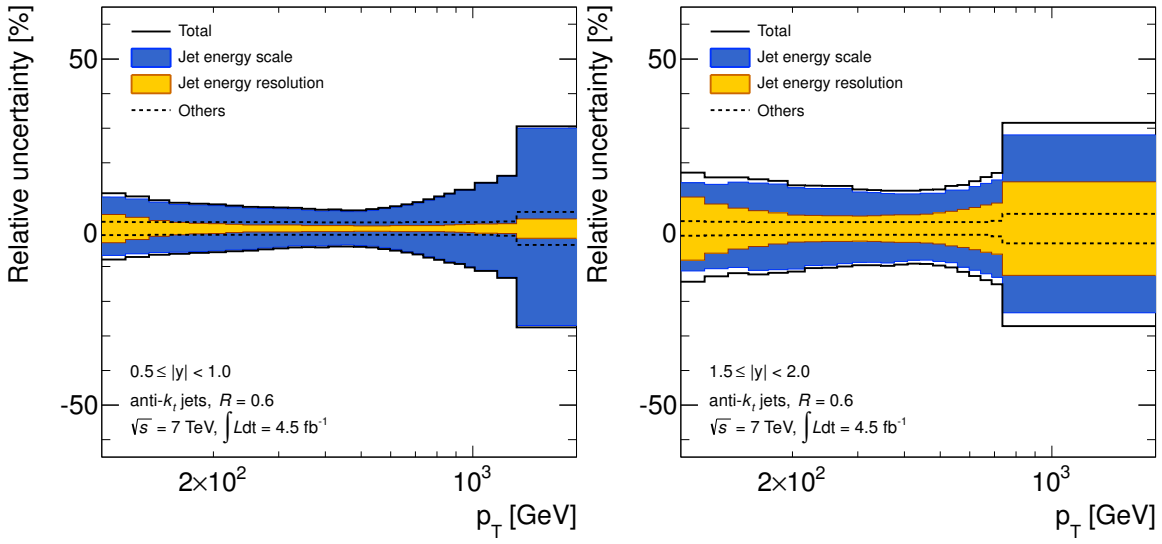

Figure 8.13: Dominant components of the total systematic uncertainty. The following systematic uncertainty components are labeled as 'Others': jet quality, integrated luminosity, jet angular resolution, and matching efficiency.

predictions interfaced with PYTHIA showering for two different tunes and NLOJet++ predictions for various PDF sets. Predictions generated using NLOJET++ were corrected for non-perturbative and electroweak effects (cf. Sec 3.3). The uncertainties on the theory from different sources were considered as detailed in Sec. 3.2. In case of the POWHEG predictions only statistical uncertainties are shown. An overlay of the steeply falling jet cross-sections obtained from collision data and predicted by NLOJET++ using the CT10 PDF set is shown in Fig. 8.14 and in Fig. 8.15.

The NLOJET++ predictions were generated using the following PDF sets: CT10, MSTW2008, and NNPDF2.3. The comparisons to data for the jet distance parameters $R = 0.4$ and $R = 0.6$ are shown in Fig. 8.16 and 8.17, respectively. The theory agrees within the uncertainties with the collision data. At low-p_T data is described best in all rapidity bins. At high-p_T a deviation of up to 40% can be observed, where the predictions overestimate the measured cross-section which is covered by the systematic uncertainties. For $|y| < 1.0$ CT10 provides the best description for jets reconstructed using $R = 0.4$. In case of $R = 0.6$ jets, CT10 underestimates data, where MSTW2008 and NNPDF2.3 provide the best predictions. For $|y| > 1.0$ MSTW2008 and NNPDF2.3 give the best description in the high-p_T regime. CT10 overestimates the data in this region for $R = 0.4$ and $R = 0.6$ jets. In the low-p_T region CT10 provides a similarly good agreement with data as MSTW2008 and NNPDF2.3 for $R = 0.6$ jets. An overestimation can be observed for all three PDFs for jets reconstructed with $R = 0.4$.

The ratios of the POWHEG predictions with respect to data for anti-k_T jets with $R = 0.4$ and $R = 0.6$ are shown in Fig. 8.18 and 8.19. POWHEG was interfaced with PYTHIA for parton showering and predictions were produces for the AUET2B and Perugia2011 tunes. The shape is described well for both tunes in the rapidity region between $1.5 < |y| < 3.0$ over the entire p_T range for both jet distance parameters. In the central rapidity region the POWHEG predictions underestimate the data. The deviations amount up to 5% in the

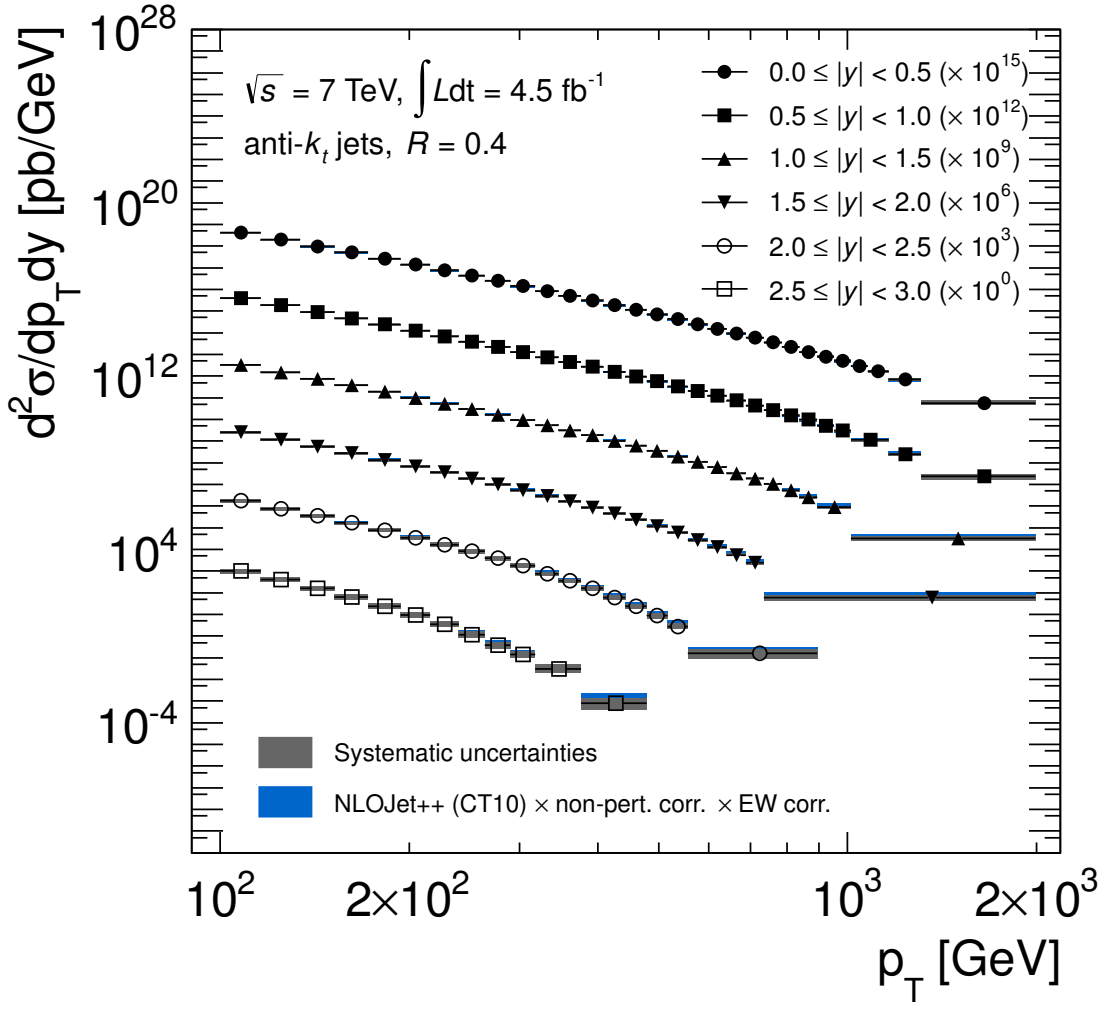

Figure 8.14: Double-differential inclusive jet cross-section for all rapidity bins included in the measurement. The unfolded data spectra are compared to NLOJET++ predictions, which are corrected for non-perturbative and electroweak effects. The blue filled areas indicate the theoretical uncertainty. The gray filled areas show the total systematic uncertainty. The jets were reconstructed using the distance parameter $R = 0.4$.

low-p_T regime. They become larger dependent on p_T and extend up to 20% in the high-p_T region. Comparing the POWHEG predictions with data for different anti-k_T distance parameters $R = 0.4$ and $R = 0.6$ a slightly better prediction is provided for $R = 0.6$ jets. The predictions using the Perugia2011 tune predicts an approximately 10% higher cross-section compared to the AUET2B tune in the low-p_T region. This deviation decreases as p_T increases.

8.5.2 Dijet Cross-Section Measurement

The double-differential cross-section was measured as function of the dijet mass m_{12} for different y^* bins ranging from 0 to 2.5. The anti-k_t algorithm with distance parameters $R = 0.4$ and $R = 0.6$ was used to reconstruct jets. The measurement starts at 260 GeV in the region $0.0 \leq y^* < 0.5$ and at approximately 1.5 TeV in the region $2.0 \leq y^* < 2.5$

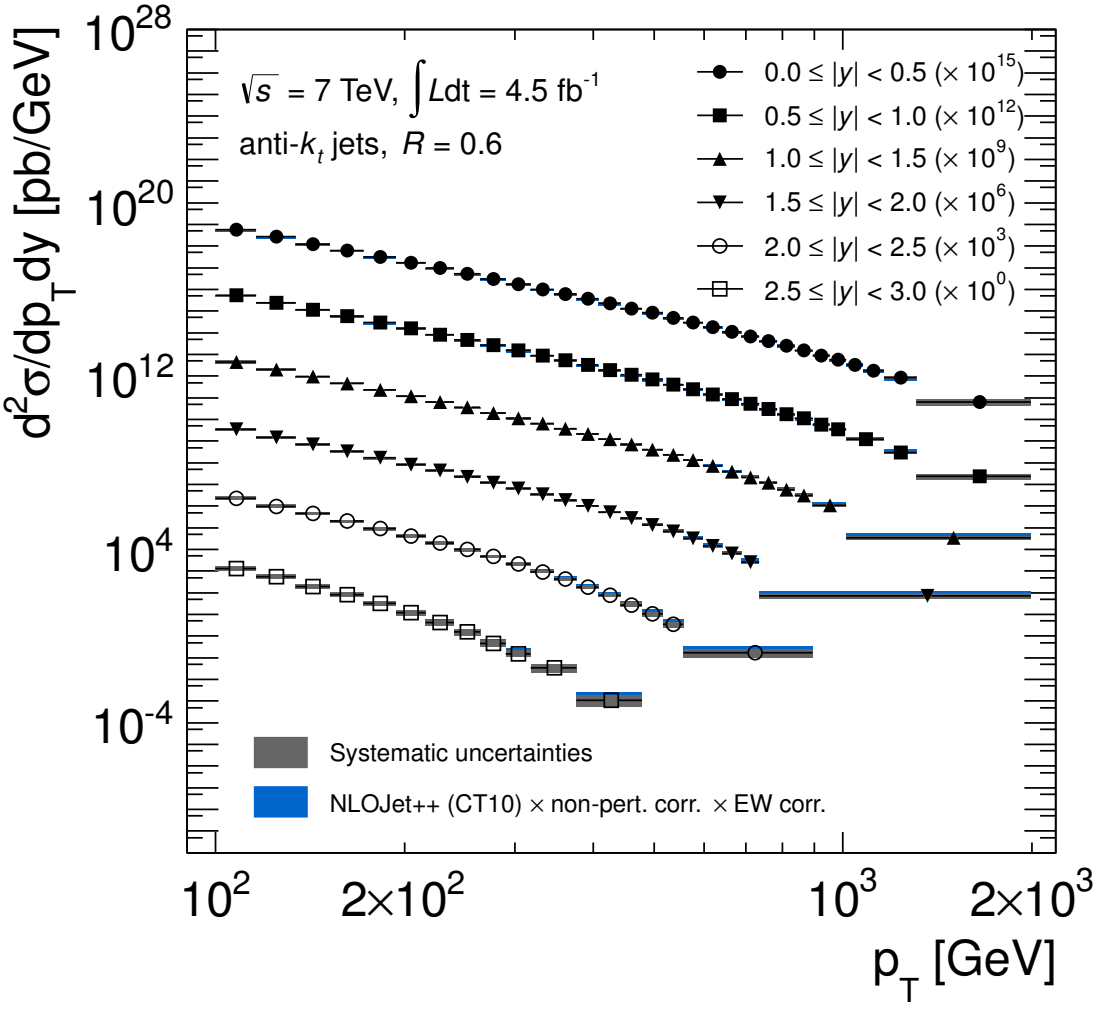

Figure 8.15: Double-differential inclusive jet cross-section for all rapidity bins included in the measurement. The unfolded data spectra are compared to NLOJet++ predictions, which are corrected for non-perturbative and electroweak effects. The blue filled areas indicate the theoretical uncertainty. The gray filled areas show the total systematic uncertainty. The jets were reconstructed using the distance parameter $R = 0.6$.

and extends to around 5 TeV spanning six orders of magnitude of the cross-section. The measurement was corrected for detector effects using the unfolding procedure described in Sec. 8.3.1. The resulting cross-sections are compared to Powheg predictions interfaced with Pythia showering for two different tunes and NLOJet++ predictions for various PDF sets. In case of NLOJet++ predictions non-perturbative and electroweak corrections were applied. Theoretical uncertainties from different sources were included as described in Sec. 3.2. In case of the Powheg predictions only statistical uncertainties are shown. An overlay of the steeply falling jet cross-section obtained from collision data and theoretical predictions using NLOJet++ with the CT10 PDF set are shown in Fig. 8.20 and 8.21.

The NLOJet++ predictions were generated using the following PDF sets: CT10, MSTW2008, and NNPDF2.3. The comparisons to data for the jet distance parameters $R = 0.4$ and $R = 0.6$ are shown in Fig. 8.22 and 8.23, respectively. The predicted spectra

agree within the uncertainties with the unfolded spectra using data. The best description is provided in the low-m_{12} region in the rapidity separation interval $0.0 \leq y^* < 1.0$. In the high-m_{12} regime deviations of up to 45% can be observed, where the prediction overestimates the data. The discrepancies are covered by the corresponding uncertainties. All three predictions behave in a similar way in the low-m_{12} region. At high-m_{12} MSTW2008 and NNPDF2.3 provide the best description. In the interval $1.0 \leq y^* < 2.5$ the predictions underestimate the data in the low-m_{12} regime, where the deviation amounts up to 20%. The ratios of the theory spectra with respect to data behave in a similar way as in case of $R = 0.4$ and $R = 0.6$ jets, where ratios calculated using $R = 0.6$ jets are below of that using $R = 0.4$ jets.

The ratios of the POWHEG predictions with respect to data for anti-k_T jets with $R = 0.4$ and $R = 0.6$ are shown in Fig. 8.24 and 8.25. POWHEG was interfaced with PYTHIA for parton showering and predictions were produces for the AUET2B and Perugia2011 tunes. The shape is described best in the rapidity separation region $1.0 < |y| < 2.0$ over the entire m_{12} range for both jet distance parameters. In the region $0.0 < |y| < 1.0$ the POWHEG predictions underestimate the data as also observed in the inclusive jet analysis. The deviations amount up to 5% in the low-m_{12} regime and become up to 20% as m_{12} increases. Comparing POWHEG with data for different anti-k_T distance parameters $R = 0.4$ and $R = 0.6$ slightly better predictions are provided for $R = 0.6$ jets. The predictions using the Perugia2011 tune predicts an approximately 10% higher cross-section compared to the AUET2B tune in the low-m_{12} region. This deviation decreases as m_{12} increases.

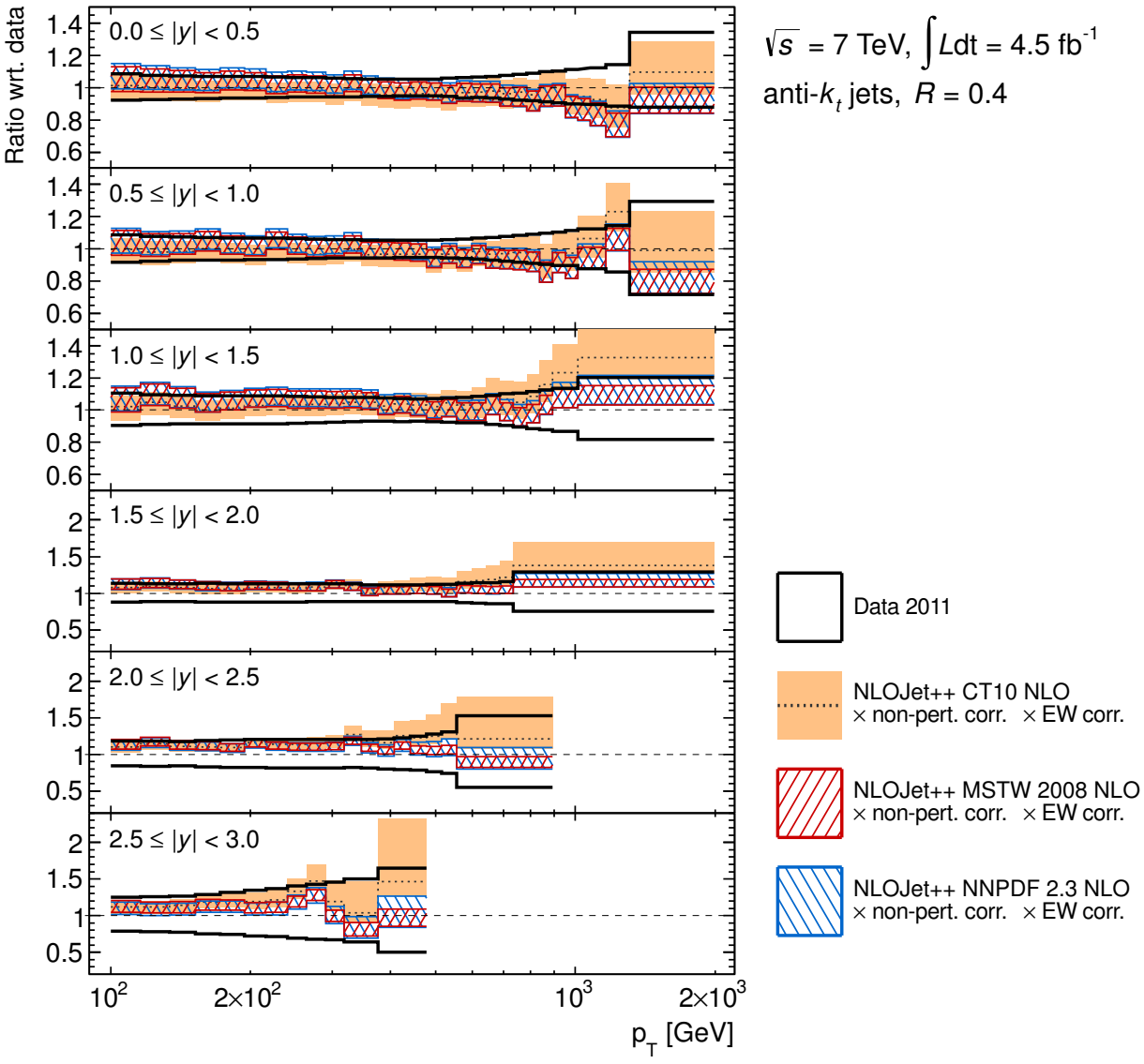

Figure 8.16: Ratios of NLOJET++ inclusive jet cross-section predictions using different PDFs with respect to the unfolded data. The following PDFs were used: CT10, MSTW2008, and NNPDF2.3. The ratios are shown for six different rapidity slices. The jets were reconstructed using the distance parameter $R = 0.4$. The black lines indicate the total systematic uncertainty.

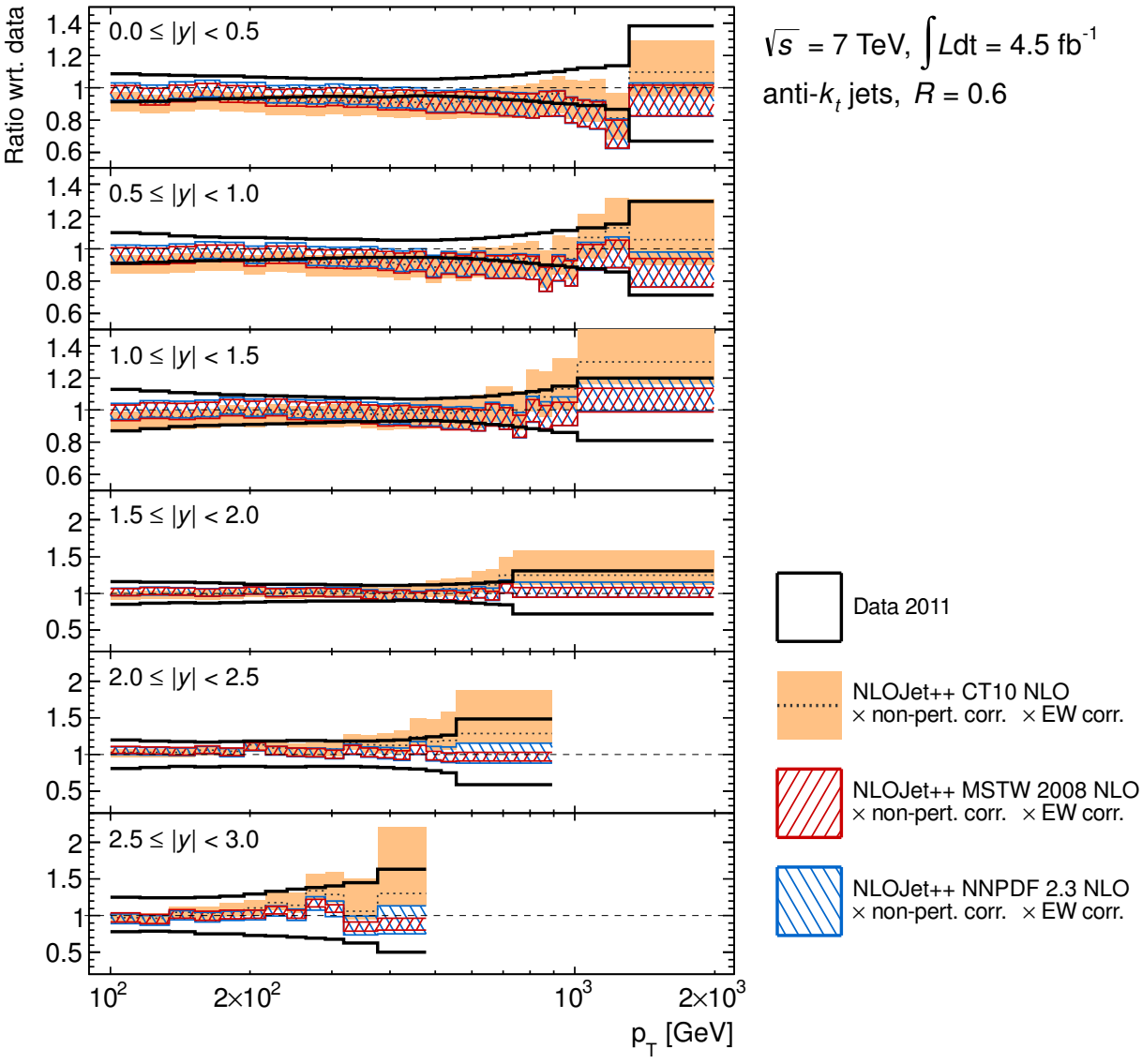

Figure 8.17: Ratios of NLOJET++ inclusive jet cross-section predictions using different PDFs with respect to the unfolded data. The following PDFs were used: CT10, MSTW2008, and NNPDF2.3. The ratios are shown for six different rapidity slices. The jets were reconstructed using the distance parameter $R = 0.4$. The black lines indicate the total systematic uncertainty.

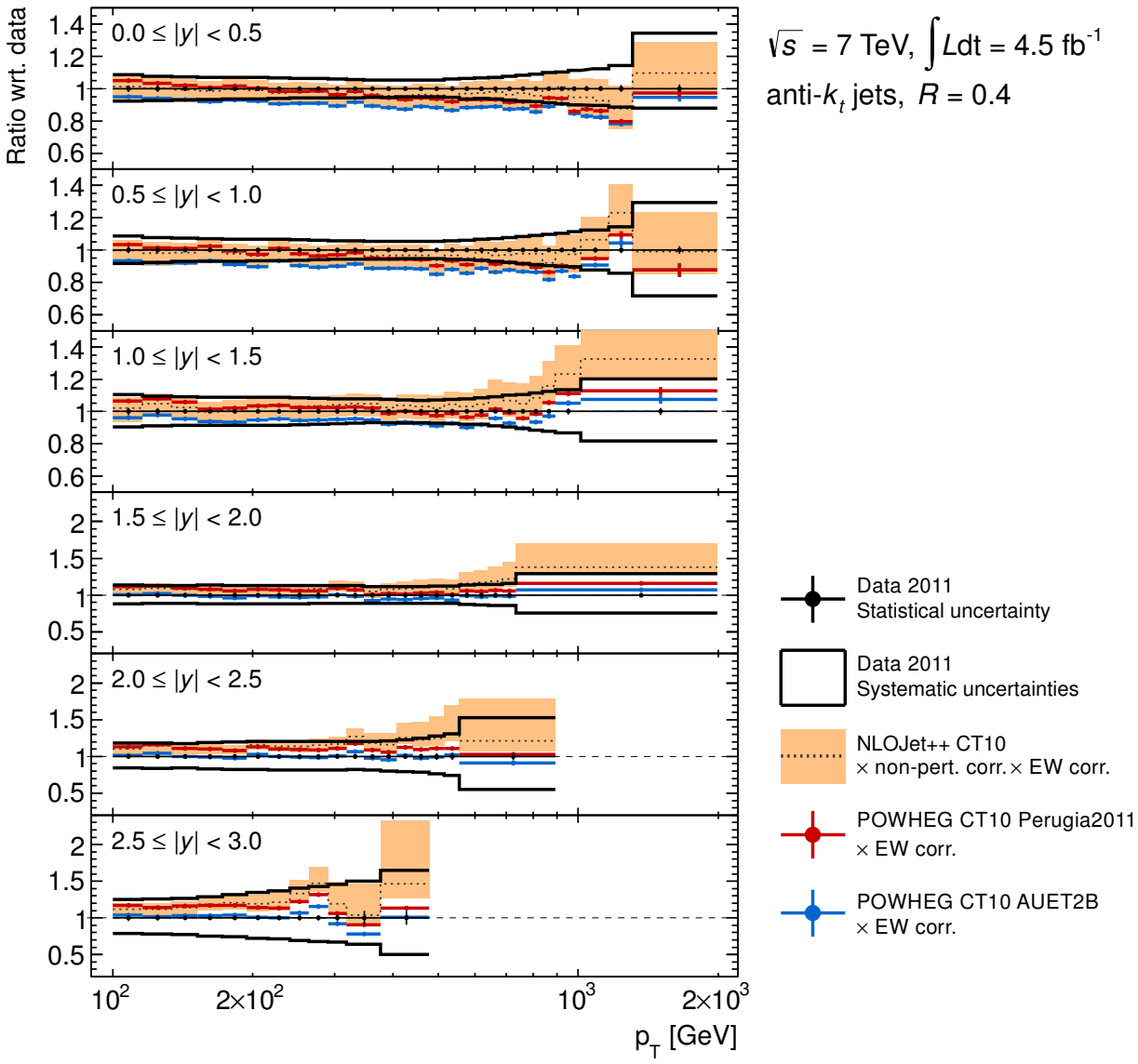

Figure 8.18: Ratios of NLOJET++ and POWHEG inclusive jet cross-section predictions using the CT10 PDF with respect to the unfolded data. The ratios are shown for six different rapidity slices. The jets were reconstructed using the distance parameter $R = 0.4$. The black lines indicate the total systematic uncertainty.

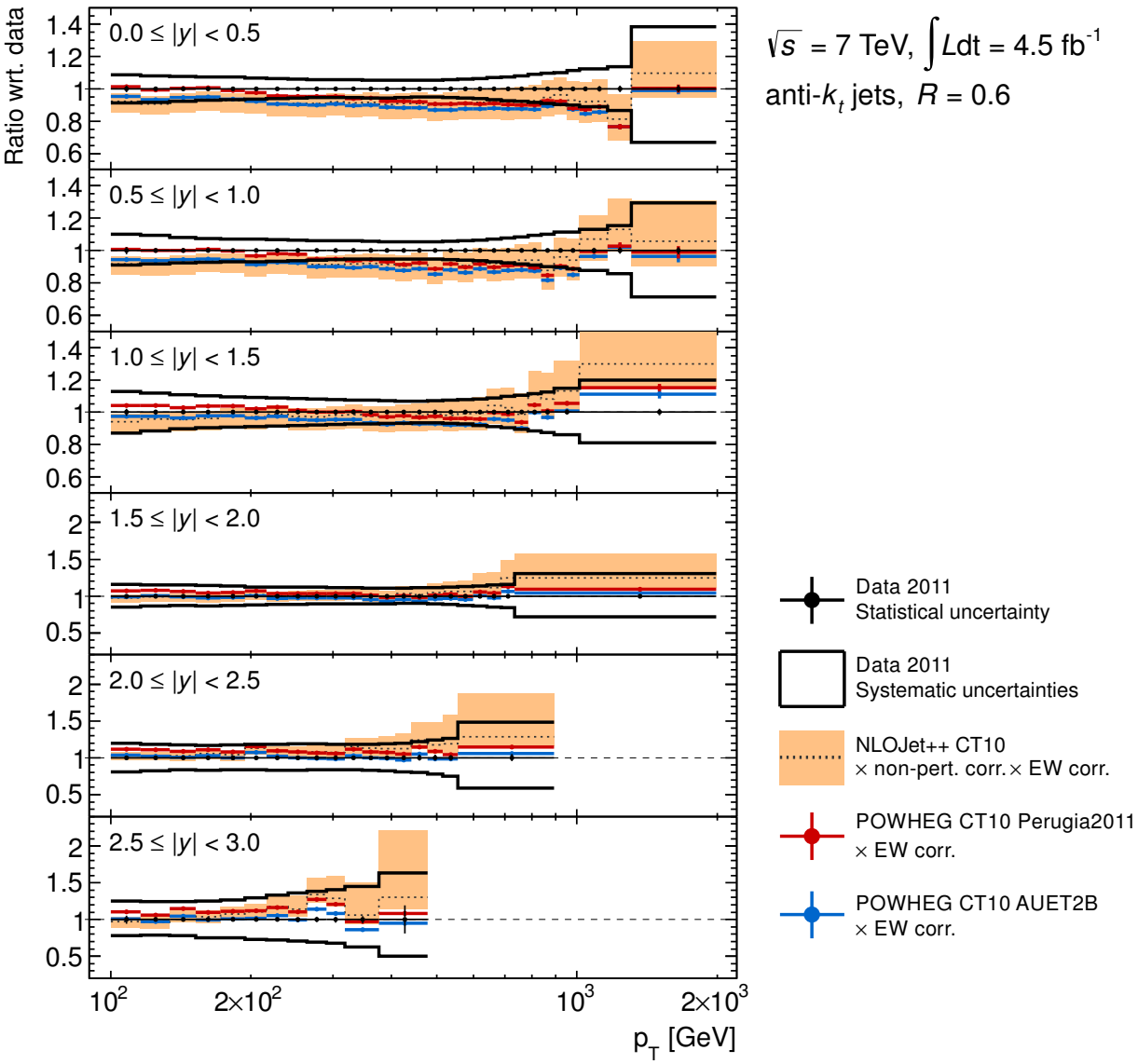

Figure 8.19: Ratios of NLOJET++ and POWHEG inclusive jet cross-section predictions using the CT10 PDF with respect to the unfolded data. The ratios are shown for six different rapidity slices. The jets were reconstructed using the distance parameter $R = 0.6$. The black lines indicate the total systematic uncertainty.

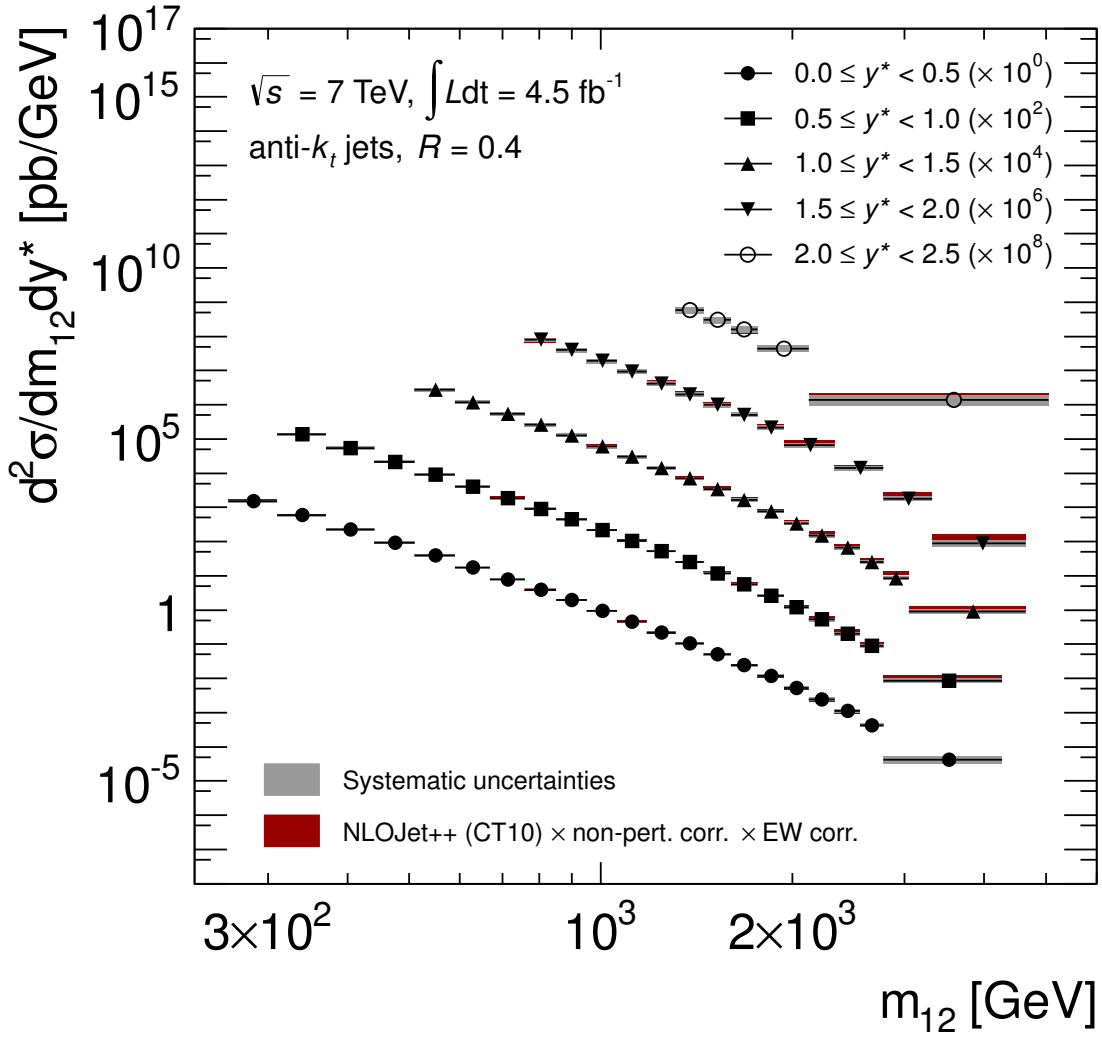

Figure 8.20: Double-differential dijet cross-section for all rapidity separation bins included in the measurement. The unfolded data spectra are compared to NLOJet++ predictions, which are corrected for non-perturbative and electroweak effects. The red filled areas indicate the theoretical uncertainty. The gray filled areas show the total systematic uncertainty. The jets were reconstructed using the distance parameter $R = 0.4$.

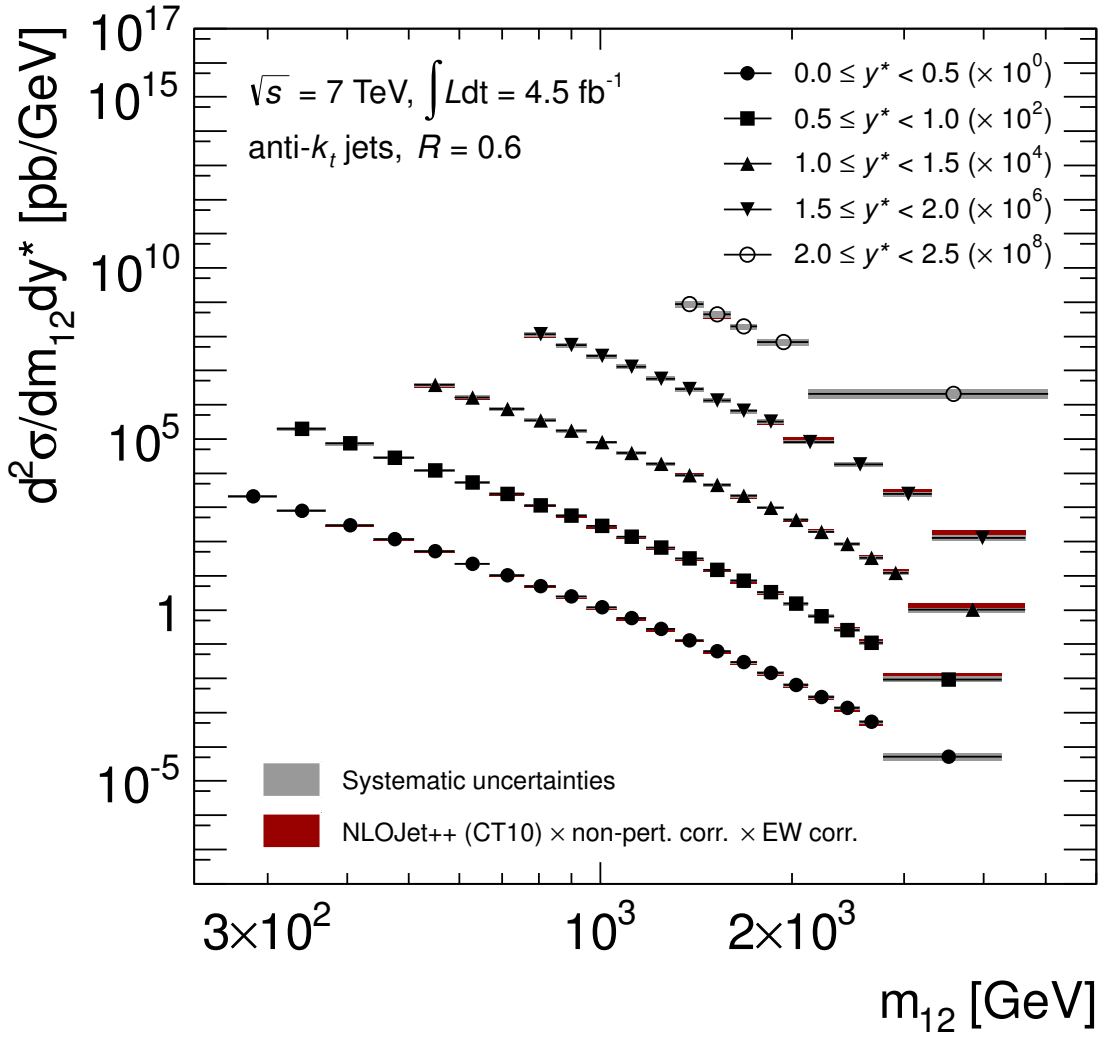

Figure 8.21: Double-differential dijet cross-section for all rapidity separation bins included in the measurement. The unfolded data spectra are compared to NLOJet++ predictions, which are corrected for non-perturbative and electroweak effects. The red filled areas indicate the theoretical uncertainty. The gray filled areas show the total systematic uncertainty. The jets were reconstructed using the distance parameter $R = 0.6$.

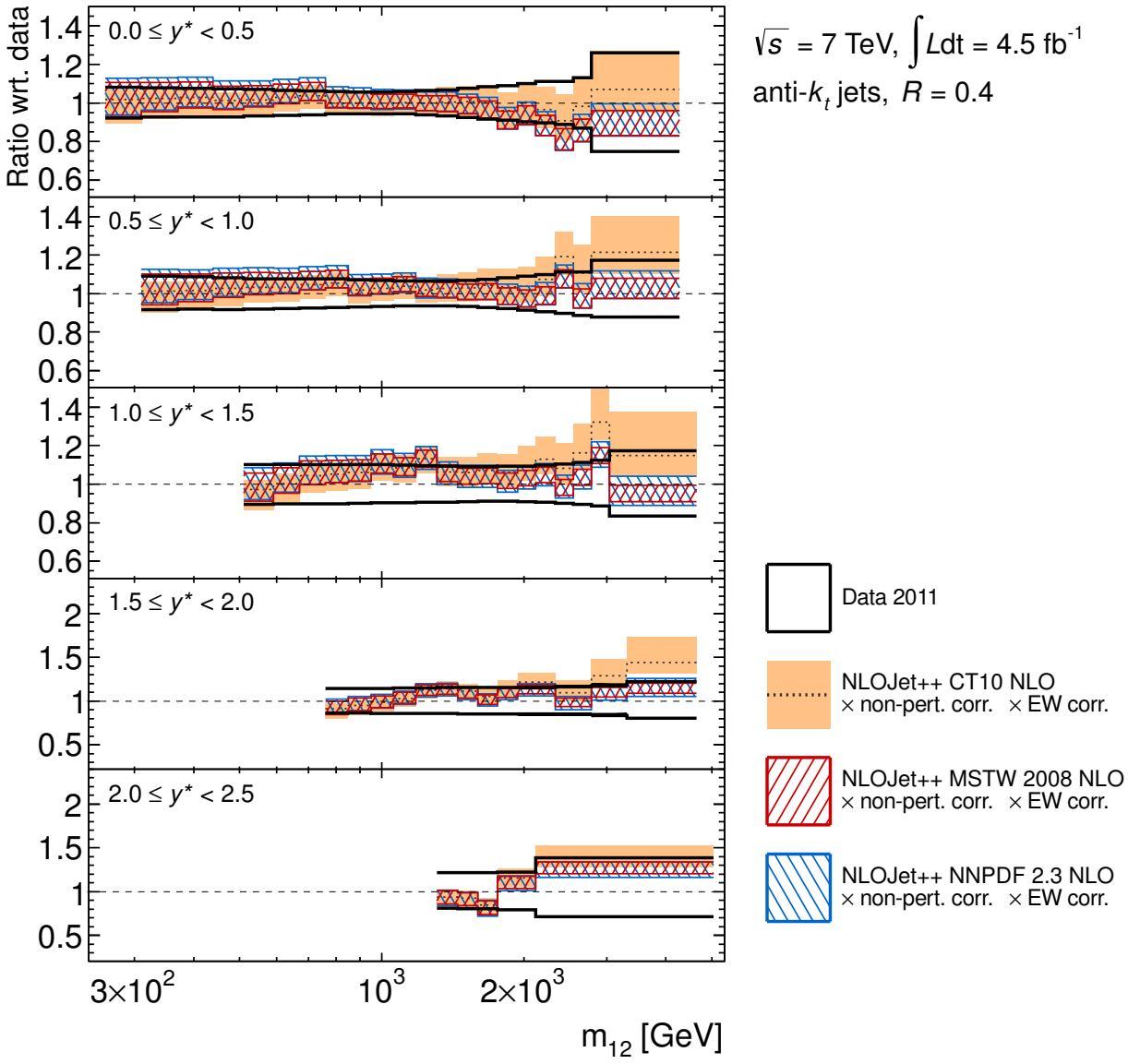

Figure 8.22: Ratios of NLOJET++ dijet cross-section predictions using different PDFs with respect to the unfolded data. The following PDFs were used: CT10, MSTW2008, and NNPDF2.3. The ratios are shown for five different rapidity separation slices. The jets were reconstructed using the distance parameter $R = 0.4$. The black lines indicate the total systematic uncertainty.

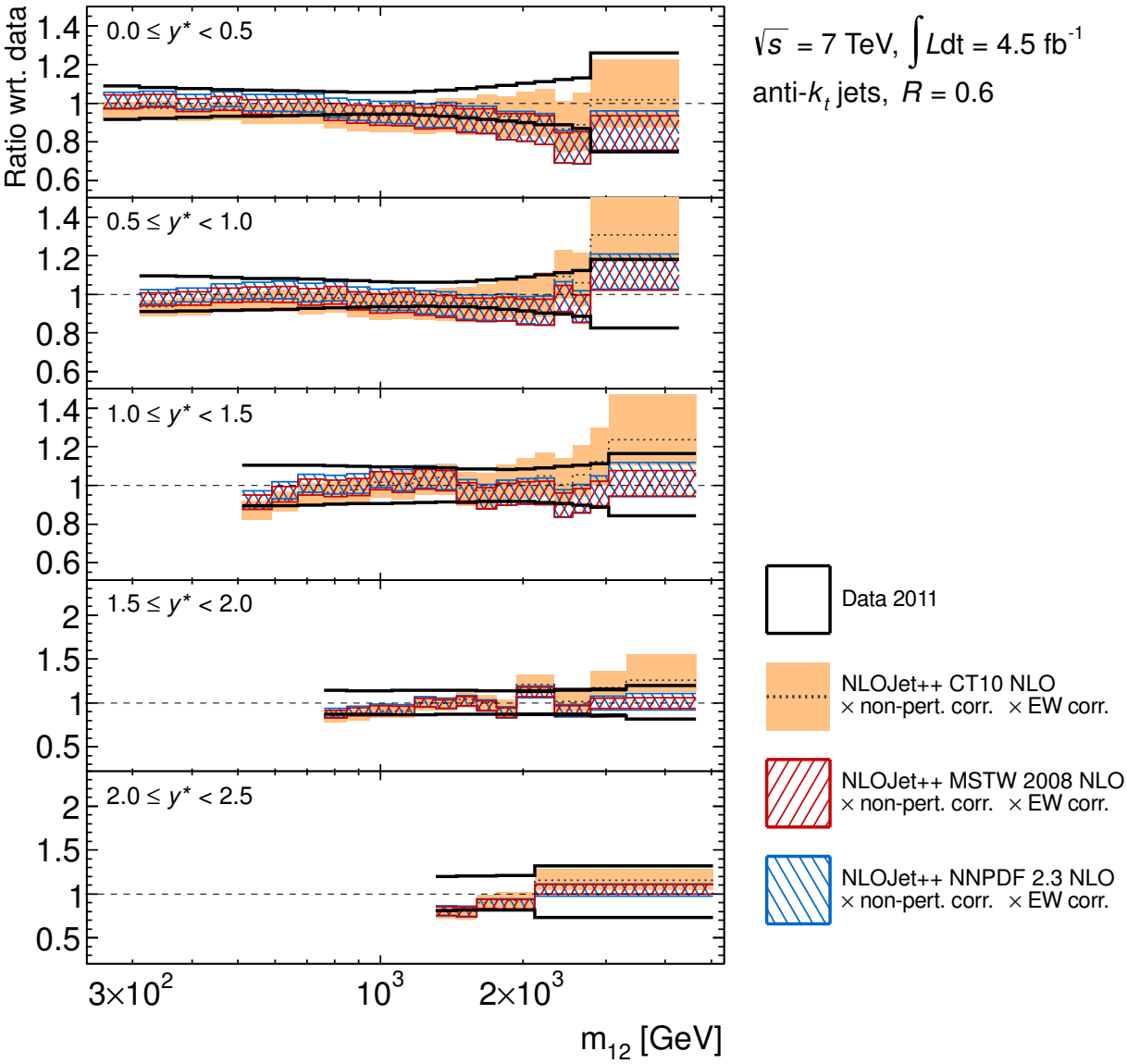

Figure 8.23: Ratios of NLOJET++ dijet cross-section predictions using different PDFs with respect to the unfolded data. The following PDFs were used: CT10, MSTW2008, and NNPDF2.3. The ratios are shown for five different rapidity separation slices. The jets were reconstructed using the distance parameter $R = 0.6$. The black lines indicate the total systematic uncertainty.

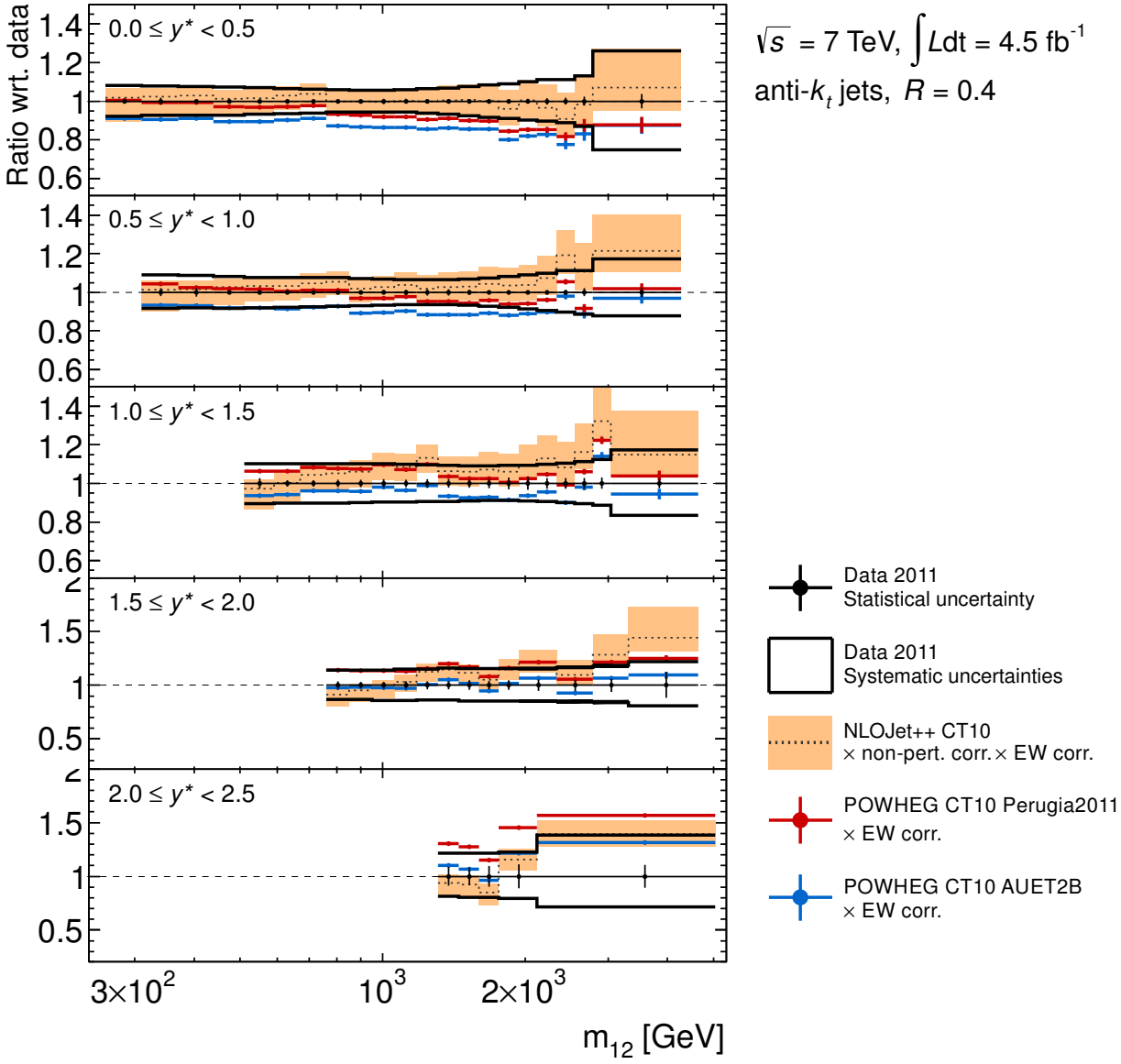

Figure 8.24: Ratios of NLOJET++ and POWHEG dijet cross-section predictions using the CT10 PDF with respect to the unfolded data. The ratios are shown for five different rapidity separation slices. The jets were reconstructed using the distance parameter $R = 0.4$.

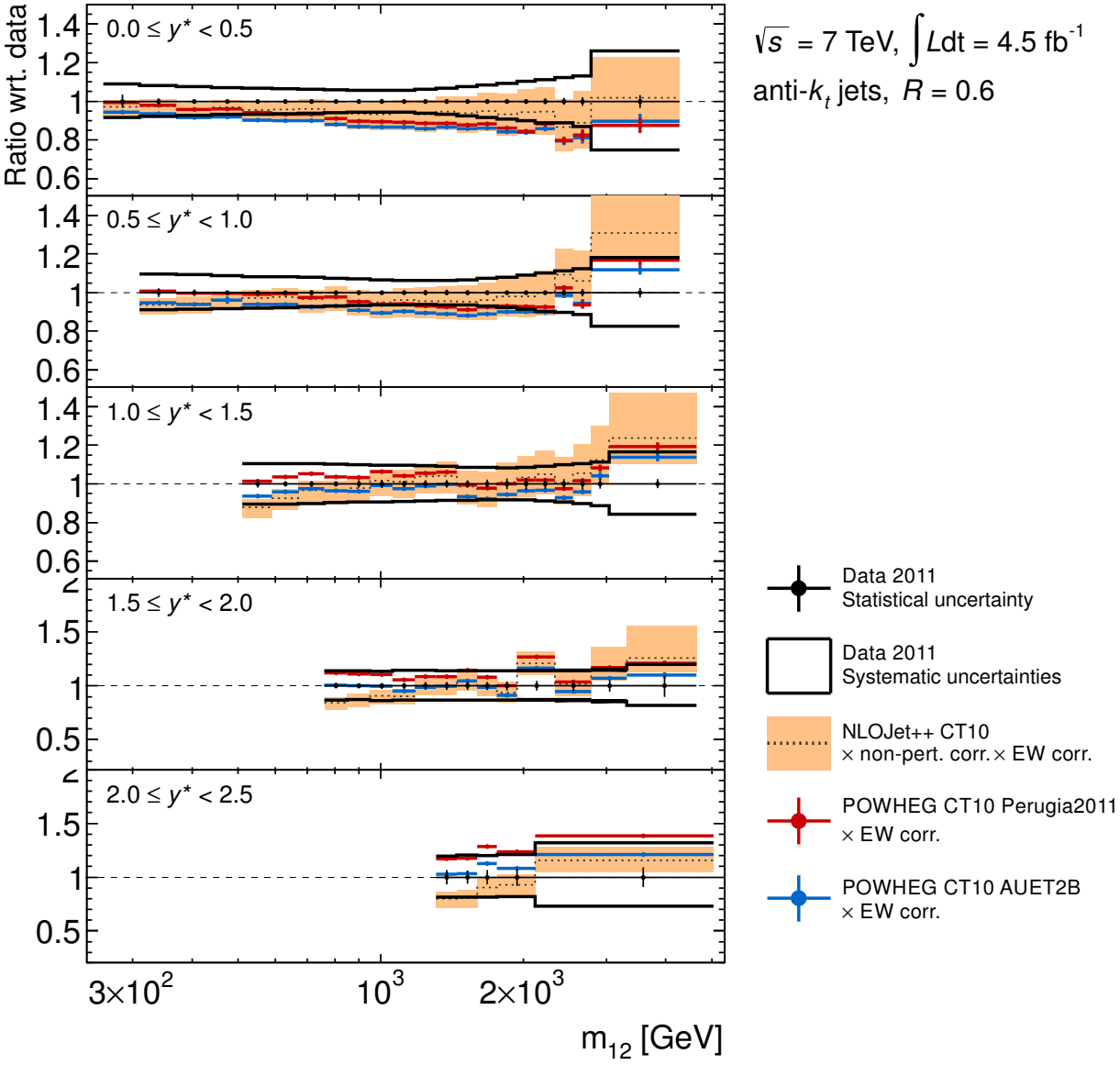

Figure 8.25: Ratios of NLOJET++ and POWHEG dijet cross-section predictions using the CT10 PDF with respect to the unfolded data. The ratios are shown for five different rapidity separation slices. The jets were reconstructed using the distance parameter $R = 0.6$.

9 Search for New Resonant-like Phenomena with Dijets

Several models beyond the Standard Model were developed, which predict massive particles produced in hard scattering processes. The models used in this analysis have a high probability to decay in quarks and gluons resulting in dijet final states. The models considered are introduced in Sec. 2.3. If such a new particle with a mass within the kinematic range covered by ATLAS exists, a local excess in the dijet mass spectrum could be observed. In the context of this search, 4.8 fb^{-1} of data was used. In Sec. 9.1 the event and jet selection is briefly discussed and the method to estimate the background is presented. In Sec. 9.2 statistical techniques are discussed, which were used to search for local deviations from the estimated background. In Sec. 9.3 the methods to determine the exclusion limits are presented. In the last part (cf. Sec. 9.4) of this chapter strategies are discussed, which can be used to improve the sensitivity to new physics phenomena. The results produced in context of this thesis were published in Ref. [148] and Ref. [33].

9.1 Event and Jet Selection

The event and jet selection deviates in some points from the selection used for the cross-section measurement described in Sec. 8.2. For instance, the cross-section measurements cover a wider kinematic range. In case of the search for new physics (NP) the kinematic range was restricted in order to improve the sensitivity to NP. The Jets were reconstructed using the anti-k_t clustering algorithm with the distance parameter $R = 0.6$ using topological cluster as input (cf. Sec. 5.1). The calibration was performed using the EM+JES scheme (cf. Sec. 5.4). The jet energy and direction were calibrated using Monte Carlo (MC) simulation and additionally further data-based corrections were applied, which compensate effects due to mis-modeling in MC simulation. By choosing the largest available jet distance parameter R, the probability to include the final-state radiation within the jet increases. In presence of a NP particle a larger radius would increase the sensitivity, because more events would be reconstructed around the mass of the new particle. On the other hand the radius is not large enough to compensate this effect due to influences from initial state radiation and underlying event[1] [32].

The observable used is the dijet invariant mass m_{jj} defined as follows[2]:

$$m_{\text{jj}} = \sqrt{(E_{\text{jet1}} + E_{\text{jet2}})^2 - (\vec{p}_{\text{jet1}} + \vec{p}_{\text{jet2}})^2}, \tag{9.1}$$

[1] The amount of contribution to the jet energy from in-time pile-up depends on the distance parameter R, therefore a jet distance parameter dependent pile-up correction was applied (cf. Sec. 5.4.1). This correction intends to make the jet energy measurement independent of the pile-up environment. Also, pile-up does not introduce bump-like structures which could be interpreted as a NP signal.

[2] The dijet mass used for the cross-section measurement is referred to as m_{12}. Different subscripts were chosen in order to distinguish between the two different analyses.

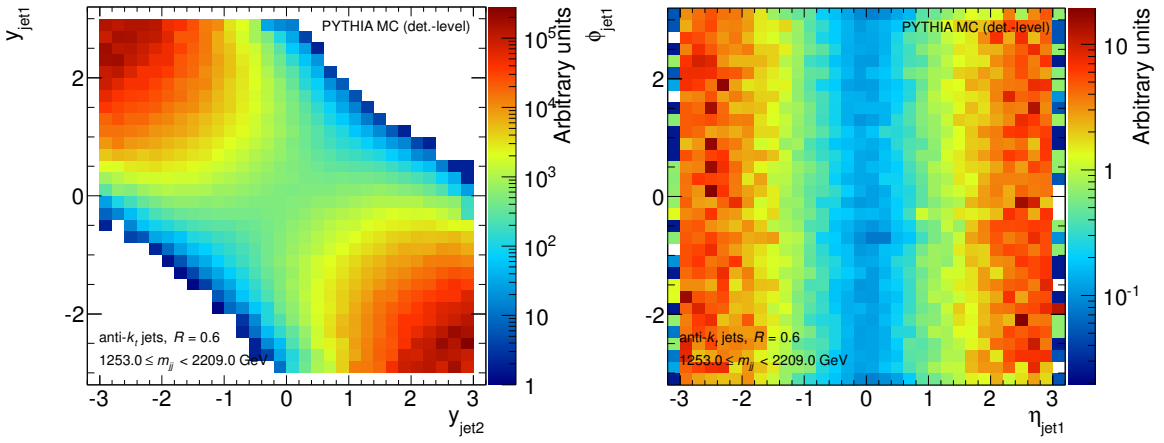

Figure 9.1: Left: distribution of dijet events according to the rapidities y_{jet1} and y_{jet2} of the first two leading jets. The distributions were made using Monte Carlo prediction at detector-level. Right: distribution of leading jets in dijet events according to ϕ_{jet1} and η_{jet1}. The jets were reconstructed using the anti-k_T algorithm with distance parameter $R = 0.6$ and were fully calibrated.

where E_{jet1} is the energy and $\vec{p}_{\text{jet1}}$ the momentum of the leading jet. By analogy, E_{jet2} is the energy and $\vec{p}_{\text{jet2}}$ the momentum of the second-leading jet. The event and jet selection was used in case of data and MC predictions. In the following the applied cuts are briefly discussed and are summarized in Tab. 9.1. This table provides detailed information on the number of rejected events. The remaining events were used to construct the final dijet mass spectrum. The order of the cuts in this table corresponds to the order given in the following.

Data quality and MC pile-up cuts: As the first step all luminosity blocks containing data which were recorded in presence of of temporary defects of detector components are rejected. A brief introduction on this subject can be found in Sec. 6.1.1. This selection of events was applied on data only.

Several cuts were applied in order to remove events causing large statistical error, which originate from the combination of pile-up simulation and the applied re-weighting strategy in MC. These cuts are described in Sec. 6.4 and applied to MC QCD simulation only.

Trigger selection: The single jet-triggers used in context of this thesis are introduced in Sec. 4.2.6 and 6.2. For the purpose of the search for NP, the 'EF Jet $E_T > 240$ GeV' high-level trigger was used. This trigger was not down-scaled during the data-taking period in 2011 and therefore no trigger re-weighting was applied. The trigger selection was performed on data only.

Primary collision vertex: The collision candidates were selected by requiring the presence of at least one reconstructed primary vertex which is consistent with the position of the collision point and which has at least two associated charged particle tracks with a reconstructed $p_T > 400$MeV. This cut removes events originating from beam-backgrounds as contributions from beam-gas collisions and other non-collision sources [117].

LArError-flag: The LArError-flag was introduced in Sec. 6.1.2. It indicates noise bursts and data integrity errors and was applied to data only.

Jet multiplicity: In order to be able to calculate the dijet mass m_{jj} at least two jets are required. Therefore a cut on the jet multiplicity is applied. This cut was used in the selection of the data and MC simulation. It has no effect, because all events at this point contain at least two jets.

Non-operational cells and non-instrumented regions: Non-operational cells and non-instrumented regions affect the jet measurement. This issue is discussed in greater detail in Sec. 6.1.2. The jet energy within these regions is estimated. This estimate is used to determine jet energy fractions in these regions. If one of the energy fractions is greater than 0.5, a jet is tagged. This cut rejects events if the leading or the second-leading jet is tagged according to this classification. If any other jet is tagged and has a $p_T > 0.3 \cdot p_{T,\mathrm{jet2}}$, the event is also rejected. This cut was applied in order to avoid events where e.g. the measured energy of the true second-leading jet is affected and its transverse momentum $p_{T,\mathrm{jet2}}$ is measured to be below $p_{T,\mathrm{jet3}}$. Because of the greater transverse momentum, the third-leading jet is used as input for the dijet mass calculation and thus the dijet mass is affected in this scenario. This cut was applied in collision data and MC simulations.

LAr calorimeter issue: As detailed in Sec. 6.1.2 due to malfunction of some LAr calorimeter components in approximately 1 fb^{-1} of the collected data, a veto on jets pointing to the affected region was applied. The affected region is localized between $-0.88 < \phi < -0.5$ and $-0.1 < \eta < 1.5$. In contradiction to the cross-section measurement events were removed where either of the two leading jets falls in the affected region or any of the other jets fall in this region and has a $p_T > 0.3 \cdot p_{T,\mathrm{jet2}}$. The motivation for the latter cut is the same as discussed in the context of non-operational and non-instrumented regions. Only events recorded within the period of malfunctioning of the LAr calorimeter were rejected. This cut was applied in data and MC simulation.

Jet quality: In order to remove events triggered by cosmic muons and other non-collision background, jet quality cuts were applied. The set of cuts in question was described in Sec. 6.1.2. For the search a looser cut set was chosen compared to the cross-section measurement referred to as Looser. This cut set is used in case of data and MC simulations.

Kinematic selection: In order to be consistent with the theoretical predictions produced using NLOJet++ (cf. Chap. 3) and the dijet cross-section measurement (cf. Chap. 8), events were retained, if $p_{T,\mathrm{jet1}} > 100$ GeV and $p_{T,\mathrm{jet2}} > 50$ GeV.

Further kinematic cuts were applied on the jet rapidity. The absolute value of the pseudorapidity of each jet was required to be within 2.8, where the lowest uncertainty on jet measurement is provided. In order to separate s- and t-channel processes, a cut on $|\Delta y| < 1.2$ was applied. This value was derived from an optimization study using the excited quark benchmark model and the Monte Carlo QCD prediction at detector-level. This study was performed using the pseudorapidity η which is approximately equal to the rapidity y. In Fig. 9.2 (left) the distribution of events according to the difference $\Delta\eta = \eta_{\mathrm{jet1}} - \eta_{\mathrm{jet2}}$ for excited quarks with a mass of 2 TeV is shown. The maximum number of events can be found around $\Delta\eta = 0$. In case of QCD, the minimum number

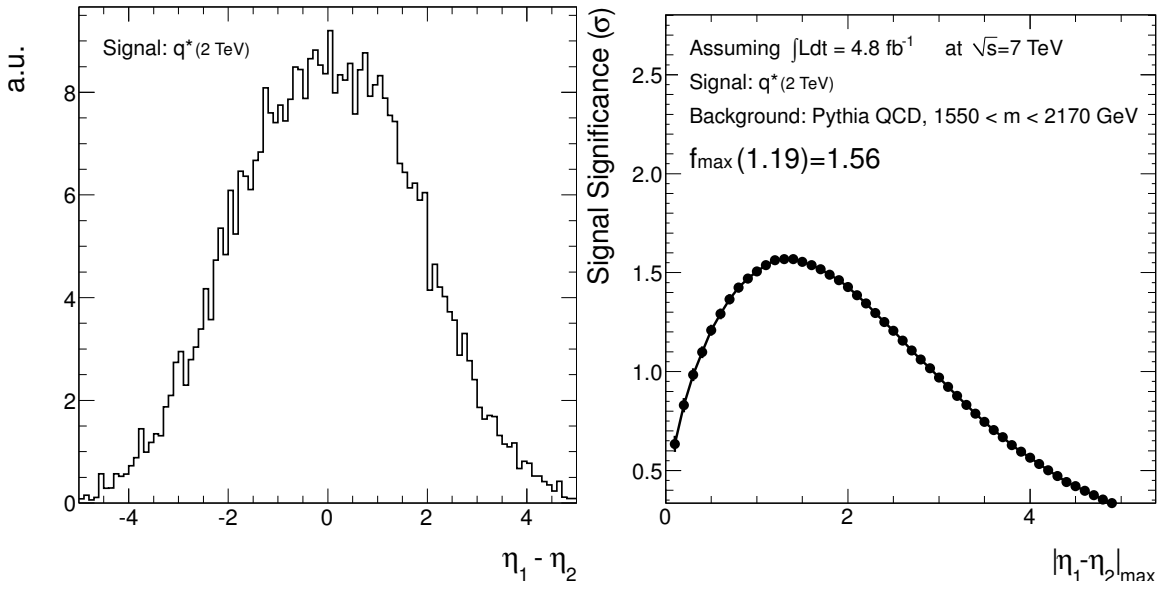

Figure 9.2: Left: $\Delta\eta = \eta_1 - \eta_2$ distribution for excited quarks (q*). Right: the signal-over-background ratio (significance) as function of the cut on $|\Delta\eta| < |\eta_1 - \eta_2|_{\max}$. The optimal cut threshold was found to be at 1.2 and thus the cut on the absolute value of the rapidity difference was chosen to be $|\Delta y| < 1.2$.

of events can be found around $\Delta\eta = 0$ as can be observed in Fig. 9.1 (left). In Fig. 9.2 (right) the significance as function $|\eta_{\text{jet1}} - \eta_{\text{jet2}}|_{\max}$ is shown, where $|\eta_{\text{jet1}} - \eta_{\text{jet2}}|_{\max}$ is the choice of the $|\Delta\eta|$ cut and the significance is defined as $S/\sqrt{B}$. The number of excited quark events S and the number of QCD MC events B was determined in the region 1550 GeV $< m_{\text{jj}} <$ 2170 GeV. The maximum of this distribution is located around the cut $|\Delta\eta| < 1.2$. Based on this information the cut $|\Delta y| < 1.2$ was applied in data and MC simulation. This behavior is independent of the type and mass of the NP particle used in context of this thesis.

The search for new phenomena was performed in the high-m_{jj} regime using the 'EF Jet $E_T > 240$ GeV' trigger. This trigger was not down-scaled during the data-taking. The method applied to determine the trigger efficiency as function of the dijet mass m_{jj} is described in Sec. 6.2. To be in the plateau where the trigger efficiency is above 99% the dijet mass m_{jj} was required to fulfill $m_{\text{jj}} > 847$ GeV. This threshold is chosen to be the lower edge of the bin, where the trigger efficiency requirement is fulfilled. The kinematic cuts were applied to data and MC simulations.

9.1.1 QCD Background Estimation

To avoid problems due to mis-modeling in Monte Carlo simulation, a data-driven method was used to estimate the background. For this purpose a smooth, monotonically decreasing function was fitted to the dijet mass spectrum at detector-level. The functional form was defined in Eq. 6.10 and is given in the following for convenience:

$$f(x) = p_1(1-x)^{p_2} x^{p_3 + p_4 \ln x}. \tag{9.2}$$

Cut type	N_{events}	f_{total}	r_{prev}
Total number of events	29255783	100%	
Data quality	26974246	92.2%	7.8%
Trigger selection	5092571	17.4%	81.1%
Primary collision vertex	5092011	17.4%	0.1 ‰
LArError-flag	5069998	17.3%	4.3 ‰
Jet multiplicity	5069998	17.3%	< 0.1 ‰
Non-operational cells and non-instrumented regions	5069961	17.3%	< 0.1 ‰
LAr calorimeter issue	5025839	17.2%	8.7 ‰
Jet quality: LOOSER scheme	5024530	17.2%	0.3 ‰
Kinematic selection: transverse momenta	5024332	17.2%	< 0.1 ‰
Kinematic selection: rapidity	2020161	16.9%	59.8%
Kinematic selection: dijet mass	792471	2.7%	60.8%

Table 9.1: List of cuts used for the event and jet selection in collision data. N_{events} is the number of remaining events after the application of a cut. f_{total} is the fraction of N_{events} with respect to the total number of events. r_{prev} is the fraction of rejected events with respect to the remaining number of events after the application of the previous cut.

In the dijet resonance search the definition of the variable x is given as $x \equiv m_{jj}/\sqrt{s}$, which reduces the number of parameters to four compared to the function defined in Eq. 6.10. The functional form of Eq. 6.10 is phenomenologically motivated and a detailed description of the properties are given in Sec. 6.2. The free parameters $p_{1..4}$ were constrained such that for $x \to 0$ the function tends to $f(x) \to +\infty$ and for $x \to +\infty$ the function tends to $f(x) \to 0$. This is realized by forcing the parameter p_2 to be negative only, namely $p_2 < 0$.

The distribution of the number of events in each bin is described by the Poisson p.d.f.[3] To get the best description of the data a so-called Likelihood fit was performed based on the Poisson p.d.f. as detailed in Sec. 6.2. To take effects due to non-equidistant binning into account, the bin width normalized spectra were taken as input for the fitting procedure. In order to justify the usage of the function as background estimate, the function was fitted to the Monte Carlo QCD predicted spectrum at reconstruction-level. The Monte Carlo simulation at reconstruction-level is available at leading-order (LO), bin-by-bin correction factors were applied to estimate the next-to-leading order (NLO) dijet mass spectrum. These correction factors are denoted as k-factors. The k-factor for a given bin i is defined as follows:

$$k_i = \frac{N_i^{\text{NLO}}}{N_i^{\text{Pythia show}}}. \tag{9.3}$$

The NLO dijet mass spectrum (N_i^{NLO}) was produced using the NLOJet++ generator with the CT10 parton density function (PDF). The LO spectrum ($N_i^{\text{Pythia show}}$) was generated using Pythia 6 using the CT10 PDF with parton showering enabled only. Non-perturbative effects including the primordial k_T, hadronization, and underlying event

[3] Using the Gaussian p.d.f. in the fitting procedure cause biased results in the high-m_{jj} tail due to low statistical power.

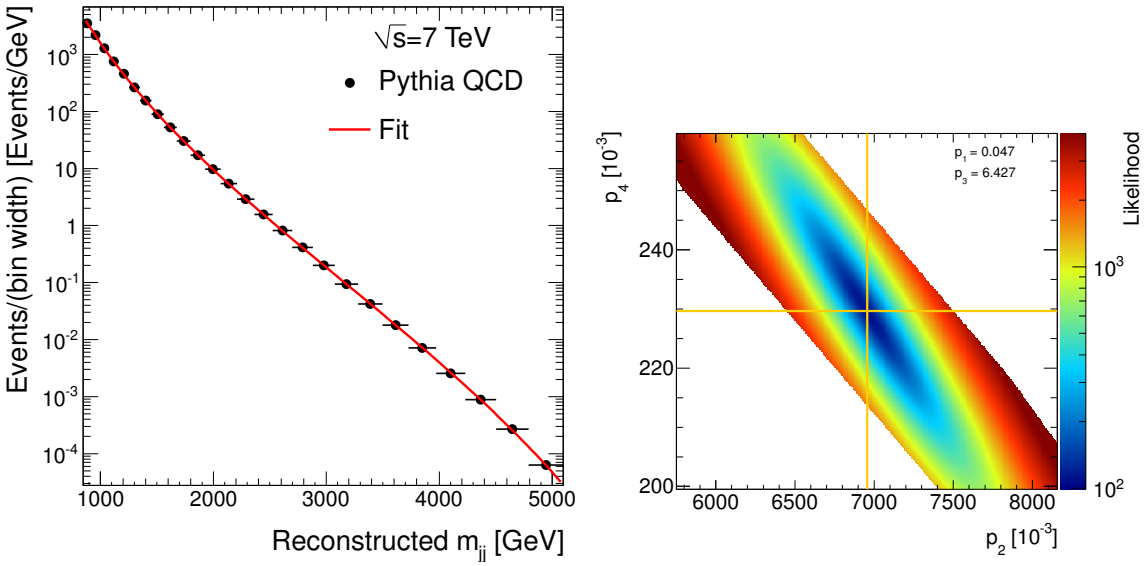

Figure 9.3: Left: bin width corrected number of simulated events as function of the dijet mass m_{jj}. This spectrum was corrected using k-factors defined in Eq. 9.3. The red line shows the smooth fit using the function defined in Eq. 9.2. This function was used in order estimate the background from the dijet mass spectrum obtained using collision data. Right: the parameter space for $p_1 = 0.047$ and $p_3 = 6.427$. The horizontal and vertical lines indicate the values found by the minimizer. The parameter space was also scanned 'brute force' and the parameter values determined using the minimizer algorithm were found to define the global minimum of the Likelihood.

(UE) were disabled (cf. Sec. 2.1.2 and Chap. 3). The aim of this method is to extract the differences of the NLO calculation compared to the Pythia shower model by simultaneously preserving the non-perturbative effects. The k-factor correction increases with the dijet mass. The distribution is corrected by approximately 3% at 1 TeV, 10% at 3 TeV and 20% at 4 TeV [149]. In Fig. 9.3 (left) the predicted QCD dijet mass spectrum and the corresponding fit are shown. As can be observed from this figure, the function given in Eq. 9.2 is capable to describe the Monte Carlo simulated spectrum at reconstruction-level and therefore can be used for the data-driven background estimation.

The following parameters with a $\chi^2/\mathrm{NDF} = 17.65/22 = 0.80$ were found by the minimizer using the data spectrum as input: $p_1 = 0.047 \pm 0.001$, $p_2 = 6.96 \pm 0.06$, $p_3 = 6.43 \pm 0.01$, and $p_4 = 0.230 \pm 0.004$. The fit was performed taking the value at the bin center as input. The projection (p_2 vs. p_4) of the parameter space with fixed parameters p_1 and p_3 is shown in Fig. 9.3 (right). The parameters are correlated and several local minima with similar likelihood values in the vicinity of the global minimum exist. That means several solutions are possible yielding comparably good fit results[4]. Nevertheless, this function was found to describe the data and Monte Carlo prediction best [148] and was chosen for the background estimation. An additional advantageous characteristic of this function is the behavior of the fit in presence of a narrow resonance-like structure. The function

[4] A brute force scan of the four-dimensional parameter space was performed and the results obtained by *Minuit2* were confirmed.

is not capable of fitting a resonance. Nevertheless in such a scenario the background estimation is biased. Therefore a mechanism was introduced to detect the position of the anomaly and re-fit the data-spectrum omitting the affected bins to minimize the bias (cf. Sec. 9.2.2). The χ^2 p-value[5] was used to activate this mechanism, where the threshold was chosen to be 0.1. The final dijet mass spectrum and the background estimate are shown in Fig. 9.4. This is the basis for the search for NP. In the upper panel the spectrum obtained using data (filled points) and the background estimation (solid line) are shown. In consistency with the input data for the fit, the background was converted to a histogram using the fit function evaluated at the bin center. The panel in the middle of this figure shows the ratio between the spectrum obtained using data and the background estimate. In both panels the expected signal for three different excited quark masses (cf. Sec. 2.3) was added to the background and is shown in three different colors as open circles: red, blue, and magenta. The lower panel shows the bin-by-bin significance. It is derived from the Poisson distribution characterized by the number of background events. For this distribution the p-value (cf. Sec. 9.2) was determined on the basis of this Poisson p.d.f. using data. The p-value is translated to a significance using a Gaussian p.d.f. The resulting quantity is called z-value[6]. The negative sign was introduced artificially to indicate that the number of data events is below of that obtained from the background [150].

9.2 Search for New Physics

In the following different goodness of fit tests are discussed. The aim is to test the consistency of collision data D with the background-only hypothesis H_0 derived from data as described in Sec. 9.1.1. An significant inconsistency between D and H_0 suggests a discovery[7] and further tests can be performed with signal hypotheses to characterize the new phenomenon.

For each test a so-called test statistic t was defined to quantify the difference between D and H_0. By construction, t increases with increasing discrepancy. The result of a test is the so-called p-value defined in Eq. 9.4. The p-value is the probability for a single measured test statistic t of being greater than or equal to the observed test statistic t_0. Small p-values indicate a disagreement between data and the background from the point of view of the background-only hypothesis. The p-value can be calculated exactly if the probability density function describing the statistic t is known analytically:

$$p\text{-value} = \int_{t_0}^{\infty} g(t|H_0)dt. \tag{9.4}$$

An estimate of the distribution $g(t|H_0)$ can be produced using pseudo-experiments and

[5] The χ^2 p-value was determined analytically using the χ^2 distribution for a given number of degrees of freedom (cf. Sec. 9.2.1).

[6] In order to determine the z-value the inverese error function was used: 'sqrt(2) $\cdot$ TMath :: ErfInverse(1$-$2 $\cdot$ p-value)'.This function is provided by the ROOT framework. [150]

[7] If a significant inconsistency between D and H_0 is observed, the first step is to figure out, whether the observation can be explained e.g. by detector or calibration effects. If these possibilities are excluded further steps can be taken to analyze the new phenomenon.

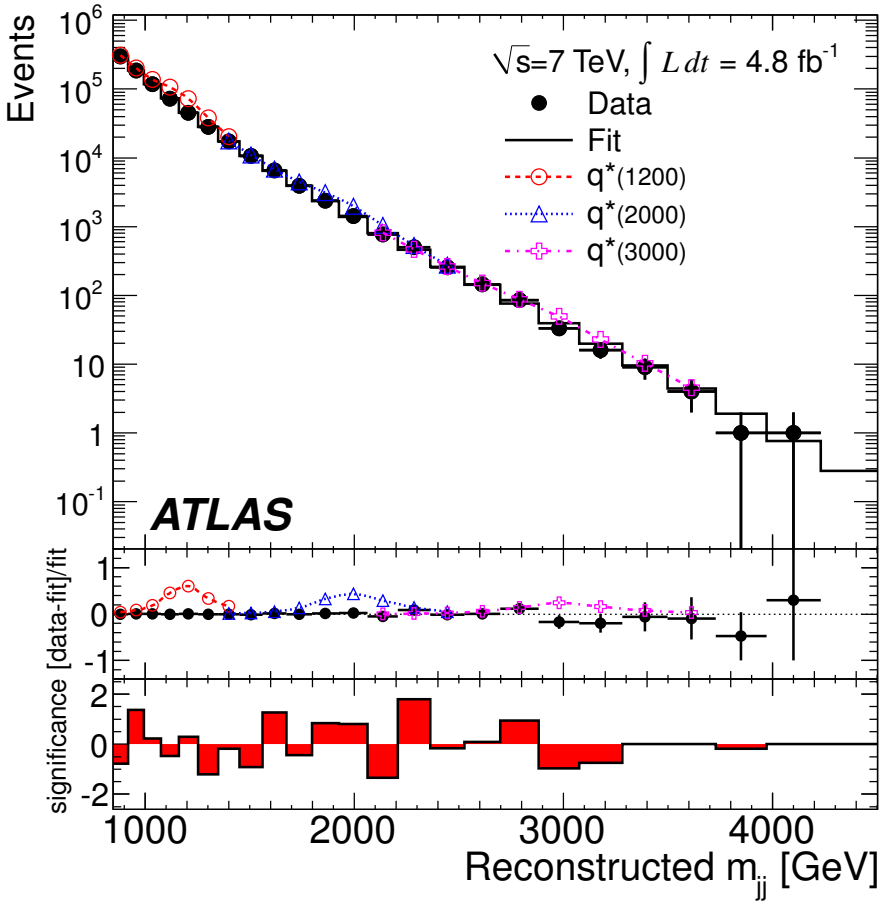

Figure 9.4: The reconstructed dijet mass distribution (filled points) fitted with a smooth functional form. The resulting fit was converted to a histogram (solid line). Mass distribution predictions for three q* masses added to the background are shown additionally. The middle part of the figure shows the data minus the background fit, divided by the fit. The bin-by-bin significance of the data-background difference is shown in the lower panel. [33]

the p-value can be estimated as follows:

$$p\text{-value} = \frac{N_{\mathrm{PE}}(t \geq t_0)}{N_{\mathrm{PE}}}, \tag{9.5}$$

where $N_{\mathrm{PE}}(t \geq t_0)$ is the number of pseudo-experiments with test statistic t above the observed statistic t_0 and N_{PE} the total number of pseudo-experiments. The pseudo-experiments were generated according to the Poisson p.d.f. assuming the background-only hypothesis. The random numbers were generated using the expectation values obtained from the function fitted to the data spectrum. The pseudo-data spectra were treated in the same way as the observed data. For each pseudo-experiment the same function was fitted and was taken as background estimate (H_0). This treatment ensures consistency in methodology and takes the fit uncertainty due to statistical fluctuations into account. For each of the pseudo-experiments a test statistic t was calculated to generate a distribution, which is used to calculate p-values.

Three types of tests are discussed in the following: Pearson's χ^2, $-\ln L$, and BumpHunter. The χ^2 and $-\ln L$ tests are used to test the background-only hypothesis. The latter method is designed to find the most significant local excess based on the $-\ln L$ test. The systematic uncertainties were not used in the context of the goodness of fit tests to avoid the reduction of the significance in presence of new resonance-like structures. The full treatment of systematic uncertainties was performed in the limit setting procedure described in Sec. 9.3.

9.2.1 $\chi 2$ and $-\ln L$

The test statistic in context of Pearson's χ^2 text is defined as follows:

$$t_{\chi^2} \equiv \chi^2 \equiv \sum_i \left(\frac{d_i - b_i}{\sqrt{b_i}} \right)^2 , \tag{9.6}$$

where d_i is the number of events in data in bin i, and b_i the number of background events derived using the fit. The resulting p-value is 0.73, indicating a good agreement between data and background estimate. This p-value corresponds to a z-value of $-0.6\ \sigma$. The test statistic t_{χ^2} is defined in the context of Gaussian distributed random numbers. The Gaussian distribution is an approximation of the real probability density function and provides a poorer description in bins with low event statistics. The $-\ln L$ test statistic $t_{-\ln L}$ was constructed from the product of Poisson probabilities in each dijet mass bin i and is expected to provide a better description of the true underlying p.d.f.:

$$t_{-\ln L} = -\ln \prod_i \left(\frac{b_i^{d_i}}{d_i!} \cdot \mathrm{e}^{-b_i} \right) = -\sum_i \ln \frac{b_i^{d_i}}{d_i!} \cdot \mathrm{e}^{-b_i} \tag{9.7}$$

The p-value was calculated using Eq. 9.5 and was found to be 0.55 which corresponds to a z-value of $-0.1\ \sigma$. The outcome of both goodness of fit tests is consistent with the background-only hypothesis.

9.2.2 BumpHunter

The statistical tests discussed in the previous sub-section are not providing information on the position of a local discrepancy. In principle this is the case for the bin-by-bin significance shown in Fig. 9.4. But a scan for statistical significant discrepancies introduces the so-called look-elsewhere effect (LEE), because the probability to observe a local statistically significant excess increases with the number of tests performed. This effect has to be taken into account when deriving the p-value of the most discrepant bin.

The BumpHunter [151] algorithm scans for local excesses with search windows of various sizes at various positions. The dijet mass binning is constructed such that a narrow signal would have a width of at least two bins which is taken as the minimum window size for the scan. By analogy with the goodness of fit tests in the previous sub-section the BumpHunter test statistic distribution was derived using pseudo-experiments. The observed test statistic t_0 was used to determine the BumpHunter p-value according to Eq. 9.5. For a given position and window size, the sum of the number of events in each

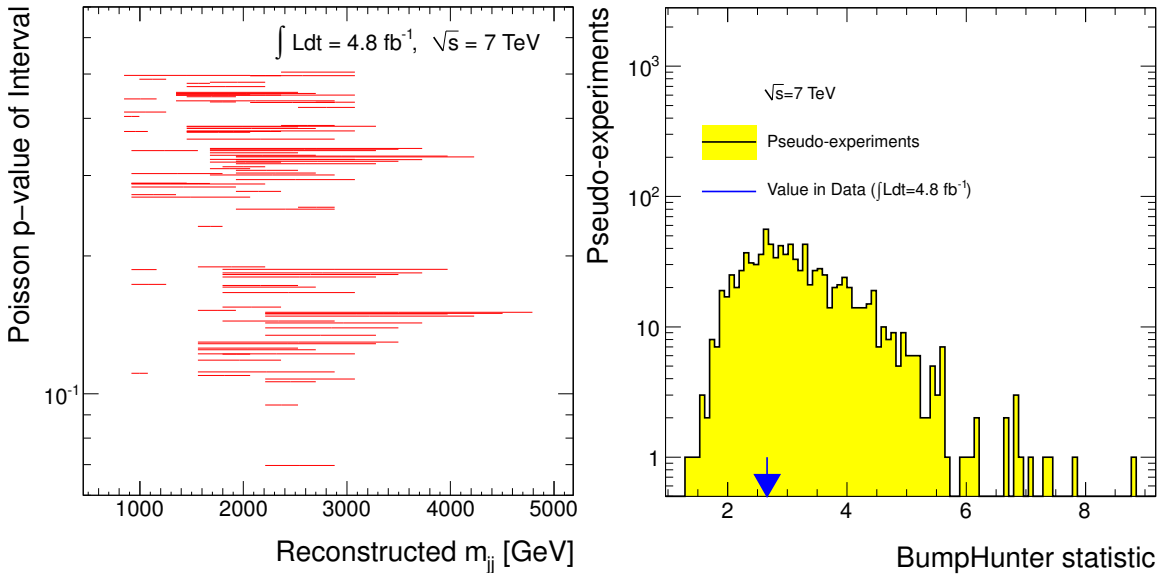

Figure 9.5: Left: the so-called BumpHunter tomography plot. It shows the Poisson p-values for all intervals scanned by the BumpHunter algorithm using data and background as input. Right: the BumpHunter test statistic (cf. Eq. 9.8) distribution derived by generating pseudo-experiments using the background estimate as basis. For this purpose 1000 pseudo-experiments were generated. The observed test statistic is indicated as the blue arrow.

bin k within the interval i in data $D_i = \sum_k d_k$ and the sum of the background events $B_i = \sum_k b_k$ in the same interval was used to determine the Poisson distribution $P_i(D_i, B_i)$. The constructed Poisson distributions $P_i(D_i, B_i)$ were used to calculate the p_i-value for each setup i. This Poisson p-values for all scanned intervals are shown in Fig. 9.5 (left). The so-called BumpHunter test statistic is defined as:

$$t = -\ln(\min\{p_i\text{-value}\}). \tag{9.8}$$

The minus sign and the natural logarithm function are an arbitrary choice, which ensures an increasing t as $\min\{p_i\text{-value}\}$ decreases and avoids small values of t. The BumpHunter p-value is by construction already corrected for the LEE. The distribution according to the BumpHunter test statistic t is shown in Fig. 9.5 (right).

The most significant discrepancy identified by the BumpHunter algorithm in the observed dijet mass distribution is a 4-bin excess in the region 2.21 TeV $< m_{\text{jj}} <$ 2.88 TeV. This interval is associated with the lowest Poisson p-value as indicated in Fig. 9.5 (left). The BumpHunter p-value was found to be 0.69 as indicated in Fig. 9.5 (right). It is the area of the distribution above the observed BumpHunter test statistic t_0, which is shown as blue arrow. This p-value corresponds to a z-value of $-0.5\ \sigma$. This test shows no evidence for significant resonant structures in the dijet mass spectrum.

9.3 Limit Setting

As discussed in Sec. 9.2 no evidence for narrow resonant-like phenomena was found in the dijet mass spectrum. Thus exclusion limits on cross-section times acceptance $\sigma \times \mathcal{A}$ as function of the predicted masses ν for several NP models decaying into dijets as introduced in Sec. 2.3 are presented. The acceptance $\mathcal{A}$ covers the detector acceptance and other inefficiencies introduced by the event and jet selection. A Bayesian method was chosen to determine exclusion limits for NP models considered.

9.3.1 The Bayesian Approach

The Bayes' theorem can be written as follows [17]:

$$P(\text{theory}|\text{data}) \propto P(\text{data}|\text{theory})P(\text{theory}), \tag{9.9}$$

where $P(\text{theory})$ is the prior probability for the theory, which reflects the degree of belief before carrying out the measurement, and $P(\text{data}|\text{theory})$ is the probability to have gotten the data actually obtained, given the theory. The latter conditional probability is also called likelihood. In context of the limit setting, the likelihood function L_ν is defined as the product of Poisson probabilities. For a given model and mass ν, the likelihood of having observed data $D = \{d_i\}$ given an amount of signal $S = \{s_i\}$ and given the background $B_\nu = \{b_{\nu_i}\}$ is defined as:

$$L_\nu(D|B_\nu, S) = \prod_i \frac{(b_{\nu_i} + s_i)^{d_i}}{d_i!} \cdot \mathrm{e}^{-(b_{\nu_i}+s_i)}, \tag{9.10}$$

where d_i is the number of events in bin i, b_{ν_i} is the number of events derived using the fit in bin i, and s_i is the number of signal events in bin i. For a given number of signal events S the distribution of s_i in each dijet mass bin i as well as the the number of events b_{ν_i} are dependent on various systematic uncertainties. Thus the likelihood can be written as $L_\nu(D|S, \lambda_{1..n})$, where the considered systematic uncertainties are represented by the nuisance parameters $\lambda_{1,..,n}$, where n is the numbers of the latter. The posterior probability density function defined using the Bayes' theorem (cf. Eq. 9.9) is then:

$$P_\nu(S, \lambda_{1..n}|D) = L_\nu(D|S, \lambda_{1..n}) \frac{\pi(S, \lambda_{1..n})}{\mathcal{N}_\nu}, \tag{9.11}$$

where $\pi(s, \lambda_{1..n})$ is the prior and $\mathcal{N}_\nu$ is a normalization factor ensuring $P_\nu(S, \lambda_{1..n}|D)$ to be a probability density function. The nuisance parameters $\lambda_{1..n}$ were assumed to be independent and distributed according to the Gaussian distribution. Therefore the prior can then be written as:

$$\pi(S, \lambda_{1..n}) = \pi(S)\pi(\lambda_1)\pi(\lambda_2)\pi(\lambda_3)..\pi(\lambda_n) \text{ with } \pi(\lambda_{1..n}) = \frac{1}{\sqrt{2\pi}} \cdot \mathrm{e}^{-\lambda_{1..n}^2/2} \tag{9.12}$$

The integral of both sides of Eq. 9.11 in $\lambda_{1..n}$ using Eq. 9.12 gives:

$$P_\nu(S|D) = \frac{\pi(S)}{\mathcal{N}_\nu} \int\int\int\int L_\nu(D|S, \lambda_{1..n}) \prod_{i=1}^{n} \pi(\lambda_i) d\lambda_i. \tag{9.13}$$

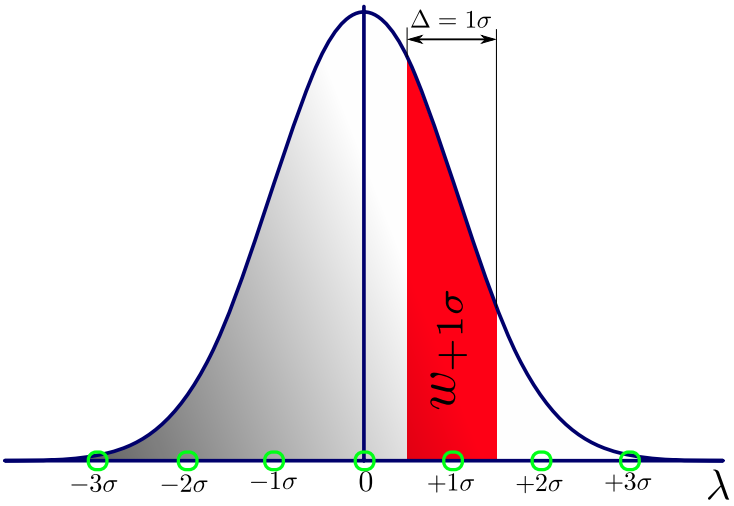

Figure 9.6: Sketch of a Gaussian distribution around 0 with $\sigma = 1$. In this case 7 grid points (green circles) are shown ranging from -3σ to $+3\sigma$ with a distance of $\Delta = 1\sigma$ between two adjacent points. The weight w is the result of the integral given in Eq. 9.15 exemplary shown for $\lambda = +1\sigma$.

The prior probability $\pi(S)$ was assumed to be flat in the number of signal events S. The choice of a constant prior p.d.f. reflects the fact that no NP models were preferred. The integral in Eq. 9.13 was calculated numerically using the trapezoidal approximation technique. The 95% quantile of the posterior p.d.f. $P_\nu(S|D)$ was used to determine the exclusion limit S_{95} for a given mass ν:

$$0.95 = \int_0^{S_{95}} P_\nu(S|D)dS. \tag{9.14}$$

The resulting number of signal events S_{95} is the upper limit at 95% *Credibility Level* (CL) on the signal S. In other words, S_{95} has a probability of 5% to be present in data D. To translate the number of signal events S_{95} into cross-section times acceptance $\sigma \times \mathcal{A}$, S_{95} was divided by the integrated luminosity L, which amounts to 4.8 fb^{-1}.

Two different types of limits were calculated denoted as *observed* and *expected*. The observed limits were calculated as described above using the observed data D as input. The expected limits were calculated using pseudo-experiments which were produced using the method described in Sec. 9.2. The data D were substituted by the pseudo-data to calculate the posterior probabilities given in Eq. 9.13. The result is a distribution of exclusion limits on $\sigma \times \mathcal{A}$, where the expected limit was obtained from the median of the distribution. Furthermore the 68% and a 95% asymmetric errors were derived from the resulting limit distribution. To set limits on the mass, the hypothetical cross-section and the acceptance $\mathcal{A}$ for each mass point ν were used to construct a curve. The mass limit is the intersection between the linearly interpolated limit curves and the theory curve of the NP model.

9.3.2 Convolution of Systematic Uncertainties

The systematic uncertainties were treated as nuisance parameters $\lambda_{1..n}$ and were convolved described by Eq. 9.13. Each nuisance parameter represents an uncertainty type respectively. Systematic uncertainties on the jet energy scale (JES), the jet energy resolution (JER), the background estimation, the integrated luminosity L and the acceptance $\mathcal{A}$ were considered.

The systematic uncertainties were propagated to the upper limit on $\sigma \times \mathcal{A}$ using a technique referred to as *grid convolution*. For this purpose an n-dimensional grid was constructed, where each grid point is associated with a particular combination of possible variations of $\lambda_{1..n}$. Each nuisance parameter ranges from -3 to $+3$ in steps of $\Delta = 0.5$, which results in 13 possible values. The dimension n of the grid corresponds to the number of nuisance parameters considered. For example, a four-dimensional grid consists of $13^4 = 28561$ points. Each grid point is associated with a weight $w(\lambda_{1..n})$. The weights for each grid point were calculated using the Gaussian p.d.f. with the expectation value 0 and $\sigma = 1$. As illustrated in Fig. 9.6 for an one-dimensional case, the weights corresponds to the integral for a given grid point with the distance $\Delta_{1..n}$ between adjacent points and are calculated as follows:

$$w(\lambda_{1..n}) = \prod_{i=1}^{n} \int_{\lambda_i - \Delta_i/2}^{\lambda_i + \Delta_i/2} \frac{1}{\sqrt{2\pi}} \mathrm{e}^{-x_i^2/2} dx_i \tag{9.15}$$

The weight $w(\lambda_{1..n})$ reflects the term $\prod_{i=1}^{n} \pi(\lambda_i)$ in Eq. 9.13 which expresses an average of the posterior p.d.f. $P_\nu(S|D)$. The advantage of this method is the low number of pseudo-experiments needed to propagate the systematic uncertainties, which is e.g. 13 in the one-dimensional case. This holds if the number of nuisance parameters is small, which is the case when $n \leq 3$. For large numbers of n computational issues become significant and other techniques can be used to calculate exclusion limits [152].

Jet Energy Scale and Jet Energy Resolution

As discussed in Chap. 7 the jet energy scale (JES) uncertainty consists of 63 subcomponents. The relative uncertainty components σ_i were reduced to the square sum of the individual components $\sigma^2_{\mathrm{JES}} = \sum \sigma_i^2$, treating each uncertainty component as independent[8]. The JES uncertainty is reflected by the nuisance parameter λ_1, which was used to create 13 different JES scenarios. The four-vector shift of each jet was performed using the method explained in Sec. 8.4.2, where the standard deviation of the JES uncertainty σ_{JES} was multiplied by λ_1 ranges from $\lambda_1 = -3$ to $\lambda_1 = +3$. For each JES scenario a shifted signal template was produced, which is associated with the corresponding λ_1. For each value of λ_1 the corresponding signal template was used to calculate the posterior probability given in Eq. 9.13 using the grid convolution technique. The JES affects mainly the position of a given signal as function of the dijet mass m_{jj} as shown exemplary in Fig. 9.7 (left) for an *Excited Quark* with a mass of 2750 GeV.

By analogy with the treatment of the JES uncertainty, 13 different signal templates were generated using different detector resolution scenarios. The resolution was worsened

[8] It has been shown that the impact of correlations between uncertainty components on the exclusion limit are negligible due to the fact that narrow resonances were used to propagate the uncertainty.

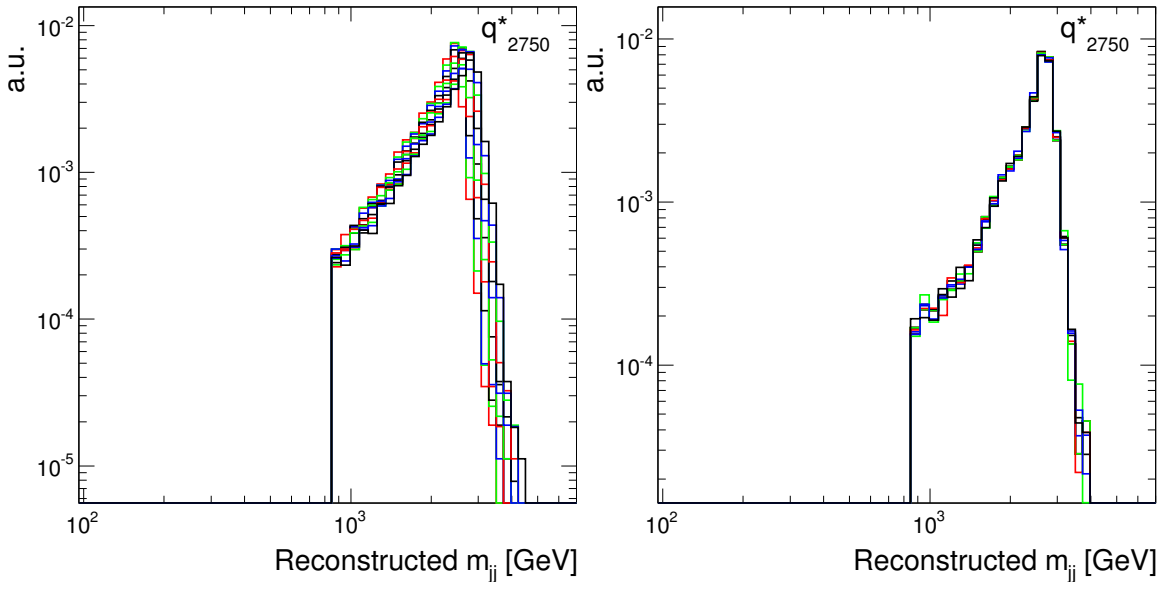

Figure 9.7: Left: excited quark (2750 GeV) signal distributions produced using different jet energy scale scenarios at detector-level. Right: excited quark (2750 GeV) signal distributions produced using different jet energy resolution scenarios at detector-level.

according to the JER uncertainty using the technique described in Sec. 8.4.2, which is expected to affect the width of a given signal. The outcome is shown in Fig. 9.7 (right) exemplary for an excited quark distribution with a mass of 2750 GeV. The difference between templates produced with different resolution scenarios compared to the nominal resolution is small. The impact on the posterior p.d.f. $P_\nu(S|D)$ was found to be negligible and therefore the JER uncertainty was not included in the uncertainty convolution procedure.

Luminosity and Acceptance

The uncertainty on the integrated luminosity L was treated differently compared to JES and JER uncertainties. It was used to convert the number of signal events S_{95} (cf. Eq. 9.14) to the limit on cross-section times acceptance $\sigma \times \mathcal{A}$, whereas the JES and JER uncertainties influence the shape and position of the new physics signal template as function of m_{jj}. The uncertainty on the integrated luminosity L is 3.9% [153]. In contrast to the cross-section measurements (cf. Chap. 8) the uncertainty on the luminosity was larger, because this analysis was done before an improved luminosity measurement was available. In addition a conservative estimate of the uncertainty on the acceptance was taken into account. The uncertainty was estimated by determine acceptances for various masses ν of the Excited Quark using different JES scenarios. The acceptances were re-weighted using the grid convolution technique yielding an acceptance distribution for each mass ν. In order to determine the uncertainty, a Gaussian fit was performed, where the standard deviation was used as uncertainty estimate. The results are shown in Fig. 9.8 (left). The function used to describe the relative acceptance uncertainty is $f(x) = \mathrm{e}^{p_0/x}/(p_1 - p_2 \cdot x)$. The acceptance uncertainty and the uncertainty on the integrated luminosity are not correlated and were combined in quadrature. The correlation with the JES uncertainty

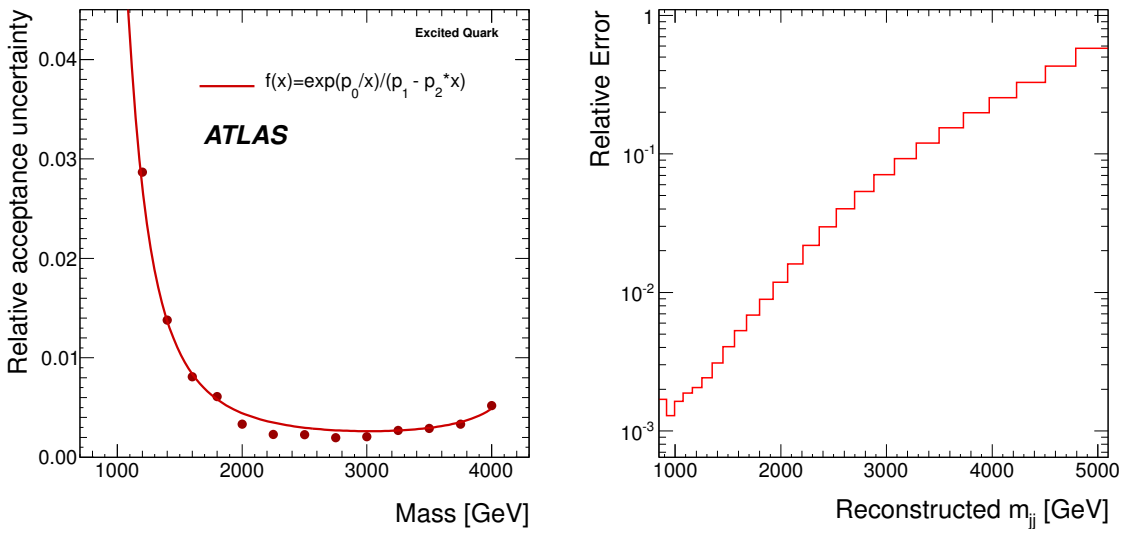

Figure 9.8: Left: relative acceptance uncertainty as function of the excited quark mass. The large uncertainty for excited quarks with lowest masses is due to large variation of the acceptance due to the mass cut at 847 GeV. [33] Right: relative fit uncertainty as function of the dijet mass.

was neglected. By analogy with the treatment of JES uncertainties, λ_2 was assumed to be distributed according to a Gaussian probability function decomposed in 13 different scenarios ranging from -3 to $+3$ standard deviations.

Background Estimation

The function defined in Eq. 9.2 is a four parameter function. The parameters were not treated as nuisance parameters individually. Instead, the uncertainty on the background estimation is characterized by a single parameter λ_3. It was estimated by fluctuating the number of events in each bin independently according to the Poisson distribution. The expectation values ν of the Poisson p.d.f. in each bin were taken from the observed data or the pseudo-data respectively. For each pseudo-experiment a fit to the resulting pseudo-spectrum was performed. The function values of the fits were used to derive distributions in each bin. The uncertainty on the fit was taken as the root mean square (RMS). The result is shown in Fig. 9.8 (right). The background fit was treated as fully correlated in m_{jj} shifting the fit values according to the estimated uncertainty in each dijet mass bin. Using this approach the correlations between the fit parameters are avoided.

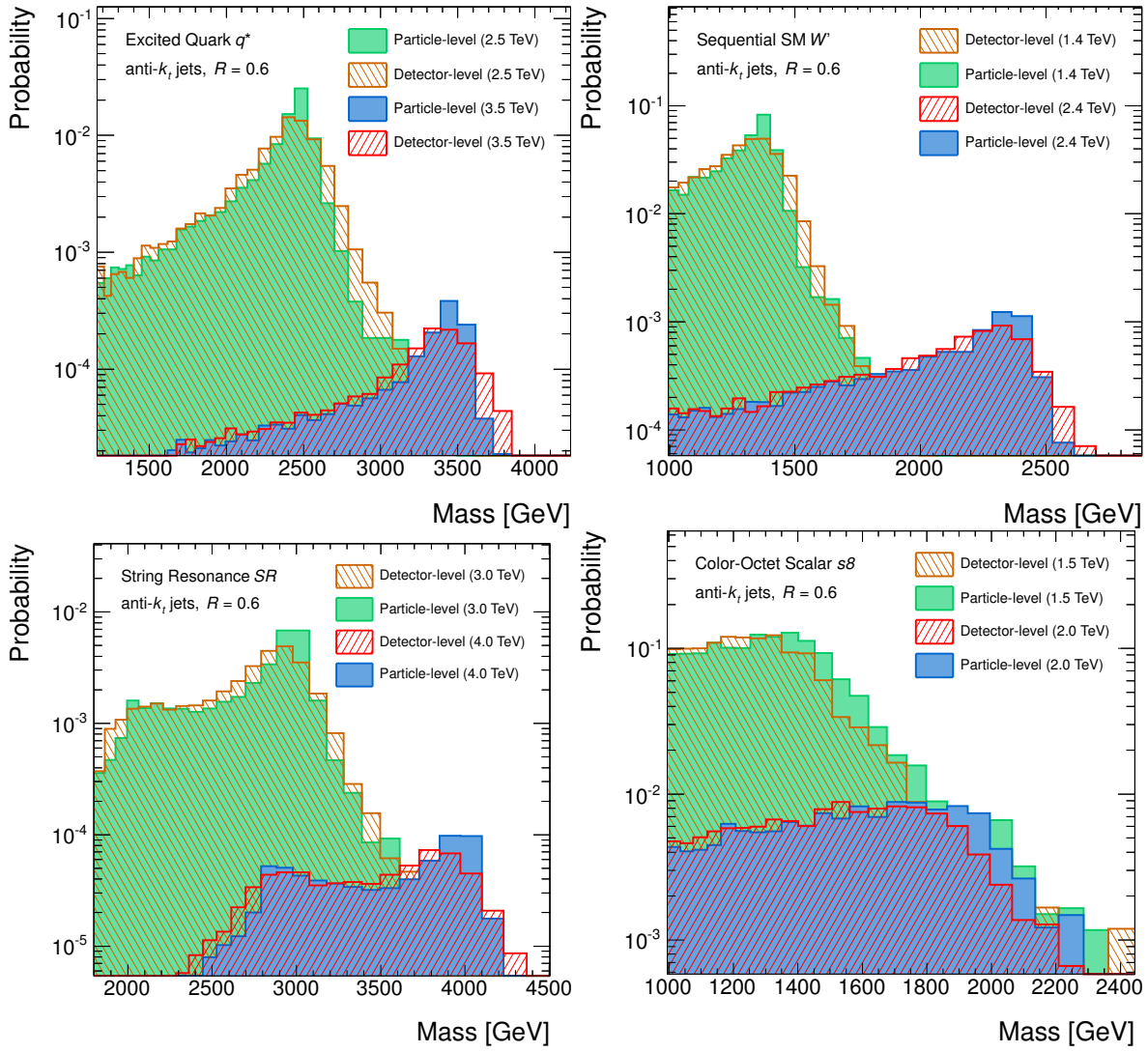

Figure 9.9: Top left: the invariant mass distributions at detector-level and particle-level for two different excited quark masses: $M_{q^*} = 2.5$ TeV and $M_{q^*} = 3.5$ TeV. Top right: the invariant mass distributions at detector-level and particle-level for two different W' masses: $M_{W'} = 1.4$ TeV and $M_{W'} = 2.4$ TeV. Bottom left: the invariant mass distributions at detector-level and particle-level for string resonant structures at two different string scales: $M_s = 3$ TeV and $M_s = 4$ TeV. Bottom right: the invariant mass distributions at detector-level and particle-level for two different Color-Octet Scalar S_8 masses: $M_{S_8} = 1.5$ TeV and $M_{S_8} = 2.0$ TeV. The jets were reconstructed using the anti-k_T jet algorithm with the distance parameter $R = 0.6$. The signal distributions at detector-level were taken for the limit setting procedure.

9.3.3 Results

This analysis is adaptable to resonant phenomena with couplings, which are strong compared to the scale of perturbative QCD at a given signal mass. Therefore the interference with QCD terms were neglected. For the models q^*, $s8$, and SR all final states were simulated. Therefore the branching ratio (BR) for the dijet channel is implicitly included

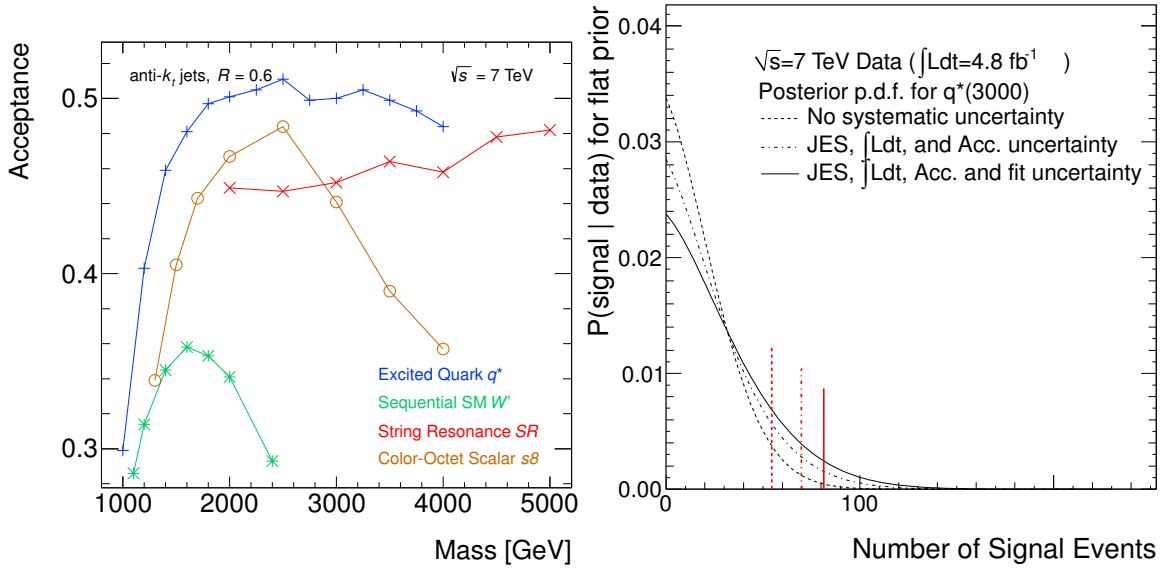

Figure 9.10: Left: the acceptance as function of the signal mass for various NP models considered in the limit setting procedure. These acceptances were used to construct the theory curve, which was used to set exclusion limits on the mass. They are also listed in App. A.1-A.4. Right: posterior p.d.f. $P(\text{signal}|\text{data})$ as function of the number of signal events for different types of systematic uncertainty combinations. In this case, the excited quark signal distribution at 3 TeV was used. The vertical lines indicate the upper limits at 95% Credibility Level (CL) S_{95} (cf. Eq. 9.14) on the signal S, which were obtained from the posterior p.d.f.

in the acceptance $\mathcal{A}$. In case of the W', the hadronic modes were simulated only. The signal distributions at detector-level used for the limit setting procedure for two different masses are exemplary shown in Fig. 9.9. The systematic uncertainties due to the JES, luminosity, acceptance, and fit were incorporated as detailed in Sec. 9.3.2. The systematic uncertainty due to the jet energy resolution was found to be negligible and was not used in the convolution procedure. The uncertainties associated with the considered models as originating from the PDF, Monte Carlo tune etc. were not included, because NP models are benchmarks with a particular model parameter choice[9]. The impact on the posterior p.d.f. due to systematic uncertainties is exemplary shown for the excited quark signal distribution at 3 TeV in Fig. 9.10 (right).

In Fig. 9.11 shown are the expected and observed 95% CL upper limits on the production cross-section times acceptance (times branching ratio) $\sigma \times \mathcal{A}$ ($\times$BR) for the q^*, W', $s8$, and SR as function of the NP mass. The σ is the production cross-section of a given NP model. In total limits for 36 different templates were calculated, 14 for the $q*$, 7 for the W', 8 for the $s8$, and 7 for SR. Detailed lists of the observed and expected limits for each model and NP mass ν are given in App. A.1-A.4. The expected limit on $\sigma \times \mathcal{A}$ ($\times$BR) is a measure on the sensitivity to NP for a given mass. The observed limits fluctuate around the expected limit within the 95% uncertainty band, which is an indication

[9]Studies showed that the impact due to the the choice of different Monte Carlo parameters on the exclusion limit is small [154].

that the observed data is compatible with the background expectation. The limits on the mass for a given NP model are the intersection point between the theory prediction and the observed and expected limits, respectively. The limit values were derived by linear interpolation between the mass points considered.

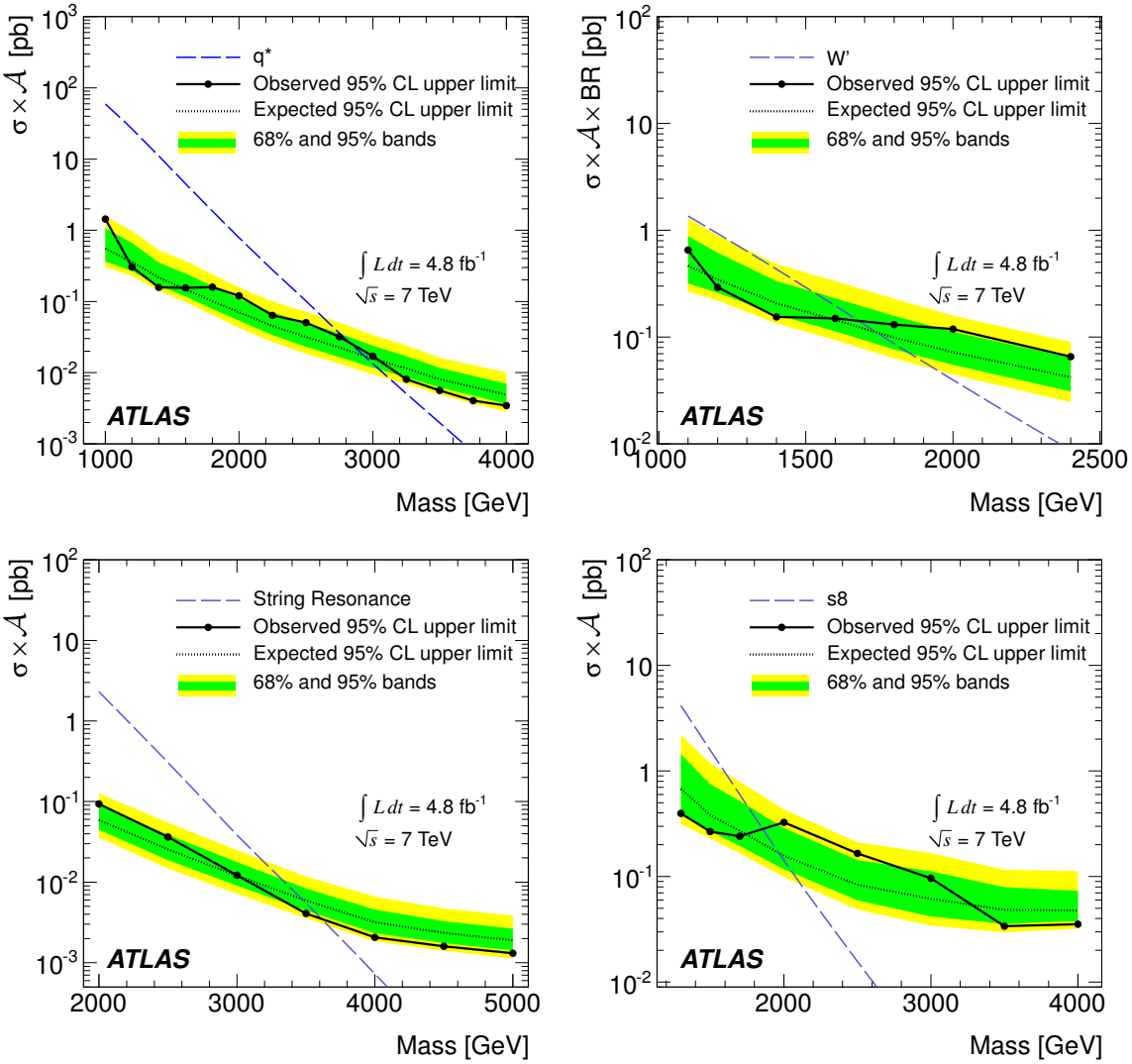

Figure 9.11: The 95% CL upper limits on $\sigma \times \mathcal{A}$ ($\sigma \times \mathcal{A} \times$ BR) as a function of particle mass (black filled circles). The black dotted curve shows the 95% CL upper limit expected in the absence of any resonance signal, and the green and yellow bands represent the 68% and 95% contours of the expected limit, respectively. The theoretical prediction of $\sigma \times \mathcal{A}$ for different models is shown as a dashed curve. The observed (expected) mass limit occurs at the crossing of the dashed $\sigma \times \mathcal{A}$ curve with the observed (expected) 95% CL upper limit curve. Lmits for the following models are shown: Excited Quark q^* (top left), Sequential SM W' (top right), String Resonances SR (bottom left), and Color-Octet Scalar $s8$ (bottom right). [33]

In the following the results of the limit setting procedure is summarized. All expected and observed limits for the four models used are listed in Tab. 9.2. The exclusion limits

for q^* are shown on in Fig. 9.11 (top left). Masses m_{q^*} between 1.0 TeV and 4.0 TeV were used to set limits, where the acceptance A ranges from 30% to 51% and is above 46% for masses above 1.2 TeV as shown in Fig. 9.10 (left). The loss of acceptance is mainly due to requirements on Δy as discussed in Sec. 9.1. The expected lower mass 95% CL limit for q^* is 2.94 TeV, and the observed limit is 2.83 TeV.

The limits for the SSM W' are shown in Fig. 9.11 (top right). For these signal distributions, dijet final-states have been simulated only. The BR is around 0.75 for all masses $m_{W'}$ and has a weak dependence on the mass of the resonance. Mass values between 1.1 TeV and 3.6 TeV were used for the limit setting, where the acceptance ranges from 29% to 36% (cf. Fig. 9.10 (left)). The expected limit at 95% CL is 1.74 TeV and the observed limit is 1.68 TeV. This is the first SSM W' ATLAS limit for hadronic decays. For the considered W' model the SM couplings to quarks are assumed. For a similar model predicting stronger couplings, the calculated limits could be used to estimate new limits on the mass by shifting the theoretical curve upward.

The limits for SR are shown in Fig. 9.11 (bottom left). The SR acceptance ranges from 45% to 48% for masses between 2.0 TeV and 5.0 TeV (cf. Fig. 9.10 (left)). The expected mass limit at 95% CL is 3.47 TeV and the observed limit is 3.61 TeV.

The limits for $s8$ are shown in Fig. 9.11 (bottom right). The acceptances range from 34% to 48% for masses between 1.3 TeV and 4.0 TeV (cf. Fig. 9.10 (left)). The expected mass limit at 95% is 1.97 TeV and the observed limit is 1.86 TeV.

New physics model	Expected [TeV]	Observed [TeV]
Excited Quark q^*	2.94	2.83
Sequential SM W'	1.74	1.68
Color-Octet Scalar $s8$	1.97	1.86
String Resonances SR	3.47	3.61

Table 9.2: Listed are expected and observed 95% CL mass limits determined for the following models: Excited Quark q^*, Sequential SM W', Color-Octet Scalar $s8$, and String Resonances SR.

Model-independent Limits

The model-independent limit setting was introduced in Ref. [154] and was also performed in context of this analysis. The aim is to provide a tool in order to estimate exclusion limits for an arbitrary NP model of interest without a detailed knowledge on the detector response and the associated systematic uncertainties. For this purpose Gaussian shaped signal distributions with different widths σ_{G} and central values m_{G} were used in order to determine the observed limits. Signal distributions of three different types were used: $\sigma_{\mathrm{G}}/m_{\mathrm{G}} = \{0.07, 0.10, 0.15\}$. The choice of the width as function of m_{G} is motivated by the ratio $\sigma_{\mathrm{G}}/m_{\mathrm{G}}$ in case of excited quarks. The lowest value was chosen to be above the relative dijet mass resolution which is discussed in Sec. 6.5. The convolution of systematic uncertainties was performed using techniques described in Sec. 9.3.2. In case of the JES

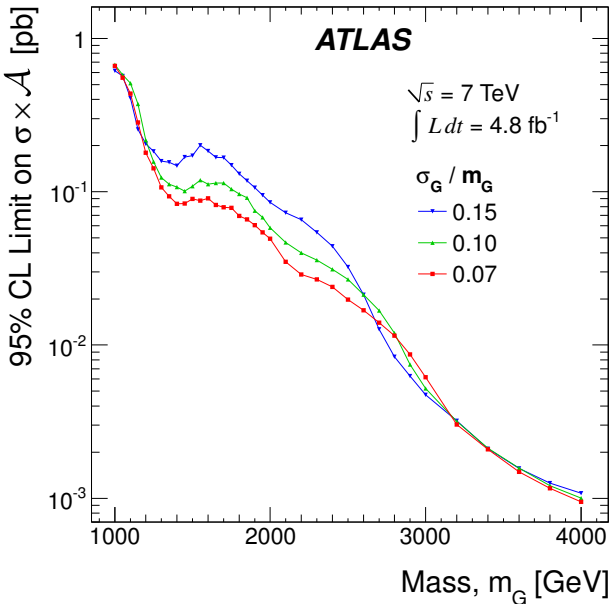

Figure 9.12: Model-independent 95% CL limits on $\sigma \times \mathcal{A}$ as function of the mass m_{G} for three different ratios $\sigma_{\mathrm{G}}/m_{\mathrm{G}}$ [33].

uncertainty[10], the central value of the Gaussian distributions were shifted assuming an uncertainty of 4%. The 95% CL limits on $\sigma \times \mathcal{A}$ as function of the mass m_{G} are shown in Fig. 9.12. The limits are thus expressed in terms of number of events observed after the event selection. The variation of the limits as function of width and mass reflect the statistical fluctuation in the spectrum obtained using data. A detailed list of the observed limits is given in App. A.2.

In the following the recipe is summarized, which was suggested in Ref. [148] in order to estimate the exclusion limits for a given NP model. This method can be applied to resonances which are approximately Gaussian shaped within the kernel of the signal distribution. It is also assumed that the contribution of events reconstructed in the tails of the dijet mass signal distribution is negligible. As the first step the acceptance is determined. For this purpose, the signal distribution has to be determined at particle-level using the kinematic selection detailed in Sec. 9.1. Furthermore the distribution has to be smeared according to the dijet mass resolution given in Ref. 6.5. The non-Gaussian tails of the smeared distribution have to be removed keeping events in the interval $0.8 \times$ Mass to $1.2 \times$ Mass. The remaining number of events have to be used to estimate the acceptance $\mathcal{A}$. The mean mass of the truncated distribution corresponds to m_{G}. In case, the mean mass of the truncated signal distribution is between two given masses m_{G}, the larger of the two limits has to be used to be conservative. Furthermore a procedure has to be applied in order to match the ratio $\sigma_{\mathrm{G}}/m_{\mathrm{G}}$. This information can be used to obtain limits given in Fig. 9.12. In order to determine mass limits the production cross-section of the signal of interest has to be corrected by the acceptance estimated in this context. The mass limit is the intersection between the interpolated limit curves and the theory curve of the NP model corrected for the acceptance $\mathcal{A}$.

[10]Because no dijet events and thus jets are available in this case, the different JES scenarios were estimated.

9.3.4 Comparison to other analyses

Since data-taking began in 2010, the ATLAS collaboration has published three dijet analyses dealing with the search for physics beyond the Standard Model. The first analysis used 36 pb^{-1} data collected in 2010 [154]. Two analyses were published using data recorded in 2011. The former used a subset of 1 fb^{-1} [148] and the latter the entire 4.8 fb^{-1} [33] data set. The center-of-mass energy $\sqrt{s}$ was configured to be 7 TeV in all cases. In Tab. 9.3 a comparison of the expected 95% CL upper limits are shown for these three analyses. The Excited Quark q^* was the only benchmark model used in all three publications. The Color-Octet Scalar $s8$ was used in the 2011 data publications only. The exclusion limit for q^* using the 4.8 fb^{-1} data was calculated using a slightly different Monte Carlo configuration compared to previous analyses. It was found that the q^* dijet mass m_{jj} distribution with the default Pythia 6 settings is too narrow, because of an incorrect treatment of QCD p_T-ordered final-state radiation (FSR) vetoing. The correct FSR behavior was restored by changing one parameter[11]. The outcome is a broader q^* dijet mass distribution which affects the sensitivity and therefore the exclusion limits. The impact on the expected q^* mass limit was found to be small. The difference between the limits was determined to be 0.1 TeV, where the mass limit using signal distributions generated with the default Pythia 6 settings gives a greater value. The first ATLAS result on the expected mass limit for the q^* using the 36 pb^{-1} data is 2.07 TeV. The first 2011 data mass limit, where approximately 960 fb^{-1} more data was collected compared to the previous one, was calculated to be 2.81 TeV. For the second 2011 data result approximately five times more data was used resulting in an expected mass limit of 3.04 TeV [12].

In addition to the dijet mass distribution, angular distributions were used to search for NP and to obtain exclusion limits. The angular observable used to set limits for the Excited Quark q^* is the so-called $F_\chi(m_{\text{jj}})$ which is defined as [33] :

$$F_\chi(m_{\text{jj}}) = \frac{N(m_{\text{jj}}, y* < 0.6)}{N(m_{\text{jj}}, y* < 1.7)}, \tag{9.16}$$

where $y^* = 0.5 \times |\Delta y|$, $N(m_{\text{jj}}, y* < 0.6)$ is the number of dijet events in the central region $y* < 0.6$ and $N(m_{\text{jj}}, y* < 1.7)$ the total number of dijet events within $y* < 1.7$ in a given m_{jj} bin. In contrast to the analysis presented, the background expectation for $F_\chi(m_{jj})$ was generated using Monte Carlo simulation. They are sensitive to narrow resonance-like features as well as widely distributed phenomena. The expected 95% CL mass limit for q^* determined using this analysis amounts to 2.85 TeV. This limit was obtained using the same configuration as used in Sec. 9.3.3 and thus this value has to be compared to the expected limit of 2.94 TeV obtained using the dijet mass spectrum. As can be observed from these numbers, the analysis presented in this thesis yields a 3% greater limit.

Within ATLAS several other channels were used to determine exclusion limits for models considered in this thesis. A search for q^* was performed using photon-jet final-states in 2.11 fb^1 of the 2011 data [155]. The q^* is expected to decay in photon-jet final-states with

[11] To restore the correct behavior, the Pythia authors suggested to set the parameter MSTJ(47) to 0. This is a correction to the gluon shower emission rate [18].

[12] Note: this lower mass limit is obtained with the default Pythia 6 configuration for comparison purposes. The expected limit obtained using corrected Pythia 6 settings is 2.94 TeV as discussed in Sec. 9.3.3.

a branching ratio of 0.006 [156]. The observed mass limit was obtained to be 2.46 TeV. The expected limit is approximately equal to the observed limit, which is not quoted in the publication, but can be guessed from the limits plot. The resulting expected limit is less stringent than the limit calculated using dijet final-states in 4.8 fb^{-1} as well as the 1.0 fb^{-1} data. The ATLAS collaboration has also used leptonic channels to search and set exclusion limits for the Sequantial SM W' [157]. The expected limit determined in context of this analysis amounts to 2.55 TeV, which is approximately 30% greater compared to 1.74 TeV obtained using dijet final-states[13].

The CMS collaboration published exclusion limits for several models decaying into dijet final-states using 5 fb^{-1} of data at $\sqrt{s} = 7$ TeV [158]. The limits for all models considered were set using 3 templates. The templates used to determine limits for q^* [14] and SR were produced using the $q* \rightarrow qg$ channel and upper limits on $\sigma \times \mathcal{A} \times \text{BR}$ were calculated. The expected limit on the mass for q^* is 3.05 TeV, which is compatible with the result obtained in context of this thesis. The expected mass limits for SR are not compatible, since different models were used, which is reflected in the production cross-section and thus in the theory curve. The expected limit determined by CMS amounts to 4.29 TeV. In case of $s8$ signal templates for gg final-states and in case of W' $q\bar{q}$ templates were used. The CMS expected limit for $s8$ is 2.24 TeV, which is 12% more stringent compared to this analysis. The expected mass limit for SSM W' calculated by CMS amounts to 1.78 TeV and is compatible to the result determined in this analysis. All limits determined at $\sqrt{s} = 7$ TeV and discussed in this sub-section are listed in Tab. 9.3.

In 2012 approximately 20 fb^{-1} of pp collision data at $\sqrt{s} = 8$ TeV was recorded by ATLAS and CMS . The expected limits determined using ATLAS are [159]: 3.99 TeV (q^*), 2.83 TeV ($s8$), and 2.51 TeV (W'). The listed limits are approximately 140% greater compared to the limits determined using 2011 data. This gain is achieved due to the higher center-of-mass energy and four times more collected data. The limits obtained by the CMS collaboration are [160]: 3.7 TeV (q^*), 2.5 TeV ($s8$, observed), and 2.2 TeV (W'). These limits are systematically less stringent compared to the ATLAS analysis using 2012 data.

9.4 Enhancement of Sensitivity

In this section strategies are discussed to enhance the sensitivity to new phenomena in the context of the dijet mass search. For a given center-of-mass energy and collected amount of data, the sensitivity to new physics mainly depends on the strength of separation between the QCD background and a hypothetical new resonance. An example of sensitivity enhancement is the separation of s- and t-channels by applying the $|\Delta\eta|$ cut as discussed in Sec. 9.1. Further improvements can be achieved by using quark/gluon tagging techniques. The approach aims at discriminating quarks and gluons by using substructure observables. Using multivariate approaches more than 95% of gluon jets can be rejected while keeping more than 50% of light-quark jets[15] with similar performance in

[13] In case of the lepton analysis another limit setting approach is used. This could lead to discrepancies due to different limit setting procedures.

[14] It has to be assumed that the CMS collaboration used the default PYTHIA settings to produce the q^* signal distributions and thus qg templates.

[15] These are jets originating from an u-, d-, s-quark.

NP model (Analysis)	36 pb^{-1} (2010)	1.0 fb^{-1}	2.1 fb^{-1}	4.8 fb^{-1} (2011)
q^* (ATLAS dijet)	2.07 TeV [154]	2.81 TeV [148]	-	2.94 TeV [33]
q^* (ATLAS angular)	2.12 TeV [154]	-	-	2.85 TeV [33]
q^* (ATLAS photon-jet)	-	-	2.46 TeV [155]	-
q^* (CMS dijet)	-	2.68 TeV [161]	-	3.05 TeV [158]
W' (ATLAS dijet)	-	-	-	1.74 TeV [33]
W' (ATLAS lepton)	1.45 TeV [162]	2.23 TeV [40]	-	2.55 TeV [157]
W' (CMS dijet)	-	1.40 TeV [161]	-	1.78 TeV [158]
$s8$ (ATLAS dijet)	-	1.77 TeV [148]	-	1.97 TeV [33]
$s8$ (CMS dijet)	-	-	-	2.24 TeV [158]
SR (ATLAS dijet)	-	-	-	3.47 TeV [33]
SR (CMS dijet)	-	3.90 TeV [161]	-	4.29 TeV [158]

Table 9.3: Listed are expected 95% CL mass limits for the models used: Excited Quark q^*, Sequential SM W', Color-Octet Scalar $s8$, and String Resonances SR. For the purpose of comparison exclusion limits determined in other analyses are listed.

all jet-p_T regimes [163].

The reconstructed jets reflect the outgoing partons. This "connection" can be distorted by pile-up, the choice of the jet-finding algorithm, initial-state radiation etc. The flavor of a reconstructed jet is defined by matching the jet to a parton which is produced in the $2 \to 2$ hard scatter process at leading-order in perturbation theory and used as input for the parton shower. This was done by analogy with the matching procedure used in Sec. 8.3.1, where the matching radius was chosen to be $\Delta R = 0.3$. The expression quark-jet includes all quark flavor simulated[16]. The predicted QCD dijet mass spectrum at reconstruction-level separated in different final-state flavor compositions is shown in Fig. 9.13 (left). The spectrum was produced using Pythia LO simulation passing the event and jet selection detailed in Sec. 9.1. The dominant dijet final states at 1 TeV consists of quark/gluon-jets (qg-jets), where either the leading jet is a q-jet and the second-leading jet is a g-jet or vice versa. In the high-m_{jj} regime mainly qq-jet final states occur. The predicted hadronic final states for the Excited Quark at 2 TeV are shown in Fig. 9.13 (right). The spectrum is dominated by qg-jets final states (cf. Sec. 2.3.1). The removal of dijet events consisting of qq-jets would obviously enhance the sensitivity to Excited Quarks especially at high-m_{jj}.

One of the most powerful discriminants is the charged track multiplicity within a jet denoted as N_{trk}. An overlay of the N_{trk} distribution for q- and g-jets is shown in Fig. 9.14 (left). In the lower panel of the figure the likelihood is shown, which is defined as the probability that a jet with an observed value N_{trk} is a q-jet:

$$P(q|N_{\mathrm{trk}}) = \frac{f_q h(N_{\mathrm{trk}}|q)}{f_q h(N_{\mathrm{trk}}|q) + f_g h(N_{\mathrm{trk}}|g)}, \tag{9.17}$$

[16] In literature the discrimination of light-quarks and gluons is subject of interest. This is due to the fact that dedicated algorithms exist to identify heavy-quark jets as e.g. originating from b-quarks. B-jets have a similar substructure as gluons, because of the longer decay chain of b-hadrons [164].

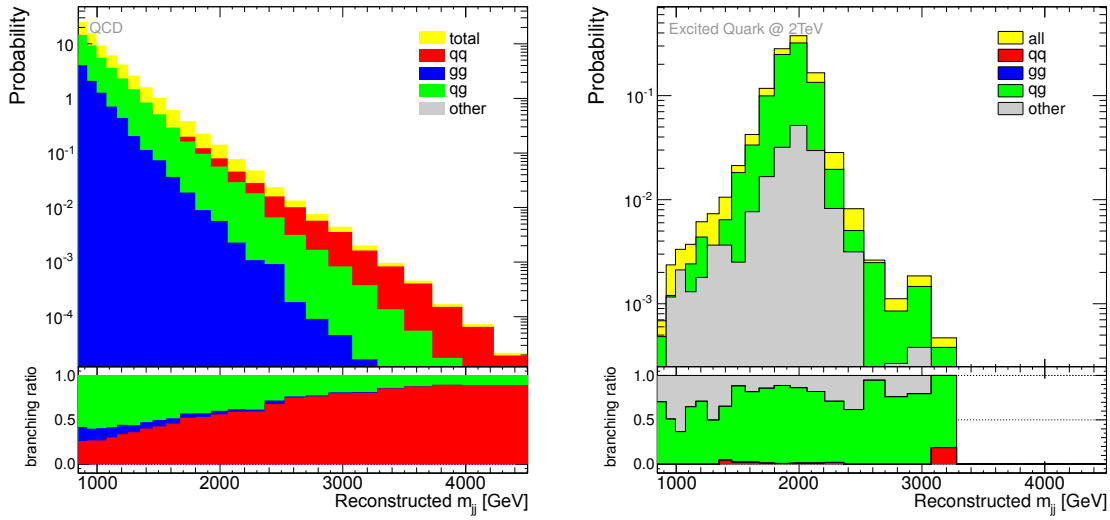

Figure 9.13: Left: composition of dijet final states in the dijet mass spectrum at detector-level. The spectrum was determined using events generated with Pythia 6. The lower panel shows the fraction of different dijet final state types. Right: by analogy with the QCD spectrum the composition of dijet final states in case of the excited quark at 2 TeV.

where f_q is the fraction of quarks and $f_g = 1 - f_q$ is the fraction of gluons, and $h(N_{\text{trk}}|q)$ and $h(N_{\text{trk}}|g)$ the p.d.f.s for q- and g-jets respectively. The probability $P(q|N_{trk})$ defined in Eq. 9.17 corresponds to $N_q/(N_q + N_g)$ given N_{trk}, where N_q is the number of q-jets and N_g the number of g-jets in a given N_{trk} bin. In case of QCD in the dijet mass region between 2699 GeV and 2882 GeV. As can be observed from this figure (cf. Fig. 9.14) the probability to measure a q-jet within the dijet system if $N_{\text{trk}} < 10$ is around 100%. q-jets dominate the spectrum in this kinematic region and the expected number of reconstructed charged particle tracks for gluon-jets is greater than that for q-jets. In Fig. 9.14 (right) the impact of the N_{trk} cut on the sensitivity is demonstrated. As figure of merit the BumpHunter p-value was used (Sec. 9.2.2). The p-values were converted to z-values, which are referred to as significance. A Color-Octet Scalar signal template at 3 TeV was added to the QCD background. The Color-Octet Scalar decays exclusively in two gluons, whereas the QCD background is dominated by qq- and qg-jets at dijet masses around 3 TeV. In this artificial scenario a large impact on the significance is expected. The aim was to reject qq- and qg-jets, which has been achieved by removing events with $N_{\text{trk}}^{\text{jet1}}$ and $N_{\text{trk}}^{\text{jet2}} < N_{\text{trk}}^{\text{cut}}$. The cross-section of the signal was adjusted such that the resulting significance is -1σ with no cut on track multiplicity applied. In this particular case the optimal cuts $N_{\text{trk}}^{\text{cut}}$ are between $23-30$ tracks, yielding an improvement of the significance to around 2σ. To cover the measured phase space the cut should be optimized as function of the dijet mass, due to the dependence of the track multiplicity and flavor composition on m_{jj}. Three different final state compositions are possible. The benchmark models can be used to derive optimal cuts for each scenario. Further improvements can be achieved by including more substructure observables, which are ideally weakly or not correlated with the charged track multiplicity N_{trk}. It was shown that high discrimination power could be achieved by using the combination of just two sub-structure observables [163]. As side-effect it is expected to determine better exclusion limits by tagging quarks and

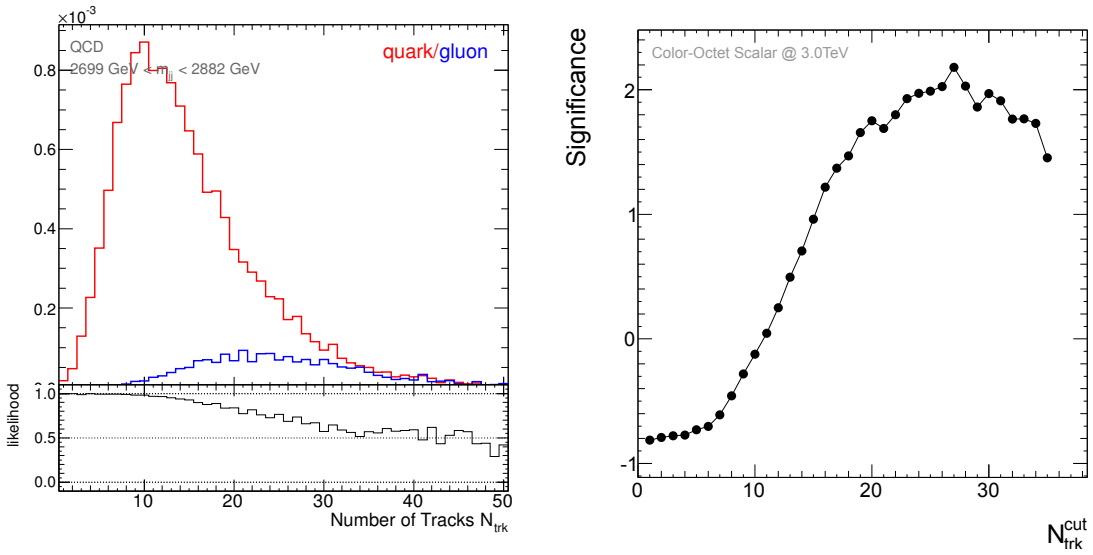

Figure 9.14: Left: jet distribution according to the number of reconstructed tracks N_{trk} within the jet separated in q-jets (red) and g-jets (blue). Only jets from the dijet system were taken into account. The dijet mass was constrained to be between 2699 GeV and 2882 GeV in this example. In the lower panel the likelihood is shown which is defined in Eq. 9.17. Right: significance (BumpHunter z-value) as function of $N_{\text{trk}}^{\text{cut}}$. For this purpose the Color-Octet Scalar model at 3 TeV was used.

gluons. Many benchmark models are already excluded in the low-m_{jj} regime. Nevertheless, in nature these hypothetical models might be realized with lower cross-sections as predicted. At dijet masses below the m_{jj} cut of 800 GeV qg-jets and gg-jets are the dominant flavor channels [165]. The sensitivity to particles decaying mainly in qq-jets could lead to similar sensitivity improvements as it is the case for resonances decaying into gg-jets in the high-m_{jj} regime demonstrated above. In case a resonance would be found, the quark- and gluon-tagging could deliver hints to the final state flavor composition of the new phenomenon.

Further improvements of the sensitivity could also be achieved by optimizing the distance parameter R of the jet finding algorithm. The choice of the largest available jet radius R in ATLAS used for the search was driven by the sensitivity to new physics signals. Jets reconstructed with larger jet radii ($R > 0.6$) result in narrower signal distributions and could potentially improve the sensitivity to this signal in context of the search for NP [32]. This improvement is partly compensated due to the increase of background events in a given dijet mass bin, because more energy is collected compared to jets reconstructed using smaller jet radii. Another difficulty arises due to the presence of pile-up, because the amount of measured energy within a jet due to pile-up is dependent on the jet distance parameter R. First studies trying to improve the sensitivity show a negligible improvement of sensitivity to NP.

10 Conclusion and Outlook

Jet measurements provide the possibility to probe the Standard Model and to search for so far unknown physics phenomena. This thesis reported on the measurements of the inclusive jet and dijet double-differential cross-sections, and the search for new resonant-like phenomena in proton-proton collisions at a center-of-mass energy of 7 TeV.

The measurements were performed using the ATLAS detector at LHC. An integrated luminosity of 4.5 fb^{-1} recorded in 2011 was used. Jets were reconstructed using the anti-k_T algorithm with distance parameters $R = 0.4$ and $R = 0.6$. The inclusive jet cross-section measurement covered the kinematic region 100 GeV $\leq p_T <$ 2 TeV within $|y| < 3.0$. The dijet cross-section measurement covered the kinematic regime 260 GeV $\leq m_{12} <$ 5 TeV and $y^* < 2.5$. The measured spectra were corrected for detector effects and compared to theoretical predictions at particle-level. For this purpose theoretical QCD predictions at next-to-leading order with non-perturbative and electroweak corrections applied, were used. The events were generated using NLOJet++. Three different PDF sets were used to generate predictions: CT10, MSTW2008, and NNPDF 2.3. Furthermore theoretical uncertainties were determined by varying several components of the theory independently. Additionally, the measured cross-sections were compared to Powheg predictions interfaced with Pythia showering for two different underlying event tunes. The experimental uncertainties as function of p_T (resp. m_{12}) and $|y|$ (resp. y^*) were propagated to the particle level using different techniques exploiting the unfolding procedure. The jet energy scale uncertainty was found to be the dominant experimental uncertainty. A large portion of this uncertainty is due to the difference between MC predictions using different generators. Agreement between the theoretical predictions and the measurements was found within the estimated uncertainties.

Jets with transverse momenta of up to 2 TeV were measured in the central rapidity region, providing smaller statistical uncertainties in the high-p_T regime compared to previous measurements. The measurements were performed in presence of unprecedented pile-up activity. The impact of pile-up on the measurements was studied and conclusions on the systematic uncertainties were drawn. The total uncertainty was decreased compared to the analysis performed using data recorded in 2010. The decrease of statistical and systematic uncertainties allows further constraint of the parton density functions (PDF) of the proton.

The search for new physics was performed using 4.8 fb^{-1} of 2011 data at a center-of-mass energy of 7 TeV. Jets were reconstructed using the anti-k_T algorithm with the distance parameter $R = 0.6$. This choice was motivated by the sensitivity to new physics. The dijet mass region covered is 850 GeV $\leq m_{jj} <$ 4 TeV. In order to achieve a better separation between the background, which is dominated by QCD t-channel processes, and the new physics signals, the dijet rapidity separation is constrained to $y^* < 0.6$. The background was estimated using a data-based technique. The search for local excesses was performed using several statistical tools. No evidence for significant local discrepancies between the measurement and background expected was found. To determine exclusion limits a Bayesian approach was used. The signal distributions of four different benchmark models

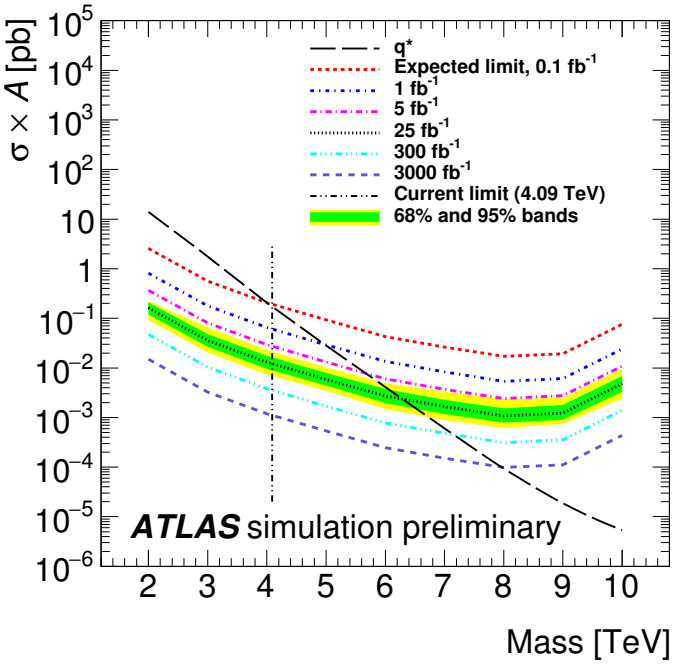

Figure 10.1: Expected limits on $\sigma \times \mathcal{A}$ determined using excited quarks q^*. The limits were calculated using different amount of simulated data at $\sqrt{s} = 14$ TeV ranging from 0.1 fb^{-1} to 3000 fb^{-1}. The dashed vertical line indicates the current published mass limit of 4.09 TeV (observed, cf. Sec. 9.3.4) determined using 20.3 fb^{-1} data at $\sqrt{s} = 8$ TeV. As can be observed from this figure the current mass limit will be reached with 0.1 fb^{-1} at $\sqrt{s} = 14$ TeV and doubled with 3000 fb^{-1}. [166]

were exploited to calculate observed and expected mass limits. Four different systematic uncertainty types were taken into account: jet energy scale, integrated luminosity, acceptance, and fit. Furthermore, model-independent limits on cross-section times acceptance were set using Gaussian-shaped distributions as input. The determined expected 95% CL upper mass limits are: 2.94 TeV (Excited Quark q^*), 1.74 TeV (Sequential SM W'), 1.97 TeV (Color-Octet Scalar $s8$), and 3.47 TeV (String Resonances SR).

In 2015 the LHC will be configured for a center-of-mass energy of 13 TeV and will be increased to 14 TeV in the following years. It is expected to record up to 15 fb^{-1} of data in the first year and up to 100 fb^{-1} for the following two years [167], which is going to be 20 times more compared to the 2011 and five times more compared to the 2012 data record. The larger data set will provide improved statistical power in the high-p_T (-m_{12}) regime of the inclusive jet and dijet cross-section spectra. Additionally, further reductions of systematic uncertainties in this regime will provide an improved input for PDF fits.

The expected exclusion limits determined using excited quarks q^* for a center-of-mass energy of 14 TeV are shown in Fig. 10.1. A data set with an integrated luminosity of 5 fb^{-1} at $\sqrt{s} = 14$ TeV is expected to improve the mass limit to approximately 6 TeV. This mass limit is approximately two times more stringent compared to that determined in the analysis presented in this thesis. The current observed upper mass limit is 4.09 TeV [159]. This limit was determined using approximately 20 fb^{-1} at $\sqrt{s} = 8$ TeV. It is expected to be reached with 0.1 fb^{-1} of data at $\sqrt{s} = 14$ TeV. Besides the increase of the center-of-mass energy and the amount of recorded data, advanced selection techniques can be

used to improve sensitivity to new physics. This can be done by using e.g. gluon-quark tagging methods as demonstrated in this thesis.

Bibliography

[1] L. Brown and L. Hoddeson, *The Birth of Particle Physics*,.

[2] M. R. Lillian Hoddeson, Laurie Brown and M. Dresden, *The Rise of the Standard Model: A History of Particle Physics from 1964 to 1979*,.

[3] V. E. e. a. Barnes, *Observation of a Hyperon with Strangeness Minus Three*, Phys. Rev. Lett. **12** (1964) 204–206. http://link.aps.org/doi/10.1103/PhysRevLett.12.204.

[4] M. Gell-Mann, *A Schematic Model of Baryons and Mesons*, Phys.Lett. **8** (1964) 214–215.

[5] G. Zweig, *An SU_3 model for strong interaction symmetry and its breaking; Version 2*,. Version 1 is CERN preprint 8182/TH.401, Jan. 17, 1964.

[6] P. W. Higgs, *Broken Symmetries and the Masses of Gauge Bosons*, Phys. Rev. Lett. **13** (1964) 508–509. http://link.aps.org/doi/10.1103/PhysRevLett.13.508.

[7] S. Weinberg, *A Model of Leptons*, Phys. Rev. Lett. **19** (1967) 1264–1266. http://link.aps.org/doi/10.1103/PhysRevLett.19.1264.

[8] C. P. et al., *Parity non-conservation in inelastic electron scattering*, Physics Letters B **77** no. 3, (1978) 347 – 352. http://www.sciencedirect.com/science/article/pii/0370269378907220.

[9] UA1 Collaboration, *Experimental Observation of Isolated Large Transverse Energy Electrons with Associated Missing Energy at $s^{1/2} = 540$ GeV*, Phys. Lett. **B122** (1983) 103–116.

[10] UA1 Collaboration, *Experimental observation of lepton pairs of invariant mass around 95 GeV/c^2 at the CERN SPS collider*, Physics Letters B **126** no. 5, (1983) 398 – 410.

[11] S. e. a. Abachi, *Search for High Mass Top Quark Production in $p\overline{p}$ Collisions at $\sqrt{s} = 1.8$ TeV*, Phys. Rev. Lett. **74** (1995) 2422–2426. http://link.aps.org/doi/10.1103/PhysRevLett.74.2422.

[12] F. e. a. Abe, *Observation of Top Quark Production in $\overline{p}p$ Collisions with the Collider Detector at Fermilab*, Phys. Rev. Lett. **74** (1995) 2626–2631. http://link.aps.org/doi/10.1103/PhysRevLett.74.2626.

[13] *Evidence for the spin-0 nature of the Higgs boson using {ATLAS} data*, Physics Letters B **726** no. 13, (2013) 120 – 144. http://www.sciencedirect.com/science/article/pii/S0370269313006527.

[14] A. Collaboration), *Measurement of Higgs boson production in the diphoton decay channel in pp collisions at center-of-mass energies of 7 and 8 TeV with the ATLAS detector*, Phys. Rev. D **90** (2014) 112015. http://link.aps.org/doi/10.1103/PhysRevD.90.112015.

[15] Planck Collaboration Collaboration, P. Ade et al., *Planck 2013 results. XVI. Cosmological parameters*, Astron.Astrophys. **571** (2014) A16, arXiv:1303.5076 [astro-ph.CO].

[16] *Planck Mission Brings Universe Into Sharp Focus, News 2013-109*,.

[17] J. B. et al. Particle Data Group, *The Review of Particle Physics*, Phys. Rev. **D86** (2012) 010001 (2012) and 2013 partial update for the 2014 edition.

[18] T. Sjöstrand, S. Mrenna, and P. Skands, *PYTHIA 6.4 physics and manual*, JHEP **0605** (2006) 026.

[19] M. Bahr, S. Gieseke, M. Gigg, D. Grellscheid, K. Hamilton, et al., *Herwig++ Physics and Manual*, Eur.Phys.J. **C58** (2008) 639–707, arXiv:0803.0883 [hep-ph].

[20] G. P. Salam, *Elements of QCD for hadron colliders*, arXiv:1011.5131 [hep-ph].

[21] P. Skands, *Introduction to QCD*, arXiv:1207.2389 [hep-ph].

[22] T. Gleisberg, S. Hoeche, F. Krauss, A. Schalicke, S. Schumann, et al., *SHERPA 1. alpha: A Proof of concept version*, JHEP **0402** (2004) 056, arXiv:hep-ph/0311263 [hep-ph].

[23] ATLAS Collaboration Collaboration, G. Aad et al., *Measurement of underlying event characteristics using charged particles in pp collisions at* $\sqrt{s} = 900GeV$ *and 7 TeV with the ATLAS detector*, Phys.Rev. **D83** (2011) 112001, arXiv:1012.0791 [hep-ex].

[24] A. Martin, W. Stirling, R. Thorne, and G. Watt, *Parton distributions for the LHC*, Eur.Phys.J. **C63** (2009) 189–285, arXiv:0901.0002 [hep-ph].

[25] G. Altarelli and G. Parisi, *Asymptotic freedom in parton language*, Nuclear Physics B **126** no. 2, (1977) 298 – 318. http://www.sciencedirect.com/science/article/pii/0550321377903844.

[26] M. Guzzi, P. Nadolsky, E. Berger, H.-L. Lai, F. Olness, et al., *CT10 parton distributions and other developments in the global QCD analysis*, arXiv:1101.0561 [hep-ph].

[27] R. D. Ball, S. Carrazza, L. Del Debbio, S. Forte, J. Gao, et al., *Parton Distribution Benchmarking with LHC Data*, JHEP **1304** (2013) 125, arXiv:1211.5142 [hep-ph].

[28] M. Cacciari, G. P. Salam, and G. Soyez, *FastJet User Manual*, Eur.Phys.J. **C72** (2012) 1896, arXiv:1111.6097 [hep-ph].

[29] G. P. Salam, *Towards Jetography*, Eur.Phys.J. **C67** (2010) 637–686, arXiv:0906.1833 [hep-ph].

[30] G. P. Salam and G. Soyez, *A Practical Seedless Infrared-Safe Cone jet algorithm*, JHEP **0705** (2007) 086, arXiv:0704.0292 [hep-ph].

[31] M. Cacciari, G. P. Salam, and G. Soyez, *The Anti-k(t) jet clustering algorithm*, JHEP **0804** (2008) 063, arXiv:0802.1189 [hep-ph].

[32] G. Soyez, *Optimal jet radius in kinematic dijet reconstruction*, JHEP **1007** (2010) 075, arXiv:1006.3634 [hep-ph].

[33] ATLAS Collaboration Collaboration, G. Aad et al., *ATLAS search for new phenomena in dijet mass and angular distributions using pp collisions at* $\sqrt{s} = 7$ *TeV*, JHEP **1301** (2013) 029, arXiv:1210.1718 [hep-ex].

[34] U. Baur, M. Spira, and P. M. Zerwas, *Excited-quark and -lepton production at hadron colliders*, Phys. Rev. D **42** (1990) 815–824. http://link.aps.org/doi/10.1103/PhysRevD.42.815.

[35] O. Çak ır and R. Mehdiyev, *Excited quark production at the CERN LHC*, Phys. Rev. D **60** (1999) 034004. http://link.aps.org/doi/10.1103/PhysRevD.60.034004.

[36] UA2 Collaboration Collaboration, J. Alitti et al., *A Search for new intermediate vector mesons and excited quarks decaying to two jets at the CERN* $\bar{p}p$ *collider*, Nucl.Phys. **B400** (1993) 3–24.

[37] D0 Collaboration Collaboration, V. Abazov et al., *Search for new particles in the two jet decay channel with the D0 detector*, Phys.Rev. **D69** (2004) 111101, arXiv:hep-ex/0308033 [hep-ex].

[38] CDF Collaboration Collaboration, T. Aaltonen et al., *Search for new particles decaying into dijets in proton-antiproton collisions at s**(1/2) = 1.96-TeV*, Phys.Rev. **D79** (2009) 112002, arXiv:0812.4036 [hep-ex].

[39] G. Altarelli, B. Mele, and M. Ruiz-Altaba, *Searching for New Heavy Vector Bosons in* $p\bar{p}$ *Colliders*, Z.Phys. **C45** (1989) 109.

[40] ATLAS Collaboration Collaboration, G. Aad et al., *Search for a heavy gauge boson decaying to a charged lepton and a neutrino in 1 fb-1 of pp collisions at* $\sqrt{s} = 7$ *TeV using the ATLAS detector*, Phys.Lett. **B705** (2011) 28–46, arXiv:1108.1316 [hep-ex].

[41] S. Weinberg, *ULTRAVIOLET DIVERGENCES IN QUANTUM THEORIES OF GRAVITATION*,.

[42] K. Stelle, *String Theory, Unification and Quantum Gravity*, Lect.Notes Phys. **863** (2013) 3–30, arXiv:1203.4689 [hep-th].

[43] N. Kitazawa, *A Closer look at string resonances in dijet events at the LHC*, JHEP **1010** (2010) 051, arXiv:1008.4989 [hep-ph].

[44] M. Hashi and N. Kitazawa, *Detectability of the second resonance of low-scale string models at the LHC*, JHEP **1303** (2013) 127, arXiv:1212.5372 [hep-ph].

[45] N. Kitazawa, *Event Generation of String Resonances using CalcHEP*, http://chercher.phys.se.tmu.ac.jp/StringEventsCalcHEP.html (2011).

[46] A. Sherstnev and R. Thorne, *Parton Distributions for LO Generators*, Eur. Phys. J. **C55** (2008) 553–575.

[47] P. Sikivie, *AN INTRODUCTION TO TECHNICOLOR*,.

[48] C. D. Carone, *Technicolor with a 125 GeV Higgs Boson*, Phys.Rev. **D86** (2012) 055011, arXiv:1206.4324 [hep-ph].

[49] T. Han, I. Lewis, and Z. Liu, *Colored Resonant Signals at the LHC: Largest Rate and Simplest Topology*, JHEP **1012** (2010) 085, arXiv:1010.4309 [hep-ph].

[50] J. Alwall, M. Herquet, F. Maltoni, O. Mattelaer, and T. Stelzer, *MadGraph 5 : Going Beyond*, JHEP **1106** (2011) 128, arXiv:1106.0522 [hep-ph].

[51] J. Pumplin et al., *New generation of parton distributions with uncertainties from global QCD analysis*, JHEP **0207** (2002) 012.

[52] R. Sekhar Chivukula, E. H. Simmons, and N. Vignaroli, *Distinguishing dijet resonances at the LHC*, Phys.Rev. **D91** no. 5, (2015) 055019, arXiv:1412.3094 [hep-ph].

[53] S. Catani and M. Seymour, *A General algorithm for calculating jet cross-sections in NLO QCD*, Nucl.Phys. **B485** (1997) 291–419, arXiv:hep-ph/9605323 [hep-ph].

[54] Z. Nagy, *Next-to-leading order calculation of three jet observables in hadron hadron collision*, Phys.Rev. **D68** (2003) 094002, arXiv:hep-ph/0307268 [hep-ph].

[55] ATLAS Collaboration Collaboration, G. Aad et al., *Measurement of inclusive jet and dijet production in pp collisions at $\sqrt{s} = 7$ TeV using the ATLAS detector*, Phys.Rev. **D86** (2012) 014022, arXiv:1112.6297 [hep-ex].

[56] T. Carli, D. Clements, A. Cooper-Sarkar, C. Gwenlan, G. P. Salam, et al., *A posteriori inclusion of parton density functions in NLO QCD final-state calculations at hadron colliders: The APPLGRID Project*, Eur.Phys.J. **C66** (2010) 503–524, arXiv:0911.2985 [hep-ph].

[57] A. Martin, R. Roberts, W. Stirling, and R. Thorne, *Uncertainties of predictions from parton distributions. 1: Experimental errors*, Eur.Phys.J. **C28** (2003) 455–473, arXiv:hep-ph/0211080 [hep-ph].

[58] H.-L. Lai et al., *New parton distributions for collider physics*, Phys. Rev. **D82** (2010) 074024.

[59] The ATLAS collaboration, *ATLAS tunes of PYTHIA 6 and Pythia 8 for MC11*, ATL-PHYS-PUB-2011-009 (2011).

[60] P. Z. Skands, *Tuning Monte Carlo Generators: The Perugia Tunes*, Phys.Rev. **D82** (2010) 074018, arXiv:1005.3457 [hep-ph].

[61] S. Gieseke, C. Rohr, and A. Siodmok, *Colour reconnections in Herwig++*, Eur.Phys.J. **C72** (2012) 2225, arXiv:1206.0041 [hep-ph].

[62] S. Dittmaier, A. Huss, and C. Speckner, *Weak radiative corrections to dijet production at hadron colliders*, JHEP **1211** (2012) 095, arXiv:1210.0438 [hep-ph].

[63] S. Alioli, K. Hamilton, P. Nason, C. Oleari, and E. Re, *Jet pair production in POWHEG*, JHEP **1104** (2011) 081, arXiv:1012.3380 [hep-ph].

[64] P. Nason and C. Oleari, *Generation cuts and Born suppression in POWHEG*, arXiv:1303.3922 [hep-ph].

[65] ATLAS Collaboration, G. Aad et al., *Measurement of the inclusive jet cross section in pp collisions at sqrt(s)=2.76 TeV and comparison to the inclusive jet cross section at sqrt(s)=7 TeV using the ATLAS detector*, Eur.Phys.J. **C73** no. 8, (2013) 2509, arXiv:1304.4739 [hep-ex].

[66] S. Frixione, P. Nason, and G. Ridolfi, *The POWHEG-hvq manual version 1.0*, arXiv:0707.3081 [hep-ph].

[67] O. S. Brüning et al., *LHC Design Report Volume I. The LHC Main Ring.* CERN, Geneva, 2004.

[68] TOTEM Collaboration, G. Antchev et al., *Measurement of proton-proton elastic scattering and total cross-section at $\sqrt{s} = 7$ TeV*, Europhys.Lett. **101** (2013) 21002.

[69] ATLAS Collaboration, G. Aad et al., *Measurement of the Inelastic Proton-Proton Cross-Section at $\sqrt{s} = 7$ TeV with the ATLAS Detector*, Nature Commun. **2** (2011) 463, arXiv:1104.0326 [hep-ex].

[70] LHCb Collaboration, J. Alves, A. Augusto et al., *The LHCb Detector at the LHC*, JINST **3** (2008) S08005.

[71] ALICE Collaboration, K. Aamodt et al., *The ALICE experiment at the CERN LHC*, JINST **3** (2008) S08002.

[72] CMS Collaboration, S. Chatrchyan et al., *The CMS experiment at the CERN LHC*, JINST **3** (2008) S08004.

[73] ATLAS Collaboration, G. Aad et al., *The ATLAS Experiment at the CERN Large Hadron Collider*, JINST **3** (2008) S08003.

[74] LHCf Collaboration, O. Adriani et al., *The LHCf detector at the CERN Large Hadron Collider*, JINST **3** (2008) S08006.

[75] TOTEM Collaboration, G. Anelli et al., *The TOTEM experiment at the CERN Large Hadron Collider*, JINST **3** (2008) S08007.

[76] MoEDAL Collaboration, B. Caron, H. Dekhissi, M. Placidi, K. Kinoshita, A. Houdayer, et al., *MONOPOLE AND EXOTIC PARTICLE DETECTOR AT THE LHC*,. http://moedal.web.cern.ch/content/moedal-detector.

[77] ATLAS Collaboration. https://twiki.cern.ch/twiki/bin/view/AtlasPublic/LuminosityPublicResults#2011_pp_Collisions. Accessed: 2013/12/28.

[78] ATLAS Collaboration, G. Aad et al., *Improved luminosity determination in pp collisions at $\sqrt{s}$ = 7 TeV using the ATLAS detector at the LHC*, Eur.Phys.J. **C73** (2013) 2518, arXiv:1302.4393 [hep-ex].

[79] G. Aad, M. Ackers, F. Alberti, M. Aleppo, G. Alimonti, et al., *ATLAS pixel detector electronics and sensors*, JINST **3** (2008) P07007.

[80] A. Ahmad, Z. Albrechtskirchinger, P. Allport, J. Alonso, L. Andricek, et al., *The Silicon microstrip sensors of the ATLAS semiconductor tracker*, Nucl.Instrum.Meth. **A578** (2007) 98–118.

[81] ATLAS TRT Collaboration Collaboration, E. Abat et al., *The ATLAS Transition Radiation Tracker (TRT) proportional drift tube: Design and performance*, JINST **3** (2008) P02013.

[82] ATLAS Collaboration Collaboration, *Particle Identification Performance of the ATLAS Transition Radiation Tracker*, Tech. Rep. ATLAS-CONF-2011-128, CERN, Geneva, Sep, 2011. http://cds.cern.ch/record/1383793.

[83] G. Aad et al., *The ATLAS Inner Detector commissioning and calibration*, European Physical Journal C **70** (2010) 787–821, arXiv:1004.5293 [physics.ins-det].

[84] ATLAS Collaboration Collaboration, *Performance of primary vertex reconstruction in proton-proton collisions at $\sqrt{s}$ =7 TeV in the ATLAS experiment*, Tech. Rep. ATLAS-CONF-2010-069, CERN, Geneva, Jul, 2010. http://cds.cern.ch/record/1281344.

[85] V. Lacuesta, *Track and Vertex Reconstruction in the ATLAS Experiment*, JINST **8** (2013) C02035.

[86] ATLAS Collaboration Collaboration, *Observation of an excess of events in the search for the Standard Model Higgs boson in the gamma-gamma channel with the ATLAS detector*, Tech. Rep. ATLAS-CONF-2012-091, CERN, Geneva, Jul, 2012. http://cds.cern.ch/record/1460410.

[87] F. Cavallari, *Performance of calorimeters at the LHC*, Journal of Physics: Conference Series **293** no. 1, (2011) 012001. http://stacks.iop.org/1742-6596/293/i=1/a=012001.

[88] M. e. a. Aharrouche, *Energy linearity and resolution of the ATLAS electromagnetic barrel calorimeter in an electron test-beam*, Nuclear Instruments and Methods in Physics Research A **568** (2006) 601–623, physics/0608012.

[89] A. A. et al., *The ATLAS Forward Calorimeter*, Journal of Instrumentation **3** no. 02, (2008) P02010. http://stacks.iop.org/1748-0221/3/i=02/a=P02010.

[90] Bazan, A. and others, *The ATLAS liquid argon calorimeter read-out system*, IEEE Trans.Nucl.Sci. **53** (2006) 735–740.

[91] W. Cleland and E. Stern, *Signal processing considerations for liquid ionization calorimeters in a high rate environment*, Nucl.Instrum.Meth. **A338** no. 2-3, (1994) 467–497.

[92] A. Collaboration, *ATLAS liquid argon calorimeter: Technical design report*,.

[93] P. Klimek and on behalf of the ATLAS Tile Calorimeter group), *Signal reconstruction performance with the ATLAS Hadronic Tile Calorimeter*, Journal of Physics: Conference Series **404** no. 1, (2012) 012046. http://stacks.iop.org/1742-6596/404/i=1/a=012046.

[94] ATLAS Collaboration, C. Clement and P. Klimek, *Identification of Pile-up Using the Quality Factor of Pulse Shapes in the ATLAS Tile Calorimeter*,.

[95] ATLAS Collaboration Collaboration, *Luminosity Determination Using the ATLAS Detector*, Tech. Rep. ATLAS-CONF-2010-060, CERN, Geneva, Jul, 2010. https://cds.cern.ch/record/1281333.

[96] P. Jenni, M. Nordberg, M. Nessi, and K. Jon-And, *ATLAS Forward Detectors for Measurement of Elastic Scattering and Luminosity*. Technical Design Report. CERN, Geneva, 2008.

[97] V. Cindro, D. Dobos, I. Dolenc, H. Frais-Kolbl, H. Frais-Koelbl, et al., *The ATLAS beam conditions monitor*, JINST **3** (2008) P02004.

[98] ATLAS Collaboration Collaboration, *ATLAS muon spectrometer: Technical Design Report*. Technical Design Report ATLAS. CERN, Geneva, 1997. http://cds.cern.ch/record/331068.

[99] D. Casadei, *Performance of the ATLAS trigger system*, Journal of Physics: Conference Series **396** no. 1, (2012) 012011. http://stacks.iop.org/1742-6596/396/i=1/a=012011.

[100] R. Achenbach et al., *The ATLAS level-1 calorimeter trigger*, JINST **3** (2008) P03001.

[101] B. sman et al., *The ATLAS Level-1 Calorimeter Trigger: PreProcessor implementation and performance*, Journal of Instrumentation **7** no. 12, (2012) P12008. http://stacks.iop.org/1748-0221/7/i=12/a=P12008.

[102] ATLAS Collaboration, G. Aad et al., *Performance of the ATLAS Trigger System in 2010*, Eur.Phys.J. **C72** (2012) 1849, arXiv:1110.1530 [hep-ex].

[103] ATLAS Collaboration, *Expected Performance of the ATLAS Experiment - Detector, Trigger and Physics*, arXiv:0901.0512 (2009).

[104] T. Golling, H. Hayward, P. Onyisi, H. Stelzer, and P. Waller, *The ATLAS Data Quality Defect Database System*, Eur.Phys.J. **C72** (2012) 1960, arXiv:1110.6119 [physics.ins-det].

[105] M. Elsing, L. Goossens, A. Nairz, and G. Negri, *The ATLAS Tier-0: Overview and operational experience*, Journal of Physics: Conference Series **219** no. 7, (2010) 072011. http://stacks.iop.org/1742-6596/219/i=7/a=072011.

[106] ATLAS Collaboration Collaboration, G. Aad et al., *The ATLAS Simulation Infrastructure*, Eur.Phys.J. **C70** (2010) 823–874, arXiv:1005.4568 [physics.ins-det].

[107] GEANT4 Collaboration, *GEANT4: A simulation toolkit*, Nucl. Instrum. Meth. **A506** (2003) 250.

[108] ATLAS Collaboration, G. Aad et al., *Single hadron response measurement and calorimeter jet energy scale uncertainty with the ATLAS detector at the LHC*, Eur.Phys.J. **C73** no. 3, (2013) 2305, arXiv:1203.1302 [hep-ex].

[109] ATLAS Collaboration, A. Collaboration, *The simulation principle and performance of the ATLAS fast calorimeter simulation FastCaloSim*,.

[110] Z. Marshall and the Atlas Collaboration, *Simulation of Pile-up in the ATLAS Experiment*, Journal of Physics: Conference Series **513** no. 2, (2014) 022024. http://stacks.iop.org/1742-6596/513/i=2/a=022024.

[111] S. Menke, "Talk at BOOST 2013, Pile-Up in Jets in ATLAS." https://cds.cern.ch/record/1598801. ATL-PHYS-SLIDE-2013-540.

[112] ATLAS Collaboration, G. Aad et al., *Electron performance measurements with the ATLAS detector using the 2010 LHC proton-proton collision data*, Eur.Phys.J. **C72** (2012) 1909, arXiv:1110.3174 [hep-ex].

[113] ATLAS Collaboration Collaboration, G. Aad et al., *Jet energy measurement and its systematic uncertainty in proton-proton collisions at $\sqrt{s} = 7$ TeV with the ATLAS detector*, Eur.Phys.J. **C75** no. 1, (2015) 17, arXiv:1406.0076 [hep-ex].

[114] G. Pospelov, *The overview of the ATLAS local hadronic calibration*, J.Phys.Conf.Ser. **160** (2009) 012079.

[115] ATLAS Liquid Argon Calorimeter Collaboration, P. Giovannini, *Local hadron calibration with ATLAS*, J.Phys.Conf.Ser. **293** (2011) 012057.

[116] P. Billoir and S. Qian, *Fast vertex fitting with a local parametrization of tracks*, Nucl.Instrum.Meth. **A311** (1992) 139–150.

[117] ATLAS Collaboration Collaboration, G. Aad et al., *Jet energy measurement with the ATLAS detector in proton-proton collisions at $\sqrt{s} = 7$ TeV*, Eur.Phys.J. **C73** (2013) 2304, arXiv:1112.6426 [hep-ex].

[118] D. E. Groom, *Energy flow in a hadronic cascade: Application to hadron calorimetry*, Nuclear Instruments and Methods in Physics Research A **572** (2007) 633–653, physics/0605164.

[119] C. Cuenca Almenar, A. Corso-Radu, H. Hadavand, Y. Ilchenko, S. Kolos, et al., *ATLAS online data quality monitoring*, Nucl.Phys.Proc.Suppl. **215** (2011) 304–306.

[120] A. Barriuso Poy, H. Boterenbrood, H. Burckhart, J. Cook, V. Filimonov, et al., *The detector control system of the ATLAS experiment*, JINST **3** (2008) P05006.

[121] ATLAS Collaboration Collaboration, S. Farrell, *ATLAS Offline Data Quality System Upgrade*, J.Phys.Conf.Ser. **396** (2012) 052032.

[122] ATLAS, "LAr cleaning and object quality - TWiki: LArError event flag." `https://twiki.cern.ch/twiki/bin/view/AtlasProtected/LArCleaningAndObjectQuality#larError_event_flag`.

[123] ATLAS Collaboration Collaboration, G. Aad et al., *Characterisation and mitigation of beam-induced backgrounds observed in the ATLAS detector during the 2011 proton-proton run*, JINST **8** (2013) P07004, `arXiv:1303.0223 [hep-ex]`.

[124] E. Ladygin, "Trying to observe HEC Spikes in Lab." `http://indico.cern.ch/event/102931/material/slides/1?contribId=3`.

[125] B. Chase, M. Citterio, F. Lanni, D. Makowiecki, V. Radeka, et al., *Characterization of the coherent noise, electromagnetic compatibility and electromagnetic interference of the ATLAS EM calorimeter front end board,*.

[126] ATLAS Collaboration, G. Aad et al., *Measurement of dijet cross sections in pp collisions at 7 TeV centre-of-mass energy using the ATLAS detector*, JHEP **1405** (2014) 059, `arXiv:1312.3524 [hep-ex]`.

[127] F. James and M. Roos, *MINUIT: a system for function minimization and analysis of the parameter errors and corrections*, Comput. Phys. Commun. **10** no. CERN-DD-75-20, (1975) 343–367. 38 p.

[128] I. Antcheva et al., *ROOT – A C++ framework for petabyte data storage, statistical analysis and visualization*, Computer Physics Communications **180** no. 12, (2009) 2499 – 2512.

[129] V. Lendermann, J. Haller, M. Herbst, K. Kruger, H.-C. Schultz-Coulon, et al., *Combining Triggers in HEP Data Analysis*, Nucl.Instrum.Meth. **A604** (2009) 707–718, `arXiv:0901.4118 [hep-ex]`.

[130] ATLAS Collaboration, *Performance of the ATLAS Electron and Photon Trigger in p-p Collisions at sqrts = 7 TeV in 2011,*.

[131] ATLAS Collaboration, *Electron performance measurements with the ATLAS detector using the 2010 LHC proton-proton collision data*, Eur. Phys. J. **C72** (2012) 1909.

[132] ATLAS Collaboration, G. Aad et al., *Measurement of the inclusive isolated prompt photon cross section in pp collisions at $\sqrt{s} = 7$ TeV with the ATLAS detector*, Phys.Rev. **D83** (2011) 052005, `arXiv:1012.4389 [hep-ex]`.

[133] ATLAS Collaboration Collaboration, *ATLAS Computing: technical design report.* Technical Design Report ATLAS. CERN, Geneva, 2005. `http://acode-browser2.usatlas.bnl.gov/lxr-rel17/source/atlas/Reconstruction/`.

[134] ATLAS, "JetEtmissApproved2013Jer2011- TWiki: Public Results." https://twiki.cern.ch/twiki/bin/view/AtlasPublic/JetEtmissApproved2013Jer2011.

[135] D0 Collaboration, B. Abbott et al., *High-p_T jets in $\bar{p}p$ collisions at $\sqrt{s} = 630$ GeV and 1800 GeV*, Phys.Rev. **D64** (2001) 032003, arXiv:hep-ex/0012046 [hep-ex].

[136] UA2 Collaboration, Bern-CERN-Copenhagen-Orsay-Pavia-Saclay Collaboration Collaboration, P. Bagnaia et al., *Measurement of Jet Production Properties at the CERN anti-p p Collider*, Phys.Lett. **B144** (1984) 283.

[137] ATLAS Collaboration, G. Aad et al., *Jet energy resolution in proton-proton collisions at $\sqrt{s} = 7$ TeV recorded in 2010 with the ATLAS detector*, Eur.Phys.J. **C73** no. 3, (2013) 2306, arXiv:1210.6210 [hep-ex].

[138] M. L. Mangano, M. Moretti, F. Piccinini, R. Pittau, and A. D. Polosa, *ALPGEN, a generator for hard multiparton processes in hadronic collisions*, JHEP **0307** (2003) 001, arXiv:hep-ph/0206293 [hep-ph].

[139] ATLAS Collaboration Collaboration, E. Abat et al., *Study of energy response and resolution of the ATLAS barrel calorimeter to hadrons of energies from 20-GeV to 350-GeV*, Nucl.Instrum.Meth. **A621** (2010) 134–150.

[140] P. Adragna, C. Alexa, K. Anderson, A. Antonaki, A. Arabidze, et al., *Measurement of pion and proton response and longitudinal shower profiles up to 20 nuclear interaction lengths with the ATLAS tile calorimeter*, Nucl.Instrum.Meth. **A615** (2010) 158–181.

[141] ATLAS Collaboration, G. Aad et al., *Readiness of the ATLAS Tile Calorimeter for LHC collisions*, Eur.Phys.J. **C70** (2010) 1193–1236, arXiv:1007.5423 [physics.ins-det].

[142] ATLAS Collaboration, *Pile-up corrections for jets from proton-proton collisions at $\sqrt{s} = 7$ TeV in ATLAS in 2011*,.

[143] ATLAS Collaboration, G. Aad et al., *Light-quark and gluon jet discrimination in pp collisions at $\sqrt{s} = 7$* TeV *with the ATLAS detector*, Eur.Phys.J. **C74** no. 8, (2014) 3023, arXiv:1405.6583 [hep-ex].

[144] ATLAS Collaboration Collaboration, *Azimuthal Decorrelations in Dijet Events at sqrts = 7 TeV*,. http://cds.cern.ch/record/1298853.

[145] ATLAS Collaboration, G. Aad et al., *Measurement of the inclusive jet cross-section in proton-proton collisions at $\sqrt{s} = 7$ TeV using 4.5 fb^1 of data with the ATLAS detector*, JHEP **1502** (2015) 153, arXiv:1410.8857 [hep-ex].

[146] B. Malaescu, *An Iterative, Dynamically Stabilized(IDS) Method of Data Unfolding*, arXiv:1106.3107 [physics.data-an].

[147] B. Malaescu, *An Iterative, dynamically stabilized method of data unfolding*, arXiv:0907.3791 [physics.data-an].

[148] ATLAS Collaboration, G. Aad et al., *Search for New Physics in the Dijet Mass Distribution using 1 fb^{-1} of pp Collision Data at $\sqrt{s} = 7$ TeV collected by the ATLAS Detector*, Phys.Lett. **B708** (2012) 37–54, arXiv:1108.6311 [hep-ex].

[149] N. Boelaert, *Private Communications*. 2012.

[150] G. Choudalakis and D. Casadei, *Plotting the differences between data and expectation*, European Physical Journal Plus **127** (2012) 25, arXiv:1111.2062 [physics.data-an].

[151] G. Choudalakis, *On hypothesis testing, trials factor, hypertests and the BumpHunter*, arXiv:1101.0390v2 (2011).

[152] W. Gilks, S. Richardson, and D. Spiegelhalter, *Markov Chain Monte Carlo in Practice*. Chapman and Hall, 1996.

[153] ATLAS Collaboration Collaboration, *Luminosity Determination in pp Collisions at sqrt(s) = 7 TeV using the ATLAS Detector in 2011*, Tech. Rep. ATLAS-CONF-2011-116, CERN, Geneva, Aug, 2011. http://cds.cern.ch/record/1376384.

[154] ATLAS Collaboration, G. Aad et al., *Search for New Physics in Dijet Mass and Angular Distributions in pp Collisions at $\sqrt{s} = 7$ TeV Measured with the ATLAS Detector*, New J.Phys. **13** (2011) 053044, arXiv:1103.3864 [hep-ex].

[155] ATLAS Collaboration Collaboration, G. Aad et al., *Search for production of resonant states in the photon-jet mass distribution using pp collisions at $\sqrt{s} = 7$ TeV collected by the ATLAS detector*, Phys.Rev.Lett. **108** (2012) 211802, arXiv:1112.3580 [hep-ex].

[156] O. Çak ır, C. Leroy, and R. Mehdiyev, *Search for excited quarks with the ATLAS experiment at the CERN LHC: Double jets channel*, Phys. Rev. D **62** (2000) 114018. http://link.aps.org/doi/10.1103/PhysRevD.62.114018.

[157] ATLAS Collaboration, G. Aad et al., *ATLAS search for a heavy gauge boson decaying to a charged lepton and a neutrino in pp collisions at $\sqrt{s} = 7$ TeV*, Eur.Phys.J. **C72** (2012) 2241, arXiv:1209.4446 [hep-ex].

[158] CMS Collaboration, S. Chatrchyan et al., *Search for narrow resonances and quantum black holes in inclusive and b-tagged dijet mass spectra from pp collisions at $\sqrt{s} = 7$ TeV*, JHEP **1301** (2013) 013, arXiv:1210.2387 [hep-ex].

[159] ATLAS Collaboration, G. Aad et al., *Search for new phenomena in the dijet mass distribution using $p - p$ collision data at $\sqrt{s} = 8$ TeV with the ATLAS detector*, Phys.Rev. **D91** no. 5, (2015) 052007, arXiv:1407.1376 [hep-ex].

[160] CMS Collaboration, V. Khachatryan et al., *Search for resonances and quantum black holes using dijet mass spectra in proton-proton collisions at $\sqrt{s} = 8$ TeV*, Phys.Rev. **D91** no. 5, (2015) 052009, arXiv:1501.04198 [hep-ex].

[161] CMS Collaboration, S. Chatrchyan et al., *Search for Resonances in the Dijet Mass Spectrum from 7 TeV pp Collisions at CMS*, Phys.Lett. **B704** (2011) 123–142, arXiv:1107.4771 [hep-ex].

[162] ATLAS Collaboration, G. Aad et al., *Search for high-mass states with one lepton plus missing transverse momentum in proton-proton collisions at $\sqrt{s} = 7$ TeV with the ATLAS detector*, Phys.Lett. **B701** (2011) 50–69, arXiv:1103.1391 [hep-ex].

[163] J. Gallicchio and M. D. Schwartz, *Quark and Gluon Tagging at the LHC*, Phys.Rev.Lett. **107** (2011) 172001, arXiv:1106.3076 [hep-ph].

[164] M. Lehmacher, *b-Tagging Algorithms and their Performance at ATLAS*, arXiv:0809.4896 [hep-ex].

[165] J. Gallicchio and M. D. Schwartz, *Pure Samples of Quark and Gluon Jets at the LHC*, JHEP **1110** (2011) 103, arXiv:1104.1175 [hep-ph].

[166] *Dijet resonance searches with the ATLAS detector at 14 TeV LHC*, Tech. Rep. ATL-PHYS-PUB-2015-004, CERN, Geneva, Mar, 2015. http://cds.cern.ch/record/2002136.

[167] B. Heinemann, "Future Searches for New Physics at the LHC with ATLAS and CMS." https://indico.fnal.gov/materialDisplay.py?contribId=444&sessionId=31&materialId=slides&confId=6890.

A Appendix

A.1 A Detailed List of Exclusion Limits

m_{q*} [GeV]	Observed	Expected	Expected $\pm1\sigma$	Expected $\pm2\sigma$	$\mathcal{A}$
1000	1.43	0.55	0.36/1.064	0.31/1.58	0.299
1200	0.30	0.36	0.27/0.66	0.23/0.99	0.403
1400	0.16	0.22	0.17/0.35	0.14/0.52	0.459
1600	0.16	0.15	0.12/0.25	0.098/0.37	0.481
1800	0.16	0.10	0.079/0.16	0.065/0.24	0.497
2000	0.12	0.071	0.054/0.11	0.043/0.16	0.501
2250	0.064	0.045	0.034/0.070	0.027/0.10	0.505
2500	0.050	0.032	0.023/0.050	0.018/0.071	0.511
2750	0.032	0.023	0.016/0.036	0.013/0.051	0.499
3000	0.017	0.016	0.012/0.024	0.0094/0.034	0.500
3250	0.0081	0.011	0.0086/0.017	0.0069/0.024	0.505
3500	0.0056	0.0081	0.0062/0.012	0.0049/0.016	0.499
3750	0.0041	0.0063	0.0047/0.0090	0.0037/0.013	0.493
4000	0.0034	0.0049	0.0036/0.0070	0.0028/0.010	0.484

Table A.1: A list of *observed* and *expected* upper limits on $\sigma \times \mathcal{A}$ [pb] for the excited quark model q^* shown in Fig. 9.11. The expected $\pm1\sigma$ and $\pm2\sigma$ limits were used to construct the 68% and 95% error band respectively. The theory curve was calculated using the acceptances $\mathcal{A}$ given in this table (cf. Sec. 9.3.1).

$m_{W\prime}$ [GeV]	Observed	Expected	Expected $\pm1\sigma$	Expected $\pm2\sigma$	$\mathcal{A}$
1100	0.65	0.46	0.32/0.88	0.27/1.30	0.286
1200	0.29	0.35	0.26/0.62	0.22/0.90	0.314
1400	0.15	0.21	0.16/0.33	0.13/0.48	0.345
1600	0.15	0.14	0.11/0.23	0.094/0.33	0.358
1800	0.13	0.099	0.077/0.16	0.063/0.23	0.353
2000	0.12	0.072	0.055/0.11	0.045/0.16	0.341
2400	0.065	0.042	0.031/0.064	0.025/0.090	0.293

Table A.2: A list of *observed* and *expected* upper limits on $\sigma \times \mathcal{A}$ [pb] for the W' shown in Fig. 9.11. The expected $\pm1\sigma$ and $\pm2\sigma$ limits were used to construct the 68% and 95% error band respectively. The theory curve was calculated using the acceptances $\mathcal{A}$ given in this table (cf. Sec. 9.3.1).

m_{s8} [GeV]	Observed	Expected	Expected $\pm1\sigma$	Expected $\pm2\sigma$	$\mathcal{A}$
1300	0.40	0.68	0.38/1.45	0.31/2.20	0.339
1500	0.27	0.38	0.27/0.75	0.23/1.18	0.405
1700	0.24	0.27	0.20/0.52	0.17/0.79	0.443
2000	0.33	0.16	0.12/0.29	0.099/0.43	0.467
2500	0.17	0.084	0.059/0.14	0.049/0.21	0.484
3000	0.097	0.062	0.042/0.11	0.034/0.17	0.441
3500	0.034	0.049	0.036/0.079	0.030/0.12	0.390
4000	0.035	0.048	0.038/0.073	0.032/0.11	0.357

Table A.3: A list of *observed* and *expected* upper limits on $\sigma \times \mathcal{A}$ [pb] for the scalar octet shown in Fig. 9.11. The expected $\pm1\sigma$ and $\pm2\sigma$ limits were used to construct the 68% and 95% error band respectively. The theory curve was calculated using the acceptances $\mathcal{A}$ given in this table (cf. Sec. 9.3.1).

m_{SR} [GeV]	Observed	Expected	Expected $\pm1\sigma$	Expected $\pm2\sigma$	$\mathcal{A}$
2000	0.094	0.059	0.041/0.080	0.032/0.12	0.449
2500	0.036	0.026	0.017/0.034	0.013/0.048	0.447
3000	0.012	0.012	0.0077/0.016	0.0061/0.022	0.452
3500	0.0041	0.0059	0.0036/0.0069	0.0028/0.010	0.464
4000	0.0021	0.0032	0.0020/0.0038	0.0016/0.0058	0.458
4500	0.0016	0.0023	0.0016/0.0029	0.0013/0.0040	0.478
5000	0.0013	0.0019	0.0012/0.0024	0.0010/0.0034	0.482

Table A.4: A list of *observed* and *expected* upper limits on $\sigma \times \mathcal{A}$ [pb] for the string resonance shown in Fig. 9.11. The expected $\pm1\sigma$ and $\pm2\sigma$ limits were used to construct the 68% and 95% error band respectively. The theory curve was calculated using the acceptances $\mathcal{A}$ given in this table (cf. Sec. 9.3.1).

A.2 Model-Indpendent Limits

m_G [GeV]	$\sigma_G/m_G = 7\%$	$\sigma_G/m_G = 10\%$	$\sigma_G/m_G = 15\%$
1000	0.66	0.67	0.61
1100	0.56	0.58	0.57
1150	0.44	0.51	0.41
1200	0.28	0.37	0.26
1250	0.18	0.22	0.21
1300	0.14	0.16	0.18
1050	0.11	0.12	0.16
1350	0.093	0.11	0.16
1400	0.083	0.11	0.15
1450	0.084	0.10	0.17
1500	0.090	0.11	0.17
1550	0.087	0.12	0.20
1600	0.090	0.11	0.18
1650	0.082	0.11	0.17
1700	0.079	0.11	0.17
1750	0.078	0.10	0.15
1800	0.069	0.097	0.13
1850	0.066	0.091	0.12
1900	0.061	0.075	0.11
1950	0.054	0.068	0.095
2000	0.049	0.058	0.085
2100	0.035	0.047	0.073
2200	0.029	0.040	0.066
2300	0.027	0.036	0.054
2400	0.024	0.031	0.044
2500	0.020	0.027	0.032
2600	0.017	0.021	0.021
2700	0.014	0.017	0.013
2800	0.012	0.012	0.0084
2900	0.0087	0.0075	0.0063
3000	0.0062	0.0052	0.0047
3200	0.0030	0.0032	0.0032
3400	0.0021	0.0021	0.0021
3600	0.0015	0.0016	0.0016
3800	0.0012	0.0012	0.0013
4000	0.0010	0.0010	0.0011

Table A.5: Observed 95% CL upper limits on $\sigma \times \mathcal{A}$ in untis of pb for various masses ranging from 1 TeV to 4 TeV.

In Order to enable the possibility to estimate exclusion limits for a given NP model, Gaussian-shaped signal distributions were used. The method is discribed in Sec. 9.3.3. The observed 95% CL upper limits on $\sigma \times \mathcal{A}$ in untis of pb for various masses ranging

from 1 TeV to 4 TeV are listed in Tab. A.5.

A.3 Monte Carlo Simulation Details

The Monte Carlo simulation is used in order to construct transfer matrices, which are used as input for the unfolding procedure. For this purpose Pythia 6 with the Perugia2011 tune [60] was used. The MC is sub-divided in so-called JX samples. For this purpose the simulated events are organized in slices of the average transverse momentum $\hat{p}_{T,\mathrm{avg}}$ of the leading and second-leading final-state parton. The reason for this procedure is to provide MC samples with low statistical uncertainties in the high-p_T region. Not using a re-weighting procedure would lead to large statistical uncertainties in high-p_T due to the steeply falling nature of the p_T spectrum and limited CPU time. The number of generated events and the corresponding cross-sections are listed in Tab. A.6. For each JX sub-sample the distribution of interest is constructed which is weighted. These event-based weights are calculated as the corresponding cross-section divided by the number of events provided by the JX sample. Due to the fact that pile-up is modeled in MC, the transverse momentum of a low-p_T jet could migrate to higher p_T regions. The events of those low-p_T jets carry large weights and thus can cause large statistical uncertainties.

JX sample	Cross-section [pb]	Number of events	$\hat{p}_{T,\mathrm{avg}}$ interval [GeV]
J0	8.1442E+09	2798297	4 - 8
J1	5.2454E+08	2798443	8 - 17
J2	3.0399E+07	2795891	35 - 70
J3	1.6092E+06	2797982	70 - 140
J4	6.6284E+04	2797431	140 - 280
J5	1.9254E+03	2796405	280 - 560
J6	3.1137E+01	2796826	560 - 1120
J7	1.3513E-01	1398937	1120 - 2240
J8	5.0907E-06	1397377	2240 -

Table A.6: Details of the Pythia MC JX samples used e.g. in context of the cross-section measurements.

A.4 Impact of Out-of-time Pile-up in the Low-p_T Regime on Jet Measurement

In this section several distributions are shown which provide further information on the impact of out-of-time pile-up on the jet measurements. Explanations and conclusions are give in the corresponding captions of the figures. The following figures are shown in this context: A.1, A.2, A.3, A.4, and A.5. Out-of-time pile-up affects the inclusive jet cross-section measurement in the low-p_T region as discussed in Sec. 8.4.2.

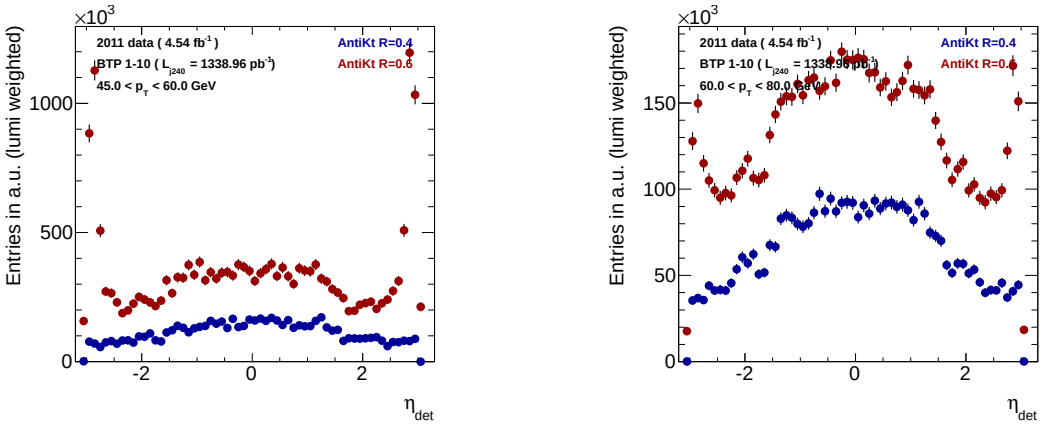

Figure A.1: Distributions of jets according to the pseudorapidity η from events in the bunch train position interval BTP1-10 determined using data. The jets were reconstructed using the distance parameter $R = 0.4$ (blue) and $R = 0.6$ (red). The distributions are shown for jets reconstructed in the transverse momentum regions 45 GeV $\leq p_T <$ 60 GeV (left) and 60 GeV $\leq p_T <$ 80 GeV (right). As can be observed from these figures $R = 0.6$ jets are strongly affected. The impact of this effect depends on the transverse momentum of the jet as can be also observed in Fig. A.2.

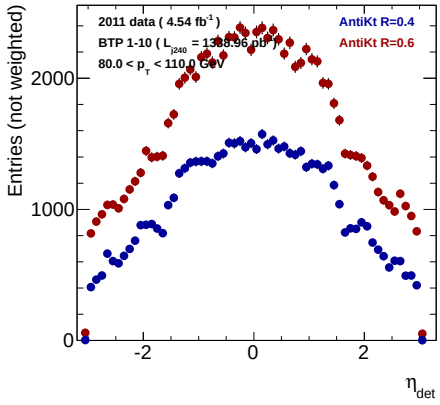

Figure A.2: Distributions of jets according to the pseudorapidity η from events in the bunch train position interval BTP1-10 determined using data. The jets were reconstructed using the distance parameter $R = 0.4$ (blue) and $R = 0.6$ (red). The distributions are shown for jets reconstructed in the transverse momentum region 80 GeV $\leq p_T <$ 110 GeV. The jet yield is hardly affected by out-of-time pile-up in case of jet transverse momenta above 80 GeV.

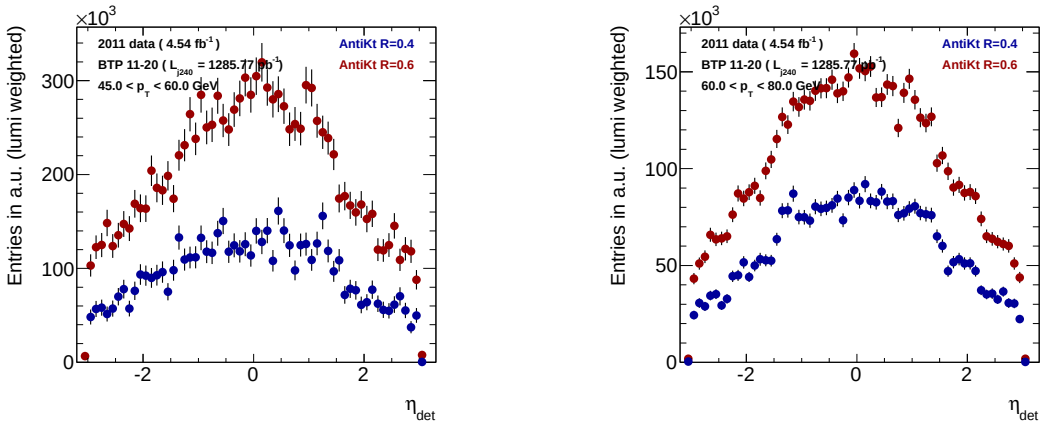

Figure A.3: Distributions of jets according to the pseudorapidity η from events in the bunch train position interval BTP11-20 determined using data. The jets were reconstructed using the distance parameter $R = 0.4$ (blue) and $R = 0.6$ (red). The distributions are shown for jets reconstructed in the transverse momentum regions 45 GeV $\leq p_T <$ 60 GeV (left) and 60 GeV $\leq p_T <$ 80 GeV (right). The effect shown in Fig. A.1 can no be observed for events originating from BTP 11-20.

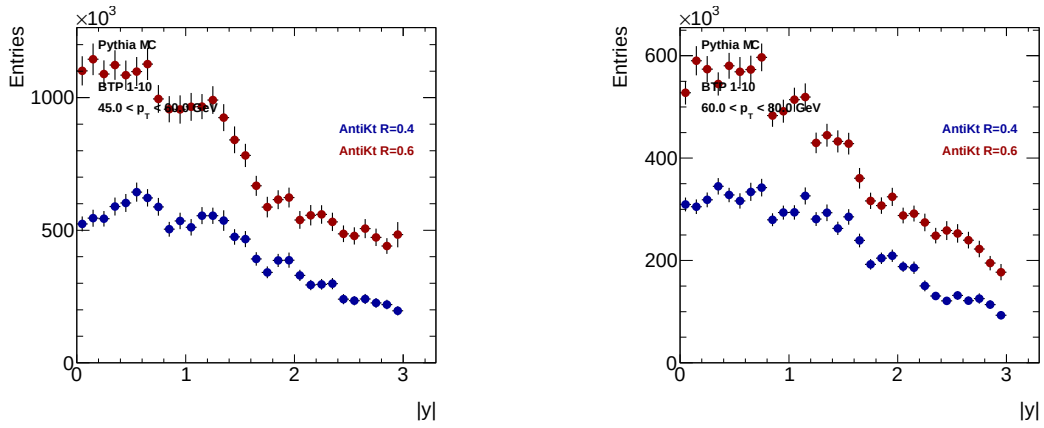

Figure A.4: Distributions of jets according to the absolute value of the rapidity from events in the bunch train position interval BTP1-10 determined using MC. The jets were reconstructed using the distance parameter $R = 0.4$ (blue) and $R = 0.6$ (red). The distributions are shown for jets reconstructed in the transverse momentum regions 45 GeV $\leq p_T <$ 60 GeV (left) and 60 GeV $\leq p_T <$ 80 GeV (right). The effect shown in Fig. A.1 is not simulated in MC.

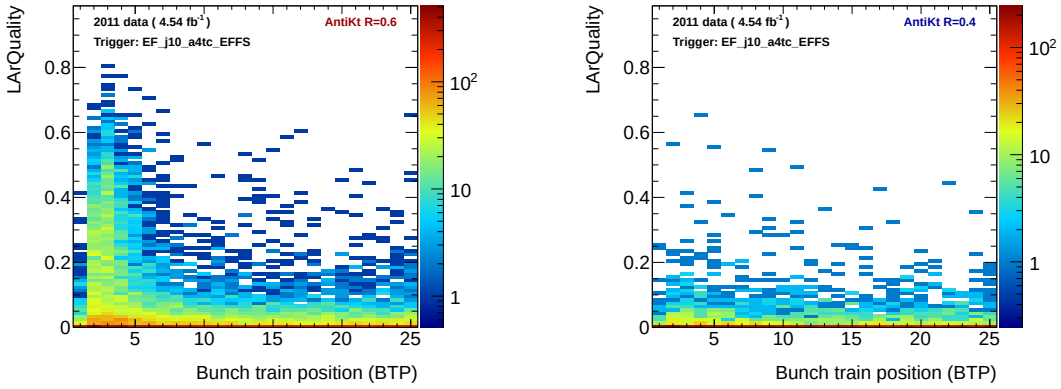

Figure A.5: LArQuality as function of bunch train position (BTP) for jets reconstructed using $R = 0.6$ (left) $R = 0.4$ (right). The quantity LArQuality $\equiv Q^{\mathrm{LAr}}_{\mathrm{mean}}$ is defined in Sec. 6.1.2. The trigger labeled as 'EF_j10_a4tc_EFFS' corresponds to the transverse momentum interval 50 GeV $\leq p_T <$ 56 GeV (cf. Tab. 6.3 in Sec. 6.2). A portion of jets with $R = 0.6$ have a large number of cells with distorted pulse shapes. This effect is correlated with the bunch train positions of the corresponding events.

Entfernt auf Grund datenschutzrechtlicher Bestimmungen.

Entfernt auf Grund datenschutzrechtlicher Bestimmungen.